

# Global simulated soil biogenic nitric oxide (NO) emissions: Impact, improvement and innovation

Dissertation zur Erlangung des Grades  
„Doktor der Naturwissenschaften“  
im Promotionsfach Geographie

am Fachbereich Chemie, Pharmazie und Geowissenschaften der  
Johannes Gutenberg-Universität Mainz

Jörg Steinkamp

geboren am 5.9.1976 in Stuttgart Bad Cannstatt, Deutschland

Mainz, 2011

Dekan:

1. Berichterstatter:

2. Berichterstatter:

Tag der mündlichen Prüfung: 16. Februar 2011

D77 – Mainzer Dissertation

# Contents

<b>List of figures</b>	<b>iii</b>
<b>List of tables</b>	<b>vii</b>
<b>Abstract</b>	<b>ix</b>
<b>Zusammenfassung</b>	<b>xi</b>
<b>Preface</b>	<b>xii</b>
<b>1 Introduction</b>	<b>1</b>
1.1 Nitrogen in the terrestrial biosphere . . . . .	2
1.2 Soil NO emissions . . . . .	4
1.2.1 Nitrification . . . . .	5
1.2.2 Denitrification . . . . .	5
1.2.3 Chemodenitrification . . . . .	5
1.2.4 Pulsing: event based bursts of NO soil emissions . . .	6
1.2.5 Measurement of NO soil emission . . . . .	8
1.2.6 Modelling NO soil emissions . . . . .	9
1.3 Nitrogen oxide in the atmosphere . . . . .	13
1.4 Aims . . . . .	18
<b>2 Modelled NO soil emissions, related trace gases and oxidizing efficiency</b>	<b>19</b>
Abstract . . . . .	20
2.1 Introduction . . . . .	21
2.2 Model description and setup . . . . .	23
2.2.1 General . . . . .	23
2.2.2 Soil NO emission algorithm . . . . .	24
2.3 Results and discussion . . . . .	27
2.3.1 Influence of NO emissions on related trace gases . . .	28
2.3.2 Influence of SNO <sub>x</sub> on the oxidizing efficiency . . . . .	42
2.4 Conclusions and outlook . . . . .	44

<b>3 Simulated soil NO emission improvement</b>	<b>47</b>
Abstract . . . . .	48
3.1 Introduction . . . . .	49
3.2 Model framework and measurement compilation . . . . .	50
3.2.1 State of the Art Model . . . . .	51
3.2.2 Compilation of measurements . . . . .	54
3.3 Emission model updates . . . . .	57
3.3.1 Pulsing . . . . .	59
3.3.2 Ecosystem/Landcover (LC) . . . . .	61
3.3.3 Influence of model resolution . . . . .	61
3.3.4 Fertilizer induced NO emission (LC+FIE) . . . . .	63
3.3.5 Soil moisture state (LC+FIE+VSM) . . . . .	65
3.3.6 Emission Factors (YL95/SL11) . . . . .	66
3.3.7 Canopy reduction factor (CRF) . . . . .	74
3.4 Comparison to satellite-derived emission estimates . . . . .	76
3.5 Discussion . . . . .	78
3.6 Conclusions and outlook . . . . .	83
<b>4 Novel soil biogenic NO emission algorithm</b>	<b>85</b>
Abstract . . . . .	86
4.1 Introduction . . . . .	87
4.2 Algorithm description . . . . .	88
4.3 Results and discussion . . . . .	91
4.4 Conclusion and outlook . . . . .	96
<b>5 Final conclusions and outlook</b>	<b>99</b>
Final conclusions . . . . .	100
Outlook . . . . .	101
<b>Literature</b>	<b>116</b>
<b>Appendices</b>	<b>117</b>
A Supplementary material for chapter 2 . . . . .	119
B Supplementary material for chapter 3 . . . . .	150
C Supplementary material for chapter 4 . . . . .	157

# List of Figures

1.1	Global natural nitrogen cycle. Figure is adopted from Steinkamp (2007). Quantities are based on <sup>a</sup> Galloway et al. (1995), <sup>b</sup> Holland et al. (1999), <sup>c</sup> Olivier et al. (1998), <sup>d</sup> Schumann and Huntrieser (2007) and <sup>e</sup> Seinfeld and Pandis (1998). . . . .	3
1.2	Hole in the pipe model, modified after Firestone and Davidson (1989) . . . . .	4
1.3	A conceptual model of controls on nitrification from Williams et al. (1992b), ©1992 AGU, reproduced with permission. . .	6
1.4	Conceptual representation of the products by nitrification and denitrification depending on the water filled pore space (WFPS) from Kirkman (2001). . . . .	7
1.5	NO emission depending on the ecosystem and wet or dry emission factor and temperature according to Yienger and Levy (1995). . . . .	12
1.6	Rain induced pulsing based on the amount of precipitation during one day after a certain period of dryness according to Yienger and Levy (1995). . . . .	13
2.1	Scatterplots of measured versus modeled NO emission flux from soils in different ecosystems. Measurements under natural conditions are colored in green and anthropogenically influenced measurements are in blue, mean and standard deviation slightly darker. . . . .	26
2.2	Simulated SNO <sub>x</sub> flux for (a) December 1994 to February 1995 and (b) June to August 1995 in $\frac{\text{ng}}{\text{m}^2\text{sec}}$ . . . . .	28
2.3	Zonal mean relative contribution of the eight major OH producing reactions in the BASE simulation integrated over one year. . . . .	31
2.4	Relative difference ( $\frac{\text{NOBIONO}-\text{BASE}}{\text{BASE}} * 100\%$ ) of the lower tropospheric mixing ratio of NO <sub>x</sub> in % (regions with values below 30 pmol mol <sup>-1</sup> in the BASE simulation are excluded from the calculation) averaged for (a) December, January, February and (b) June, July and August. . . . .	32

2.5	Zonal mean relative difference ( $\frac{\text{NOBIONO}-\text{BASE}}{\text{BASE}} * 100\%$ ) of the $\text{NO}_x$ mixing ratio in % averaged for (a) December, January, February and (b) June, July and August. Note that the y-axis is linearly scaled, since the focus of this work lies in the lower troposphere. . . . .	33
2.6	Relative difference ( $\frac{\text{REDOTHER}-\text{BASE}}{\text{BASE}} * 100\%$ ) of the lower tropospheric mixing ratio of $\text{NO}_x$ in % (regions with values below $30 \text{ pmol mol}^{-1}$ in the BASE simulation are excluded from the calculation) averaged for (a) December, January, February and (b) June, July and August. . . . .	34
2.7	Zonal mean relative difference ( $\frac{\text{REDOTHER}-\text{BASE}}{\text{BASE}} * 100\%$ ) of the $\text{NO}_x$ mixing ratio in % averaged for (a) December, January, February and (b) June, July and August. . . . .	36
2.8	Relative difference ( $\frac{\text{NOBIONO}-\text{BASE}}{\text{BASE}} * 100\%$ ) of the lower tropospheric mixing ratio of PAN in % (regions with values below $50 \text{ pmol mol}^{-1}$ in the BASE run are excluded from the calculation) averaged for (a) December, January, February and (b) June, July and August. . . . .	37
2.9	Zonal mean relative difference ( $\frac{\text{NOBIONO}-\text{BASE}}{\text{BASE}} * 100\%$ ) of the PAN mixing ratio in % averaged for (a) December, January, February and (b) June, July and August. . . . .	38
2.10	Relative difference ( $\frac{\text{NOBIONO}-\text{BASE}}{\text{BASE}} * 100\%$ ) of the lower tropospheric mixing ratio of $\text{HNO}_3$ in % (region with values below $30 \text{ pmol mol}^{-1}$ in the BASE simulation are excluded from the calculation) averaged for (a) December, January, February and (b) June, July and August. . . . .	39
2.11	Relative difference ( $\frac{\text{NOBIONO}-\text{BASE}}{\text{BASE}} * 100\%$ ) of the lower tropospheric mixing ratio of $\text{O}_3$ in % (regions with values below $25 \text{ nmol mol}^{-1}$ in the BASE simulation are excluded from the calculation) averaged for (a) December, January, February and (b) June, July and August. . . . .	40
2.12	Relative difference ( $\frac{\text{NOBIONO}-\text{BASE}}{\text{BASE}} * 100\%$ ) of the lower tropospheric concentration of OH in % (regions with values below $10^4 \text{ molec cm}^{-3}$ in the BASE simulation are excluded from the calculation) averaged for (a) December, January, February and (b) June, July and August. . . . .	41
2.13	Zonal mean relative difference ( $\frac{\text{NOBIONO}-\text{BASE}}{\text{BASE}} * 100\%$ ) of the OH concentration in % averaged for (a) December, January, February and (b) June, July and August. . . . .	42
2.14	Zonal mean relative change in the OH production of the four major OH producing reactions in the NOBIONO simulation compared to the BASE simulation over one year. . . . .	43

---

2.15	Zonal mean relative change in the OH production of the four major OH producing reactions in the REDOTHER simulation compared to the BASE simulation over one year. . . . .	44
2.16	Seasonal cycle of monthly mean lifetime of CH <sub>4</sub> from December 1994 to December 1995 in years (calculated according to Lawrence et al., 2001). . . . .	45
2.17	Relative increase of $\tau_{\text{CH}_4}$ ( $\frac{\tau_{\text{CH}_4,\text{simulation}} - \tau_{\text{CH}_4,\text{BASE}}}{\tau_{\text{CH}_4,\text{BASE}}} * 100\%$ ) for the NOBIONO (red) and REDOTHER (blue) simulation in various zonal subdomains of the atmosphere (calculated according to Lawrence et al., 2001). . . . .	46
3.1	SNOx flux in the YL95EMAC simulation (in ng m <sup>-2</sup> s <sup>-1</sup> ), along with the locations of measurements (dots) and the regions referred to in section 3.3.6. . . . .	54
3.2	Logarithmic histogram and probability density function of all measured SNOx in the compilation with standard distribution, calculated mean and standard deviation. Black lines are all measurements, green are measurements under natural conditions and blue are anthropogenically altered measurements. The small peak at $-9.2 \approx -4 \cdot \ln(10)$ towards the left of the plot is because we replaced values $\leq 0$ with $10^{-4}$ . The dashed lines are the standard distributions including these replaced values and the dotted lines are the standard distributions where values $\leq 0$ were removed from the dataset, respectively. Number of measurements are in brackets. . . . .	56
3.3	Logarithmic histogram and probability density function per MODIS landcover and Koeppen main climate class (in brackets) of measured SNOx in the compilation. Color and line type as in Fig. 3.2. . . . .	57
3.4	Scatterplot of simulated SNOx in YL95EMAC for each corresponding period of the year versus each measurement along with the mean values and standard deviations. . . . .	58
3.5	Averaged SNOx flux in the whole simulation period (in ng m <sup>-2</sup> s <sup>-1</sup> ) for the LC simulation (upper panel) and the change compared to the YL95EMAC simulation (lower panel). . . . .	62
3.6	Change of soil biogenic NO emission with pulsing (green boxes), without pulsing (blue circles) and the pulsing fraction (triangles) for the LC simulation at four different horizontal resolutions. . . . .	63
3.7	Percentage of wet soil conditions during the whole simulation period. . . . .	66

*List of figures*

---

3.8	Distribution of calculated emissions factors for anthropogenically altered (orange, above center line) and unperturbed (blue, below center line) measurements. The number of calculated emission factors and number of measurements per crop are given on the right side, respectively. . . . .	68
3.9	Averaged SNOx flux in the whole simulation period (in $\text{ng m}^{-2} \text{s}^{-1}$ ) for the YL95/SL11 simulation (upper panel) and the change compared to the LC+FIE+VSM simulation (lower panel). . .	74
3.10	Distribution of calculated emissions factors for different crop types in the landcover “agriculture” with the number of calculated emission factors and number of measurements per crop class in brackets. . . . .	75
3.11	Averaged SNOx flux for the year 2000 of the Jaeglé et al. (2005) (J05) inverse modeling study (in $\text{ng m}^{-2} \text{s}^{-1}$ ) (upper panel) and the difference between the YL95/SL11 year 2000 simulation and the J05 results (YL95/SL11 – J05) (lower panel). . . . .	77
3.12	Difference between YL95EMAC and Jaeglé et al. (2005) (YL95-EMAC – J05) (in $\text{ng m}^{-2} \text{s}^{-1}$ ) for the year 2000. . . . .	78
3.13	Scatterplots of SNOx measurements versus model results for the YL95/SL11 simulations. . . . .	80
3.14	Density function plot of SNOx measurements (orange, right of center line) versus model output (blue, left of center line) for the YL95/SL11 simulation using the program by Kampstra (2008). . . . .	81
4.1	Dependency of median optimum WFPS on the annual precipitation. . . . .	89
4.2	Global pattern of simulated WFPS for the years 1990–2000. . .	91
4.3	Simulated SNOx flux in $\text{ng m}^{-2} \text{s}^{-1}$ using the same linear model for all landcovers. . . . .	95
4.4	Simulated SNOx flux in $\text{ng m}^{-2} \text{s}^{-1}$ using the same linear regression for all natural landcovers and a separate linear regression for agriculture . . . . .	95



# List of Tables

1.1	Dry and wet emission factors for the NO soil emission calculation according to Yienger and Levy (1995) . . . . .	11
1.2	Stomatal area indices used to calculate the canopy reduction factor. . . . .	14
2.1	Setup of the ECHAM5/MESSy model and applied submodels.	22
2.2	Ecosystems and emission factors according to Yienger and Levy (1995). . . . .	25
2.3	Simulated total NO <sub>x</sub> emissions, SNO <sub>x</sub> in Tg(N) in the BASE simulation and in brackets relative contribution of SNO <sub>x</sub> to the total NO emissions for different regions and periods. . . .	27
2.4	Correlation coefficient ( $R^2$ ) between surface SNO <sub>x</sub> flux values and the difference (NOBIONO-BASE) of the tracer burden in the overlying model surface layer (SL) lower troposphere (LT; >500 hPa) by gridcell, averaged over the corresponding period; only gridcells with a land surface fraction of at least 75% were included. . . . .	30
3.1	World surface areas of the YL95EMAC ecosystems and new YL95/SL11 landcover classes in the EMAC model. For YL95-EMAC the first number is as adopted from Olson (1992) and the number in brackets gives the area reduced by (1 – cultivation index) for non-agricultural areas and the cultivated area for agriculture with the cultivation index after Bouwman et al. (2002b). . . . .	52
3.2	Measured and simulated SNO <sub>x</sub> for the YL95EMAC ecosystems (in ng m <sup>-2</sup> s <sup>-1</sup> ). Measurements are taken from our compilation of measurements (numbers per ecosystem in brackets) and the simulated SNO <sub>x</sub> values are for the corresponding period of each simulated year. . . . .	59

3.3	The original (YL95) emission factors and the soil biogenic NO emissions calculated with the old ecosystems (YL95EMAC) and with the new landcover (LC). When not shown, standard deviations are less than or equal to 0.001. . . . .	60
3.4	Relative annual underestimation of SNOx in the coarser simulations compared to the T106 resolution of the YL95EMAC and LC simulation. Relative deviation if the emission factors (left value) or the gridcell emission flux (right value) is scaled by the previous underestimation. The last column lists the global area defined as wet in 10 <sup>6</sup> km <sup>2</sup> (which equals 111.8 10 <sup>6</sup> km <sup>2</sup> for the T106 simulation). . . . .	63
3.5	The adopted (YL95/SL11) emission factors (geometric mean) and associated soil biogenic NO emissions. When not shown, standard deviations are less than or equal to 0.001. . . . .	69
3.6	The adopted (YL95/SL11) emission factors (arithmetic mean) and associated soil biogenic NO emissions. . . . .	70
3.7	Comparison of new SNOx to a top-down study in eastern China. . . . .	79
4.1	Linear regression models of calculated SNOx at the optimum WFPS in relation to physical and chemical soil properties for different landcovers (as described by Steinkamp and Lawrence (2010)) and lumped landcover classes (grassland = all savannah, all grassland and woody savannah; temperate/boreal forests = closed shrubland, mixed f., dec. br.-leaved f. (A, B, C) and evergr. needlel. f.; tropical forests = forests in A and B climate). Significance codes: ‡ <i>p</i> < 0.001, † <i>p</i> < 0.005, ◊ <i>p</i> < 0.01, * <i>p</i> < 0.05, • <i>p</i> < 0.1. . . . .	93
4.2	Simulated SNOx flux in Tg(N) yr <sup>-1</sup> for individual landcover classes for SL10 and the different results derived by the regression models. . . . .	96

## Abstract

Nitric oxide (NO) is important for several chemical processes in the atmosphere. Together with nitrogen dioxide (NO<sub>2</sub>) it is better known as nitrogen oxide (NO<sub>x</sub>). NO<sub>x</sub> is crucial for the production and destruction of ozone. In several reactions it catalyzes the oxidation of methane and volatile organic compounds (VOCs) and in this context it is involved in the cycling of the hydroxyl radical (OH). OH is a reactive radical, capable of oxidizing most organic species. Therefore, OH is also called the “detergent” of the atmosphere. Nitric oxide originates from several sources: fossil fuel combustion, biomass burning, lightning and soils. Fossil fuel combustion is the largest source. The others are, depending on the reviewed literature, generally comparable to each other. The individual sources show a different temporal and spatial pattern in their magnitude of emission. Fossil fuel combustion is important in densely populated places, where NO from other sources is less important. In contrast NO emissions from soils (hereafter SNO<sub>x</sub>) or biomass burning are the dominant source of NO<sub>x</sub> in remote regions.

By applying an atmospheric chemistry global climate model (AC-GCM) I demonstrate that SNO<sub>x</sub> is responsible for a significant part of NO<sub>x</sub> in the atmosphere. Furthermore, it increases the O<sub>3</sub> and OH mixing ratio substantially, leading to a ~10% increase in the oxidizing efficiency of the atmosphere. Interestingly, through reduced O<sub>3</sub> and OH mixing ratios in simulations without SNO<sub>x</sub>, the lifetime of NO<sub>x</sub> increases in regions with other dominating sources of NO<sub>x</sub>, leading to a counterintuitive increase in the NO<sub>x</sub> mixing ratio there.

With a compilation of previous and recent measurements from the literature I improve the algorithm to calculate SNO<sub>x</sub> without changing the underlying mathematical principles. This leads to increased emissions, which are in better agreement with satellite derived emissions. To support future development in the field, I identify regions without measurements.

The most commonly applied algorithm to calculate SNO<sub>x</sub> uses a classification of twelve ecosystem, four that do not include any emissions and two are treated separately. The remaining six are categorized in either a wet or a dry soil moisture state and emissions are calculated as a function of soil temperature. However, global models have become more complex since the development of the previous algorithm, and therefore I can make use a continuous function of the soil moisture and soil temperature to calculate SNO<sub>x</sub>. I apply additional physical parameters, taken from a world soil database, and chemical parameters, taken from a biosphere model, to derive a new method for simulating SNO<sub>x</sub>. The results vary between 22 Tg(N) yr<sup>-1</sup> and 31 Tg(N) yr<sup>-1</sup>, which are above previous estimates (5.5 – 21 Tg(N) yr<sup>-1</sup>). However, the spatial pattern in general agrees well with previous estimates, indicating the promise of this future direction for SNO<sub>x</sub>.



## Zusammenfassung

Stickoxid ( $\text{NO}_x = \text{NO} + \text{NO}_2$ ) spielt eine wichtige Rolle bei vielen chemischen Prozessen in der Atmosphäre. Es ist vor allem sehr wichtig für die Produktion und Zerstörung von Ozon ( $\text{O}_3$ ). In mehreren Reaktionsschritten katalysiert  $\text{NO}_x$  die Oxidation von Methan und anderen leicht flüchtigen organischen Verbindungen. Bei diesen Reaktionen ist auch das Hydroxyl-Radikal (OH) beteiligt, welches aufgrund seiner hohen Oxidationswirkung auch als Waschmittel der „Atmosphäre“ bezeichnet wird. NO wird von verschiedenen Quellen emittiert: Verbrennung fossiler Brennstoffe, Biomasseverbrennung, Blitze und aus dem Boden (ab hier SNO<sub>x</sub>), wobei die Verbrennung fossiler Brennstoffe den größten Anteil hat und die übrigen, je nach Studie, miteinander vergleichbar sind. Fossile Verbrennung ist in dichtbesiedelten Regionen dominant, in entlegenen Regionen sind je nach Lage und Jahreszeit Biomassebrände oder SNO<sub>x</sub> die dominierende Quelle für NO.

Mit Hilfe eines globalen Atmosphärenchemie-Klimamodells zeige ich, daß SNO<sub>x</sub> für einen wesentlichen Anteil des atmosphärischen  $\text{NO}_x$  verantwortlich ist. Des Weiteren führen die erhöhte Konzentration von  $\text{O}_3$  und OH in der Atmosphäre durch SNO<sub>x</sub> zu einer  $\sim 10\%$ -igen Erhöhung der Oxidationseffektivität der Atmosphäre. Interessanterweise wird die Lebensdauer von  $\text{NO}_x$ , durch niedrigere  $\text{O}_3$  und OH Konzentrationen in einer Sensitivitätsstudie ohne SNO<sub>x</sub> verlängert. Dies führt zu einer, nicht unmittelbar zu vermutenden, Erhöhung der  $\text{NO}_x$  Konzentrationen in Regionen mit anderen dominierenden Quellen von NO als SNO<sub>x</sub>.

Mit einer Sammlung publizierter Messungen aus der Literatur verbessere ich den Algorithmus zur Berechnung von SNO<sub>x</sub>, ohne die zu Grunde liegenden mathematischen Prinzipien zu verändern. Dies führt, im Einklang mit satellitengestützten Studien, zu erhöhten SNO<sub>x</sub>. Zur Unterstützung von Messkampagnen zeige ich Regionen auf, in denen bisher noch keine Messungen durchgeführt wurden.

Der am meisten genutzte Algorithmus um SNO<sub>x</sub> zu berechnen unterscheidet zwölf Ökosysteme, vier weisen keine SNO<sub>x</sub> auf und zwei werden separat behandelt. Die übrigen sechs werden im zeitlichen Verlauf nach feuchten oder trockenen Bedingungen unterschieden und SNO<sub>x</sub> als Funktion der Temperatur berechnet. Über die Jahre sind globale Klimamodelle komplexer geworden und daher kann ich nun SNO<sub>x</sub> anhand einer kontinuierlichen Funktion mit der Bodenfeuchte und Bodentemperatur berechnen. Zusätzlich verwende ich sowohl chemische Bodenparameter aus einem Biosphärenmodell, als auch physikalische Parameter aus einem weltweiten Datensatz einer Bodenkarte. Mit der neuen Methode berechnen sich Werte von SNO<sub>x</sub> zwischen 22 und 31 Tg Jahr<sup>-1</sup>, die über bisherigen Abschätzungen von 5.5–21 Tg Jahr<sup>-1</sup> liegen. Eine hohe Übereinstimmung in der relativen geographischen Verteilung sieht für zukünftige Anwendungen sehr vielversprechend aus.

## Preface

This thesis is divided in 4 chapters and 3 appendices, where the three appendices are supplementary material to Chapter 2–4.

**Chapter 1:** Here I provide a general overview of nitric oxide (NO) emissions from the soil and important chemical reactions in the atmosphere involving NO. First I introduce the role of nitrogen and how NO is produced in the soil. Then I briefly describe how NO flux from soils is measured and different approaches to model NO soil emissions. Finally, the relevant species and reactions are described.

**Chapter 2:** This is a sensitivity modeling study. I compare differences in the chemical composition of a state-of-the-art model base simulation versus two sensitivity simulations: 1.) soil NO emissions are turned off, and 2.) other NO sources at the surface are reduced by the same amount. This covers changes in the mixing ratio of ozone ( $O_3$ ), hydroxyl radicals (OH) and the lifetime of methane ( $CH_4$ ) and considers feedback processes on nitrogen oxide ( $NO_X = NO + NO_2$ ). This work has been published in *Atmospheric Chemistry and Physics*.

**Chapter 3:** Within this chapter the most widely applied algorithm to calculate NO emission from soils is updated without changing the underlying physical and mathematical principles. This is a necessary step, since the development of this algorithm is more than 15 years old and there is an enormous amount of new measurements of soil NO emission fluxes available in the literature. This work is published in *Atmospheric Chemistry and Physics Discussion* and I present the revised version, which will be published in *Atmospheric Chemistry and Physics*.

**Chapter 4:** This chapter introduces a new algorithm to calculate soil NO emission. It is still suitable for atmospheric chemistry global climate models (AC-GCMs) without a detailed terrestrial carbon and nitrogen cycle, but it takes advantage of several important chemical parameters taken from a biosphere model and physical parameters from a global soil database. This chapter is foreseen for publication in *Geophysical Research Letters*.

This work has been made possible by a scholarship of the International Max Planck Research School (IMPRS) for atmospheric chemistry of the Max Planck Institute of chemistry in Mainz, Germany. The IMPRS and also the Max Planck Institute enabled me to visit the autumn school on “Climate Change: Causes & Impacts” in Cyprus and the summer school “Earth System Modeling School” in Helsinki. I have also been fortunate to take part at several international scientific conferences and to present my work there.

Prescribed by the regulations of the internet publisher (ArchiMed) the personal acknowledgment was deleted for data protection reasons. However, I am very grateful and appreciated all the support I got during my PhD time by the people listed in the printed version of this thesis.





# 1 Introduction

The carbon-based life on our planet consists mainly of the elements carbon, hydrogen, oxygen, nitrogen, phosphorus and sulfur. These elements account for a fraction of 95% of the biosphere. At least another 20 essential elements are necessary for life to exist as we know it (Schlesinger, 1997). Nitrogen is part of amino acids in living matter, but most of the nitrogen on earth is in the atmosphere in the form of molecular  $N_2$ , with a strong triple bond, which makes it poorly accessible for most life-forms. There is much less than 1% of the total atmospheric nitrogen available in other molecules, the most important ones are ammonia ( $NH_3$ ), nitrous oxide  $N_2O$ , nitric oxide (NO) and nitrogen dioxide ( $NO_2$ ), where the last two ones are rapidly interconverted in the atmosphere and are therefore called nitrogen oxide ( $NO_x$ ).  $NO_x$  is a very important compound and depending on its mixing ratio it is crucial for the formation and destruction of atmospheric ozone ( $O_3$ ) (Chameides et al., 1992).

The molecular nitrogen ( $N_2$ ) can enzymatically be fixed by very few microorganisms to make it bioavailable. Lightning also breaks up the triple bond of  $N_2$  and oxidizes nitrogen to nitric oxide (NO). Beginning in the industrial era, combustion processes have become a significant source of “fixed” nitrogen (nitrogen in another compound than  $N_2$ ) and since the first quarter of the 20th century molecular nitrogen can also be anthropogenically fixed by the Haber process. Today, the amount of synthetically fixed nitrogen has exceeded the amount of nitrogen fixed by natural processes (Galloway et al., 1995, 2004; Vitousek et al., 1997).

As soon as the nitrogen is transformed to a “fixed” or “reactive” form and is available in the biosphere or pedosphere it is subject to metabolic and chemical processes and becomes part of the terrestrial nitrogen cycle (Fig. 1.1). Once fixed, most of the nitrogen is recycled within the biosphere, but some nitrogen is transformed to gaseous molecules including NO and is emitted to the atmosphere.

## 1.1 Nitrogen in the terrestrial biosphere

As already mentioned, nitrogen is an essential element for life and it is an important determinant of ecosystem functioning. However, enhanced levels of fixed nitrogen lead to eutrophication of terrestrial and aquatic ecosystems and consequently to a loss of species diversity (Galloways et al., 2002; Mat-

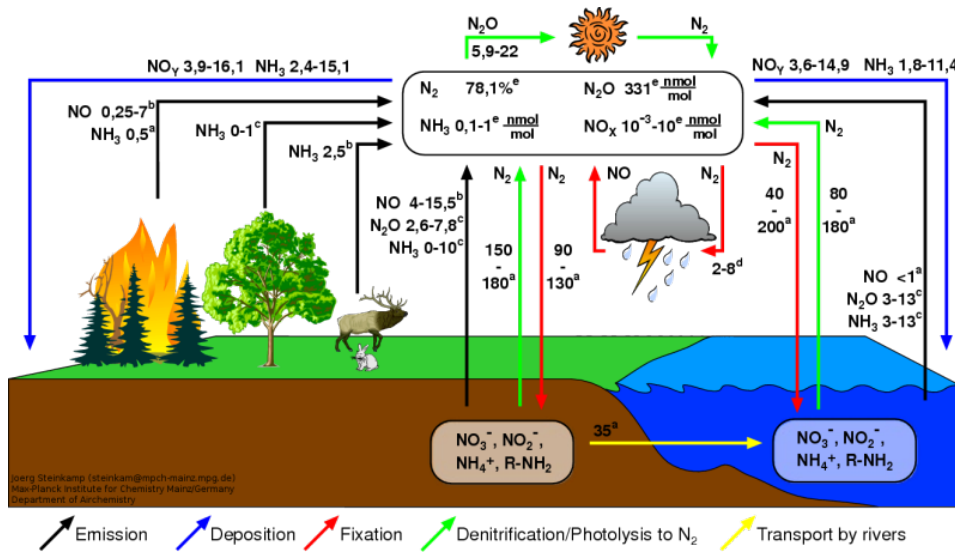


Figure 1.1: Global natural nitrogen cycle. Figure is adopted from Steinkamp (2007). Quantities are based on <sup>a</sup>Galloway et al. (1995), <sup>b</sup>Holland et al. (1999), <sup>c</sup>Olivier et al. (1998), <sup>d</sup>Schumann and Huntrieser (2007) and <sup>e</sup>Seinfeld and Pandis (1998).

son et al., 2002; Rabalais, 2002). The growth rate in most global ecosystems is thought to be limited by available nitrogen with a few exceptions, like ecosystems on very old soils in the tropics (Vitousek and Howarth, 1991). By biological fixation 90 to 130  $Tg(N) yr^{-1}$  enter the terrestrial biosphere. This value has meanwhile been approximately exceeded by synthetically fixed nitrogen with a total of 140  $Tg(N) yr^{-1}$  (Galloway et al., 1995). Once the nitrogen becomes part of the terrestrial biosphere, most of it is tied in organic molecules and is recycled, with a recycling rate of 1,200  $Tg(N) yr^{-1}$  according to Schlesinger (1997). When living matter dies, it is subject to decomposition and the organically bound nitrogen is transformed to ammonium ions ( $NH_4^+$ ); this process is called mineralization. At least in boreal forests, plants are also able to take up amino acids (Perrson and Näsholm, 2001). Most plants prefer to take up nitrate ( $NO_3^-$ ). The  $NO_3^-$  is provided by the metabolic process called nitrification, where  $NH_4^+$  is transformed to  $NO_3^-$  by microorganisms. Microorganisms as well as plants in regions with reduced nitrification can take up  $NH_4^+$  and recycle the nitrogen by assembling into their biomass again. Under low oxygen or anoxic conditions the process of denitrification takes place: Microorganisms are able to use  $NO_3^-$

as an electron acceptor and reduce  $\text{NO}_3^-$  to  $\text{NO}_2^-$  and further to molecular nitrogen, which finally leaves the terrestrial nitrogen cycle. During the processes of nitrification and denitrification a small part of the nitrogen is emitted as  $\text{N}_2\text{O}$  and  $\text{NO}$ . This loss can be seen as a black box process described by the so called “Hole in the pipe” model (HIP, see also Fig. 1.2) introduced by Firestone and Davidson (1989). The parameters controlling these processes are described in section 1.2.1 and 1.2.2.

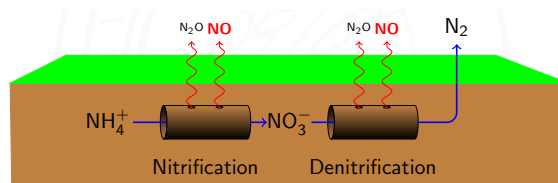


Figure 1.2: Hole in the pipe model, modified after Firestone and Davidson (1989)

## 1.2 Soil NO emissions

Estimates of  $\text{NO}$  emissions from soil range as widely as from 5.5 to 21  $\text{Tg(N) yr}^{-1}$  (Yienger and Levy, 1995; Davidson and Kinglerlee, 1997), which is the same order of magnitude as  $\text{NO}$  emissions from biomass burning and lightning. The dominant source of  $\text{NO}$  emissions is fossil fuel combustion (20–21  $\text{Tg(N) yr}^{-1}$ ) in power plants and vehicles (Denman et al., 2007). However, the spatial and temporal pattern of the emissions is different for the individual sources. In highly populated places, the fossil fuel source is dominant, whereas in remote regions biomass burning and soils are dominant (van der A et al., 2008).

The synthetically fixed nitrogen for usage as fertilizer has become a significant source of additional nitrogen, which is now available for the metabolic processes. Several studies so far have tried to estimate what fraction of fertilizer used for crop production is lost as  $\text{NO}$ . The amount of additional  $\text{NO}$  emission caused by the usage of fertilizer is called fertilizer induced emission (FIE). FIE ranges from zero (Galbally et al., 1987; Slemr and Seiler, 1991; Matson et al., 1996; Maljanen et al., 2007) to more than 10% (Tilsner et al., 2003; Fang and Mu, 2009; Pang et al., 2009).

If the  $\text{NO}$  mixing ratio in the atmosphere is high, soils can also act

as a sink for NO, because NO is also consumed by some microorganisms. The atmospheric mixing ratio above which emission changes to deposition is called the “compensation concentration” (Slemr and Seiler, 1984, 1991; Conrad, 1995).

As already mentioned, fixed nitrogen is an essential element of life and is subject to several metabolic processes and chemical transformations. Among these transformations, the following three natural processes can lead to soil emissions of NO:

### 1.2.1 Nitrification

In aerobic soil conditions nitrification takes place:  $\text{NH}_4^+$  is oxidized for example by *Nitrosomas*, *Nitrospira* to nitrite ( $\text{NO}_2^-$ ) and for example *Nitrobacter* further oxidizes  $\text{NO}_2^-$  to  $\text{NO}_3^-$  (Williams et al., 1992b). It is hypothesised, that 0.1 to 10% of the processed nitrogen is lost as NO during the process of nitrification (Chapin III et al., 2002). The exact pathway leading to NO production and emission in the soil is not yet understood, but there are a lot of factors influencing the rate of nitrification (Fig. 1.3), which partly interdepend on each other. The most important ones are the temperature and water content of the soil (Meixner and Yang, 2006) and the type of litter or litter quality (Jambert et al., 1994; Papke and Papen, 1998; Bargsten et al., 2010). The last one depends on the type of vegetation, the ecosystem or landcover.

### 1.2.2 Denitrification

Denitrification occurs under low oxygen conditions and therefore takes place mainly in wetlands and anoxic microsites in aerobic soils (Firestone and Davidson, 1989; Remde and Conrad, 1991; Conrad, 1995). The less oxygen is available, the more the production by denitrification is shifted towards the more reduced forms of nitrogen as depicted in Fig. 1.4 (Davidson et al., 1998; Kirkman, 2001). The parameters look similar to those controlling nitrification in figure 1.3.

### 1.2.3 Chemodenitrification

This process plays a minor role in the production of NO (Johansson and Galbally, 1984), but should not be forgotten to be mentioned. A prerequisite

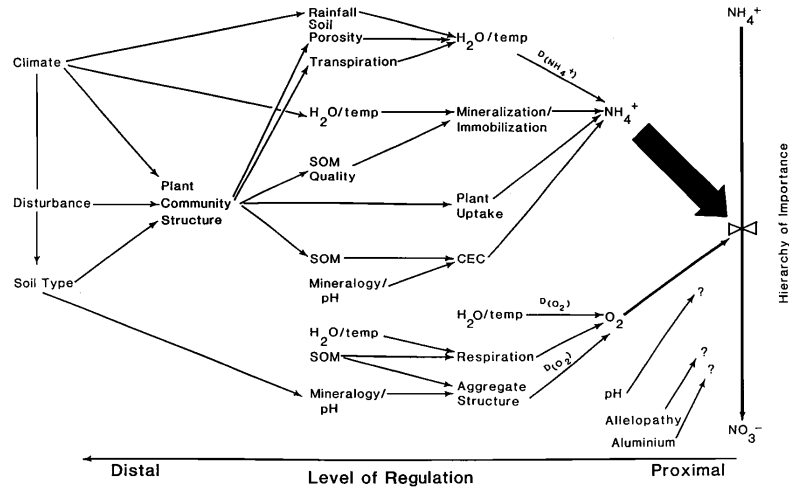
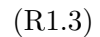
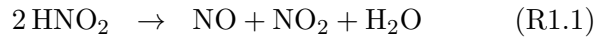


Figure 1.3: A conceptual model of controls on nitrification from Williams et al. (1992b), ©1992 AGU, reproduced with permission.

for chemodenitrification is a high  $\text{NO}_2^-$  concentration, low pH value and high organic matter content, leading to the formation of nitrous acid ( $\text{HNO}_2$ ), which is instable and can spontaneously decompose following one of these two reactions (van Cleemput and Samater, 1996):



### 1.2.4 Pulsing: event based bursts of NO soil emissions

It has been reported that certain events can trigger a sudden few-fold increase in NO emissions, leading to an enhanced atmospheric NO<sub>x</sub> source, which can last for several hours to days. Davidson (1992) review these pulses of NO emission induced by precipitation after a certain period of dryness, accounting for 10–22% of the total annual emissions. According to Davidson (1992) and Yan et al. (2005) the duration of the antecedent dry period is important for the rain-induced pulsing, whereas for Yienger and Levy (1995) the amount of precipitation plays a key role for the magnitude of the pulse.

Several explanations can be found in the literature describing the pulsing mechanism, amongst which the most important ones are:

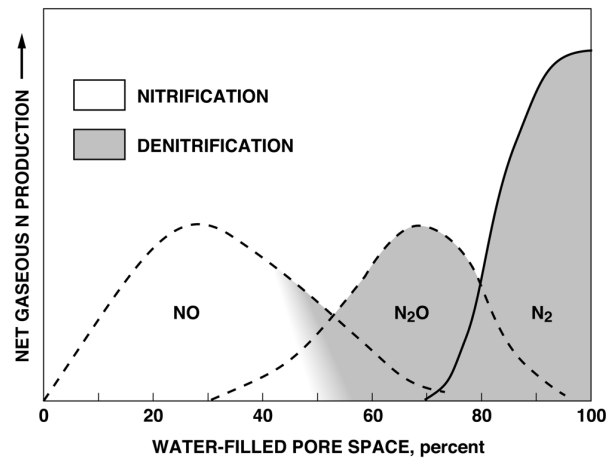


Figure 1.4: Conceptual representation of the products by nitrification and denitrification depending on the water filled pore space (WFPS) from Kirkman (2001).

1. Activation of soil microorganisms: Easily available organic matter has accumulated during an antecedent period of dryness. As soon as water becomes available, an intense increase in microbial activity of nitrifying and/or denitrifying microorganisms leads to an extreme rise in NO emissions.
2. Chemodenitrification: If the already mentioned prerequisites are met, like high  $\text{NO}_2^-$  concentration and low pH, the  $\text{H}^+$  ions react with the  $\text{NO}_2^-$  to  $\text{HNO}_2$ , which spontaneously decomposes according to reactions R1.1 or R1.2.
3. Displacement of NO-enriched air: NO-enriched air in the soil pores is replaced by water infiltrating the soil after a precipitation event. This NO enriched air is emitted to the atmosphere.

The magnitude of the rain-induced pulse ranges from no observed increase (Garcia-Montiel et al., 2003) to more than more 100 times the pre-wetting emission flux (Davidson et al., 1991). If there is sufficiently heavy precipitation, the water can suppress the gas diffusion in the soil, leading even to lower fluxes after wetting (Rondón et al., 1993).

However, not only precipitation events induce pulsing. Pulses have also been observed after fertilization, plowing or fire (Sanhueza, 1997).

### 1.2.5 Measurement of NO soil emission

There are different methods for sampling air to analyze the NO<sub>x</sub> concentration. The underlying measurement principle is chemiluminescence. NO is oxidized by O<sub>3</sub> leading to an excited NO<sub>2</sub> molecule, emitting red to infrared light, while going to the ground state. This light emission can be measured. To measure NO<sub>x</sub>, the NO<sub>2</sub> first has to be thermally transformed to NO. The NO<sub>2</sub> concentration can be calculated by taking the difference of the NO<sub>x</sub> and NO concentrations (Archer et al., 1995; Navas et al., 1997). The sampling methods, which can be applied at different spatial scales are:

#### **Chamber measurement**

A cylinder of a few decimeter in diameter is placed on the soil. It has to be sealed, so that no air is exchanged with the surroundings. Two different kinds of chamber methods exist, providing comparable results (Valente et al., 1995):

**Static or closed chamber:** The chamber is closed only for a certain period of measurement, during which the change in concentration is measured several times. By integrating the change over the measurement time, the flux can be calculated (Valente et al., 1995).

**Dynamic, open chamber or flow through chamber:** Air is flushed, at a constant volumetric flow rate, through the chamber. After the establishment of an equilibrium, the concentration difference between inlet and outlet is measured. This can be done with ambient air or NO-free air. NO-free air has the disadvantage that no deposition can be observed (Meixner et al., 1997; Gut et al., 2002).

#### **Micrometeorological measurement**

This method is also called “eddy flux measurement”. The inlets are installed at different altitudes, mostly at towers where the vertical differences in concentrations and vertical wind velocities are correlated, to derive a flux (Bakwin et al., 1992; Maggionto et al., 2000). This method allows accounting for bigger areas than the previous ones, but is difficult to apply for fast



reacting compounds like  $\text{NO}_x$ , since the mixing ratio of  $\text{O}_3$  also has to be taken into account.

### Satellite and inverse modelling

Regionalized or globalized emissions calculations based on the previous measurements are called “bottom-up” approaches. The method described here uses data remotely-sensed from enter space, and is called “top-down” approach.

Satellites measure the amount of  $\text{NO}_2$  in the atmospheric line-of-sight (slant) columns by measuring the backscattered sunlight with wavelengths between 425 and 450 nm. This has to be corrected interference by stratospheric  $\text{NO}_2$  and for the atmospheric scattering, as well as for cloud cover (Martin et al., 2003; Bertram et al., 2005). By fitting an *a priori* emission inventory of different sources in a model by their respective errors, an *a posteriori* emission inventory is derived, which fits better to the satellite-derived amount of  $\text{NO}_2$ . Also additional satellite-derived products like fire counts can be used, as done by Jaeglé et al. (2005). These methods have been widely applied on regional or global scales (Martin et al., 2003; Jaeglé et al., 2005; Wang et al., 2007; Stavrou et al., 2008; Hudman et al., 2010, and many more).

#### 1.2.6 Modelling NO soil emissions

Different approaches with different levels of complexity exist to calculate NO emissions from soils in bottom-up approaches. The most important ones are introduced in the following sections, starting with those models with the lowest complexity. However, it should be mentioned that there is not always a clear boundary for this classification.

#### Emission inventories

The most important emission inventory is the one introduced by Davidson and Kinglerlee (1997). They review the published literature about measurements of NO soil emissions and group them by ecosystem type. Based on a biome classification, they propose mean annual emissions by biome with a global flux of 21 Tg(N) yr<sup>-1</sup>.

## Empirical models

The most important empirical model is the algorithm introduced by Yienger and Levy (1995). Since this is also the algorithm used in chapter 2 and 3, it is described in detail. In general this approach is based on fewer publications than the emission inventory by Davidson and Kinglerlee (1997), but it is also based on the expert knowledge of the authors. They distinguish between 12 ecosystems or biome classes (Table 1.1). Based on the precipitation history of the antecedent 14 days the soil can either be in a dry ( $< 10$  mm) or in a wet ( $\geq 10$  mm) state. For their ecosystems Yienger and Levy (1995) determined wet and dry emission factors according to the soil moisture state (Table 1.1). To calculate the emission flux from each ecosystem and depending on the soil temperature  $T$  the emission factors are inserted into Formula 1.1 for dry conditions and in formula 1.2 for wet conditions. Yienger and Levy (1995) used the temperature from the lowermost atmospheric layer in their model according to Williams et al. (1992a) for wet conditions and 5 K are added for dry soil conditions, to derive the soil temperature. The emissions from agricultural areas are assumed to always be wet, and during the growing season a fraction of 2.5% of the applied fertilizer is added to the emission. For the rainforest the emissions are assumed to be constant at  $8.6 \text{ ng m}^{-2} \text{ s}^{-1}$  for the five driest months and  $2.6 \text{ ng m}^{-2} \text{ s}^{-1}$  for the remaining seven wet months. In the EMAC model (Jöckel et al., 2006), which is applied in Chapters 2 and 3 we use the soil water content to distinguish between the dry and wet soil moisture state, and we use the soil temperature, which is directly calculated in the model.

$$F_{soil}(T, A_w) = \begin{cases} 0.28 \cdot T \cdot A_w & 0^\circ\text{C} < T \leq 10^\circ\text{C} \\ e^{0.103 \cdot T} \cdot A_w & 10^\circ\text{C} < T \leq 30^\circ\text{C} \\ 21.97 \cdot A_w & T > 30^\circ\text{C} \end{cases} \quad (1.1)$$

$$F_{soil}(T, A_d) = \begin{cases} \frac{T}{30} \cdot A_d & 0^\circ\text{C} < T \leq 30^\circ\text{C} \\ A_d & T > 30^\circ\text{C} \end{cases} \quad (1.2)$$

The rain-induced pulsing is triggered by the amount of precipitation after 14 days with less precipitation than 10 mm during the antecedent 14 days.

Table 1.1: Dry and wet emission factors for the NO soil emission calculation according to Yienger and Levy (1995)

ID	Ecosystem	A <sub>w</sub>	A <sub>d</sub>
1	Water	0	0
2	Ice	0	0
3	Desert	0	0
4	Scrubland	0	0
5	Tundra	0.05	0.37
6	Grassland	0.36	2.65
7	Woodland	0.17	1.44
8	Deciduous forest	0.03	0.22
9	Coniferous forest	0.03	0.22
10	Drought deciduous forest	0.06	0.4
11	Rainforest	–	–
12	Agriculture	0.36	–

Yienger and Levy (1995) assume an initial increase with an exponential decay and calculate a pulsing factor according to equation 1.3.

$$P = a \cdot e^{b \cdot t} \quad (1.3)$$

They define three pulsing regimes depending on the amount of precipitation per day. “Sprinkle”, “shower” and “heavy rain” start with with 5, 10 and 15 times the background emission lasting for  $t = 3, 7$  and  $14$  days, where  $a$  equals 11.19, 14.68 and 18,46 and  $b$  equals -0.805, -0.384 and -0.208, respectively. The pulsing factor is depicted in Figure 1.6. Once NO has escaped the soil, it is rapidly converted to NO<sub>2</sub> through oxidation, mainly by O<sub>3</sub>. The NO<sub>2</sub> can be deposited onto the leaf surface or even taken up by the plant stomata (Bakwin et al., 1992). This effect is accounted for by the canopy reduction factor, which reduces the NO emission to the atmosphere by a certain fraction based on the leaf area index (LAI) and the stomatal area index (SAI). The CRF is calculated based on Bakwin et al. (1992) according to the following equation:

$$CRF = \frac{e^{-8.75 \cdot SAI} + e^{-0.24 \cdot LAI}}{2} \quad (1.4)$$

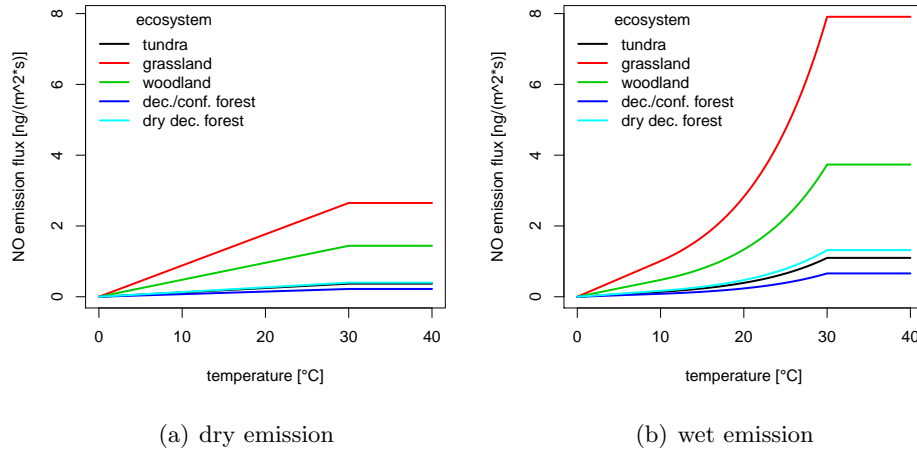


Figure 1.5: NO emission depending on the ecosystem and wet or dry emission factor and temperature according to Yienger and Levy (1995).

Yienger and Levy (1995) use a constant LAI per ecosystem, whereas in ECHAM5/MESy a global map of LAI is used. The SAI (Table 1.2) is applied year round for the tropics without dry deciduous forest, tundra, grassland and coniferous forest and seasonally for the others.

At the end the emission flux from the ecosystem is multiplied by the pulsing factor  $P$ , and the canopy reduction factor  $CRF$  to yield the soil NO flux to the atmosphere.

### Statistical models

Statistical models try to find statistical relationships between the measured NO emission rates and other environmental variables. This either can be done globally, where Yan et al. (2005) find a dependence on soil organic carbon, pH, landcover type, climate and nitrogen deposition. Delon et al. (2007, 2008) apply neural network calculations to derive nonlinear dependence on other variables on a more regional scale. Stehfest and Bouwman (2006) provide a statistical analysis for agricultural crop and grassland based on a large compilation of measurements.

### Process based models

To my knowledge there are two process based models in existence, which need very detailed input to calculate the nitrification rate and diffusion in the

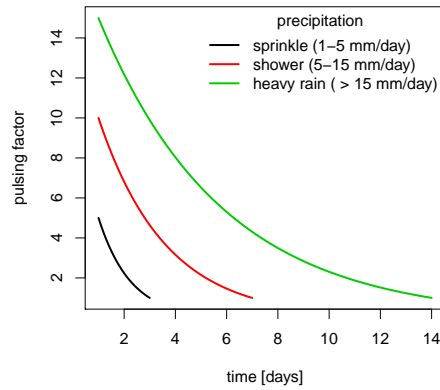
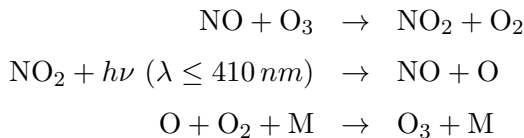


Figure 1.6: Rain induced pulsing based on the amount of precipitation during one day after a certain period of dryness according to Yienger and Levy (1995).

soil. One is the Carnegie-Ames-Stanford (CASA) biosphere model (Potter et al., 1996) and the other one is PNeT-DNDC (Li et al., 2000).

### 1.3 Nitrogen oxide in the atmosphere

Nitrogen oxide ( $\text{NO}_x$ ) is used for the two radicals  $\text{NO}$  and  $\text{NO}_2$ . In several reactions they react with a turnover time of  $\sim 100$  s from one form to the other.  $\text{NO}_x$  is mostly emitted as  $\text{NO}$  from the different sources, including combustion, biomass burning, lightning and the soil. Once emitted,  $\text{NO}$  is rapidly oxidized by  $\text{O}_3$  to  $\text{NO}_2$ . During daytime  $\text{NO}_2$  photolyses back to  $\text{NO}$  and forms an oxygen atom, which reacts with an oxygen molecule. These reactions form a photostationary state:

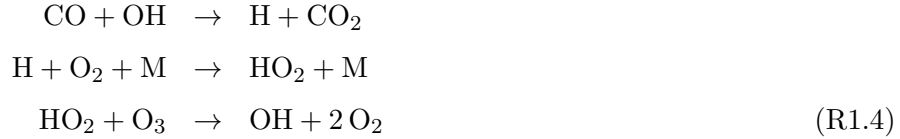


$\text{NO}_x$  catalyzes various oxidizing reactions in the atmosphere, depending on the mixing ratio of  $\text{NO}_x$  it is responsible for the destruction or formation of  $\text{O}_3$ . In a low- $\text{NO}_x$  environment  $\text{O}_3$  is destroyed for example by the oxidation

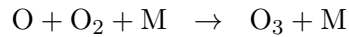
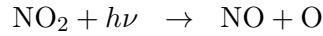
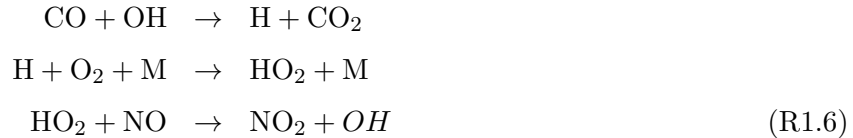
Table 1.2: Stomatal area indices used to calculate the canopy reduction factor.

<b>Temperate 30°–polewards</b>	
Tundra	0.01
Grassland	0.018
Coniferous f.	0.036
Deciduous f.	0.025
Agriculture <sup>a</sup>	0.032
<b>Tropical 30°N–30°S</b>	
Grassland	0.02
Woodland	0.04
Drought-dec. f.	0.075
Rainforest	0.12
Agriculture <sup>b</sup>	0.032

of carbon monoxide (CO):



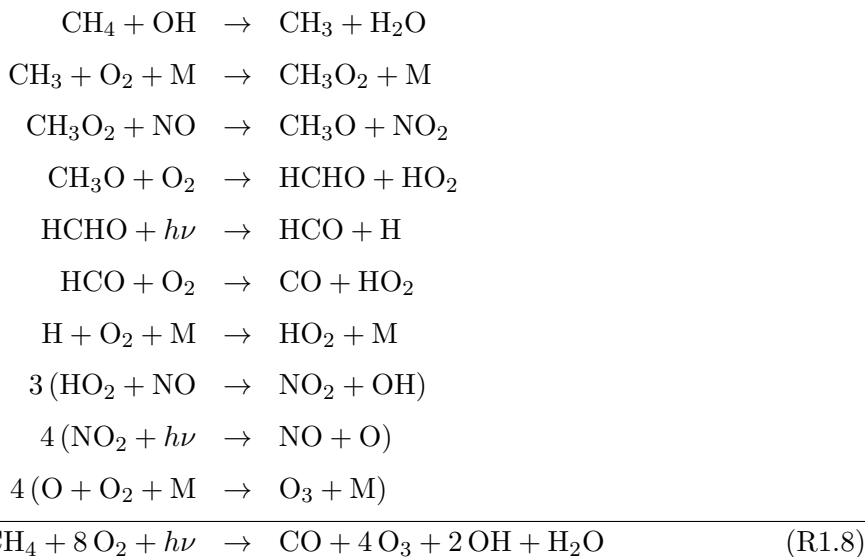
In a high-NO<sub>x</sub> environment O<sub>3</sub> is formed during the oxidation of CO:



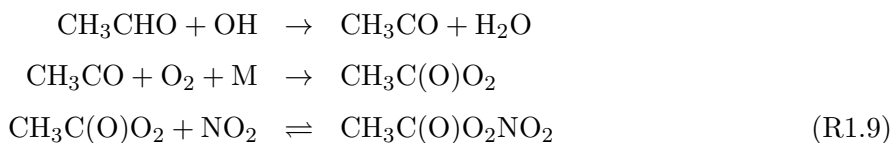
Under low-NO<sub>x</sub> conditions reaction R1.4 dominates over reaction R1.6 under high-NO<sub>x</sub> conditions, leading to the depletion of O<sub>3</sub>. The threshold between low and high NO<sub>x</sub> conditions is approximately 5–30 pmol mol<sup>-1</sup> (Logan, 1981; Brasseur et al., 1999). At low altitudes over the continents the high NO<sub>x</sub> is more common, whereas over the ocean and at high altitudes the low NO<sub>x</sub> environment is more common (von Kuhlmann et al., 2003). In

both high and low  $\text{NO}_x$  environments the participating OH and  $\text{HO}_2$  are recycled as well as  $\text{NO}_x$ . The molecule M denotes mostly a nitrogen or oxygen molecule, the most abundant molecules, as energy acceptor.

Another important set of reaction in high  $\text{NO}_x$  environment is the oxidation of the important greenhouse gas  $\text{CH}_4$ , during which  $\text{O}_3$  is produced:



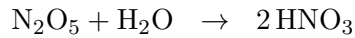
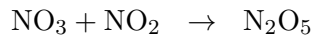
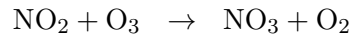
$\text{NO}_x$  not only catalyzes these reactions, it also reacts with organic compounds in the atmosphere and forms nitrates, amongst which the most abundant one is peroxyacetyl nitrate (PAN) starts with the oxidation of acetaldehyde:



Reaction R1.9 is strongly temperature dependent, at high temperatures (low altitudes) it is shifted to the left and at low temperatures (high altitudes) it is shifted to the right. When PAN is formed and lifted up to high altitudes it can be transported, due to its longer lifetime, to remote regions and when the air mass containing PAN subsides back to the surface,  $\text{NO}_2$  is released from PAN again (Bridier et al., 1991; Moxim et al., 1996). This kind of species is called a reservoir species.

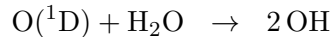
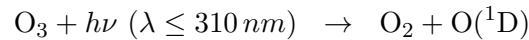
Another important reservoir species is nitric acid ( $\text{HNO}_3$ ). During day-

time it is formed through the reaction of OH with NO<sub>2</sub> (R1.10). Without light during the night HNO<sub>3</sub> is formed as follows by the set of reaction summarized in R1.11.



At low altitudes HNO<sub>3</sub> is removed via dry and wet deposition, since there is more water available and the photolysis is not very fast. At higher altitudes in contrast it is an important reservoir species.

Nearly all of the above reaction include the OH and HO<sub>2</sub> (HO<sub>x</sub>) radicals. OH in the lower troposphere has its origin in the photolysis of O<sub>3</sub>:



At higher altitudes reaction R1.12 becomes more important relative to the previous one due to less water at higher altitudes.



The OH radical, also created by other reactions, is one of the most reactive molecules in the atmosphere. It is the main oxidant and is therefore often also called “detergent” of the atmosphere. The removal of CH<sub>4</sub> by OH (first step in reaction chain R1.8) is used as a measure for the oxidizing efficiency of the atmosphere (Lawrence et al., 2001). Both OH and O<sub>3</sub> are also responsible for the formation of HNO<sub>3</sub> (reactions R1.10 and R1.11) and therefore for the removal of NO<sub>x</sub>. The production of O<sub>3</sub>, an important pollutant and greenhouse gas, not only depends on the NO<sub>x</sub> mixing ratio, but also on the concentration of volatile organic compounds (VOC) (Chameides et al., 1992). Several measures have been proposed to distinguish between a NO<sub>x</sub> or VOC “limitation” of the O<sub>3</sub> production (Milford et al., 1994; Sillman, 1995; Kleinman et al., 1997; Hammer et al., 2002).



The lifetime of  $\text{NO}_x$  in the troposphere is less than one day and it is deposited near its source location, whereas  $\text{O}_3$  has depending on altitude and season a lifetime of several days to several months, and can therefore be transported further away from the location where it was produced. The lifetime of  $\text{HNO}_3$  also depends on the altitude, but not as strongly as for PAN. In contrast OH has a lifetime of less than one second, meaning that it reacts immediately, where it was produced.

## **1.4 Aims**

As discussed in the preceding parts of this introduction, the simulation of NO emission from soils is still stuck in its infancy, since the processes leading to the emissions are very heterogeneous in space and time. Nevertheless, since the first algorithms to approximate the amount and geographical distribution of NO emissions were developed, many more measurements have been published and our knowledge of the mechanism of soil NO emissions has grown substantially. The aims of this work are:

1. to evaluate the influence of soil NO emissions on the chemical processes in the troposphere, especially on O<sub>3</sub>, OH production and the oxidizing efficiency of the atmosphere, showing that soil NO emissions play a key role in this reaction chain provide a motivation for further study.
2. to improve the existing soil NO emission algorithm (Yienger and Levy, 1995), implemented in most contemporary AC-GCMs and CTMs; this will employ a compilation of measurements collected in Steinkamp (2007), which will be extended to include further observations.
3. The same compilation is used to generalize an algorithm based on laboratory investigation (Meixner and Yang, 2006) with the use of model data. This novel algorithm will improve the representation of soil NO emission in global models substantially, since it incorporates more physical and chemical parameters than previous attempts.

## 2 Influence of modelled soil biogenic NO emissions on related trace gases and the atmospheric oxidizing efficiency

*J. Steinkamp*<sup>1</sup>, *L. N. Ganzeveld*<sup>2</sup>, *W. Wilcke*<sup>3</sup>, *M. G. Lawrence*<sup>1</sup>

<sup>1</sup> Department of Atmospheric Chemistry, Max-Planck-Institute for Chemistry, Mainz, Germany

<sup>2</sup> Department of Environmental Sciences, Chairgroup Earth System Sciences, Wageningen University and Research Centre, Wageningen, The Netherlands

<sup>3</sup> Geographic Institute, Johannes Gutenberg University, Mainz, Germany

---

**This chapter has been published as:**

Steinkamp, J., Ganzeveld, L. N., Wilcke, W., and Lawrence, M. G.: Influence of modelled soil biogenic NO emissions on related trace gases and the atmospheric oxidizing efficiency, *Atmos. Chem. Phys.*, 9, 2663–2677, doi:10.5194/acp-9-2663-2009, 2009.

## **Abstract**

The emission of nitric oxide (NO) by soils (SNO<sub>x</sub>) is an important source of oxides of nitrogen (NO<sub>x</sub>=NO+NO<sub>2</sub>) in the troposphere, with estimates ranging from 4 to 21 Tg of nitrogen per year. Previous studies have examined the influence of SNO<sub>x</sub> on ozone (O<sub>3</sub>) chemistry. We employ the ECHAM5/MESy atmospheric chemistry model (EMAC) to go further in the reaction chain and investigate the influence of SNO<sub>x</sub> on lower tropospheric NO<sub>x</sub>, O<sub>3</sub>, peroxyacetyl nitrate (PAN), nitric acid (HNO<sub>3</sub>), the hydroxyl radical (OH) and the lifetime of methane ( $\tau_{\text{CH}_4}$ ). We show that SNO<sub>x</sub> is responsible for a significant contribution to the NO<sub>x</sub> mixing ratio in many regions, especially in the tropics. Furthermore, the concentration of OH is substantially increased due to SNO<sub>x</sub>, resulting in an enhanced oxidizing efficiency of the global troposphere, reflected in a  $\sim 10\%$  decrease in  $\tau_{\text{CH}_4}$  due to soil NO emissions. On the other hand, in some regions SNO<sub>x</sub> has a negative feedback on the lifetime of NO<sub>x</sub> through O<sub>3</sub> and OH, which results in regional increases in the mixing ratio of NO<sub>x</sub> despite lower total emissions in a simulation without SNO<sub>x</sub>. In a sensitivity simulation in which we reduce the other surface NO<sub>x</sub> emissions by the same amount as SNO<sub>x</sub>, we find that they have a much weaker impact on OH and  $\tau_{\text{CH}_4}$  and do not result in an increase in the NO<sub>x</sub> mixing ratio anywhere.

## 2.1 Introduction

Nitric oxide (NO) in the soil is produced by the microbial processes of nitrification and denitrification (Firestone and Davidson, 1989). The NO emission originates from a natural pool of nitrogen and a fraction from fertilizer application (Yienger and Levy, 1995; Stehfest and Bouwman, 2006). The estimates of NO emitted yearly by soils (hereafter called SNOx) ranges from 4 to 21 Tg(N) (Yienger and Levy, 1995; Davidson and Kinglerlee, 1997, and references therein). NO reacts rapidly with other atmospheric compounds, establishing an equilibrium between NO and nitric dioxide (NO<sub>2</sub>). These two species are frequently referred to the oxides of nitrogen (NO<sub>x</sub>). Through reactions, deposition and stomatal uptake directly within the vegetation layer not all NO emitted by the soil escapes the canopy layer as NO<sub>x</sub> (Yienger and Levy, 1995; Ganzeveld et al., 2002b). SNOx is topped by the anthropogenic combustion of fossil fuels (20–24 Tg(N) yr<sup>-1</sup>) (Denman et al., 2007) and is comparable to the production of NO<sub>x</sub> from lightning and biomass burning, but especially in remote continental regions of the mid- and low-latitudes SNOx is the dominant source of NO<sub>x</sub>. In this work SNOx refers to the flux from the canopy to the atmosphere. The fraction of NO<sub>x</sub> that reaches the atmosphere reacts as a catalyst for production of ozone (O<sub>3</sub>), an important greenhouse gas. This O<sub>3</sub> production is driven by the oxidation of carbon monoxide (CO) and volatile organic compounds (VOC), if the concentration of NO is higher than about 5–30 pmol mol<sup>-1</sup> (Brasseur et al., 1999). The unit used in this work is the molar (or “volume”) mixing ratio as mol tracer per mol air (e.g. pmol mol<sup>-1</sup>). Atmospheric NO<sub>x</sub> is also involved in the production of the hydroxyl radical (OH), which is responsible for the oxidation and depletion of methane (CH<sub>4</sub>), another greenhouse gas. Beyond these climate related issues, high NO<sub>x</sub> and O<sub>3</sub> mixing ratios also have a direct impact on human health and on the vegetation (Sitch et al., 2007). NO<sub>x</sub> is removed from the atmosphere by reaction with hydroxyl radicals (OH) or oxidation to dinitrogen pentoxide (N<sub>2</sub>O<sub>5</sub>) and subsequent deposition as nitric acid (HNO<sub>3</sub>). It can also react with organic tracers to form peroxy nitrates, mainly peroxyacetyl nitrate (PAN), which, once it is lifted to higher altitudes, can be transported over large distances releasing NO<sub>x</sub> when it is transported back downward again.

Previous model studies of the influence of SNOx on atmospheric chem-

Table 2.1: Setup of the ECHAM5/MESSy model and applied submodels.

Horizontal resolution	T42 ( $\sim 2.8^\circ \times 2.8^\circ$ )	
Vertical resolution	L31 (up to 10 hPa)	
Internal timestep	20 min	
Timestep of output	5 h	
Period of simulation	1994–1995	
Used submodels	Calculation of	Literature ref.
CLOUD	Clouds and precipitation	Jöckel et al. (2006)
CONVECT	Convection	Tost et al. (2006b)
CVTRANS	Convective tracer transport	Tost (2006)
DRYDEP	Dry deposition	Kerkweg et al. (2006a)
JVAL	Rates of photolysis	Jöckel et al. (2006)
LNOX	Lightning NO <sub>x</sub>	Tost et al. (2007)
MECCA	Chemical atmospheric reactions <sup>a</sup>	Sander et al. (2005)
OFFLEM <sup>b</sup>	Offline emissions	Kerkweg et al. (2006b)
ONLEM <sup>c</sup>	Online emissions	Kerkweg et al. (2006b)
RAD4ALL	Radiation	Jöckel et al. (2006)
SCAV	Wet deposition	Tost et al. (2006a)
TNUDGE	Tracer nudging	Kerkweg et al. (2006b)
TROPOP	Calculation of the tropopause	Jöckel et al. (2006)

<sup>a</sup> Tropospheric reaction with NMHC and without halogens.

<sup>b</sup> Biomass burning and fossil fuel NO emission reduced in REDOTHER.

<sup>c</sup> Soil NO emissions switched off in NOBIONO simulation.

istry mainly focused either on the NO<sub>x</sub> source itself, on O<sub>3</sub>, mostly on a regional scale. Ganzeveld et al. (2002a,b) investigate two different modeling approaches of the role of canopy processes on the effective exchange of NO<sub>x</sub> between the canopy and atmosphere. They concluded that the application of the big leaf approach with a separate treatment of dry deposition and biogenic emissions, in which the canopy reduction factor accounts for the fraction of these emission that escapes the canopy, provides a reasonable first order estimate of NO<sub>x</sub> canopy top fluxes. Jaeglé et al. (2005) examined the global partitioning of NO<sub>x</sub> sources using inverse modelling and the space-based NO<sub>2</sub> column derived by GOME (Global Ozone Monitoring Experiment). Their a posteriori SNO<sub>x</sub> (8.9 Tg(N) yr<sup>-1</sup>) is 68% greater than their a priori SNO<sub>x</sub> (5.3 Tg(N) yr<sup>-1</sup>). Based on this, Jaeglé et al. (2005) suggest that the influence of SNO<sub>x</sub> on background O<sub>3</sub> could be underestimated in current chemistry transport models (CTMs). Bertram et al. (2005) come to a similar conclusion by inverse modelling using another satellite sensor (SCIAMACHY) above the Western United States, computing an underesti-

mation of 60%. Delon et al. (2008) modelled higher O<sub>3</sub> concentrations with higher SNO<sub>x</sub> above Western Africa. For Europe, Simpson (1995) found that SNO<sub>x</sub> hardly has any influence on controlling the O<sub>3</sub> mixing ratio. Isaksen and Hov (1987) already investigated the influence of changes in the emission intensity of different relevant trace gases on the oxidizing efficiency through an increase in OH concentration with increased NO<sub>x</sub> emissions, but they did not consider SNO<sub>x</sub> separately in their assessment. Fuglestedt et al. (1999) demonstrate the importance of the geographical region of NO<sub>x</sub> sources for the changes in the ozone concentration and the oxidizing efficiency.

In this study, we take these analysis a step further and follow the reaction chain from SNO<sub>x</sub> through O<sub>3</sub> and OH to its global influence on the oxidizing efficiency of the atmosphere. To do so, we compare two model runs with a state-of-the-art 3-D global chemistry climate model. One is a simulation with all relevant emissions and reactions (BASE), and the second simulation is without SNO<sub>x</sub> (NOBIONO = “No biogenic NO”). We expect a considerable influence of SNO<sub>x</sub> on the mixing ratios and distribution of related global tropospheric trace gases (NO<sub>x</sub>, PAN, HNO<sub>3</sub>, O<sub>3</sub> and OH). Furthermore the global oxidizing efficiency, indicated by the lifetime of CH<sub>4</sub> ( $\tau_{\text{CH}_4}$ ), is expected to decrease ( $\tau_{\text{CH}_4}$  increases) if we exclude NO<sub>x</sub> emission from soils. To investigate whether other surface NO<sub>x</sub> emissions result in similar effects, or if they differ due to differences in their distribution, we performed a third simulation (REDOTHER) in which we reduced the NO<sub>x</sub> emission from all other sources by the same amount as is emitted by the soils.

In the following section we briefly describe the model setup. We then compare the relevant tracer mixing ratios from the BASE simulation versus the NOBIONO and REDOTHER simulations. In the final section we present our conclusions and outlook.

## **2.2 Model description and setup**

### **2.2.1 General**

For this study the Modular Earth Submodel System version 1.6 (MESSy) coupled to the general circulation model ECHAM5 is employed. MESSy connects, through a standardized interface, submodels for different processes

with bidirectional feedbacks (Jöckel et al., 2005, 2006). The combined system is referred to as the ECHAM5/MESy atmospheric chemistry (EMAC) model. The meteorology for these simulations is driven by sea surface temperature (SST) from the AMIP IIb dataset (Taylor et al., 2000). The calculation of SNO<sub>x</sub> in the BASE simulation is based on the algorithm of Yienger and Levy (1995), which is the most widely used SNO<sub>x</sub> algorithm in CTMs (Ganzeveld et al., 2002a; Jaeglé et al., 2005; Delon et al., 2008). This calculation is performed in the submodel ONLEM (Kerkweg et al., 2006b). NO<sub>x</sub> produced by lightning is calculated in the submodel LNOX (1.6 Tg(N) yr<sup>-1</sup>). The remaining sources of NO<sub>x</sub> (43.5 Tg(N) yr<sup>-1</sup>) are read in from the offline EDGAR database (Olivier et al., 1994) by the submodel OFFLEM (Kerkweg et al., 2006b). NO emission from fossil fuel combustion, biomass and biofuel burning are combined and account for 43 Tg(N) yr<sup>-1</sup>, while aircraft emit only 0.6 Tg(N) yr<sup>-1</sup>. Other relevant emissions are calculated either by the ONLEM or OFFLEM submodel.

A model spinup time of eleven months (January–November 1994) was chosen and the data of the period December 1994–December 1995 is analyzed here. To achieve an identical meteorology of both simulations feedback through trace gases and water vapor is switched off. Table 2.1 recapitulates the setup of the two simulations.

In the BASE simulation a yearly emission flux of 9.7 Tg(N) was calculated. In the REDOTHER simulation the offline surface NO emission (43 Tg(N) yr<sup>-1</sup>) are reduced globally by 22.5%, which corresponds to 9.7 Tg(N) yr<sup>-1</sup>.

### **2.2.2 Soil NO emission algorithm**

The emission of NO from soils is calculated based on the algorithm developed by Yienger and Levy (1995) and depends on ecosystem type, soil moisture state and the surface temperature. Our underlying ecosystem map is compiled from Olson (1992) (Ganzeveld et al., 2006), which 72 ecosystem classes have been reduced to the twelve ecosystems defined by Yienger and Levy (1995), with corresponding dry and wet emission factors (Table 2.2). Agriculture and (tropical) rainforest is treated separately. In the original algorithm the precipitation history is used to distinguish between the dry and wet soil moisture state. In our implementation we define the dry state to be when the soil moisture is below 10% volumetric soil moisture and wet



Table 2.2: Ecosystems and emission factors according to Yienger and Levy (1995).

Ecosystem	emission factor	
	wet $A_{w,e}$	dry $A_{d,e}$
1 water	0	0
2 ice	0	0
3 desert	0	0
4 scrubland	0	0
5 tundra	0.05	0.37
6 grassland	0.36	2.65
7 woodland	0.17	1.44
8 decidous forest	0.03	0.22
9 coniferous forest	0.03	0.22
10 dry decidous forest	0.06	0.4
11 rainforest	2.6	8.6
12 agriculture	0	0

above 10%. The temperature dependence is calculated according to Eq. 2.1 for wet soil conditions and 2.2 for dry soil conditions.

$$F_{\text{NO}}(T, A_w) = \begin{cases} 0, 28 \cdot T \cdot A_w & 0^\circ\text{C} < T \leq 10^\circ\text{C} \\ e^{0,103 \cdot T} \cdot A_w & 10^\circ\text{C} < T \leq 30^\circ\text{C} \\ 21, 97 \cdot A_w & T > 30^\circ\text{C} \end{cases} \quad (2.1)$$

$$F_{\text{NO}}(T, A_d) = \begin{cases} \frac{T}{30} \cdot A_d & 0^\circ\text{C} < T \leq 30^\circ\text{C} \\ A_d & T > 30^\circ\text{C} \end{cases} \quad (2.2)$$

In the rainforest Yienger and Levy (1995) assumed SNOx to be constant: a dry emission factor is applied for the five driest months (Northern Hemisphere: May–September, Southern Hemisphere: November–March) and a wet emission factor for the remaining seven months. For agricultural areas wet grassland conditions are assumed for the whole year. On top of that, fertilizer induced emission based on Bouwman et al. (2002a) is added.

If, after a certain period of dryness, the soil receives a sufficient amount of precipitation a burst of NO emission occurs. Based on the precipitation history of the last 14 days and if the soil moisture state is defined as dry,

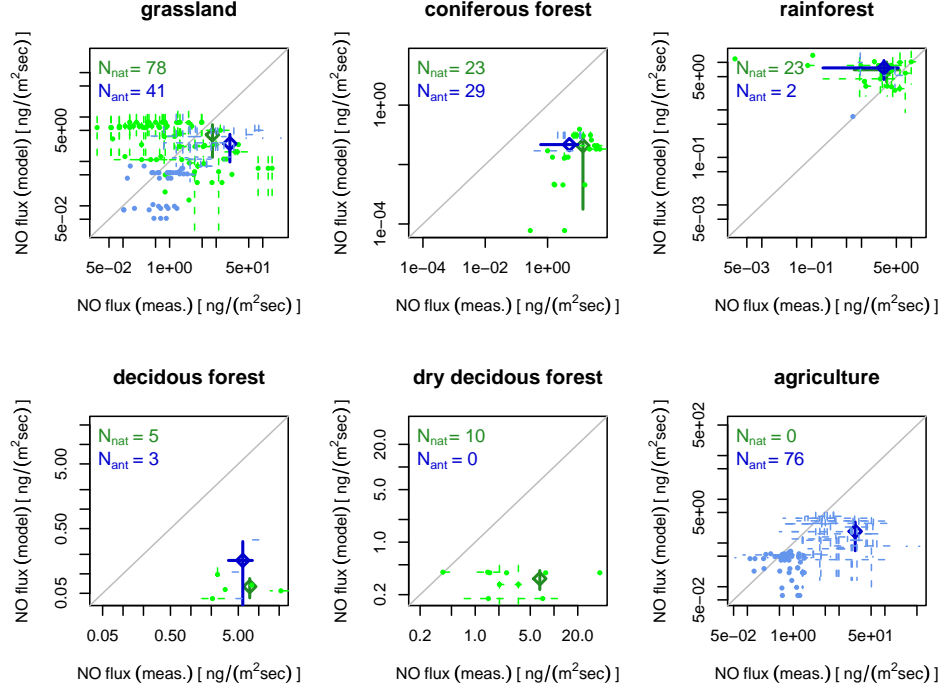


Figure 2.1: Scatterplots of measured versus modeled NO emission flux from soils in different ecosystems. Measurements under natural conditions are colored in green and anthropogenically influenced measurements are in blue, mean and standard deviation slightly darker.

this burst is implemented as pulsing factor, depending on the amount of precipitation during the last day (Eq. 2.3) and lasting for  $d$  days. If this pulse is not active, the pulsing factor equals one.

$$\text{pulse} = \begin{cases} 11, 19 \cdot e^{-0,805 \cdot d} & 1 < d < 3; & 1-5 \frac{\text{mm}}{\text{day}} \\ 14, 68 \cdot e^{-0,384 \cdot d} & 1 < d < 7; & 5-15 \frac{\text{mm}}{\text{day}} \\ 18, 46 \cdot e^{-0,208 \cdot d} & 1 < d < 14; & > 15 \frac{\text{mm}}{\text{day}} \end{cases} \quad (2.3)$$

This is the direct modeled SNO<sub>x</sub>. Within the vegetation layer the NO emitted by the soil rapidly reacts to NO<sub>2</sub> and is partly deposited back on the vegetation and the ground. This is reflected by the canopy reduction factor (CRF,  $0 \leq \text{CRF} \leq 1$ ), calculated depending on the leaf area index (LAI) and the stomatal area index (SAI).

Table 2.3: Simulated total NO<sub>x</sub> emissions, SNO<sub>x</sub> in Tg(N) in the BASE simulation and in brackets relative contribution of SNO<sub>x</sub> to the total NO emissions for different regions and periods.

Season <sup>a</sup>	Global		Low-latitudes (30° N–30° S)		Mid-latitudes (30° N–60° N) (30° S–60° S)			
	total	soil	total	soil	total	soil	total	soil
DJF	13.08	1.78 (14%)	7.64	1.60 (21%)	4.94	0.06 (1%)	0.46	0.12 (26%)
MAM	13.42	2.38 (18%)	7.27	1.72 (24%)	5.68	0.59 (10%)	0.42	0.07 (17%)
JJA	15.26	3.35 (23%)	7.72	1.76 (23%)	7.04	1.64 (23%)	0.33	0.03 (10%)
SON	14.84	2.13 (14%)	8.75	1.70 (19%)	5.61	0.36 (6%)	0.40	0.07 (18%)
All	54.79	9.74 (18%)	29.90	6.78 (23%)	22.99	2.65(12%)	1.58	0.30 (19%)

<sup>a</sup>DJF = December 1994, January, February 1995; MAM = March, April, May 1995; JJA = June, July, August 1995; SON = September, October, November 1995

The NO flux reaching the atmosphere is therefore calculated as:

$$\text{flux} = \text{CRF} \cdot \text{pulse} \cdot F_{\text{NO}}(T, A_{d/w}) \quad (2.4)$$

We have made a preliminary comparison of the model simulated soil NO emissions versus measurements for the period 1990 to 2000 without canopy reduction (Steinkamp, 2007). Figure 2.1 shows an overview of these comparisons. We found that the yearly averaged flux in the tropics compares well with measurements, whereas the fluxes in temperate regions seem to be underestimated. Since the applied algorithm is empirically based, comparison on a point by point basis are not appropriate, but the overall distribution can be compared, in general the emission flux tends to be underestimated in all ecosystems, except for the rainforest.

## 2.3 Results and discussion

The emissions of NO from soils in the BASE simulation accounts for 18% of the total annual global NO emissions (Table 2.3). The interannual variability of SNO<sub>x</sub> is low in the model (Steinkamp, 2007). The largest SNO<sub>x</sub> emissions are calculated for tropical regions. During JJA there are some exceptions further north in Northern America, Europe and North-Eastern China. These are fertilizer induced emissions in agricultural regions (Fig. 2.2 and Table 2.3).

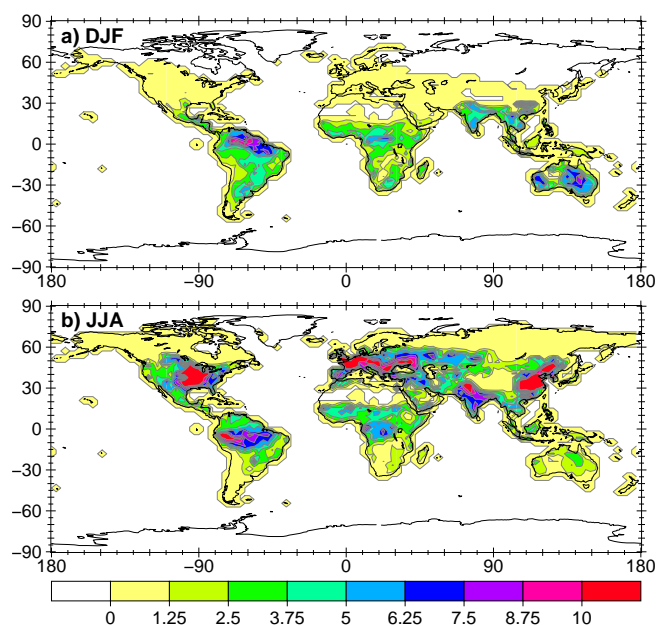


Figure 2.2: Simulated SNOx flux for (a) December 1994 to February 1995 and (b) June to August 1995 in  $\frac{\text{ng}}{\text{m}^2 \text{sec}}$ .

The data is analyzed by season with a focus on the winter and summer season. There is a notable seasonal variation with larger SNOx in the summer period of each hemisphere and with a larger contribution of SNOx to the total NO emissions during the northern hemispheric spring and summer (Table 2.3). The first point can be explained by the temperature dependence of SNOx and the second one by the greater landmasses in the Northern Hemisphere. In the northern mid-latitudes SNOx plays a less important role relative to other NO<sub>x</sub> emissions, except during the JJA period.

### 2.3.1 Influence of NO emissions on related trace gases

The column mean mixing ratios of NO<sub>x</sub>, PAN, HNO<sub>3</sub> and O<sub>3</sub> and the column mean concentration of OH in the gridcells (weighted by the air mass in the gridcells) in the lower troposphere (below 500 hPa; hereafter “LT”) from the BASE simulation are compared with the values from the NOBIONO and REDOTHER simulations in this section. Here we first consider the overall correlations between the changes in the trace gas columns and the SNOx distribution (Table 2.4), then we discuss the changes in the individual gases in the following subsections.

As expected, in the surface layer (hereafter “SL”) as well as in the LT the difference between the  $\text{NO}_x$  column mean mixing ratio in the NOBIONO simulation versus the BASE simulation is well-correlated with SNOx in all regions (Table 2.4; scatterplots are included in the appendix. A low correlation is computed for the Northern Hemisphere LT during DJF, as expected due to the small SNOx compared to the anthropogenic emissions.

There is hardly any correlation in the low-latitudes and in the northern mid-latitudes of SNOx and the difference in the column mean mixing ratio of PAN in the two simulations (Table 2.4). In contrast, there is a better correlation in the southern mid-latitudes between the difference in the LT PAN column mixing ratio and SNOx. This suggests a dominating role of SNOx in the formation of PAN in the mid-latitudes of the Southern Hemisphere. The other precursor of PAN, peroxyacyl radicals, depend on the photooxidation of VOCs, which in turn depends on  $\text{O}_3$  and OH (Roberts et al., 2001; Cleary et al., 2007). At low latitudes, convective updrafts and subsiding airmasses, combined with the strong temperature dependence of the decomposition of PAN decreases the correlation.

The correlation between SNOx and the difference in the LT  $\text{O}_3$  column mean mixing ratio is lower than for  $\text{NO}_x$ . This is partly due to the longer lifetime of  $\text{O}_3$ , which is better mixed in the LT. Furthermore the production of  $\text{O}_3$  is not only determined by the  $\text{NO}_x$  mixing ratio, but also by the concentration of VOC. The correlation of the OH column mean concentration difference in the LT with SNOx is similar to  $\text{O}_3$ . OH is a very short lived tracer, whose production depends mainly on: 1.) the photolysis of  $\text{O}_3$  and the water vapor concentration in the lower troposphere, 2.) the reaction of NO with  $\text{HO}_2$  in the upper troposphere and 3.) the reaction of  $\text{O}_3$  with  $\text{HO}_2$  (Fig. 2.3). This results, depending on the dominating reaction, in a higher or lower correlation of the OH column concentration difference versus SNOx than the correlation for the  $\text{O}_3$  column mixing ratio difference versus SNOx. The correlation of the changes in the mixing ratios of  $\text{O}_3$  and OH versus SNOx is lower in the SL than in the LT. Due to the longer lifetime of  $\text{O}_3$  compared to  $\text{NO}_x$ , the  $\text{O}_3$  distribution depends more on transport away from the source regions. The horizontal transport explains the lower correlation compared to  $\text{NO}_x$  and vertical transport can explain the higher correlation in the column compared to the SL.

Table 2.4: Correlation coefficient ( $R^2$ ) between surface SNO<sub>x</sub> flux values and the difference (NOBIONO-BASE) of the tracer burden in the overlying model surface layer (SL) lower troposphere (LT; >500 hPa) by gridcell, averaged over the corresponding period; only gridcells with a land surface fraction of at least 75% were included.

Season <sup>a</sup>	NO <sub>x</sub>		PAN		HNO <sub>3</sub>		O <sub>3</sub>		OH	
	SL	LT	SL	LT	SL	LT	SL	LT	SL	LT
Global ( $N=2462$ )										
DJF	0.82	0.83	0.54	0.43	0.41	0.46	0.44	0.53	0.48	0.51
MAM	0.90	0.88	0.42	0.34	0.56	0.52	0.31	0.40	0.41	0.49
JJA	0.90	0.87	0.30	0.22	0.50	0.33	0.15	0.26	0.24	0.35
SON	0.88	0.89	0.54	0.42	0.49	0.42	0.44	0.52	0.47	0.60
Year	0.92	0.89	0.48	0.37	0.56	0.46	0.32	0.43	0.38	0.53
Low-latitudes, 30° N–30° S ( $N=646$ )										
DJF	0.68	0.66	0.19	0.14	0.15	0.15	0.12	0.16	0.14	0.14
MAM	0.79	0.75	0.16	0.05	0.41	0.31	0.08	0.11	0.19	0.18
JJA	0.72	0.77	0.28	0.18	0.16	0.08	0.17	0.22	0.07	0.23
SON	0.75	0.78	0.26	0.15	0.18	0.08	0.12	0.14	0.09	0.18
Year	0.81	0.78	0.25	0.15	0.23	0.11	0.09	0.14	0.06	0.21
Northern mid-latitudes, 30° N–60° N ( $N=637$ )										
DJF	0.83	0.30	0.03	0.01	0.51	0.37	0.03	0.11	0.06	0.37
MAM	0.92	0.90	0.03	0.13	0.43	0.32	0.00	0.10	0.04	0.22
JJA	0.91	0.85	0.06	0.02	0.43	0.20	0.00	0.03	0.07	0.12
SON	0.90	0.81	0.13	0.12	0.59	0.49	0.10	0.23	0.20	0.35
Year	0.93	0.89	0.04	0.04	0.44	0.26	0.00	0.06	0.07	0.17
Southern mid-latitudes, 30° S–60° S ( $N=46$ )										
DJF	0.95	0.88	0.40	0.47	0.73	0.78	0.69	0.75	0.40	0.72
MAM	0.94	0.90	0.76	0.75	0.68	0.68	0.72	0.77	0.59	0.78
JJA	0.72	0.78	0.59	0.56	0.36	0.36	0.33	0.64	0.46	0.78
SON	0.95	0.89	0.78	0.71	0.51	0.61	0.77	0.78	0.61	0.83
Year	0.95	0.90	0.74	0.73	0.69	0.73	0.77	0.80	0.54	0.82

<sup>a</sup> See Table 2.3 for abbreviations.

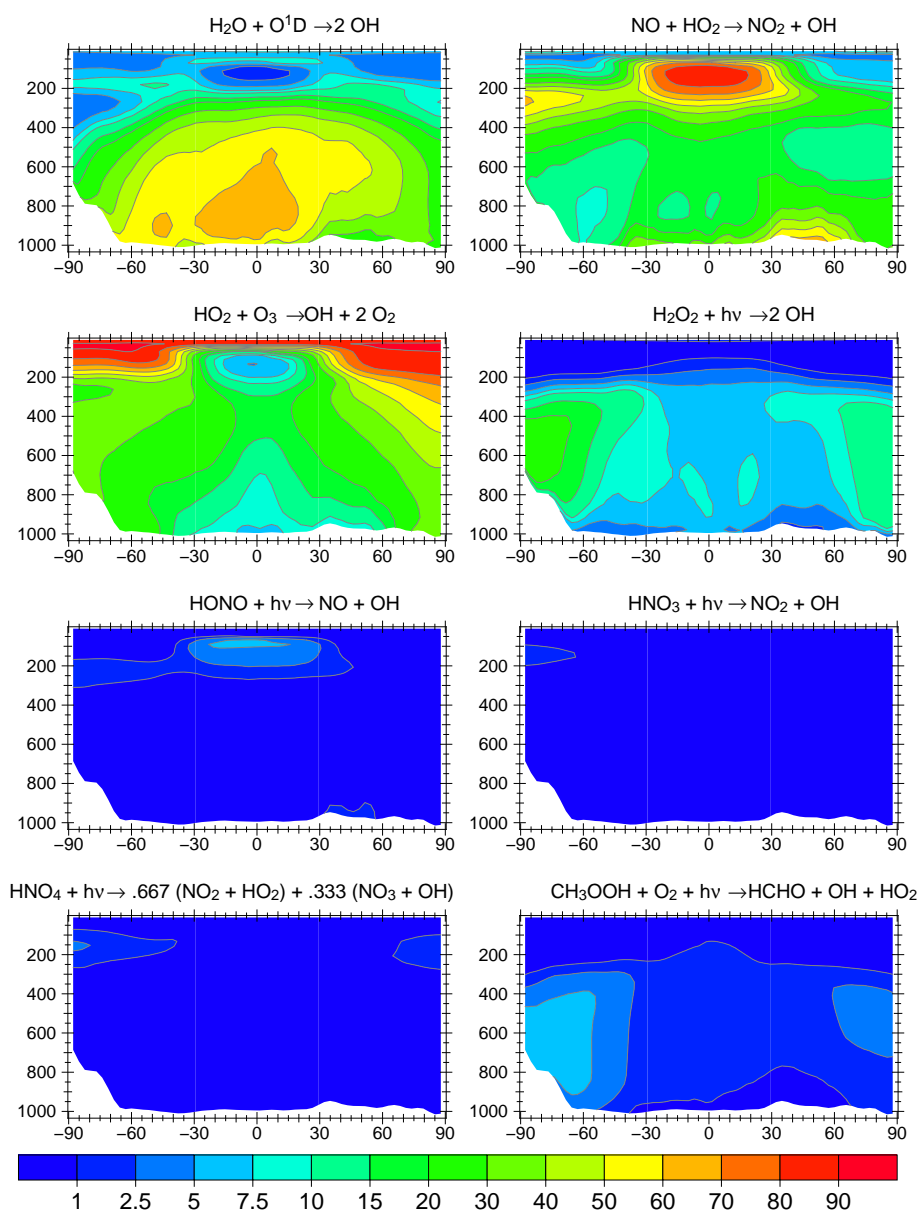


Figure 2.3: Zonal mean relative contribution of the eight major OH producing reactions in the BASE simulation integrated over one year.

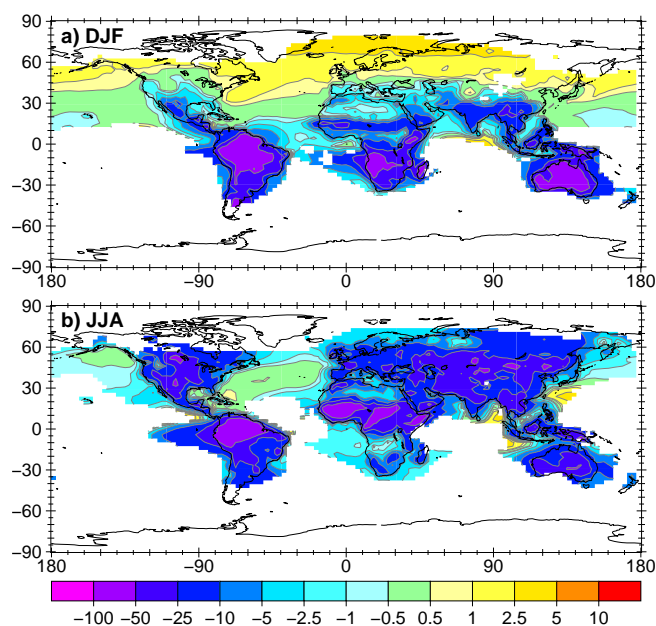


Figure 2.4: Relative difference ( $\frac{\text{NOBIONO}-\text{BASE}}{\text{BASE}} * 100\%$ ) of the lower tropospheric mixing ratio of  $\text{NO}_x$  in % (regions with values below  $30 \text{ pmol mol}^{-1}$  in the BASE simulation are excluded from the calculation) averaged for (a) December, January, February and (b) June, July and August.

## $\text{NO}_x$

The global mean mixing ratio of  $\text{NO}_x$  in the LT during DJF decreases by 7% in the NOBIONO simulation compared to the BASE simulation. During JJA it decreases by 17%. In both cases the decrease in the mixing ratio is less than the contribution of  $\text{SNO}_x$  (14% and 23%, respectively). The maximum decrease is 81% in DJF and 78% in JJA, while the maximum absolute decreases in the DJF and JJA periods are  $365$  and  $319 \text{ pmol mol}^{-1}$ , respectively (figures with absolute differences can be found in the appendix). Interestingly, during DJF the mixing ratio above large parts of the Northern Hemisphere increases, by up to 7% (Fig. 2.4a) in the NOBIONO simulation, with the largest absolute increase of  $12.3 \text{ pmol mol}^{-1}$  above Europe. In the JJA period the maximum relative increase of 7.6% is larger than in the DJF period, but the maximum absolute difference is only  $7.0 \text{ pmol mol}^{-1}$  (Fig. 2.4b).

A similar result has been noted for model sensitivity simulations with and without  $\text{NO}_x$  from lightning (Stockwell et al., 1999; Labrador et al., 2005),



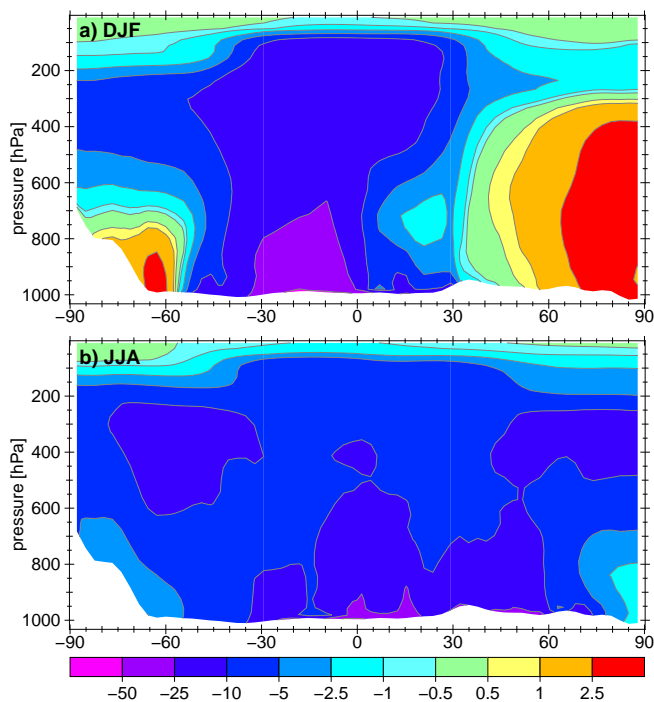


Figure 2.5: Zonal mean relative difference ( $\frac{\text{NOBIONO}-\text{BASE}}{\text{BASE}} * 100\%$ ) of the  $\text{NO}_x$  mixing ratio in % averaged for (a) December, January, February and (b) June, July and August. Note that the y-axis is linearly scaled, since the focus of this work lies in the lower troposphere.

in which a decrease in near-surface  $\text{NO}_x$  mixing ratios was computed for similar regions with increasing production of  $\text{NO}_x$  by lightning. Although  $\text{NO}_x$  produced by lightning is formed in the free troposphere and  $\text{SNO}_x$  originates from the surface, we achieve comparable results with  $\text{SNO}_x$  as with lightning  $\text{NO}_x$  by Labrador et al. (2005). To explain why the  $\text{NO}_x$  mixing ratio decreases less than the relative decrease in the emission of the NOBIONO simulation compared to the BASE simulation, and why it even increases during the DJF period in large areas in the Northern Hemisphere, the feedback through  $\text{O}_3$  and OH has to be taken into account. Stockwell et al. (1999) assumed that the general increase in  $\text{O}_3$  with lightning  $\text{NO}_x$  causes an increase in OH. This OH reduces the lifetime of  $\text{NO}_x$  ( $\tau_{\text{NO}_x}$ ) through Reaction R2.1 above regions with high non-lightning  $\text{NO}_x$  sources. Labrador et al. (2005) showed that the conversion to  $\text{HNO}_3$  via  $\text{N}_2\text{O}_5$  also contributes to the shorter  $\tau_{\text{NO}_x}$  (Reaction R2.2) with higher  $\text{NO}_x$  emissions.

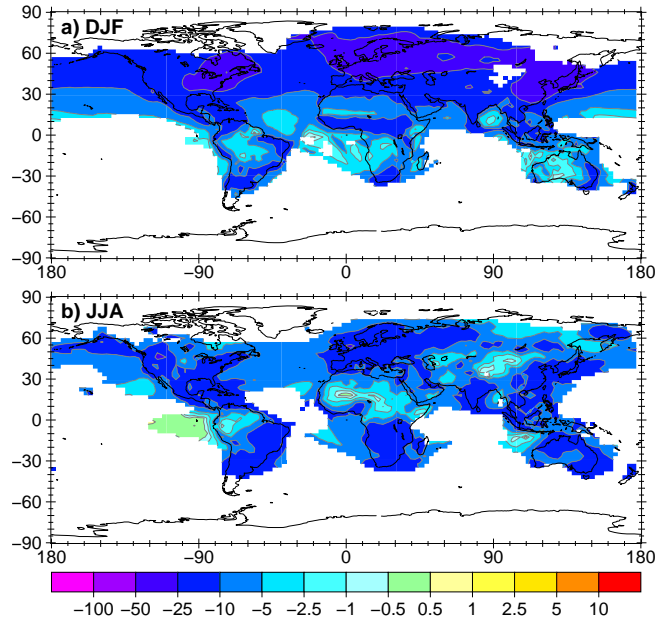
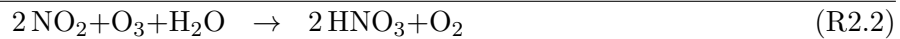
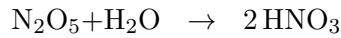
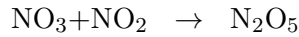
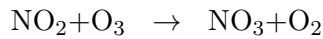


Figure 2.6: Relative difference ( $\frac{\text{REDOTHER}-\text{BASE}}{\text{BASE}} * 100\%$ ) of the lower tropospheric mixing ratio of  $\text{NO}_x$  in % (regions with values below  $30 \text{ pmol mol}^{-1}$  in the BASE simulation are excluded from the calculation) averaged for (a) December, January, February and (b) June, July and August.



Similarly we find that without  $\text{SNO}_x$ ,  $\text{O}_3$  and  $\text{OH}$  levels decrease over large regions due to the longer  $\text{O}_3$  lifetime, resulting in enhanced  $\tau_{\text{NO}_x}$ , and due to Reactions R2.1 and R2.2 the  $\text{NO}_x$  mixing ratio increases in some regions with low  $\text{SNO}_x$ . The changes in  $\text{HNO}_3$ ,  $\text{O}_3$  and  $\text{OH}$  related to this are discussed in the following sections.

In the vertical direction the strongest effects of  $\text{SNO}_x$  are simulated near the surface (DJF: 59%, JJA: 55%), and a decrease of up to 10 to

25% at higher altitudes in the zonal mean is calculated when SNO<sub>x</sub> is switched off (Fig. 2.5). The effect of convective transport to higher altitudes has a stronger influence on the difference in the total burden between 500 and 250 hPa during DJF (relative: 11.3%, absolute: 1.6 Gg) than during JJA (relative: 9.0%, absolute: 1.1 Gg). This is because the main regions where the convective transport is most effective are in the Southern Hemisphere, especially the Amazon Basin and the southern tropics of Africa (not shown). In the REDOTHER simulation the relative decrease between 500 and 250 hPa is much smaller (DJF: 5.2%, JJA: 2.9%).

The reduction of all remaining surface emissions in the REDOTHER simulation leads to a decrease in the LT NO<sub>x</sub> mixing ratio of 19% during DJF and 12% during JJA compared to the BASE simulation. A small relative increase, by less than 1%, occurs only in oceanic regions where the absolute mixing ratio is below 30 pmol mol<sup>-1</sup>. The main decreases are located above the (northern hemispheric) land surfaces (Fig. 2.6). In the zonal mean the maximum extent of the relative decrease is located closer to the surface, because the major changes are outside the tropics and are not lifted as effectively by deep convection (Fig. 2.7).

## PAN

The LT PAN mixing ratio decreases globally by 4% during DJF and 10% during JJA without SNO<sub>x</sub>. In both periods the PAN mixing ratio decreases nearly everywhere above the continents (Fig. 2.8). Above the tropical oceans, especially during JJA, there is a high relative but a negligible absolute increase in the PAN mixing ratio associated with a decrease in SNO<sub>x</sub>. As mentioned above, the formation of PAN in the northern mid- and low latitudes relies more on other trace gases than on SNO<sub>x</sub>, but more on SNO<sub>x</sub> in the southern mid-latitudes. This explains the larger decrease during DJF than during JJA. There is also no increase of PAN in the Northern Hemisphere during DJF despite higher NO<sub>x</sub> mixing ratios, which confirms a dominating role of VOC in PAN formation.

Interestingly, in the upper troposphere between 500 hPa and 250 hPa the largest decrease in the PAN mixing ratio is during DJF (6.5%), whereas it is 5.1% during JJA. In the zonal mean of the relative difference in PAN mixing ratio with and without SNO<sub>x</sub> (Fig. 2.9), the effect of convective transport in the lower latitudes is more effective during DJF than during JJA. At the

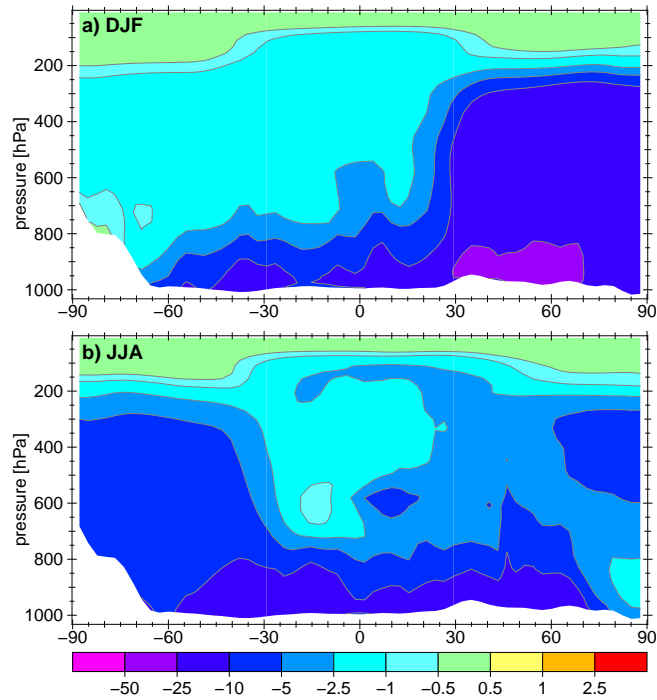


Figure 2.7: Zonal mean relative difference ( $\frac{\text{REDOTHER}-\text{BASE}}{\text{BASE}} * 100\%$ ) of the  $\text{NO}_x$  mixing ratio in % averaged for (a) December, January, February and (b) June, July and August.

higher altitudes PAN does not increase anymore, due to its longer lifetime resulting in better mixing. In the REDOTHER simulation the decrease (DJF: 4.1%, JJA: 1.4%) is smaller between 500 and 250 hPa.

The differences in the PAN mixing ratio should be interpreted with caution, because the model generally overestimates its levels compared to observations (Jöckel et al., 2006), though this may improve with a new isoprene oxidation scheme (Taraborrelli et al., 2008).

### $\text{HNO}_3$

The global LT mean mixing ratio of  $\text{HNO}_3$  decreases by 15% (DJF) and 19% (JJA) without SNOx. The greatest decrease occurs above continental regions of the low-latitudes and in the summer months in the Northern Hemisphere (Fig. 2.10). The amplified decrease in the mixing ratio of  $\text{HNO}_3$  compared to the decrease of  $\text{NO}_x$  mixing ratio is because the formation of  $\text{HNO}_3$  is not only determined by the  $\text{NO}_x$  mixing ratio, but also relies on

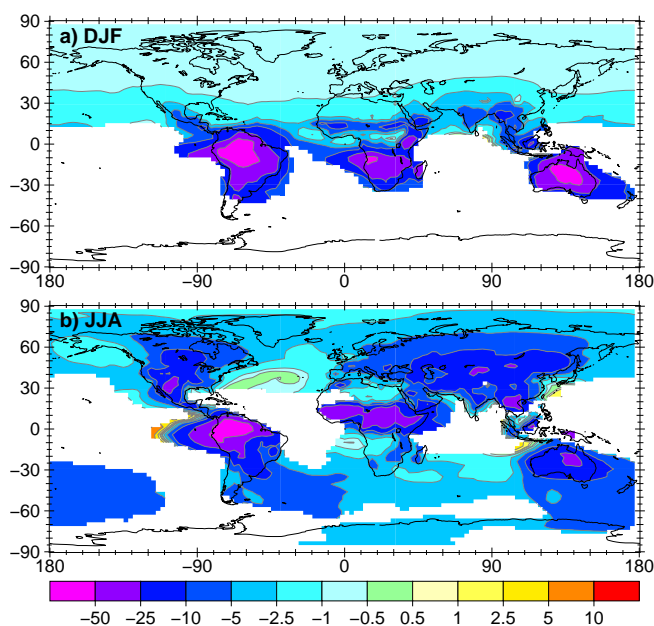


Figure 2.8: Relative difference ( $\frac{\text{NOBIONO}-\text{BASE}}{\text{BASE}} * 100\%$ ) of the lower tropospheric mixing ratio of PAN in % (regions with values below  $50 \text{ pmol mol}^{-1}$  in the BASE run are excluded from the calculation) averaged for (a) December, January, February and (b) June, July and August.

the mixing ratios of  $\text{O}_3$  and OH, which also decrease, as discussed in the following sections.

Nitric acid is mainly deposited on aerosol particles, taken up by cloud water or directly deposited on the earth's surface. The deposition of  $\text{HNO}_3$  is decreased by 18% throughout the year without SNOx. During DJF the decrease is 15% and during JJA it is 25%. In the REDOTHER simulation the deposition decrease does not substantially change during the year (18%, DJF: 19%, JJA: 17%).

### $\text{O}_3$

The mixing ratio of  $\text{O}_3$  in the NOBIONO simulation compared to the BASE simulation decreases by 5% in the LT during both seasons, with the greatest decline above the continents (Fig. 2.11). The maximum relative decrease during DJF is 38% and during JJA it is 33%. The maximum absolute decrease ( $16.2 \text{ nmol mol}^{-1}$ ) occurs during DJF above Australia (Fig. 2.11a). In contrast to what was found for  $\text{NO}_x$ , there is no region with increasing

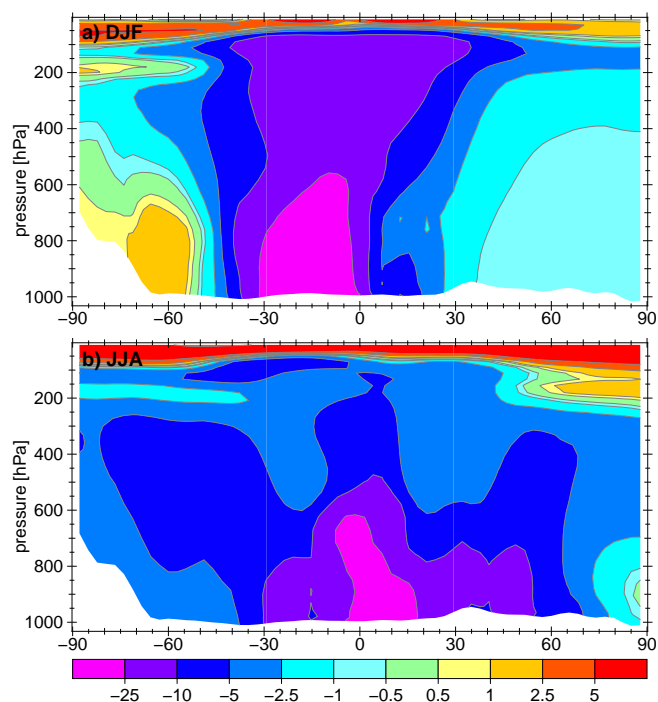


Figure 2.9: Zonal mean relative difference ( $\frac{\text{NOBIONO}-\text{BASE}}{\text{BASE}} * 100\%$ ) of the PAN mixing ratio in % averaged for (a) December, January, February and (b) June, July and August.

$\text{O}_3$  mixing ratios. The removal of  $\text{SNO}_x$  is less effective in reducing the  $\text{O}_3$  mixing ratio during JJA (17%) than during DJF (7%). This is because the formation of  $\text{O}_3$  through  $\text{SNO}_x$  competes with other strong sources of  $\text{NO}_x$  during JJA in the Northern Hemisphere, whereas  $\text{SNO}_x$  is relatively much more important the formation of  $\text{O}_3$  during DJF in the Southern Hemisphere. Furthermore, as was noted above for the PAN formation in the Northern Hemisphere the simulated  $\text{O}_3$  production depends more on VOC and other  $\text{NO}_x$  sources than  $\text{SNO}_x$ , Beekmann and Vautard (2009) show for example different photochemical regimes in Europe.

In the zonal mean distribution (not shown) a similar pattern of the influence of convection can be seen as already discussed for  $\text{NO}_x$  and PAN. But due to the longer lifetime of  $\text{O}_3$  the relative change is a maximum decrease of 13% (DJF) and 10% (JJA), which is not as strong and is more evenly distributed above all latitudes, as well as in the vertical direction. In the zonal mean there is, as with the horizontal, no region in which the mean  $\text{O}_3$  mixing ratio increases.

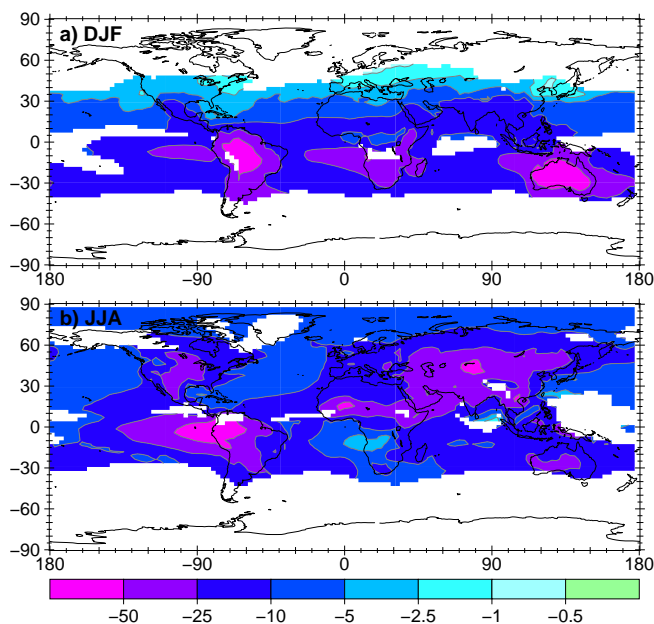


Figure 2.10: Relative difference ( $\frac{\text{NOBIONO}-\text{BASE}}{\text{BASE}} * 100\%$ ) of the lower tropospheric mixing ratio of  $\text{HNO}_3$  in % (region with values below  $30 \text{ pmol mol}^{-1}$  in the BASE simulation are excluded from the calculation) averaged for (a) December, January, February and (b) June, July and August.

Interestingly, in contrast to these results for  $\text{SNO}_x$ , in the REDOTHER simulation the mean LT  $\text{O}_3$  mixing ratio only decreases by 2.7% (DJF) and 1.8% (JJA). In the zonal mean the increase does not exceed 5%.

## OH

When we exclude the contribution of  $\text{SNO}_x$ , the mean LT OH concentration decreases by 10% during DJF and 9% during JJA. The largest relative decrease is 65% during DJF and 62% during JJA above the tropical land regions. During DJF the decrease is shifted to the southern tropics and to the northern tropics during JJA (Fig. 2.12). Note that during JJA an absolute increase above the Antarctic region is calculated, but the OH concentration here is less than  $1 \times 10^4 \text{ molec cm}^{-3}$ .

The decrease is in part induced directly by  $\text{NO}_x$  through Eq. R2.3, and in part indirectly by the lower  $\text{O}_3$  mixing ratio, leading to less primary OH production, and therefore to a decrease of the OH concentration in the LT.



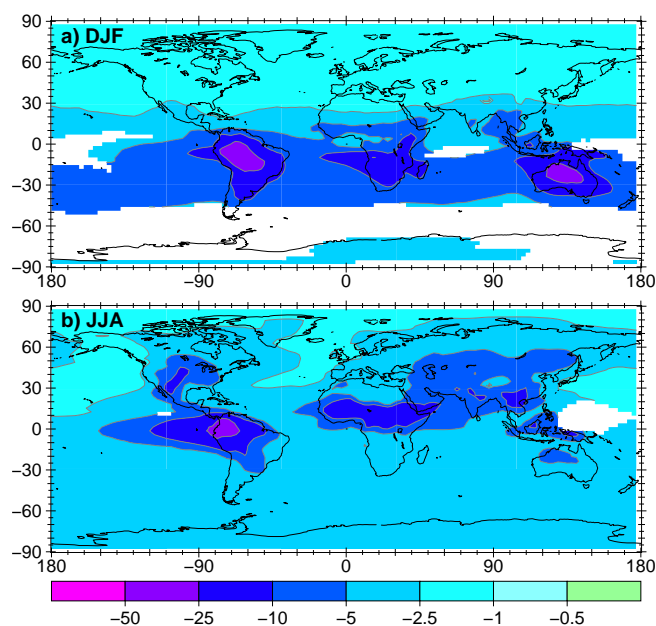


Figure 2.11: Relative difference ( $\frac{\text{NOBIONO}-\text{BASE}}{\text{BASE}} * 100\%$ ) of the lower tropospheric mixing ratio of O<sub>3</sub> in % (regions with values below 25 nmol mol<sup>-1</sup> in the BASE simulation are excluded from the calculation) averaged for (a) December, January, February and (b) June, July and August.

The largest relative decrease in the zonal mean concentration of OH is 19% during DJF and 16% during JJA. This maximum of the relative decrease in the OH concentration without SNO<sub>x</sub> is nearly detached from the surface, despite the surface source of SNO<sub>x</sub> (Fig. 2.13). At the surface OH production is mainly related to the reaction of O(<sup>1</sup>D) with water, while at higher altitudes it depends more on the reaction of NO with HO<sub>2</sub> (Eq. R2.3, see also Fig. 2.3). In the zonal mean the shift to the Southern Hemisphere during DJF is stronger than the shift during JJA to the Northern Hemisphere. The major driving reactions for the absolute decrease are the reaction of H<sub>2</sub>O with O(<sup>1</sup>D), reaction R2.3, and HO<sub>2</sub> with O<sub>3</sub> and photolysis of H<sub>2</sub>O<sub>2</sub>. The relative contribution of the four major OH producing reactions shows their strongest decrease in the lower latitudes throughout the year for the NOBIONO simulation (Fig. 2.14), whereas the the largest changes in the REDOTHER simulation are located much closer to the surface (Fig. 2.15) and are not as large as in the NOBIONO simulation.

In the REDOTHER simulation, with a 4% decrease during both seasons in the LT, the region with the strongest decrease is always located over the



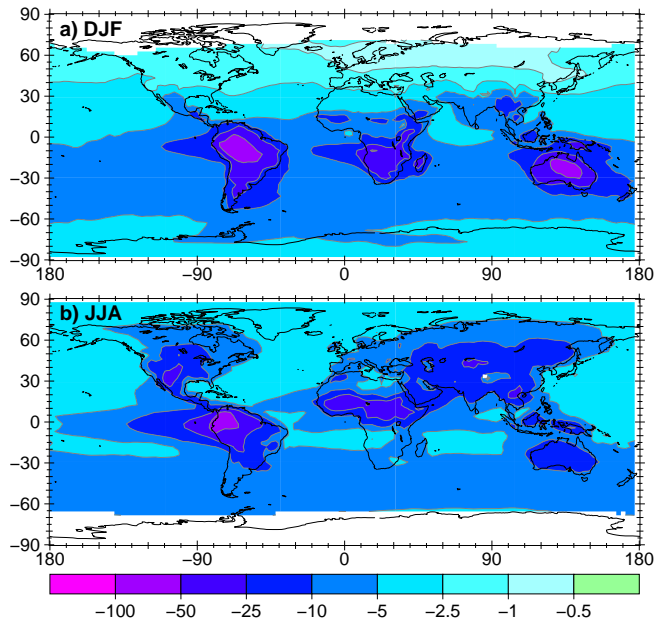


Figure 2.12: Relative difference ( $\frac{\text{NOBIONO}-\text{BASE}}{\text{BASE}} * 100\%$ ) of the lower tropospheric concentration of OH in % (regions with values below  $10^4$  molec  $\text{cm}^{-3}$  in the BASE simulation are excluded from the calculation) averaged for (a) December, January, February and (b) June, July and August.

Northern Hemisphere and the maximum relative decreases are only 15% and 11%, respectively.

### Summary for the trace gases

By following the reaction chain from  $\text{NO}_x$  through  $\text{O}_3$  and OH, including the branches of  $\text{HNO}_3$  and PAN, the correlation of the change in the mixing ratio between the BASE and NOBIONO simulation with the SNO $_x$  source declines. The strongest correlations can be found in the southern hemispheric mid-latitudes, which indicates an important role of SNO $_x$  in that region.

Although the total  $\text{NO}_x$  emission decreases in the NOBIONO simulation, we simulate an increase in the LT  $\text{NO}_x$  mixing ratio during DJF in the Northern Hemisphere. When reducing the other surface  $\text{NO}_x$  emissions in the REDOTHER simulation, we did not see an increase in the mixing ratio. This is because the influence on the  $\text{O}_3$  and OH mixing ratios in the NOBIONO simulation is stronger than for the REDOTHER simulation and

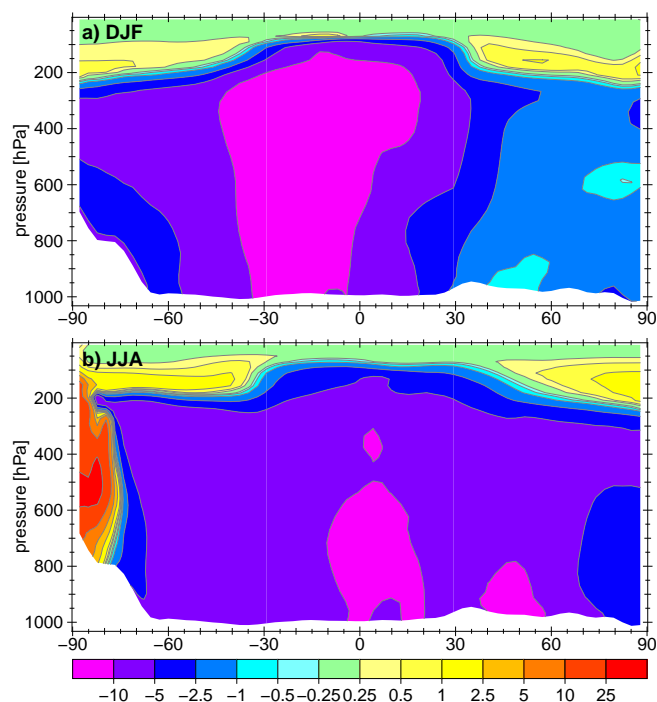


Figure 2.13: Zonal mean relative difference ( $\frac{\text{NOBIONO}-\text{BASE}}{\text{BASE}} * 100\%$ ) of the OH concentration in % averaged for (a) December, January, February and (b) June, July and August.

the feedback on  $\tau_{\text{NO}_x}$  is not strong enough in the REDOTHER simulation to increase the mixing ratio with reduced surface  $\text{NO}_x$  emissions. Our results suggest that  $\text{SNO}_x$  has a stronger influence on the related chemical processes than the remaining  $\text{NO}_x$  sources due to the geographical distribution.

### 2.3.2 Influence of $\text{SNO}_x$ on the oxidizing efficiency

The oxidation of CO and VOC in the atmosphere is mainly driven by OH. As a measure for the oxidizing efficiency of the atmosphere,  $\tau_{\text{CH}_4}$  is calculated for all simulations according to Lawrence et al. (2001). The trend of monthly mean values is depicted in Fig. 2.16. The mean  $\tau_{\text{CH}_4}$  averaged for one year (December 1994 to November 1995) for the BASE simulation is 7.25 years. It is 7.96 years in the NOBIONO simulation, a 9.8% increase without  $\text{SNO}_x$  and 7.6 years (a 4% increase) for the REDOTHER simulation. The maximum prolongation of 0.97 years (12%) occurs in February 1995 for the NOBIONO simulation and 0.38 years (4%) in December 1994

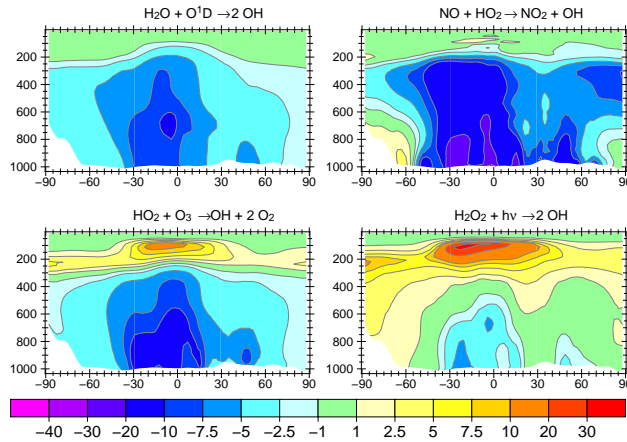


Figure 2.14: Zonal mean relative change in the OH production of the four major OH producing reactions in the NOBIONO simulation compared to the BASE simulation over one year.

for the REDOTHER simulation.

The changes in  $\tau_{\text{CH}_4}$  are not equally distributed over the globe. In the Southern Hemisphere and low-latitudes the relative influence is noticeably greater than in the northern latitudes for the NOBIONO simulation (Fig. 2.17). This agrees with the smaller relative change in the OH concentration in the northern latitudes (Fig. 2.12). In the zonal mean, the relative changes are slightly larger above 500 hPa for the NOBIONO simulation, despite the origin of SNO<sub>x</sub> at the surface. Beginning from the surface source of SNO<sub>x</sub> and following the reaction chain from NO<sub>x</sub> over O<sub>3</sub> and OH in each step, the relative difference of our two simulations becomes smaller near the surface and larger at higher altitudes. This trend corroborates the larger relative change of the oxidizing efficiency at higher altitudes. However, only  $\sim 15\%$  of the absolute amount of CH<sub>4</sub> in the troposphere is oxidized above 500 hPa (Lawrence et al., 2001).

Labrador et al. (2004) modelled a decrease of 15% in  $\tau_{\text{CH}_4}$  in a simulation with 5 Tg(N) NO<sub>x</sub> produced by lightning relative to one with no lightning NO<sub>x</sub>. Compared to this, SNO<sub>x</sub> is somewhat less effective in altering the oxidizing efficiency of the atmosphere, which is interesting, given that CH<sub>4</sub> oxidation is more effective near the surface where SNO<sub>x</sub> is emitted, due to the strong temperature dependence of the reaction of OH with CH<sub>4</sub>. The change in the oxidizing efficiency due to lightning NO<sub>x</sub> is larger than due

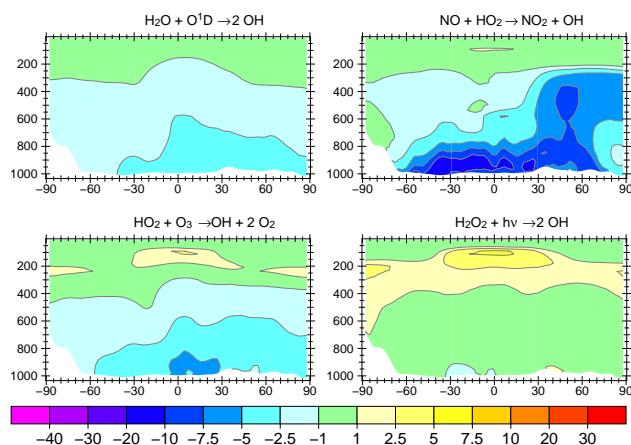


Figure 2.15: Zonal mean relative change in the OH production of the four major OH producing reactions in the REDOTHER simulation compared to the BASE simulation over one year.

to SNO<sub>x</sub>, even though the total emission rate is lower. This is because at higher altitudes the NO:NO<sub>2</sub> ratio is greater, so that with more NO the NO<sub>x</sub> lifetime is not diminished as strongly as near the surface. Furthermore at higher altitudes more NO results in higher OH yields by reaction with HO<sub>2</sub>.

## 2.4 Conclusions and outlook

The emission of NO from soils plays an important role for chemical reactions in the atmosphere in our simulations. Lower global mean NO<sub>x</sub> mixing ratios without SNO<sub>x</sub> lead to lower global O<sub>3</sub> mixing ratios in the LT. The lower O<sub>3</sub> mixing ratios result in lower OH concentrations. This results in an enhanced lifetime of NO<sub>x</sub> in regions with other dominating sources of NO<sub>x</sub>. Hence the NO<sub>x</sub> mixing ratios increases in some regions, despite lower emissions when SNO<sub>x</sub> is neglected in our NOBIONO simulation. This effect did not occur in the REDOTHER simulation, in which we comparably reduced the remaining surface NO emissions. From this it follows that although NO<sub>x</sub> is a short-lived tracer it indirectly influences chemical processes in regions with low SNO<sub>x</sub> through feedback with O<sub>3</sub> and OH. By following the reaction chain up to PAN and HNO<sub>3</sub>, we detected a dominating role of SNO<sub>x</sub> compared to VOC in the mid-latitudes of the Southern Hemisphere. Also by following the reaction chain (SNO<sub>x</sub>→NO<sub>x</sub>→O<sub>3</sub>→OH), the magnitude of relative effects

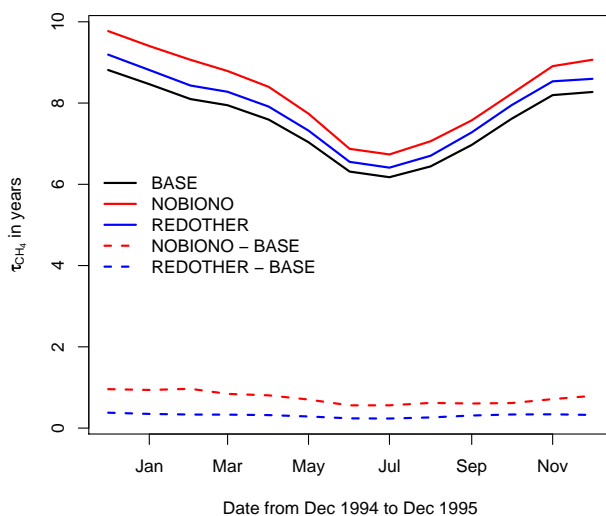


Figure 2.16: Seasonal cycle of monthly mean lifetime of  $\text{CH}_4$  from December 1994 to December 1995 in years (calculated according to Lawrence et al., 2001).

are shifted step by step to higher altitudes in the troposphere.

Through reaction of NO with  $\text{HO}_2$ , SNOx is directly involved in the production of OH. SNOx also has, through  $\text{O}_3$ , an indirect influence on OH production. With OH formed by SNOx through these pathways,  $\tau_{\text{CH}_4}$  is decreased considerably, and the influence of SNOx on the tropospheric oxidizing efficiency is considerable, approximately 10%. Reducing the other surface NO emissions by the same amount only lead to an increase of 4% in  $\tau_{\text{CH}_4}$ .

The notable modelled influence of SNOx on directly and indirectly related trace gases shown in this work supports further efforts to improve the parameterization of SNOx in CTMs, as also proposed by Jaeglé et al. (2005).

**Acknowledgements** We thank the anonymous referees for their constructive and fruitful comments. We appreciate the help of the modellers and the MESSy team, especially T. Butler, A. Kerkweg, P. Jöckel and M. Tanarhte. We acknowledge the International Max Planck Research School on Atmospheric Chemistry and Physics for financial support.

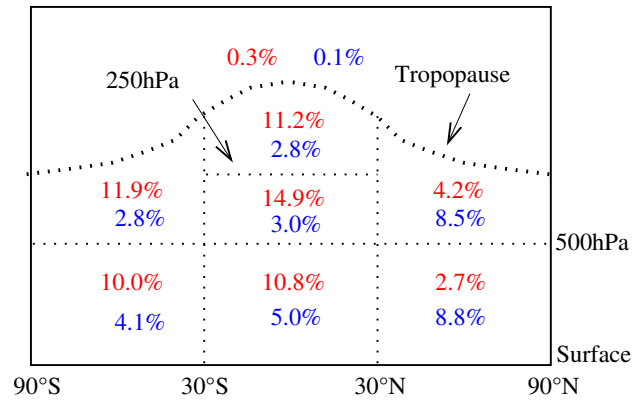


Figure 2.17: Relative increase of  $\tau_{\text{CH}_4}$  ( $\frac{\tau_{\text{CH}_4, \text{simulation}} - \tau_{\text{CH}_4, \text{BASE}}}{\tau_{\text{CH}_4, \text{BASE}}} * 100\%$ ) for the NOBIONO (red) and REDOTHER (blue) simulation in various zonal subdomains of the atmosphere (calculated according to Lawrence et al., 2001).

### 3 Improvement and evaluation of simulated global biogenic soil NO emissions in an AC-GCM

*J. Steinkamp*<sup>1</sup> and *M. G. Lawrence*<sup>1, 2</sup>

<sup>1</sup> Department of Atmospheric Chemistry, Max-Planck-Institute for Chemistry, Mainz, Germany

<sup>2</sup> University of Mainz, Institute for Physics of the Atmosphere, Mainz, Germany

---

**This chapter is the revised version of:**

Steinkamp, J. and Lawrence, M. G.: Improvement and evaluation of simulated global biogenic soil NO emissions in an AC-GCM, *Atmos. Chem. Phys. Discuss.*, 10, 16007–16054, doi:10.5194/acpd-10-16007-2010, 2010.

## **Abstract**

Biogenic NO emissions from soils (SNO<sub>x</sub>) play important direct and indirect roles in tropospheric chemistry. The most widely applied algorithm to calculate SNO<sub>x</sub> in global models was published 15 years ago by Yienger and Levy (1995), and was based on very few measurements. Since then numerous new measurements have been published, which we used to build up a compilation of world wide field measurements covering the period from 1978 to 2010. Recently, several satellite-based top-down approaches, which recalculated the different sources of NO<sub>x</sub> (fossil fuel, biomass burning, soil and lightning), have shown an underestimation of SNO<sub>x</sub> by the algorithm of Yienger and Levy (1995). Nevertheless, to our knowledge no general improvements of this algorithm, besides suggested scalings of the total source magnitude, have yet been published. Here we present major improvements to the algorithm, which should help to optimize the representation of SNO<sub>x</sub> in atmospheric-chemistry global climate models, without modifying the underlying principals or mathematical equations. The changes include: 1) using a new landcover map, with twice the number of landcover classes, and using annually varying fertilizer application rates; 2) adopting a fraction of 1.0% for the applied fertilizer lost as NO, based on our compilation of measurements; 3) using the volumetric soil moisture to distinguish between the wet and dry states; and 4) adjusting the emission factors to reproduce the measured emissions in our compilation (based on their geometric and arithmetic mean values). These steps lead to increased global annual SNO<sub>x</sub>, and our total above canopy SNO<sub>x</sub> source of 8.6 Tg yr<sup>-1</sup> (using the geometric mean) ends up being close to one of the satellite-based top-down approaches (8.9 Tg yr<sup>-1</sup>). The above canopy SNO<sub>x</sub> source using the arithmetic mean is with 27.6 Tg yr<sup>-1</sup>, which is higher than all previous estimates, but compares better with a regional top-down study in eastern China. This suggests that both top-down and bottom-up approaches will be needed in future attempts to provide a better calculation of SNO<sub>x</sub>.



### 3.1 Introduction

Nitrogen oxides ( $\text{NO}_x = \text{NO} + \text{NO}_2$ ) play an important role in the chemical processes of the atmosphere, especially in the production and destruction of ozone (Chameides et al., 1992). On a global scale,  $\text{NO}_x$  emissions are dominated by anthropogenic combustion processes, which contribute 20–24  $\text{Tg(N) yr}^{-1}$  (Denman et al., 2007). The biogenic NO emission flux from soils (hereafter SNOx) contributes 5.5 to 21  $\text{Tg(N) yr}^{-1}$  (Yienger and Levy, 1995; Davidson and Kingerlee, 1997) and is in the same range as NO produced by lightning and biomass burning. However, in a previous study we showed that due to the geographical distribution of modeled SNOx, its influence on the reaction chain from  $\text{NO}_x$  through  $\text{O}_3$  and OH to the oxidizing efficiency is stronger than for the other surface sources (Steinkamp et al., 2009).

In recent years, measurements of the  $\text{NO}_2$  column from satellites have been used in “top-down” approaches to optimize emissions from various sources, including SNOx (Martin et al., 2003; Bertram et al., 2005; Jaeglé et al., 2005; Müller and Stavrakou, 2005; Martin et al., 2006). Coming from the other direction, “bottom-up” approaches have used various algorithms for estimating SNOx based on soil and climatological parameters. The most widely used algorithm to calculate SNOx was developed 15 years ago by Yienger and Levy (1995) (hereafter YL95) and has been applied in numerous global atmospheric chemistry models (e.g. Lawrence et al., 1999; Ganzeveld et al., 2002a; Horowitz et al., 2003; Martin et al., 2003; Hauglustaine et al., 2004; Jaeglé et al., 2005; Müller and Stavrakou, 2005; Jöckel et al., 2006; Delon et al., 2008; van der A et al., 2008). In comparison to most of the top-down studies, SNOx seems to be generally underestimated by the algorithm of Yienger and Levy (1995). Since the publication of YL95, many more measurements have been carried out and published than were available at the time of YL95, which could potentially reduce the discrepancy.

Here we present major improvements to the algorithm by YL95 and derive updated emission factors, which could easily be used in other models as well. These new emission factors are calibrated in a bottom-up approach with a global compilation of measurements of SNOx. We then compare our simulated emissions to the a posteriori top-down emissions of Jaeglé et al. (2005), and discuss them in the context of other top-down studies by Müller

and Stavrakou (2005), Wang et al. (2007), Stavrakou et al. (2008), and Zhao and Wang (2009).

### **3.2 Model framework and measurement compilation**

For this study we applied the ECHAM5/MESSy Atmospheric Chemistry (EMAC) model (ECHAM5 version 5.3.01, MESSy version 1.6), which is a numerical chemistry and climate simulation system that includes sub-models describing tropospheric and middle atmospheric processes and their interaction with oceans, land and human influences (Jöckel et al., 2006). It uses the first version of the Modular Earth Submodel System (MESSy1) to link multi-institutional computer codes. The core atmospheric model is the 5th generation European Centre Hamburg general circulation model ECHAM5 (Roeckner et al., 2006). The MESSy submodels switched on here simulated cloud microphysics and stratiform precipitation (CLOUD), deep convection dynamics and precipitation (CONVECT, Tost et al. (2006b)), online emissions (ONLEM, Kerkweg et al. (2006b)) and the global solar and terrestrial radiative energy budgets (RAD4ALL).

We performed a simulation covering the period from 1990 to 2000, during which most of the measurements in our compilation were performed during this period. We nudged our simulation by the ECMWF ERA40 data (Upala et al., 2005), with a spherical truncation of T106 (approx. 1.1 by 1.1 degrees) and 31 pressure levels. Although it would be possible to compute the SNO<sub>x</sub> source directly using the ERA40 data, which provides the relevant parameters (soil moisture and temperature) at a higher resolution, we instead apply the EMAC model at a coarser spatial resolution, since the results of our study are intended for use in similarly coarse atmospheric chemistry models (and the calculation of soil moisture differs between ERA40 and EMAC (Drusch et al., 2009; Roeckner et al., 2003)).

SNO<sub>x</sub> is calculated in the submodel ONLEM according to the algorithm by Yienger and Levy (1995) implemented by Ganzeveld et al. (2002a, 2006) (hereafter called YL95EMAC). We then use the soil temperature, soil wetness and precipitation from this simulation as input for offline calculations of SNO<sub>x</sub>, with improvements applied in 4 steps (each building on the previous step):

1. Introduction of a new landcover map, using yearly varying fertilizer data for fertilizer induced emissions (FIE) and applying a modified pulsing routine (“LC”, section 3.3.1 and 3.3.2).
2. Reduction of NO emission from fertilizer application (“LC+FIE”, section 3.3.4).
3. Use of volumetric soil moisture instead of soil water column (“LC+FIE+VSM”, section 3.3.5).
4. Recalibration of emission factors with measurements (“YL95/SL11”<sup>1</sup>, section 3.3.6).

### 3.2.1 State of the Art Model

The parameterization by YL95 distinguishes between two soil moisture states. YL95 uses the precipitation rates of the previous 14 days, whereas in YL95-EMAC the water content in the soil is used to distinguish between dry and wet soil conditions. SNO<sub>x</sub> is calculated based on a statistically derived dry ( $A_d$ ) and wet ( $A_w$ ) emission factor for 12 different ecosystems and a temperature dependence according to the Eq. 3.1a and 3.1b with T in °C.

$$F_{soil}(T, A_w) = \begin{cases} 0.28 \cdot T \cdot A_w & 0^\circ C < T \leq 10^\circ C \\ e^{0.103 \cdot T} \cdot A_w & 10^\circ C < T \leq 30^\circ C \\ 21.97 \cdot A_w & T > 30^\circ C \end{cases} \quad (3.1a)$$

$$F_{soil}(T, A_d) = \begin{cases} \frac{T}{30} \cdot A_d & 0^\circ C < T \leq 30^\circ C \\ A_d & T > 30^\circ C \end{cases} \quad (3.1b)$$

For rainforests, constant emissions were assumed for the dry and wet seasons. Agricultural areas are calculated like wet grassland, plus a fraction of the applied fertilizer (see below). In the YL95EMAC simulation the twelve ecosystems (Table 3.1, 4th column) defined by YL95 are based on the 72 ecosystems of Olson (1992). The reduced emissions from “rice-producing areas” in eastern Asia and eastern India as described in YL95 are not implemented in the YL95EMAC algorithm.

---

<sup>1</sup>SL11 refers to this study

Table 3.1: World surface areas of the YL95EMAC ecosystems and new YL95/SL11 landcover classes in the EMAC model. For YL95EMAC the first number is as adopted from Olson (1992) and the number in brackets gives the area reduced by (1 – cultivation index) for non-agricultural areas and the cultivated area for agriculture with the cultivation index after Bouwman et al. (2002b).

ID	MODIS landcover	Köppen main climate <sup>a</sup>	YL95EMAC ecosystem	Area [10 <sup>6</sup> km <sup>2</sup> ]	
				YL95/SL11	YL95EMAC
0	Water	—	Water	364.18	367.15 (364.3)
1	Permanent wetland	—		0.30	
2	Snow and ice	—	Ice	16.12	15.44 (15.44)
3	Barren	D, E		2.28	
4	Unclassified	—		0.07	
5	Barren	A, B, C	Desert	17.68	17.23 (16.71)
6	Closed shrubland	—	Shrubland	0.75	0 (0)
7	Open shrubland	A, B, C		14.85	
8	Open shrubland	D, E	Tundra	11.85	11.61 (11.36)
9	Grassland	D, E		0.46	
10	Savannah	D, E		4.66	
11	Savannah	A, B, C	Grassland	9.76	33.10 (27.12)
12	Grassland	A, B, C		8.80	
13	Woody savannah	—	Woodland	10.94	14.16 (7.98)
14	Mixed forest	—	Dec. forest	6.87	5.07 (3.41)
15	Evergr. broadl. forest	C, D, E		1.97	
16	Dec. broadl. forest	C, D, E		1.66	
17	Dec. needlel. forest	—		0.93	
18	Evergr. needlel. forest	—	Conif. forest	5.78	15.81 (14.45)
19	Dec. broadl. forest	A, B	Dry dec. forest	0.62	4.70 (3.68)
20	Evergr. broadl. forest	A, B	Rainforest	12.76	10.40 (9.12)
21	Cropland	—	Agriculture	13.13	15.48 (30.01)
22	Urban and build-up lands	—		0.73	
23	Cropland/nat. veg. mosaic	—		3.01	

<sup>a</sup> A: equatorial, B: arid, C: warm temperate, D: snow, E: polar

The calculated flux is then multiplied by a pulsing factor, which emulates the physical sudden pulse of NO that is known to occur when precipitation falls after a dry period. If there was less accumulated precipitation in a gridcell during the last 14 days then 10 mm, and the precipitation then exceeds 1 mm (“sprinkle”), 5 mm (“shower”) or 15 mm (“heavy rain”) during one day, an increase of the emission rate by the factor in Eq. 3.2 at time  $t = 1$  (in days) is assumed, lasting for 3, 7 or 14 days, respectively (the values on the far right in the equations are the 24-hour rain rate which induces the pulse).

$$pulse = \begin{cases} 11.19 \cdot e^{-0.805 \cdot t} & 1 < t < 3; & 1 - 5 \frac{mm}{day} \\ 14.68 \cdot e^{-0.384 \cdot t} & 1 < t < 7; & 5 - 15 \frac{mm}{day} \\ 18.46 \cdot e^{-0.208 \cdot t} & 1 < t < 14; & > 15 \frac{mm}{day} \end{cases} \quad (3.2)$$

If the pulsing criterion is not fulfilled, then *pulse* is set to 1. Thus the direct SNOx from the soil into the vegetation layer (lowest atmospheric layer containing vegetation of various types, e. g. grass, trees or shrubs) is calculated as product of Eq. 3.1a,b and 3.2:

$$SNOx = pulse \cdot F_{soil}(T, A_{w/d}, [fertilizer]) \quad (3.3)$$

Finally, SNOx is partly removed via dry deposition in the vegetation before it is released into the free troposphere, which is represented by a canopy reduction factor (CRF), calculated based on Jacob and Bakwin (1991) as:

$$CRF = \frac{e^{-k_s \cdot SAI} + e^{-k_c \cdot LAI}}{2} \quad (3.4)$$

with  $k_s = 8.75 \text{ m m}^{-2}$  and  $k_c = 0.24 \text{ m m}^{-2}$  representing stomata and cuticle absorptivity constants. SAI is the stomatal area index (ratio of stomatal area to leaf surface area) and LAI is the leaf area index (ratio of leaf surface to the geographical surface area). The calculation of CRF is originally based on ecosystem and season specific stomatal area indices as well as a monthly leaf area index map. SNOx\* effectively released to the atmosphere is thus calculated by multiplying Eq. 3.3 with Eq. 3.4:

$$SNOx^* = CRF \cdot SNOx \quad (3.5)$$

The SNO<sub>x</sub> in the YL95EMAC simulation prior to applying the CRF is depicted in Fig. 3.1.

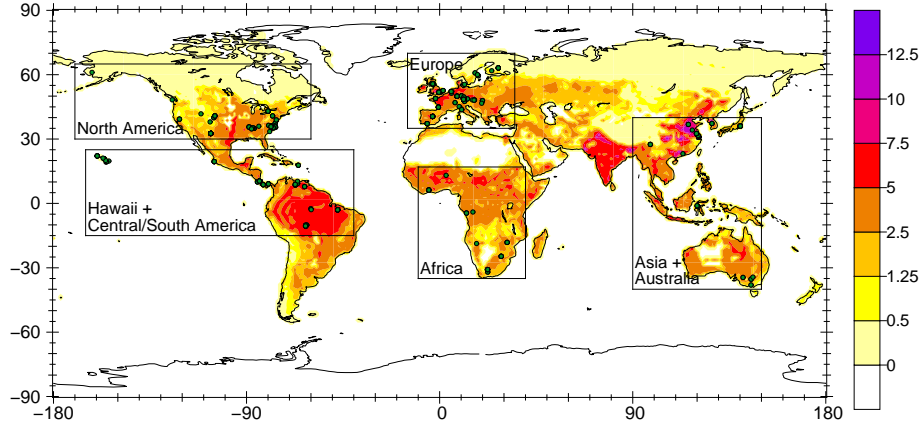


Figure 3.1: SNO<sub>x</sub> flux in the YL95EMAC simulation (in  $\text{ng m}^{-2} \text{s}^{-1}$ ), along with the locations of measurements (dots) and the regions referred to in section 3.3.6.

### 3.2.2 Compilation of measurements

Yienger and Levy (1995) had far fewer measurements available when they developed their algorithm 15 years ago than there are today. They used data at 12 different sites in 3 ecosystems taken from 4 publications with 12 to 144 single events per site to calculate the exponential factor for the wet emissions between 10 and 30°C (see Eq. 3.1a), and measurements from 24 sites in 6 of their ecosystems taken from 15 publications (plus two additional unpublished sites) were used to calculate the other emission factors under wet conditions. For the dry emission factors they used 9 sites in one ecosystem (grassland) taken from 7 publications (including two unpublished sites). For one ecosystem (dry deciduous forest), they did not indicate where the data comes from and for the others the dry emission factor is calculated as one third of the wet emission flux which is applied above 30°C (see Eq. 3.1a), which gives  $A_d = \frac{21.97}{3} A_w \approx 7.3 \cdot A_w$ . Based on one measurement in rice paddies (Galbally et al., 1987), YL95 assumed reduced agricultural emissions by a factor of  $\frac{1}{30}$  in the the whole agricultural area of eastern Asia and half the agricultural area of east and cental India. This reduction is highly debatable, and the sensitivity of the results to this reduction is discussed in Section 5.

We have compiled, building on Stehfest and Bouwman (2006), a dataset consisting of 112 articles with 583 field measurements of SNO<sub>x</sub> covering the period from 1976 to 2010, with 367 measurements during the simulation period. There are clear spatial gaps in the measurements, e.g. in central and eastern Russia as well as between Saudi Arabia and India, which can be seen by the distribution of the measurement locations in Fig. 3.1.

We employ a more recent landcover system, based on the MODIS satellite data (Friedl et al., 2006) and combine this for some landcover classes with the Koeppen main climate classes (Kottek et al., 2006) listed in Table 3.1, which doubles the number of landcover classes compared to YL95 and YL95EMAC. In order to compare to YL95EMAC, we associated the most similar ecosystem used in YL95 with the landcover class after Friedl et al. (2006) for each individual measurement based on the given description. For a better comparison to the tables, we call landcovers in A, B (and some C) climates “warm”, landcovers in (C), D and E climates “cold”, and give the ID used in the tables in brackets. The compilation and additional information like soil properties and the literature references are made available in the electronic supplement.

The range of measured SNO<sub>x</sub> spans from  $-6.89$  to  $547 \text{ ng m}^{-2} \text{ s}^{-1}$  in the whole compilation with a nearly log-normal distribution (Fig. 3.2), which is quite common for natural processes. There are 23 measured fluxes less than 0, and 8 measured fluxes equal to 0. We set these to  $10^{-4} \text{ ng m}^{-2} \text{ s}^{-1}$ , so that on the histogram a second small peak at  $-9.2 \approx -4 \cdot \ln(10)$  appears. We write the log-normal means and standard deviations for example as  $3.67^{+7.35}_{-2.45}$ , rather than in the exponential form  $e^{1.3 \pm 1.1}$ . By classifying the compilation of measurements using the MODIS landcover combined with the Koeppen main climate classes, there are measurements in 13 of the 24 new landcover classes (Table 3.1), which are used later on. As can be seen in Fig. 3.3 the log-normal distribution again matches the distribution of the measurements in individual ecosystems, when we ignore all fluxes that are equal to or less than zero. In cold open shrubland (8) there was only one measurement, therefore no histogram can be shown for it.

Due to the large variations in the measured SNO<sub>x</sub> fluxes and the coarse spatial model resolution in AC-GCMs, we will use the full compilation of measurements for optimizing the calculation of SNO<sub>x</sub> fluxes, rather than only the measured fluxes that were carried out during our simulation pe-

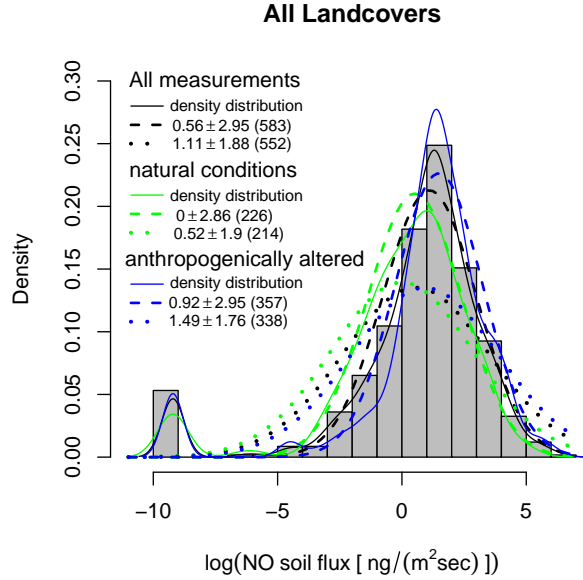


Figure 3.2: Logarithmic histogram and probability density function of all measured SNOx in the compilation with standard distribution, calculated mean and standard deviation. Black lines are all measurements, green are measurements under natural conditions and blue are anthropogenically altered measurements. The small peak at  $-9.2 \approx -4 \cdot \ln(10)$  towards the left of the plot is because we replaced values  $\leq 0$  with  $10^{-4}$ . The dashed lines are the standard distributions including these replaced values and the dotted lines are the standard distributions where values  $\leq 0$  were removed from the dataset, respectively. Number of measurements are in brackets.

riod (underlying this is an assumption of a relatively stable climate with annually varying weather and soil conditions during the measurement period). The compilation contains 219 measurements in agricultural lands, 226 measurements under more or less “undisturbed” or “natural” conditions and 138 measurements for anthropogenically altered conditions in the non-agricultural landcovers. Anthropogenic alterations include fertilizer application, irrigation, liming, clearcutting and other perturbations. The measurements under non-agricultural land with anthropogenic influence ( $4.29^{+16.08}_{-3.38}$ ) are, according to the Kolmogorov-Smirnov test with  $p < 10^{-3}$ , significantly higher than under unperturbed natural conditions ( $1.68^{+9.52}_{-1.43}$ ). Therefore wherever enough measurements were available, we use only the unperturbed measurements to calibrate our new emission factors, whereas we used all the



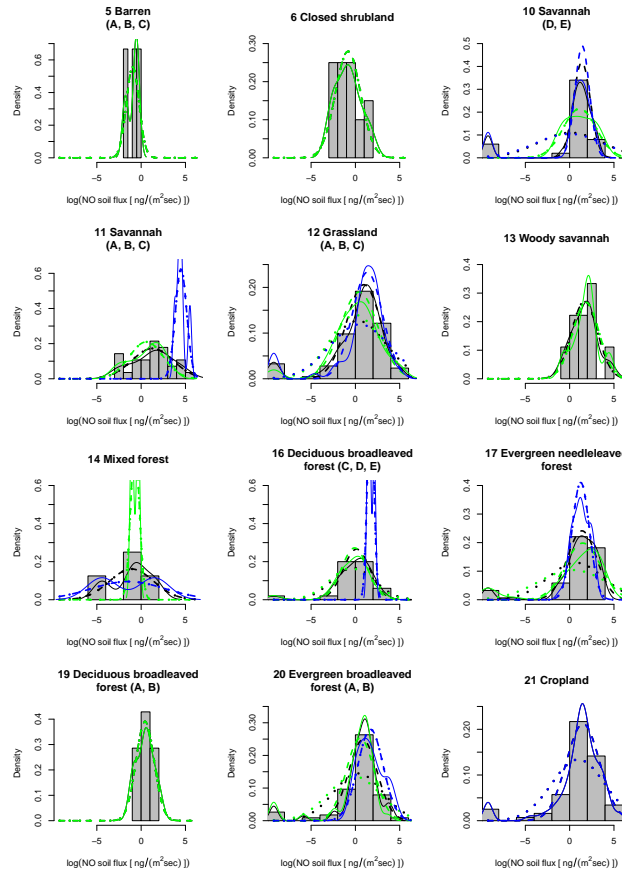


Figure 3.3: Logarithmic histogram and probability density function per MODIS landcover and Koeppen main climate class (in brackets) of measured SNO<sub>x</sub> in the compilation. Color and line type as in Fig. 3.2.

measurements whenever too few were available.

### 3.3 Emission model updates

In Fig. 3.4 we compare the simulated flux of YL95EMAC with the measured fluxes in our compilation of measurements for each ecosystem, and Table 3.2 gives the mean values for each ecosystem. From this it is obvious that the flux from each ecosystems (except tundra and rainforest) as well as the global simulated flux is underestimated by the algorithm, and an improvement is necessary. All of the fluxes in this section are without considering the CRF, since this would introduce another uncertainty. Furthermore, almost all

measurements in our compilation were chamber measurements, for which the canopy interaction does not play a significant role.

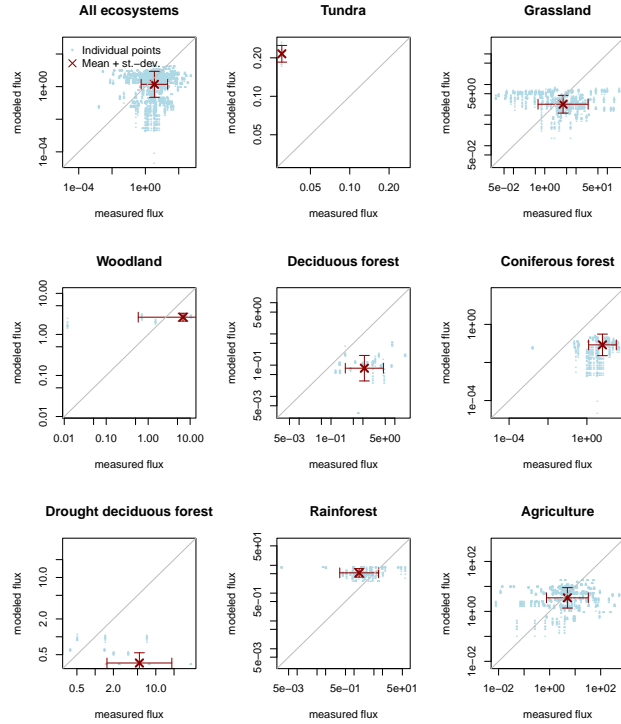


Figure 3.4: Scatterplot of simulated SNO<sub>x</sub> in YL95EMAC for each corresponding period of the year versus each measurement along with the mean values and standard deviations.

In the following sections we introduce the improvements which we implemented in the calculation of the SNO<sub>x</sub> flux in our model and discuss the changes which were caused by these improvements. We discuss the change in the pulsing routine first, since this affects all our new simulations beyond YL95EMAC. The change in the underlying landcover map and the change in how fertilizer application is dealt with cannot readily be treated separately and are discussed in one step (LC). The LC case is also used for considering the effects of resolution, before going on to the other individual developments.

Table 3.2: Measured and simulated SNO<sub>x</sub> for the YL95EMAC ecosystems (in ng m<sup>-2</sup>s<sup>-1</sup>). Measurements are taken from our compilation of measurements (numbers per ecosystem in brackets) and the simulated SNO<sub>x</sub> values are for the corresponding period of each simulated year.

Ecosystem	N	measured	YL95EMAC
Tundra	11(1)	0.03 <sup>+0</sup> <sub>-0</sub>	0.22 <sup>+0</sup> <sub>-0.03</sub>
Grassland	1695(156)	3.85 <sup>+20.48</sup> <sub>-3.24</sub>	2.27 <sup>+12.05</sup> <sub>-1.1</sub>
Woodland	55(5)	6.77 <sup>+72.29</sup> <sub>-6.19</sub>	2.63 <sup>+28.06</sup> <sub>-0.52</sub>
Deciduous forest	227(22)	1.11 <sup>+3.29</sup> <sub>-0.83</sub>	0.08 <sup>+0.24</sup> <sub>-0.05</sub>
Coniferous forest	759(71)	6.3 <sup>+26.11</sup> <sub>-5.07</sub>	0.08 <sup>+0.35</sup> <sub>-0.06</sub>
Drought deciduous forest	117(11)	5.37 <sup>+13.01</sup> <sub>-3.8</sub>	0.36 <sup>+0.88</sup> <sub>-0.12</sub>
Rainforest	552(51)	1.51 <sup>+5.75</sup> <sub>-1.2</sub>	5.36 <sup>+20.39</sup> <sub>-1.59</sub>
Agriculture	2111(196)	4.97 <sup>+27.81</sup> <sub>-4.22</sub>	3.49 <sup>+19.54</sup> <sub>-2.13</sub>
All ecosystems	5527(513)	3.48 <sup>+18.2</sup> <sub>-2.92</sub>	1.38 <sup>+7.23</sup> <sub>-1.16</sub>

### 3.3.1 Pulsing

In the YL95EMAC algorithm as implemented previously in EMAC the amount of precipitation to initiate the pulsing was queried every model timestep; therefore the pulsing hardly ever reached its maximum range of values, and contributes only 3% to the total SNO<sub>x</sub> in the YL95EMAC simulation. From the LC simulation onwards, we check the precipitation of the last 24 hours only once a day at 00:00 UTC. As a result, the fraction attributed to pulsing increases to 17% (Table 3.3). Our new result is in the range of the 10–22% proposed by Davidson (1992) and, compared to the previous YL95EMAC setup, it is much closer to the 24% originally simulated by YL95.

Nevertheless, we note that this is a very crude implementation. In the literature some measurements show small pulses (Garcia-Montiel et al., 2003), while others show much larger pulses (Davidson et al., 1991). Too much rain could also reduce the diffusivity of the soil (Rondón et al., 1993), which would reduce the strength of the pulse with strong precipitation events. Finally other events which can also generate pulses, like fire or plowing (Sanhueza, 1997), are not yet considered in our model.

Table 3.3: The original (YL95) emission factors and the soil biogenic NO emissions calculated with the old ecosystems (YL95EMAC) and with the new landcover (LC). When not shown, standard deviations are less than or equal to 0.001.

ID	Emission factors		Emission $\left[ \frac{\text{Tg(N)}}{\text{year}} \right]$			
	wet	dry	YL95EMAC		LC	
0	0	0	0		0	
1	0	0	0		0	
2	0	0	0		0	
3	0	0	0		0	
4	0	0	0		0	
5	0	0	0		0	
6	0	0	0		0	
7	0	0	0		0	
8	0.05	0.37	0.02	(3%)	0.03±0.002	(17%)
9	0.05	0.37			0.002	(18%)
10	0.05	0.37			0.03	(20%)
11	0.36	2.65	3.0±0.05	(2%)	1.65±0.03	(16%)
12	0.36	2.65			1.17±0.02	(19%)
13	0.17	1.44	0.45±0.01	(3%)	0.61±0.01	(15%)
14	0.03	0.22	0.02	(2%)	0.03	(16%)
15	0.03	0.22			0.02	(16%)
16	0.03	0.22			0.01	(17%)
17	0.03	0.22			0.002	(17%)
18	0.03	0.22	0.03	(3%)	0.02	(18%)
19	0.06	0.4	0.09	(3%)	0.02	(15%)
20	2.6	8.6	1.6±0.1	(3%)	2.33±0.05	(12%)
21	0.36	—	4.03±0.04	(3%)	3.84±0.40	(19%)
22	0.36	—			0.25±0.01	(17%)
23	0.36	—			0.95±0.06	(18%)
sum			9.24±0.16	(3%)	10.95±0.48	(17%)

<sup>a</sup> pulsing fraction in brackets.

### 3.3.2 Ecosystem/Landcover (LC)

Instead of using the twelve ecosystems originally introduced by YL95, we use the 18 MODIS landcover classes (Friedl et al., 2006) for the year 2000 and combine them with the main climates of the Koeppen climate classification (Kottek et al., 2006) to yield a new total of 24 landcover types (Table 3.1) with the emission factors listed in Table 3.3.

SNO<sub>x</sub> increases from  $9.24 \pm 0.16 \text{ Tg(N) yr}^{-1}$  to  $10.95 \pm 0.48 \text{ Tg(N) yr}^{-1}$  due to the new landcover map. We simulate a small increase in “natural” ecosystems (ID 0 – 20 in Table 3.1), changing from  $5.21 \text{ Tg(N) yr}^{-1}$  to  $5.91 \text{ Tg(N) yr}^{-1}$  and a larger increase in “anthropogenic” ecosystems (ID 21 – 23) from  $4.03$  to  $5.04 \text{ Tg(N) yr}^{-1}$ . The geographical distribution of annually simulated SNO<sub>x</sub> also changes, in particular with:

- Increased emissions over Europe, central USA, Eastern Asia and India (Fig. 3.5), especially due to the treatment of fertilizer (see section 3.3.4); and
- Lower emissions over large parts of Australia, the southern Arabian peninsula and Somalia, which was prescribed as grassland in YL95-EMAC, while these regions are now dominated by shrublands.

If we were to apply the reduced emissions in the “rice-producing areas”, this would introduce unrealistic straight borders at  $35^\circ$  North and  $60^\circ$  East with emissions reduced by  $1.24 \text{ Tg(N) yr}^{-1}$  (see Sections 3.4 and 3.5 for discussion).

### 3.3.3 Influence of model resolution

The simulations considered here are at a relatively high resolution, without the computationally expensive chemical processes in the atmosphere. When they are included, the model is usually run at a lower horizontal resolution. To investigate the influence of the resolution on SNO<sub>x</sub> we performed three additional simulations at T21 ( $\sim 5.6 \times 5.6^\circ$ ), T42 ( $\sim 2.8 \times 2.8^\circ$ ) and T63 ( $\sim 1.9 \times 1.9^\circ$ ). The effect of the resolution is depicted in Fig. 3.6.

The fraction of SNO<sub>x</sub> from rain induced pulses increases with a finer model resolution. Since in a coarser horizontal model resolution the convective precipitation is dispersed over a larger area, this leads to weaker pulses and less likelihood of reaching the pulsing threshold.

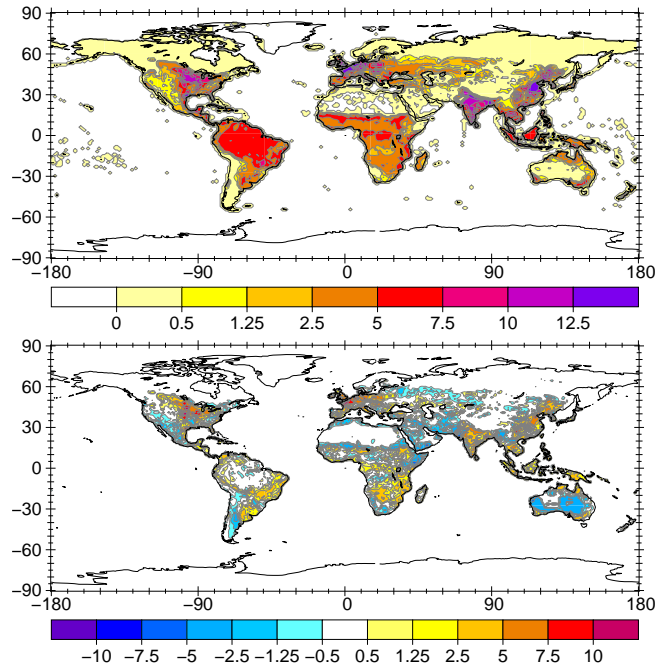


Figure 3.5: Averaged SNOx flux in the whole simulation period (in  $\text{ng m}^{-2} \text{s}^{-1}$ ) for the LC simulation (upper panel) and the change compared to the YL95EMAC simulation (lower panel).

The general increase of the emission rate with finer resolution is due to the exponential dependence on the temperature in the calculation of the wet emission flux. Although the temperature of one gridbox in the lower resolution simulation will roughly equal the mean temperature of the corresponding set of gridboxes in the high resolution simulation, the peak temperatures will be greater at higher resolution, so that due to the exponential function, SNOx will also be higher in the finer resolution simulation. One possibility to reduce the underestimation in the coarser resolution simulations would be to scale either all the emission factors or the emission flux by the ratio of the annual emission flux in the T106 simulation to the coarse resolution simulations (Table 3.4).

Scaling the emission factors results in a notable improvement (Table 3.4) but still results in an underestimation, since the area of soils defined as wet increases slightly with increasing resolution and other unresolved non-linearities influence the simulation. Scaling the emission flux with the same factor would lead to a large overestimation (due to the dependence on latitude), therefore we apply the scaling factor to the emission factors.

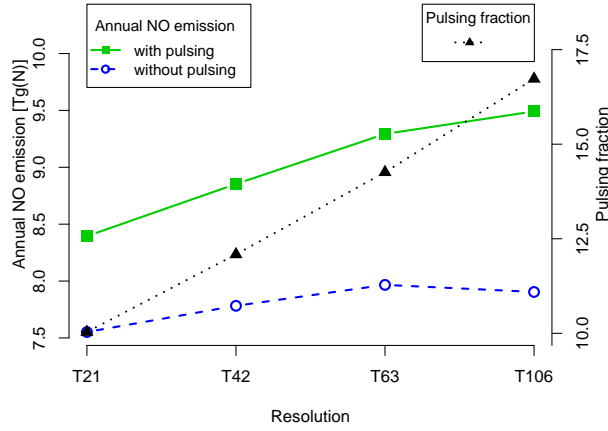


Figure 3.6: Change of soil biogenic NO emission with pulsing (green boxes), without pulsing (blue circles) and the pulsing fraction (triangles) for the LC simulation at four different horizontal resolutions.

Table 3.4: Relative annual underestimation of SNO<sub>x</sub> in the coarser simulations compared to the T106 resolution of the YL95EMAC and LC simulation. Relative deviation if the emission factors (left value) or the gridcell emission flux (right value) is scaled by the previous underestimation. The last column lists the global area defined as wet in  $10^6$  km<sup>2</sup> (which equals  $111.8 \cdot 10^6$  km<sup>2</sup> for the T106 simulation).

	YL95EMAC				LC				wet area [ $10^6$ km <sup>2</sup> ]
	underest.	factor	deviation	deviation	underest.	factor	deviation	deviation	
T21	11.8%	1.118	-4.6%	9.6%	13.1%	1.131	-5.6%	10.1%	108.6
T42	4.3%	1.043	-2.1%	13.5%	7.2%	1.072	-3.3%	20.7%	110.0
T63	2.1%	1.021	-1.8%	13.2%	2.3%	1.023	-2.0%	14.1%	111.1

### 3.3.4 Fertilizer induced NO emission (LC+FIE)

In YL95EMAC the ecosystem map was overlaid with the cultivation index by Bouwman et al. (2002b) and used the same amount of applied fertilizer for each year, from which a certain fraction (0.7%) was emitted as FIE during the growing season. However, since agriculture is already defined in the ecosystem map based on Olson (1992), but was not considered as a separate ecosystem in YL95EMAC, effectively some fraction of the emitting gridbox is neglected (otherwise some fraction would have been double-counted). Therefore SNO<sub>x</sub> from model gridboxes with a fraction of agriculture in the ecosystem map was underestimated in YL95EMAC. This can also be seen if one sums up the ecosystem areas used for the calculation of the emission

flux (values in brackets of column “YL95EMAC” in Table 3.1), which gives a total world surface area of  $504 \cdot 10^6 \text{ km}^2$ , less than the actual surface area of  $510 \cdot 10^6 \text{ km}^2$ .

The amount of globally consumed fertilizer increased within the period of our simulation by 18%, based on an analysis by the United Nations Environment Programme (UNEP, <http://geodata.grid.unep.ch>). Therefore we use yearly varying fertilizer application based on the country based FAO fertilizer consumption rate provided by UNEP, and assume that the fertilizer is applied on the area of the last three landcover classes in Table 3.1 during the growing season as described in YL95. Since using this method results in unrealistic amounts of fertilizer usage for the Lesser Antilles and the islands east of Madagascar (up to  $34,790 \text{ kg(N) ha}^{-1} \text{ yr}^{-1}$ ), we assumed an upper limit of  $500 \text{ kg(N) ha}^{-1} \text{ yr}^{-1}$ , which is high but should be viable, given that fertilizer applications up to  $378\text{-}524 \text{ kg(N) ha}^{-1} \text{ yr}^{-1}$  have been reported (Richter and Roelcke, 2000). This approach is still not very accurate, since for example fertilizer is not spatially and temporally distributed evenly over large countries like China (Ju et al., 2004), and different crop types receive different amounts of fertilizer. However, the information needed to distribute the fertilizer by crop type is presently not available, thus we can only make modest improvements, such as the annually varying fertilizer application rates.

Yienger and Levy (1995) originally assumed a fraction of 2.5% of the applied fertilizer to be lost as NO. Based on our compilation of measurements our best estimate (arithmetic mean) of FIE is  $1 \pm 2.1\%$ , therefore we set the FIE to 1% in our optimized simulation, which gives a global emission of  $1.8 \text{ Tg(N) yr}^{-1}$  induced by fertilizer application, instead of 3.69 with an FIE of 2.5%. Thus we have reduced the global NO emissions by  $1.9 \text{ Tg(N) yr}^{-1}$  by reducing the FIE in our simulation from 2.5% to 1%. The reduction is mainly located over the central USA, Europe, northeast Asia and India.

Our estimated fertilizer fraction emitted as SNO<sub>x</sub> is higher than the value of 0.55% calculated by Stehfest and Bouwman (2006) and the previous value by Bouwman et al. (2002b) of 0.7%, which contributed  $0.7 \text{ Tg(N) yr}^{-1}$  to the total flux in YL95EMAC (Ganzeveld et al., 2006). The total annual SNO<sub>x</sub> from agriculture in the LC+FIE simulation of  $3.13 \text{ Tg(N)}$  is higher than the estimate by Bouwman et al. (2002b) and Stehfest and Bouwman (2006) of 1.8 and  $1.6 \text{ Tg(N)}$ , respectively, but our value is within the large range of



uncertainty given by Stehfest and Bouwman (2006) (-80% and +406% for the 95% confidence interval).

Finally the reduction of SNO<sub>x</sub> in the “rice-producing areas” is debatable (see section 3.5). If we would reduce the emissions there, we would decrease the emissions by 0.81 Tg(N) yr<sup>-1</sup>.

### 3.3.5 Soil moisture state (LC+FIE+VSM)

Yienger and Levy (1995) used the precipitation history to distinguish between the dry and wet soil conditions. In YL95EMAC the water column in the soil as described by Roeckner et al. (2003) was used instead. Since the simulation of soil moisture has improved substantially over the last decade, we can now make use of the volumetric soil moisture content, which can be calculated with the help of the root depth (S. Hagemann, pers. comm.). We set the threshold for dry vs. wet conditions to 15% volumetric soil moisture content, which is for an average soil between the field capacity (amount of water that can be held by the soil against the gravitational force) and the permanent wilting point (below which plants can not take up the water anymore). However, for pure sand 15% is more than can be held against the gravitational force, whereas in pure clay 15% is even less moisture than the permanent wilting point (Scheffer and Schachtschabel, 2002). Fig. 3.7 shows how often the soil was defined as wet during the simulation period. Note that there may be considerable differences in the formulation of the soil moisture in other GCMs, and the distinction into wet and dry conditions would be an interesting facet of the algorithm to examine and possibly improve in a future multi-GCM intercomparison.

This modification has a major impact on the classes warm savannah (11), warm grassland (12) and woody savannah (13), with a decrease of annual SNO<sub>x</sub> flux by 0.41, 0.42, and 0.11 Tg(N), respectively. Since these landcover classes are mostly present in the Sahel region, eastern Africa and southern USA/northern Mexico, the emissions from those regions are affected most. In the other landcover classes the emissions are reduced by less than 0.01 Tg(N) yr<sup>-1</sup>. This includes the cropland classes, which do not include an explicit dependence on the soil moisture, since it is assumed that due to irrigation the soil moisture is relatively constant and normally in the wet regime, although this assumption could possibly be improved in future studies. As a result of these changes, the global annual flux in the

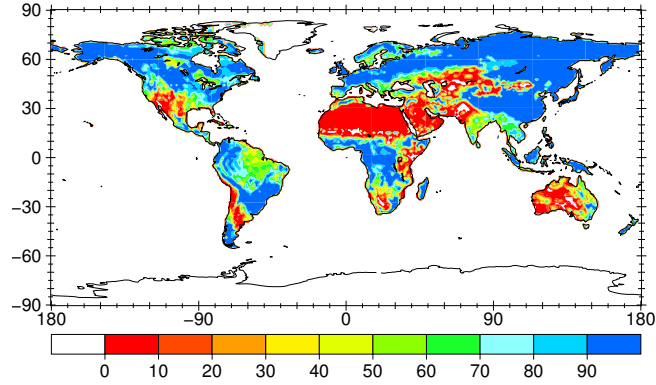


Figure 3.7: Percentage of wet soil conditions during the whole simulation period.

LC+FIE+VSM simulation is  $8.08 \text{ Tg(N) yr}^{-1}$ .

### 3.3.6 Emission Factors (YL95/SL11)

For each individual measurement in our compilation we calculated the emission factor for the appropriate period of the whole simulation (individually for each year of the simulation, then determining the mean emission factor from these) as described below. In order to reduce the statistical error we used monthly averages instead of averages only over those days for which measurements were available.

Since we have only the total SNO<sub>x</sub> for each measurement and do not have time series of the measurements, accompanied with time series of temperature and soil moisture it is impossible to calculate the emission factors analytically. Therefore, to determine new emission factors for each measurement we iteratively computed the new emission factor, starting with the original emission factor by YL95, then decreasing the difference between model and measurement by multiplication with a factor  $s$  or its reciprocal value, as shown in Eq. 3.6a-b:

$$s = 1 + \frac{|\Delta f|^{0.8}}{50 + 50 * A_w} \quad (3.6a)$$

$$A_{w/d,i} = \begin{cases} s \cdot A_{w/d,i-1} & \text{for } \Delta f \geq 0 \\ \frac{1}{s} \cdot A_{w/d,i-1} & \text{for } \Delta f < 0 \end{cases} \quad (3.6b)$$

where  $\Delta f = \text{measured flux} - \text{simulated flux}$ , and  $i$  is the number of the iteration step. For any negative values that are included in the calculation of the arithmetic mean we multiplied the factor with -1 in the first iteration step. Since the measured range of NO fluxes spans over a few orders of magnitude (0.00289 to 547  $\text{ng m}^{-2}\text{s}^{-1}$ ), we set the convergence criterion to  $\frac{\Delta f}{\text{measured flux}} \leq 10^{-4}$ , after which we stopped the iteration. For measured negative fluxes (deposition) and zero flux, we did not include the measurement in using the geometric mean (Table 3.5) to calculate the new emission factors. Ignoring measurements less than or equal to zero (dashed lines in Fig. 3.2 and 3.3) matches the distribution of measurements (solid lines) better than replacing them with by  $10^{-4}$  (dotted lines). For landcover classes with both anthropogenically altered and unperturbed measurements, we used the full set of available data in an ecosystem as well as unperturbed measurements only, to calculate the new emission factors and compare the results. The wet emission factors for unperturbed and altered conditions are depicted in Fig. 3.8. In woody savannah taking all measurements decreased the emissions by 0.44 Tg(N). This decrease is nearly compensated by slightly increased emissions from warm savannah, evergreen needleleaved forest and warm evergreen broadleaved forest.

To give a potential upper limit for SNO<sub>x</sub>, we also calculated the arithmetic mean (Table 3.6), including the negative and zero fluxes. The total global SNO<sub>x</sub> of the arithmetic mean is  $33.1 \pm 0.6 \text{ Tg(N) yr}^{-1}$  if we use unperturbed measurements only to calibrate the emission factors. This is insignificantly larger than the value  $32.86 \pm 0.6 \text{ Tg(N) yr}^{-1}$  which we compute when we also include anthropogenically altered measurements. Again we get an increase in woody savannah, which is compensated by reductions in grassland (A, B, C). The influence of omitting negative or zero fluxes increases the global total SNO<sub>x</sub> by only 1.18 Tg(N) to  $34.3 \pm 0.7 \text{ Tg(N) yr}^{-1}$  for the arithmetic mean. Given the large range of uncertainties for the emission factors, this justifies omitting measurements less than or equal to zero in the calculation of the geometric mean. A much larger effect would result from reducing emission in the “rice-producing areas”, which would decrease the emission by  $4.79 \text{ Tg(N) yr}^{-1}$  in the arithmetic mean calculation.

Although we used the timeseries of our simulated soil moisture and temperature, we can not calculate the wet and dry emission factors separately due to the lack of time series data of the measured SNO<sub>x</sub> and therefore we

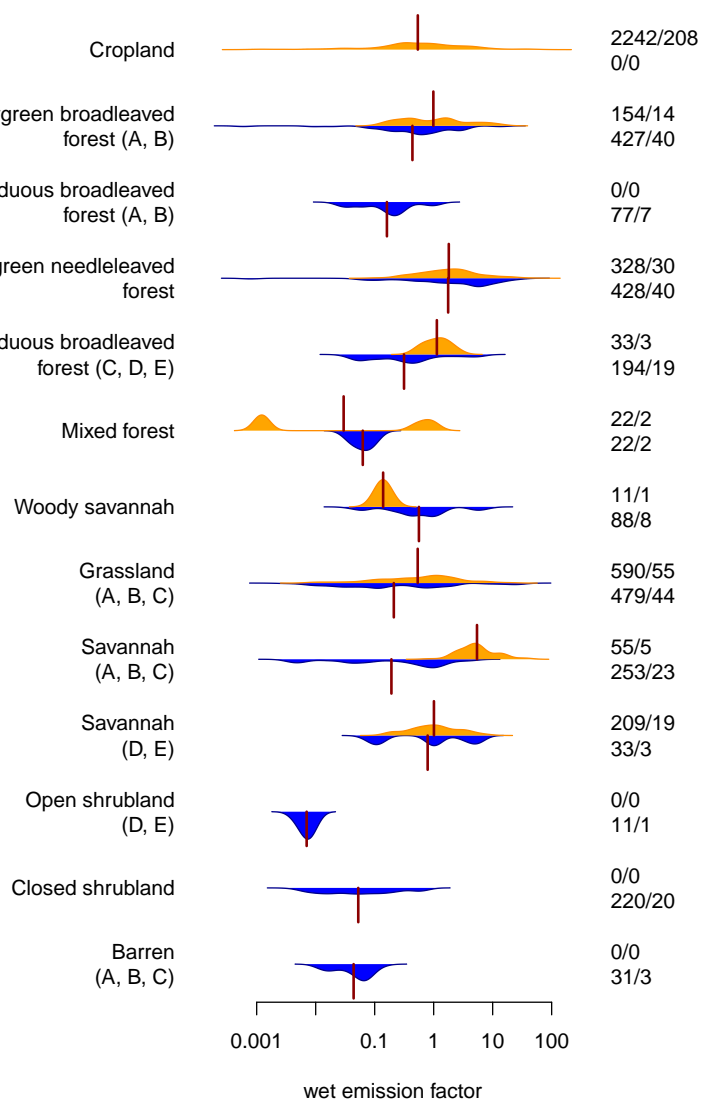


Figure 3.8: Distribution of calculated emissions factors for anthropogenically altered (orange, above center line) and unperturbed (blue, below center line) measurements. The number of calculated emission factors and number of measurements per crop are given on the right side, respectively.

Table 3.5: The adopted (YL95/SL11) emission factors (geometric mean) and associated soil biogenic NO emissions. When not shown, standard deviations are less than or equal to 0.001.

ID	N	Emission factors		Emission
		wet	dry	$\left[\frac{\text{Tg(N)}}{\text{year}}\right]$
0	0	0	0	0
1	0	0	0	0
2	0	0	0	0
3	0	0	0	0
4	0	0	0	0
5	31(3)	$0.06^{+0.02}_{-0.02}$	$0.43^{+0.15}_{-0.11}$	$0.2 \pm 0.005$
6	220(20)	$0.09^{+0.31}_{-0.07}$	$0.65^{+2.24}_{-0.50}$	0.02
7	—	0.09	0.65	$0.33 \pm 0.01$
8	11(1)	$0.01^{+0.00}_{-0.00}$	$0.05^{+0.01}_{-0.01}$	0.005
9	—	0.87	6.44	$0.03 \pm 0.02$
10	33(3)	$0.87^{+0.75}_{-0.40}$	$6.44^{+5.52}_{-2.97}$	$0.35 \pm 0.01$
11	253(23)	$0.19^{+1.21}_{-0.16}$	$1.39^{+8.87}_{-1.20}$	$0.65 \pm 0.01$
12	479(44)	$0.43^{+1.91}_{-0.35}$	$3.12^{+13.91}_{-2.55}$	$0.89 \pm 0.02$
13	88(8)	$0.77^{+0.32}_{-0.23}$	$6.48^{+2.72}_{-1.92}$	$2.29 \pm 0.03$
14	22(2)	$0.07^{+0.03}_{-0.02}$	$0.49^{+0.23}_{-0.15}$	$0.06 \pm 0.002$
15	—	0.35	2.35	$0.16 \pm 0.003$
16	194(19)	$0.35^{+1.10}_{-0.27}$	$2.35^{+7.35}_{-1.78}$	$0.11 \pm 0.003$
17	—	0.35	2.35	$0.02 \pm 0.002$
18	428(40)	$1.47^{+8.11}_{-1.24}$	$10.73^{+59.27}_{-9.08}$	$0.75 \pm 0.03$
19	77(7)	$0.08^{+0.14}_{-0.05}$	$0.62^{+1.03}_{-0.39}$	0.02
20	427(40)	$0.31^{+1.94}_{-0.27}$	$1.60^{+7.86}_{-1.33}$	$0.38 \pm 0.002$
21	2242(208)	$0.57^{+2.56}_{-0.46}$	—	$3.25 \pm 0.17$
22	—	0.57	—	$0.18 \pm 0.006$
23	—	0.57	—	$0.78 \pm 0.03$
sum				$10.51 \pm 0.24$

Table 3.6: The adopted (YL95/SL11) emission factors (arithmetic mean) and associated soil biogenic NO emissions.

ID	N	Emission factors		Emission
		wet	dry	$\left[\frac{\text{Tg(N)}}{\text{year}}\right]$
0	0	0	0	0
1	0	0	0	0
2	0	0	0	0
3	0	0	0	0
4	0	0	0	0
5	31(3)	0.06±0.01	0.45±0.10	0.21±0.005
6	220(20)	0.21±0.24	1.55±1.75	0.04
7	—	0.21	0.78	0.03±0.03
8	11(1)	0.01±0.00	0.05±0.01	0.005
9	—	0.99	7.30	0.04±0.002
10	33(3)	0.99±0.47	7.30±3.47	0.40±0.02
11	253(23)	0.64±0.91	4.72±6.66	2.20±0.04
12	490(45)	2.39±6.38	17.48±46.55	4.98±0.10
13	88(8)	0.82±0.48	6.95±4.06	2.44±0.04
14	22(2)	0.07±0.03	0.52±0.18	0.06±0.002
15	10(1) <sup>a</sup>	0.95	6.3	0.44±0.01
16	194(18)	0.95±1.49	6.3±9.9	0.31±0.01
17	—	0.95	6.3	0.06±0.01
18	472(43)	4.84±4.27	35.4±31.2	2.46±0.09
19	77(7)	0.13±0.14	0.99±1.06	0.03
20	458(42)	1.16±2.57	4.43±8.43	1.15±0.02
21	2361(219)	3.13±7.84	—	13.58±0.32
22	—	3.13	—	0.69±0.01
23	—	3.13	—	3.22±0.1
sum				33.11±0.6

<sup>a</sup> One flux measurement was 0, therefore emission factors of landcover 16 were assumed

keep the ratio between the dry and wet factor constant at 7.3, like in the algorithm by YL95.

For the geometric mean we calculated the new emission factors for each landcover class ( $A_{w/d}$ ) according to Eq. 3.7. We weight each calculated emission factor by the duration of the experimental period in  $d$  days.

$$A_{w/d} = e^{\frac{\sum_{i=1}^N (\log(A_{w/d,i}) \cdot d_i)}{\sum_{i=1}^N d_i}} \quad (3.7)$$

with  $A_{w/d,i}$  being the wet and dry emission factors for each measurement  $i$ , and  $N$  is the number of measurements per landcover. The calculation of the arithmetic mean was also weighted by the duration of the measurement.

### Emission factors calculated by region

As depicted in Fig. 3.1 we defined 5 regions with clusters of measurements. We abbreviate the regions as follows: EUR - Europe, NAM - North America, SAM - Central/South America + Hawaii, ASA - Asia and Australia and AFR - Africa. Here we recompute the geometric mean of the emission factors separately for each region, using both the unperturbed and anthropogenically influenced measurements in natural ecosystems. We discuss several of the key differences between the regions for selected landcovers (for which there are measurements in multiple landcovers), along with reasons for differences, e.g. different measured fluxes, simulated soil temperature and moisture as well as other unaccounted factors. The unaccounted factors include primarily the amount of available nitrogen and the organic material and its quality, since SNO<sub>x</sub> is mainly produced in the uppermost centimeters of the soil, including the organic layer (Jambert et al., 1994; Papke and Papen, 1998; Bargsten et al., 2010).

**Cold savannah (10):** For EUR compared to NAM we calculate an emission factor that is more than twice as high, although the emission fluxes are very similar with  $4.40_{-2.42}^{+5.38}$  and  $3.62_{-2.40}^{+7.14}$  ng m<sup>-2</sup> s<sup>-1</sup>, respectively. The calculations for EUR were taken from 2 publications (10 sites) and for NAM from 3 publications (15 sites). The difference is due to the simulated soil temperature, which is around 15°C for nearly all measurements in EUR and NAM, except for 3 measurements in EUR with measured values of 2.06, 1.67 and 6.82 ng m<sup>-2</sup> s<sup>-1</sup> at 1°C and for one with a flux of 1.9 ng m<sup>-2</sup> s<sup>-1</sup> at 6°C.

Thus, similar fluxes were measured in the two regions, but the simulated soil temperature differs. To yield the same emission factor for the EUR sites with the measured SNO<sub>x</sub> flux data, we would have to increase the temperature in EUR by 10 K in our model, which is unlikely; therefore other unaccounted factors must exist, which cause these differences.

**Warm savannah (11):** Although the measured flux in SAM is higher than in AFR, we calculate higher emission factors for AFR than for SAM. This can be explained by both the soil moisture and the temperature. In AFR we have more days with a volumetric soil moisture content below 15%, whereas in SAM the wet flux dominates. The mean temperatures in SAM are 27.0–29.4°C, just slightly below 30°C, while in AFR they are well below 30°C for most of the 17 measurements (2 at 9.9°C, 3 at 13–14.9°C and 6 at 22.3–24.3°C). Therefore a higher emission factor is necessary in AFR than in SAM, which represents other controlling factors that are not yet explicitly considered in the algorithm.

**Warm grassland(12):** The emission factors calculated for EUR and especially ASA are much higher than for the other three regions. In EUR the mean soil temperatures are all below 20°C and in ASA below 15°C. In AFR, which also has a relatively high flux, the wet soil regime is dominant, resulting in a lower emission factor. The measured flux in NAM is low compared to the other regions, yielding a lower emission factor. Due to these reasons higher emission factors are needed in EUR and ASA.

**woody savannah (13):** The emission factors are calculated to be higher in SAM than in AFR; since soil temperature and moisture do not differ very much, this is simply due to higher emission fluxes measured in SAM than in AFR.

**Deciduous broadleaved forest (16):** The calculated emission factors are higher in NAM than in EUR, mainly because the measured fluxes in NAM are higher than in EUR, and in EUR there are more wet emission periods than in NAM.

**Evergreen broadleaved forest (20):** Most of the measurements were performed in SAM, for which the calculated emission factor is nearly the same as in AFR, while a lower emission factor is calculated for ASA due to lower measured fluxes than in SAM and AFR.

**Agriculture (21):** The emission factor is only calculated for wet soil conditions as proposed by YL95. NAM has a similar mean measured emis-



sion flux to ASA, but the temperature is on average higher, resulting in a higher emission factor for ASA. In AFR we also calculate a high emission factor, but only two measurements were performed in agricultural areas in Africa with a high emission flux.

### Global results used in YL95/SL11

The final stage of the direct surface emissions (prior to implementing the canopy reduction factor) is YL95/SL11. For the new emission factors in this simulation, we used the values listed in Tables 3.5 and 3.6. When there were no measurements in a landcover class (IDs: 7, 9, 15, 17, 22, 23), we used the emission factor of the most similar class (see Table 3.1). For example, for deciduous needleleaved forest (17), we choose the same emission factor as for deciduous broadleaved forest in cold climate (16), since they are more similar than compared to evergreen needleleaved forests (Vogt et al., 1986).

In the step from LC+FIE+VSM to YL95/SL11 we find an increase of all emission factors in all landcover classes except for cold open shrubland (8), warm savannah (11) and evergreen broadleaved forest in warm climates (20), where the emissions decrease by  $0.02 \text{ Tg(N) yr}^{-1}$  (81%),  $0.58 \text{ Tg(N) yr}^{-1}$  (47%) and  $1.94 \text{ Tg(N) yr}^{-1}$  (83%), respectively. On a global scale the decrease is only visible in the tropical regions (Fig. 3.9), where the latter two landcovers are mainly located.

The strongest increases (greater than  $0.5 \text{ Tg(N) yr}^{-1}$ ) in the annual global flux were simulated for woody savannah (13), evergreen needleleaved forest (18) and cropland (21) with  $1.78$  (352%),  $0.73$  (4794%) and  $0.85 \text{ Tg(N) yr}^{-1}$  (35%) increases, respectively. Globally this leads to an increase of  $2.43 \text{ Tg(N) yr}^{-1}$  (24%) compared to the LC+FIE+VSM simulation.

Since we increase the emissions from agricultural land cover classes (21–23) from  $3.13 \text{ Tg(N) yr}^{-1}$  in the LC+FIE simulation to  $4.22 \text{ Tg(N)}$ , we further depart from the values of Stehfest and Bouwman (2006) and Bouwman et al. (2002b) ( $1.8$  and  $1.6 \text{ Tg(N) yr}^{-1}$ , respectively), but are still within their 95% confidence interval. We also calculated the emission factors per crop type separately (Fig. 3.10). Although there are not enough observations at present to implement such a further specification reliably into the algorithm, this may be interesting to pursue in future research, and we lay the groundwork for that here. These emission factors calculated per crop type span over more than an order of magnitude, with the lowest one in rice

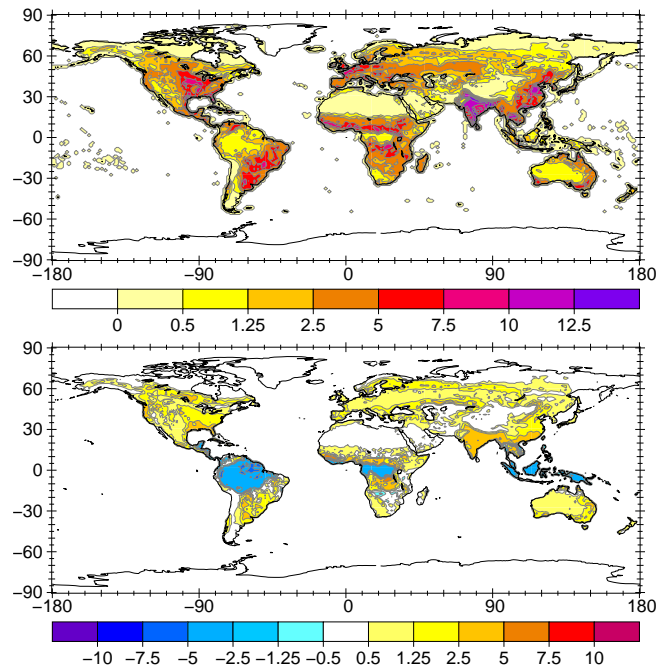


Figure 3.9: Averaged SNOx flux in the whole simulation period (in  $\text{ng m}^{-2} \text{s}^{-1}$ ) for the YL95/SL11 simulation (upper panel) and the change compared to the LC+FIE+VSM simulation (lower panel).

fields; here in particular we see the need for additional measurements, since there were only two measurements conducted in rice fields.

The new total SNOx flux is now  $10.51 \text{ Tg(N) yr}^{-1}$  without the reduction in the “rice-producing areas”, and  $9.6 \text{ Tg(N) yr}^{-1}$  when the reduction is included.

### 3.3.7 Canopy reduction factor (CRF)

We also use an updated map of the monthly mean leaf area index (LAI), published by Deng et al. (2006), to calculate the canopy reduction factor (CRF), which is relevant for the comparison with satellite-based estimates in the next section. The data of Deng et al. (2006) is available starting in 1998, so that we could not use the appropriate annual cycle of LAI for the full simulation period. Instead, we used the average of each month for the years 1999, 2002, 2003 and 2005; these were chosen because other years had unrealistic high values in the Sahel region or artificial straight lines in the data. On an annual average the CRF does not change a lot from YL95EMAC

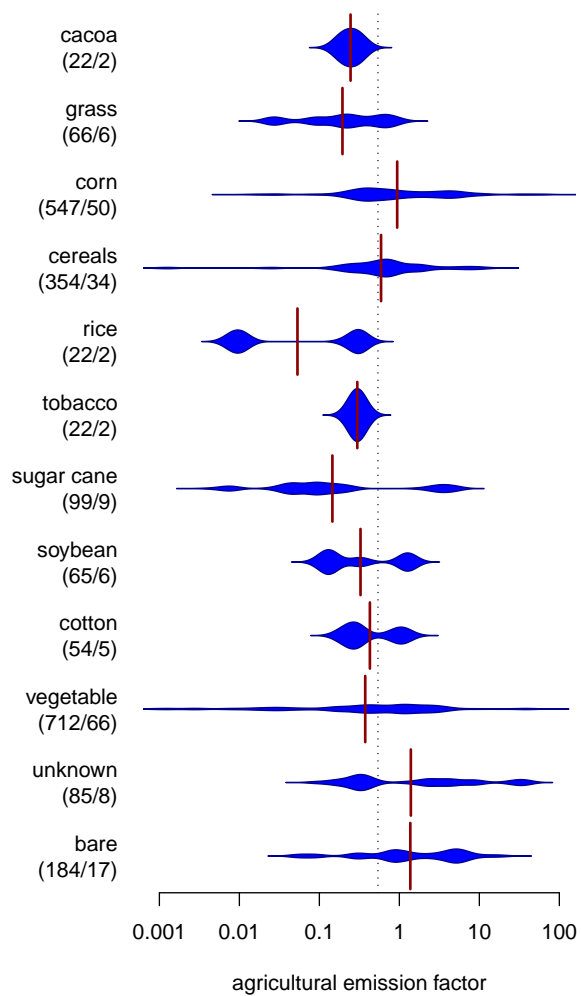


Figure 3.10: Distribution of calculated emissions factors for different crop types in the landcover “agriculture” with the number of calculated emission factors and number of measurements per crop class in brackets.

(CRF=0.74) through LC (CRF=0.77), LC+FIE (0.76) and LC+FIE+VSM (CRF=0.74). However, the reduced emissions in tropical evergreen forests and emission from deserts in the YL95/SL11 simulation the global averaged CRF increases to 0.82, yielding in an even greater net flux to the atmosphere.

### **3.4 Comparison to satellite-derived emission estimates**

Since we used all available measurements to provide the best statistics for adjusting our emission factors, there are no independent in situ measurements left to evaluate our new implementation of the SNOx algorithm by Yienger and Levy (1995). Therefore we compare our YL95/SL11 above canopy flux with the a posteriori SNOx fluxes of Jaeglé et al. (2005) for the year 2000 (Fig. 3.11), which are partly constrained by independent satellite-based measurements. In the total global flux our result ( $8.61 \text{ Tg(N) yr}^{-1}$ ) differs by 3% from their annual total flux of  $8.84 \text{ Tg(N) yr}^{-1}$  and is much closer to Jaeglé et al. (2005) than the  $6.88 \text{ Tg(N) yr}^{-1}$  above canopy flux in YL95EMAC and  $5.5 \text{ Tg(N) yr}^{-1}$  in YL95. Jaeglé et al. (2005) also use the algorithm by Yienger and Levy (1995) in their a priori simulations, but implemented in another global climate model. Jaeglé et al. (2005) apply the  $\text{NO}_2$  column derived by the GOME satellite (Burrows et al., 1999) for the year 2000 to partition between NO from fossil fuel combustion and other sources in a first step. In a second step they further partition the remaining sources in biomass burning events and soils, by using the firecounts of other satellite instruments (Langaans, 1993; Eva and Lambin, 1998; Giglio et al., 2003).

By comparing Fig. 3.11a with Fig. 3.9a we see that many of the features of our simulated bottom-up distribution are similar to their top-down study, though there are notable differences, which are highlighted in Fig. 3.11b. There are several reasons for the differences, as discussed below.

We calculate higher emissions in large areas of Europe except Spain, where Jaeglé et al. (2005) compute much higher emissions. Our simulated flux is also higher in other regions, as can be seen in Fig. 3.11. However, there are also regions where our simulated flux is lower. Over the tropical rainforest, where SNOx has the strongest impact on chemical processes in the atmosphere (Steinkamp et al., 2009) the emissions in YL95/SL11 are

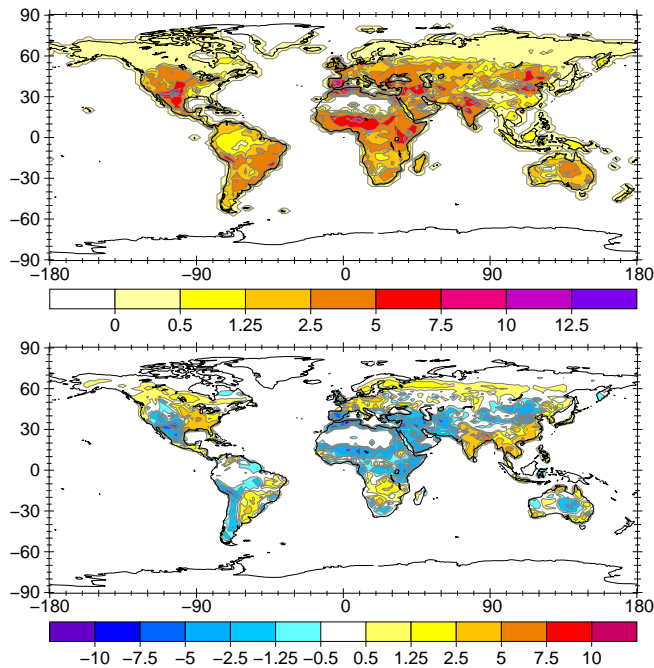


Figure 3.11: Averaged SNOx flux for the year 2000 of the Jaeglé et al. (2005) (J05) inverse modeling study (in  $\text{ng m}^{-2} \text{s}^{-1}$ ) (upper panel) and the difference between the YL95/SL11 year 2000 simulation and the J05 results (YL95/SL11 – J05) (lower panel).

similar to Jaeglé et al. (2005). It is worth noting that this reduction in the tropical emissions compared to YL95EMAC (see Fig. 3.12 for the difference between Jaeglé et al. (2005) and YL95EMAC) will reduce the influence of SNOx on global ozone chemistry, while on the other hand the general increase in SNOx will in turn increase the influence.

The reduced flux over arid regions of the Middle East to Pakistan, the Sahel region and Australia may be explained by different landcover classes. Especially along the northern African Mediterranean coast, agricultural areas in our landcover map seem to be much smaller compared to Pongratz et al. (2008). In the mountainous regions along the American west coast we also get lower emissions and we contend that it seems more sensible to have lower emissions from such regions of high altitudes. Furthermore, the higher emissions in our simulation from agriculture in the central and eastern parts of North America are reasonable compared to independent land usage distributions (Pongratz et al., 2008; Sterling and Ducharne, 2008). In the tropical region of South America our results agree well and are a clear improvement

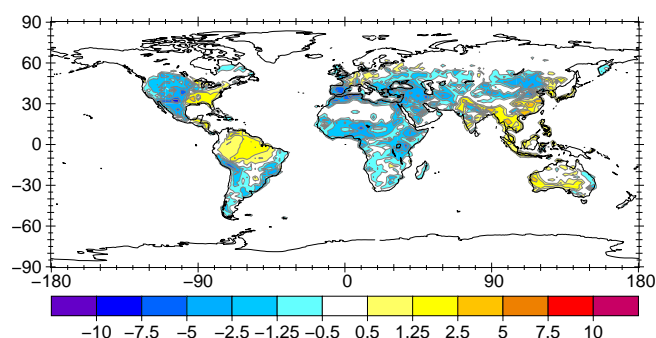


Figure 3.12: Difference between YL95EMAC and Jaeglé et al. (2005) (YL95-EMAC – J05) (in  $\text{ng m}^{-2} \text{s}^{-1}$ ) for the year 2000.

over YL95EMAC. But over tropical Africa our simulated SNOx is still lower than the results by Jaeglé et al. (2005).

There have also been a few regional applications of the top-down approach to eastern China using the GOME (Wang et al., 2007) and OMI satellite instruments (Zhao and Wang, 2009). These two studies find an increase by 260% and 240% for SNOx compared to their a priori SNOx, respectively. Their a priori estimate is comparable to our SNOx in the geometric mean calculation YL95/SL11 with reduced emissions in “rice-producing regions” (Table 3.7). The closest value to their a posteriori annual global SNOx is our emission using the arithmetic mean calculation without reduced in “rice-producing regions”, but this is even higher than their estimate. Other authors do not find such a strong relative increase in eastern China (Müller and Stavrakou, 2005; Stavrakou et al., 2008), however this is partly because Stavrakou et al. (2008) already scaled their global a priori emissions to a global value of  $8 \text{ Tg(N) yr}^{-1}$ . The a posteriori estimate of Müller and Stavrakou (2005) and Stavrakou et al. (2008) is  $10\text{--}12.1 \text{ Tg(N) yr}^{-1}$ , which is slightly larger than our best estimate using the arithmetic mean calculation.

### 3.5 Discussion

As expected, the mean value of the measurements are in good agreement with the ones simulated with the adjusted SNOx fluxes in YL95/SL11 (Fig. 3.13). The small deviations occur, because we used exactly the corresponding start and end day of the measurements for this table and figure. We still have a “cloudy” distribution around the 1:1 line (Fig. 3.13), which can be ex-

Table 3.7: Comparison of new SNO<sub>x</sub> to a top-down study in eastern China.

	DJF	MAM	JJA	SON	year
	Wang et al. (2007)				
a priori	0.016	0.06	0.12	0.04	0.236
a posteriori	0.04	0.21	0.36	0.24	0.85
	This study				
geom. mean <sup>a</sup>	0.01	0.05	0.08	0.03	0.18
geom. mean <sup>b</sup>	0.03	0.08	0.14	0.06	0.31
arithm. mean <sup>a</sup>	0.02	0.12	0.22	0.10	0.47
arithm. mean <sup>b</sup>	0.07	0.26	0.42	0.22	0.97
	<sup>a</sup> reduced emissions in “rice-growing regions”				
	<sup>b</sup> without reduced emissions in “rice-growing regions”				

pected for this kind of statistical model, since there are several unaccounted parameters which affect each landcover class, like the heterogeneity in soil parameters or the adaptation of NO producing microorganisms to different habitats. This is reflected in the logarithmic density distribution functions of the measurements (Fig. 3.14), which have much larger tails compared to the simulated fluxes.

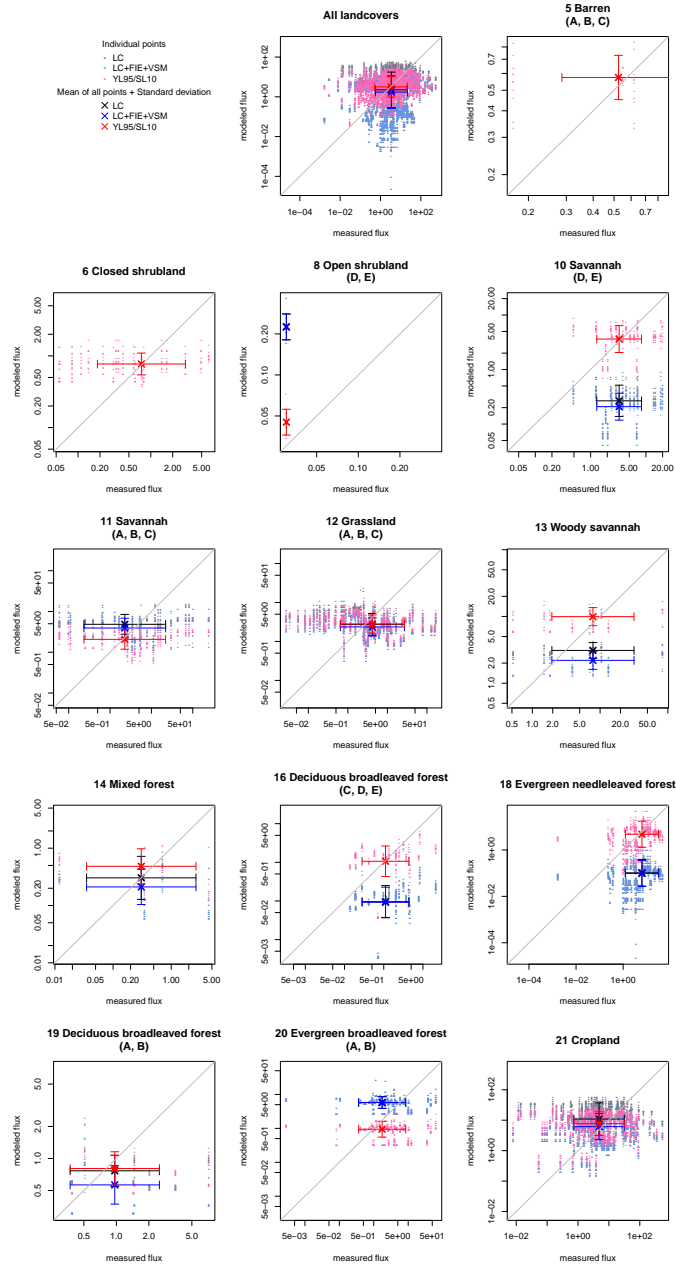


Figure 3.13: Scatterplots of SNO<sub>x</sub> measurements versus model results for the YL95/SL11 simulations.



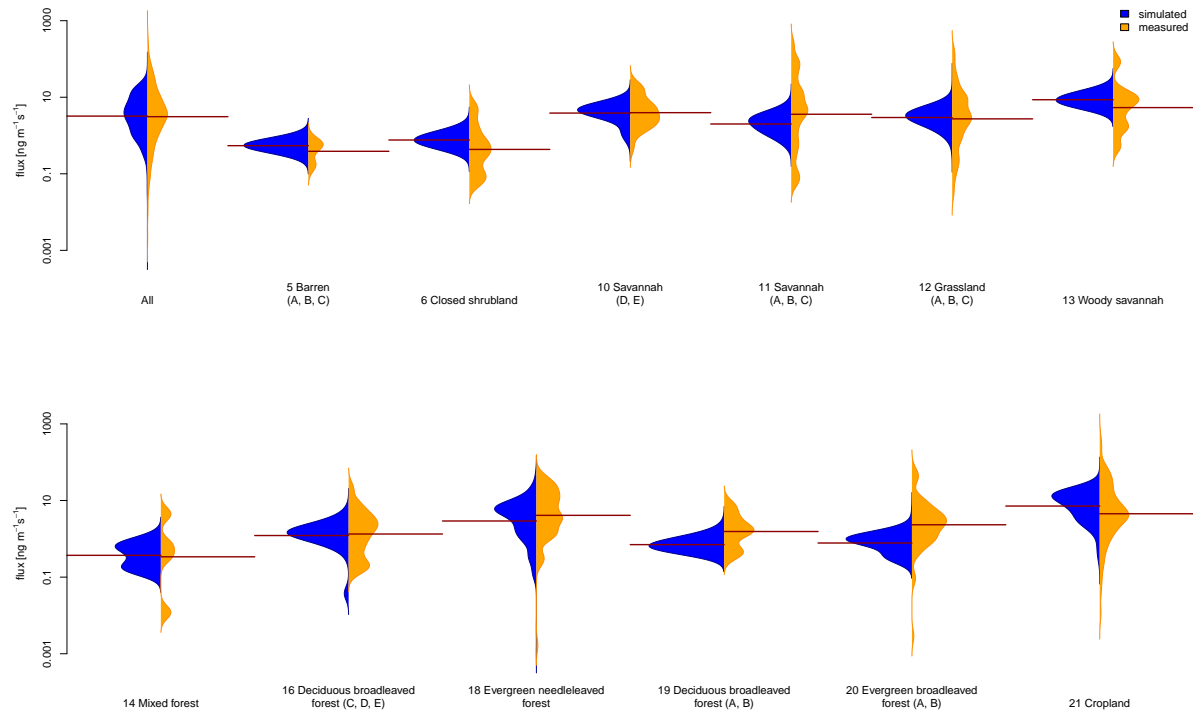


Figure 3.14: Density function plot of SNO<sub>x</sub> measurements (orange, right of center line) versus model output (blue, left of center line) for the YL95/SL11 simulation using the program by Kampstra (2008).

A similar analysis like that performed in section 3.3.6 can be performed by classifying the data by the duration of the experimental period. In particular, there were a few landcover classes (5, 11, 14, 19) with short term measurements (less than 3 months). One might expect that short term measurements will often have been performed specifically to measure special events, like rain induced pulsing or fertilizer induced emission, so that the limitation to long term measurements in our analyses could cause the calculated emission factor to decrease. However, we do not find this to be the case when we leave out these classes. In general, no connection is evident between the length of the measurement and the calculated new emission factors.

The reduction of SNO<sub>x</sub> in “rice-producing areas” that was implemented by Yienger and Levy (1995) is highly uncertain, and there are several pieces of evidence for and against it. Their original implementation was based on only one publication. Some more recent publications also support this conclusion, for instance, Zheng et al. (2003) report that periodic flooding during rice production decreases the SNO<sub>x</sub> even during non-flooded periods, and in a field campaign Fang and Mu (2009) found that the flux from rice fields is lower compared to other vegetable fields. The emission factor from rice-producing regions is also found to be lower in our analyses, but this is based on only two measurements in our dataset, and thus we agree with the earlier conclusion of the FAO and IFA (2001) that there are still not enough measurements available to draw any solid conclusions on this effect. Although we doubled the number of landcover classes there is still a large variability within individual classes, which is evident from comparing the continental/regional differences within one landcover class. Furthermore, in the probability density distributions depicted in Fig. 3.14, the measured fluxes show a much broader distribution and much stronger bi- to multimodal characteristics compared to our simulated values within each landcover class. Other important limitations of our improved algorithm are:

- The gridbox size of more than 100x100 km is too large to accurately reproduce the measured fluxes; this is a persistent problem in global models, and even if we were to decrease the cell size by a few orders of magnitude, it would not be sufficient to capture the heterogeneity in real soils.

- Instead of having only two soil moisture regimes, in reality one would expect a continuous mathematical relationship, such as that proposed and confirmed in laboratory measurements by Meixner and Yang (2006).
- Even if the algorithm itself were to be perfect, the use of simulated soil moisture and soil temperature will lead to errors, since these are also not perfectly representative of reality.

Ideally the optimization we performed here would need to be repeated for each resolution at which the model is running, otherwise SNO<sub>x</sub> will be underestimated at coarser resolutions and overestimated at finer resolutions (Fig. 3.6). One possibility to improve the total annual flux at lower resolutions would be to simply increase the emissions rate by the relative difference in the resolutions, but this would still be insufficient, due to non-linearities in the simulations: for example, the areal fraction of soils defined as “wet” is slightly increasing with finer resolution, which also causes SNO<sub>x</sub> to increase at higher temperatures.

### 3.6 Conclusions and outlook

We have made significant improvements to the soil NO emission algorithm developed by Yienger and Levy (1995) using a much larger set of in situ measurements, along with several other recent advances such as more detailed land cover classifications. The total global above-canopy flux increases by  $1.73 \text{ Tgyr}^{-1}$  and we obtain a significant difference in the geographical distribution of SNO<sub>x</sub>. Despite this overall increase in SNO<sub>x</sub>, there is a reduction of SNO<sub>x</sub> in tropical regions compared to the previous implementation in EMAC, which will in turn reduce the relative influence on atmospheric chemistry (in particular O<sub>3</sub> and OH, and the tropospheric oxidizing efficiency), as discussed in Steinkamp et al. (2009).

As long as there is no mechanistically based algorithm to calculate SNO<sub>x</sub>, which will be difficult to develop for global models due to the heterogeneity of soils, vegetation and microorganisms, a valuable approach will be to continue adjusting the calculation of SNO<sub>x</sub> as we have done with new measurements and other advances in the field. Since the algorithm by Yienger and Levy (1995) is the most-widely applied method to calculate SNO<sub>x</sub> in AC-GCMs, the method we presented here can also be easily applied in other

models, either directly applying our new fitted parameters, or attaining greater internal model consistency by applying the same fitting technique with the observations. Finally, with a growing amount of measurements of SNO<sub>x</sub> accompanied with the measurement of other relevant factors, it should eventually be possible to incorporate other factors in the parameterization, resulting in an improved agreement, in particular reducing the scatter in the comparison of modeled and observed SNO<sub>x</sub>.

**Acknowledgements** We would like to thank Stefan Hagemann from the MPI for Meteorology in Hamburg for the calculation of the volumetric soil moisture, Jos Lelieveld for the initial suggestion and very fruitful discussions, Wolfgang Wilcke for his constructive comments, Lyatt Jaeglé for providing her a posteriori top-down satellite data, and the EMAC developers and users for their support, especially L. N. Ganzeveld, P. Jöckel, A. Kerkweg and H. Tost. Jörg Steinkamp appreciates the financial support by the International Max Planck Research School (IMPRS) for atmospheric chemistry and physics.

## 4 A novel algorithm for global soil biogenic NO emissions: formulation and evaluation

*J. Steinkamp*<sup>1</sup>, *F. X. Meixner*<sup>2, 3</sup>, *S. Zaehle*<sup>4</sup>, *M. G. Lawrence*<sup>1</sup>

<sup>1</sup> Department of Atmospheric Chemistry, Max-Planck-Institute for Chemistry, Mainz, Germany

<sup>2</sup> Department of biogeochemistry, Max-Planck-Institute for Chemistry, Mainz, Germany

<sup>3</sup> Department of Physics, University of Zimbabwe, Mount Pleasant, Harare, Zimbabwe

<sup>4</sup> Biogeochemical Systems Department, Max-Planck-Institute for Biogeochemistry, Jena, Germany

---

**This chapter is forseen for publication as:**

Steinkamp, F. X. Meixner, S. Zaehle and Lawrence, M. G.: A novel algorithm for global soil biogenic NO emissions: formulation and evaluation, (to be submitted to Geophysical Research Letters).

## **Abstract**

We present a new algorithm for calculating NO emissions from soils in atmospheric chemistry models. The algorithm builds on the concept of Meixner and Yang (2006) and is based on a compilation of measured NO emission from soils, model output for soil temperature, water filled pore space, soil carbon and nitrogen, along with bulk density pH-value and clay content from a global soil database. The correlation coefficients ( $R^2$ ) of all significant (p-value  $< 0.1$ ) linear correlations in our analysis are between 0.11 and 0.75. The calculated dependencies on physical and chemical parameters used here result in higher global SNO<sub>x</sub> fluxes compared to previously published values. Using one regression model for all usable measurement sites yields in an annual global NO flux of 22 Tg(N) yr<sup>-1</sup>, while treating agricultural areas separately increases the flux to 31 Tg(N) yr<sup>-1</sup>. Finer classification increases the total flux to unrealistic values, dominated by two individual landcover classes, but for tropical forest and agricultural landcover it supplies a realistic value of 2.78 and 4.64 Tg(N) yr<sup>-1</sup>, respectively. This novel algorithm has a great potential to provide a general improvement in modeled soil NO emissions, though some further developments in the field and in the model will be needed for it to reach its full potential.

## 4.1 Introduction

Nitrogen oxides ( $\text{NO}_x = \text{NO} + \text{NO}_2$ ) are important radicals in atmospheric chemistry Chameides et al. (1992). On a global average  $\text{NO}_x$  produced by anthropogenic combustion (20 to 24  $\text{Tg(N) yr}^{-1}$ ) is the strongest source (Denman et al., 2007). Biogenically produced NO in soils (hereafter SNO<sub>x</sub>) contributes with 5.5 to 21  $\text{Tg(N) yr}^{-1}$  (Yienger and Levy, 1995; Davidson and Kinglerlee, 1997) to the global total and is in the same range as NO produced by lightning or biomass burning. However in a previous study we could show that due to the geographical distribution of modeled SNO<sub>x</sub>, its influence on the reaction chain from  $\text{NO}_x$  through  $\text{O}_3$  and OH to the oxidizing efficiency is stronger than for the other surface sources (Steinkamp et al., 2009).

The most widely used algorithm to calculate SNO<sub>x</sub> in atmospheric chemistry general circulation models (AC-GCMs) or chemistry transport models (CTMs) is the algorithm by Yienger and Levy (1995) (hereafter YL95). The algorithm incorporates the temperature and precipitation for several different ecosystems to simulate SNO<sub>x</sub>. One possible path is to improve the details of the YL95 algorithm, as done by Steinkamp and Lawrence (2010) (hereafter SL10). Another path, which we explore here based on laboratory measurements, is to develop an entirely new algorithm for use in contemporary AC-GCMs and CTMs. In this study we do not account for canopy interaction like YL95 or Ganzeveld et al. (2002a) or the uncertainty regarding the effect of “pulsing” Davidson (1992); Hudman et al. (2010). The question we focus on here is whether our novel algorithm - with its advances in physical, geographical and biological representations compared to previous parametrization such as YL95 or SL10 - is capable of providing an improvement in the emissions themselves, despite the many uncertainties in the various parameters involved.

The new algorithm presented here uses the landcover classes as introduced by SL10, which are based on MODIS data (Friedl et al., 2006) and the Koeppen main climate classes (Kottek et al., 2006). We employ the temperature of the upper soil layer, the water filled pore space (WFPS; unitless, fraction of the total pore space) derived from the AC-GCM EMAC in SL10 and carbon and nitrogen pools of different plant functional types (PFT) derived from the terrestrial biosphere model ORCHIDEE (Zaehle and

Friend, 2010) (hereafter ZF10). In the next section we describe the underlying mathematical equations to calculate the SNOx flux, how we derived the necessary input parameters and lumping of landcover classes. After that we discuss the results, before we come to our final conclusions.

## 4.2 Algorithm description

According to Meixner and Yang (2006) the soil biogenic NO emission flux is calculated depending on the water filled pore space (WFPS) at a constant reference temperature (25°C):

$$F_{25^{\circ}\text{C}} = a \cdot \text{WFPS}^b \cdot e^{c \cdot \text{WFPS}} \quad (4.1)$$

where  $F_{25^{\circ}\text{C}}$  is the flux at the reference temperature 25°C, and

$$a = \frac{\text{SNOx@WFPS}_{opt}}{\text{WFPS}_{opt}^b \cdot e^{-b}} \quad (4.2a)$$

$$b = \frac{\ln\left(\frac{\text{SNOx@WFPS}_{opt}}{\text{SNOx@WFPS}_{upp}}\right)}{\ln\left(\frac{\text{WFPS}_{opt}}{\text{WFPS}_{upp}}\right) + \frac{\text{WFPS}_{upp}}{\text{WFPS}_{opt}} - 1} \quad (4.2b)$$

$$c = \frac{-b}{\text{WFPS}_{opt}} \quad (4.2c)$$

There are two unknown points to assign: the optimum value of WFPS, where SNOx is maximal ( $\text{WFPS}_{opt}$ ,  $\text{SNOx@WFPS}_{opt}$ ); and the upper value of WFPS, along with the corresponding SNOx ( $\text{WFPS}_{upp}$ ,  $\text{SNOx@WFPS}_{upp}$ ). The optimum WFPS depends on the annual precipitation. Because of the higher  $R^2$  value, we use square root function instead of the linear relationship (Fig. 4.1) as proposed by Feig (2009). For the individual ecosystems, we reduce the precipitation by the factor of (throughfall + stemflow) divided by the total precipitation provided by Pryor and Barthelmie (2005). For  $\text{SNOx@WFPS}_{opt}$  we assume a dependence on available carbon and nitrogen per landcover present in each gridcell, taken from ZF10, and physical properties taken from the upper soil layer (20 cm) of Batjes (2006) (hereafter



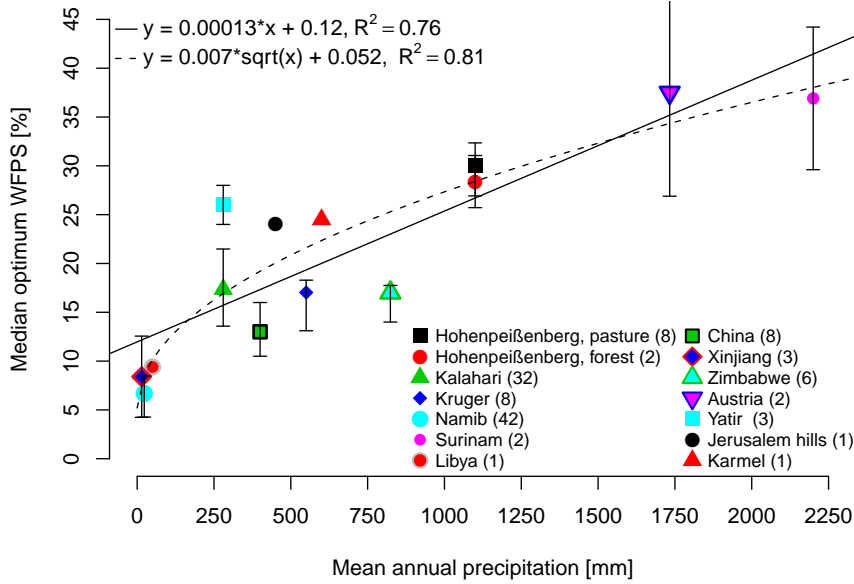


Figure 4.1: Dependency of median optimum WFPS on the annual precipitation.

WISE) per gridcell. The carbon and nitrogen content of ZF10 had to be converted from  $\text{kg m}^{-2}$  to  $\text{g g}(\text{soil})^{-1}$ , assuming 50% is located in the upper 30 cm of the soil and with the bulk density taken from WISE.

$\text{SNO}_x @ \text{WFPS}_{\text{opt}}$  is calculated iteratively for each of the available measurements provided in the electronic supplement of SL10. Following on that we performed a simple linear regression analysis of the calculated  $\text{SNO}_x @ \text{WFPS}_{\text{opt}}$  values to determine their dependence on the physical variables taken from WISE and the natural logarithm of the chemical variables taken from ZF10, because the statistical distribution of later ones can be approximated by a log-normal distribution. Since the data from ZF10 does not include the Hawaiian Archipelago, we could not use the measured  $\text{SNO}_x$  flux data from there, which slightly reduced the available measurements as well as measurements indicating deposition (negative emissions) or zero fluxes were excluded, since the above described formula only calculates positive values. If we calculated values of  $\text{WFPS}_{\text{opt}}$  above  $1,000 \text{ ng m}^{-2} \text{ s}^{-1}$ , which is already very unlikely, we excluded these points from our linear re-

gression, which happened at 45 out of 554 locations, which left us a total of 479 measurements distributed over 12 landcover classes to include in our analysis.

Meixner and Yang (2006) measured the  $WFPS_{upp}$  at 1% of  $SNOx@WFPS_{opt}$  to describe the second point for the WFPS dependence. We roughly approximate the  $WFPS_{upp}$  value depending on the  $WFPS_{opt}$  as follows:

$$WFPS_{upp} = 1. + 0.4 \cdot \log_{10}(WFPS_{opt}) \quad (4.3)$$

and  $SNOx$  at this point is assumed to be at the lower end of reported detection limits ( $0.1 \text{ ng m}^{-2} \text{ s}^{-1}$ ). We have chosen this low limit to set the  $SNOx$  at the optimum WFPS to 0.2, where the application of the linear regression resulted in unrealistic values ( $SNOx@WFPS_{opt} < SNOx@WFPS_{upp}$ ).

To calculate the temperature dependence, we assume a simple  $Q_{10}$  function (with  $Q_{10}=2$ ), which means a doubling of the emission with a 10 K increase in temperature. But we modified it to decrease above a maximum temperature  $T_{max}=42^\circ\text{C}$ .

$$F_{soil} = 2^{\frac{T-25^\circ\text{C}}{10} - e^{0.1 \cdot (T-42^\circ\text{C})}} \cdot F_{25^\circ\text{C}} \quad (4.4)$$

Although the physical properties of the soils differ in the individual landcover types, they are assumed to be the same for all landcover types in one model grid box here. The carbon and nitrogen species for each landcover class are rearranged as listed in the supplement.

The fraction of WFPS is calculated as:

$$WFPS = \frac{\theta_v}{1 - \frac{\rho_b}{2.65}} \quad (4.5)$$

where the volumetric soil moisture content ( $\theta_v$ ) is computed as described in SL10, while the bulk density  $\rho_b$  is from WISE and the particle density of quartz ( $2.65 \text{ g cm}^{-2}$ ). The mean WFPS for the simulated period is depicted in Fig. 4.2. The relative distribution of drier and wetter regions is realistic, but the soil moisture in deserts appears to be overestimated. Beside static values all over the globe per landcover to reproduce the values derived by SL10, we computed linear regressions for four different treatments of the landcover classes:

- including all landcover classes.

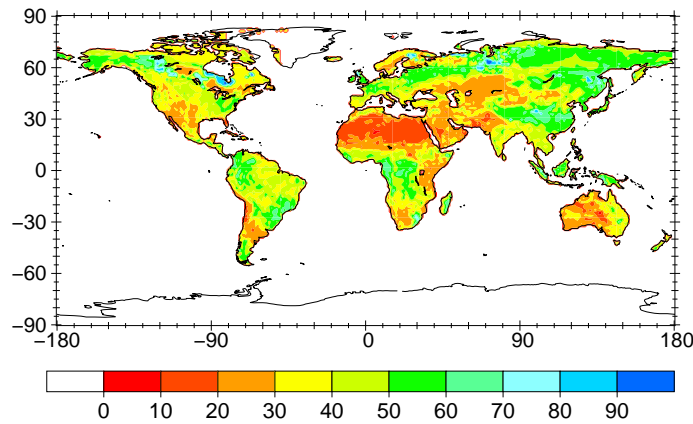


Figure 4.2: Global pattern of simulated WFPS for the years 1990–2000.

- agricultural and other landcover classes.
- grouped as
  - grassland, including savannah, open shrub and woody savannah
  - temperate and boreal forests, including closed shrubland
  - tropical forests
- individual for each available landcover with enough measurements and significant linear models (p-value < 0.1).

### 4.3 Results and discussion

The probability distribution of the measured SNO<sub>x</sub> fluxes is best represented by a log-normal distribution. The data extracted from WISE looks multimodal and can be approximated by a normal distribution, whereas the data extracted from ZF10, which also is multimodal, can again be approximated by a log-normal distribution. The correlation of concentrations for nitrogen and carbon content seems at first to be poor, but taking the coarse model resolution and the substantial heterogeneity of the real world into account, a few key patterns can be seen:

- The underestimation increases with increasing carbon and nitrogen concentrations,
- Carbon is reproduced better than nitrogen,

- The carbon and nitrogen content is underestimated for C4 grasses,
- There is no correlation of inorganic nitrogen species ( $\text{NO}_3^-$ ,  $\text{NH}_4^+$ ).

The first point can be explained by the fact that the bulk density decreases with increasing carbon content, which is not reflected in the calculation here. For the second point, the C:N ratio in the model only varies between fixed upper and lower bounds. The underestimation for C4-grasses is a known and will be improved in a parallel study. Inorganic species are highly variable in time, therefore a poor correlation can be expected based on current information, and we did not include this data in our further analysis.

The iteration resulted occasional unrealistic values for  $\text{SNOx@WFPS}_{\text{opt}}$ . If the simulated temperature was low, or the WFPS was too high or too low, the iteratively calculated  $\text{SNOx@WFPS}_{\text{opt}}$  increased above  $1,000 \text{ ng m}^{-2} \text{ s}^{-1}$ . Sometimes the emissions were so low that  $\text{SNOx@WFPS}_{\text{opt}}$  became smaller than  $\text{SNOx@WFPS}_{\text{upp}}$ . In both cases we did not include the results in the linear regression computations. In six of the landcover classes the linear regression lead to a significant dependence (Table 4.1). For some locations several different types of measurements were performed, resulting in SNOx fluxes spanning over a broad range of SNOx flux values (e.g., 0.2 to  $40.1 \text{ ng m}^{-2} \text{ s}^{-1}$  for Akiyama et al. (2000); Akiyama and Tsuruta (2002, 2003b,a)). Since the physical and chemical parameters are the same here, this weakens our linear regressions. And note that due to the fact that the nitrogen values are tied to being within a certain C:N ratio, the “independent variables” in the linear model are not really independent of each other.

Table 4.1: Linear regression models of calculated SNO<sub>x</sub> at the optimum WFPS in relation to physical and chemical soil properties for different landcovers (as described by Steinkamp and Lawrence (2010)) and lumped landcover classes (grassland = all savannah, all grassland and woody savannah; temperate/boreal forests = closed shrubland, mixed f., dec. br.-leaved f. (A, B, C) and evergr. needlel. f.; tropical forests = forests in A and B climate). Significance codes: ‡*p* < 0.001, †*p* < 0.005, ◊*p* < 0.01, \**p* < 0.05, •*p* < 0.1.

Landcover	N	R <sup>2</sup>	Intercept	WISE			ZF10 <sup>a</sup>		
				bulk density	pH <sub>aq</sub>	clay	total Nitrogen	labile Carbon	total
All	479	0.1518	11.06‡	-5.05‡	—	—	0.53‡	—	—
cropland	181	0.2004	47.9‡	-4.08†	-0.4•	—	15.72‡	—	-15.33‡
all but cropland	298	0.2156	14.43‡	-9.67‡	0.59‡	—	—	0.53‡	—
lumped landcover classes									
grassland	142	0.2136	13.98‡	-4.3*	—	—	-2.96‡	2.99‡	—
temperate/boreal forests	108	0.4657	2.11‡	—	—	—	—	—	1.87‡
tropical forests	45	0.2018	15.95‡	-7.86◊	—	-0.12◊	—	—	—
Individual landcover classes									
savannah (A, B, C)	23	0.5362	-27.7‡	—	5.45‡	—	—	—	2.84†
grassland (A, B, C)	90	0.3341	22.06‡	-8.11◊	—	—	-5.92‡	5.3‡	—
deciduous broadleaved forest (C, D, E)	22	0.2335	3.51‡	—	—	—	—	—	-1.51*
evergreen needleleaved forest	66	0.2411	-95.56†	—	2.28†	—	-38†	—	26.21‡
deciduous broadleaved forest (A, B)	5	0.8267	-28.88*	22.67*	—	—	—	—	—
evergreen broadleaved forest (A, B)	40	0.184	6.59•	-6.21*	0.79•	—	—	—	—

<sup>a</sup> Natural logarithmic values were used

For all but one of the regressions we determine a negative dependence on the bulk density, which can be expected since the air exchange increases with a larger fraction of pore space. Interestingly the only positive correlation is found for tropical deciduous forest, but there are only five measurements available there. For all non-agricultural landcovers we get a positive correlation on the pH-value, which may indicate nitrification as the source for SNO<sub>x</sub>, since nitrifying microorganisms are more sensitive to acidity than denitrifying ones (Remde and Conrad, 1991; Yamulki et al., 1997). We expected to get a positive correlation with carbon and nitrogen, acting as “fuel” for the microbial NO production, but sometimes the linear regression resulted in a negative dependence. This may be explained by interdependencies if both carbon and nitrogen were included, but for deciduous broadleaved forest (C, D, E) we calculate a negative dependence on the total carbon, which we can not explain so far.

Due to the statistical spread and the relatively low  $R^2$  values the calculation of the global SNO<sub>x</sub>@WFPS<sub>opt</sub> distribution with the derived regression formula reached unrealistic values above  $1,000 \text{ ng m}^{-2} \text{ s}^{-1}$  at some points. We used the value of  $1,000 \text{ ng m}^{-2} \text{ s}^{-1}$  for these model gridcells, which still is very high, but in our opinion suitable since we do not know how good our simulated soil moisture is exactly, although the spatial pattern looks good (Figure 4.2).

The results for the regressions using all landcover types (Table 4.2) yield the lowest values with  $21.91 \text{ Tg(N) yr}^{-1}$  and are closest to the geometric mean results from SL10. Also the spatial pattern of the simulated flux looks reasonable (Figure 4.3). Still, only the agricultural SNO<sub>x</sub> flux is lower than in SL10. When the cropland class is treated separately (Figure 4.4), it nearly doubles, but still delivers realistic results. The fluxes from the remaining landcover classes also rise and the annual global flux is then  $31.2 \text{ Tg(N) yr}^{-1}$ , close to the arithmetic mean values taken from SL10 (Table 4.2). The strongest increase occurs in open shrubland (A, B, C). The geographic distribution shows some unreasonable high fluxes in high latitudes of North and South America, but in general still looks reasonable. For the individual landcover classes where we found a significant correlation, the simulated SNO<sub>x</sub> flux increases to unrealistic values for warm and temperate grassland and savannah. The SNO<sub>x</sub> flux from tropical forests ( $2.78 \text{ Tg(N) yr}^{-1}$ ) is approximately as high as values before the optimization in SL10 ( $2.33$

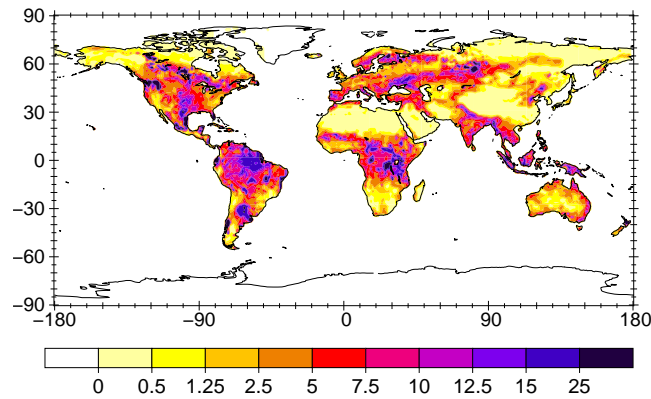


Figure 4.3: Simulated SNO<sub>x</sub> flux in  $\text{ng m}^{-2} \text{s}^{-1}$  using the same linear model for all landcovers.

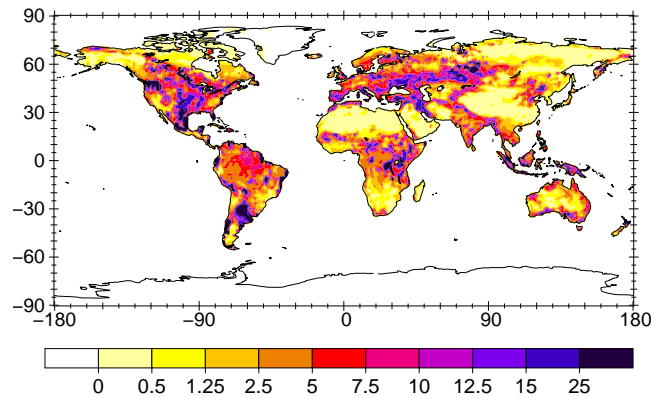


Figure 4.4: Simulated SNO<sub>x</sub> flux in  $\text{ng m}^{-2} \text{s}^{-1}$  using the same linear regression for all natural landcovers and a separate linear regression for agriculture.

$\text{Tg(N) yr}^{-1}$ ). For the evergreen needleleaved forest, where the calculated emission already drastically rose in SL10, they are found to increase even more here.

The higher annual emissions compared to all previous estimates (Yienger and Levy, 1995; Davidson and Kinglerlee, 1997; Jaeglé et al., 2005) may be explained by the discrepancy between the real optimum WFPS derived from the annual global precipitation distribution and the simulated soil moisture. If the soils are too wet (or too dry) in the model we calculate very high potential SNO<sub>x</sub> fluxes at the optimum WFPS to reproduce the measured SNO<sub>x</sub> flux.

Table 4.2: Simulated SNO<sub>x</sub> flux in Tg(N) yr<sup>-1</sup> for individual landcover classes for SL10 and the different results derived by the regression models.

ID	SL10		All	all but crop	grouped	indiv.
	geom	arithm				
Barren (A, B, C)	0.20	0.21	0.27	0.41		
Closed shrubland	0.02	0.04	0.16	0.31	0.09	
Open shrubland (A, B, C)	0.33	0.03	1.82	3.59	24.99	
Open shrubland (C, D)	0.01	0.01	0.54	1.06	1.20	
Grassland (D, E)	0.03	0.04	0.08	0.12	0.07	
Savannah (D, E)	0.35	0.40	0.59	1.29	0.93	
Savannah (A, B, C)	0.65	2.20	2.16	2.32	5.73	36.14
Grassland (A, B, C)	0.89	4.98	1.75	3.16	11.38	77.81
Woody savannah	2.29	2.44	2.31	2.70	4.88	
Mixed forest	0.06	0.06	1.18	1.61	0.84	
Evergr. broadl. forest (C, D, E)	0.16	0.44	0.54	0.81	0.44	
Dec. broadl. forest (C, D, E)	0.11	0.31	0.26	0.31	0.21	
Dec needlel. forest	0.02	0.06	0.06	0.05	0.09	
Evergreen needlel. forest	0.75	2.46	1.81	2.19	1.87	5.18
Dec. broadl. forest (A, B)	0.02	0.03	0.14	0.18	0.10	
Evergreen broadl. forest (A, B)	0.38	1.15	4.75	4.26	2.26	2.78
cropland	3.25	13.58	2.78	4.64	4.64	4.64
Urban and build-up lands	0.18	0.69	0.11	0.29	0.29	
Cropland/nat. veg. mosaic	0.78	3.22	0.62	1.85	1.85	
All	10.51	33.11	21.91	31.17	61.89	126.55

## 4.4 Conclusion and outlook

We have proposed a new algorithm for computing SNO<sub>x</sub> in global atmospheric chemistry models, and have found that the algorithm is able to reproduce the total global SNO<sub>x</sub> flux relatively well, although the more detailed we make our landcover classification the further we depart from previously published values. Opposite of our findings in SL10, where the emission in tropical forests decreased, they increased here again to realistic values. Also the flux from agriculture regions increased to realistic values. As already mentioned in SL10, it is very unfortunate that there are not enough measurements available to split agriculture into several subclasses, i.e., per crop type or crop group, since one class for the whole of agriculture is unrealistic.

Our novel algorithm presented here has several caveats. A major difficulty is that we rely on merging results from different sources; an uncertainty is especially introduced by combining results from measurements and models for use in other models. The dependence of the optimum WFPS on precipitation may not be valid at high latitudes, where the evapotranspira-



tion is very low. The heterogeneity of soil in the real world and the use of statistically derived parameters increases the scatter between the model and measurements. With improved GCMs, including evaluated layered soil moisture, this uncertainty could be improved substantially. For better regression analysis a lot more measurements are necessary, if possible accompanied by physical and chemical parameters.

**Acknowledgements** Joerg Steinkamp appreciates the financial support by the Max-Planck International Research School (IMPRS) for atmospheric Chemistry. We appreciate the ENIGMA project of the Max-Planck-Society for providing a forum and support for the discussions in this project.



## **5 Final conclusions and outlook**

## **Final conclusions**

Soil biogenic NO emissions, as calculated in state-of-the-art AC-GCMs, play a key role in the chemical processes of the atmosphere. Due to different temporal and geographical patterns, their relative influence on the atmospheric oxidizing efficiency, as indicated by the CH<sub>4</sub> lifetime is more important than the remaining sources of NO located at the surface. In Chapter 2 I demonstrated an interesting negative feedback: due to reduction in O<sub>3</sub> and consequently OH when global soil NO emissions are neglected, the NO<sub>x</sub> mixing ratio actually increases in some regions with other dominating sources of NO<sub>x</sub>, in particular the northern high latitudes during the northern hemispheric winter.

This provided the motivation to first update the existing algorithm without changing the underlying mathematical equations by iteratively recalculating the emission factors with a compilation of measurements collected from the published literature in Chapter 3. As already proposed by others, our new total annual global calculated NO emission flux released from the canopy to the atmosphere rose to 8.6 Tg(N) yr<sup>-1</sup>. The spatial pattern changes, in particular in the tropical forest, where the influence on the chemical processes in the atmosphere was strongest, NO soil emissions decreased. This would weaken the influence on the oxidizing efficiency. The emissions from coniferous forests rose in this approach, notably also in deciduous needleleaved forests. This finding should be regarded with caution, since there were no published measurements so far in the Russian Taiga, which comprises the largest fraction of this ecosystem.

In chapter 4 I presented a novel algorithm to calculate soil NO emission in global models. While this provides promising results there are still some uncertainties, e.g. introduced by combining various generalizations from other models and applying them in other models. The functionality of the new method to calculate NO emissions from the soil needs to be further improved, and the results need to be validated, particular against top-down approaches.

## Outlook

This thesis has provided the foundation for further investigations of the influence of soil NO emissions on atmospheric chemistry. Several other sensitivity studies can follow the one presented in chapter 2. First, the same kind of simulations with the updated algorithm should be examined, in combination with various improvements in the chemical mechanism for instance Taraborrelli et al. (2009). Secondly, it would be valuable to repeat the simulations in other models. In Chapters 3 and 4 deficits and gaps were noted in the mechanism, which will provide opportunities for studies by future generations of PhD students and other scientists. Among these future projects, I list the most important ones in my opinion here:

1. Refine the emission class “agriculture”, since crop types, like natural ecosystems, vary with the climatic conditions; this will be particularly important for applications in regional models.
2. Improve the pulsing by:
  - Making the dependence continuous
  - Introducing other triggers to initiate a pulse
3. Improve the canopy interaction in models, so that chemical processes in the shaded vegetation layer are accounted for; for instance in forests the ozone interaction is leading to a net NO deposition and a NO<sub>2</sub> emission.
4. Make the definitions from various sources more consistent with each other.

The last point may be a bit utopian desire, but hopefully I could provide some valuable steps and constructive suggestions in this thesis for others investigating soil NO emissions either in the field, laboratory or in models to build on.



## Literature

- Akiyama, H. and Tsuruta, H.: Effects of chemical fertilizer form on N<sub>2</sub>O, NO and NO<sub>2</sub> fluxes from andisol field, *Nutr. Cycl. Agroecosys.*, 63, 219–230, 2002.
- Akiyama, H. and Tsuruta, H.: Effects of organic matter application on N<sub>2</sub>O, NO and NO<sub>2</sub> fluxes from an andisol field, *Biogeochemistry*, 17, 1100, doi:10.1029/2002GB002016, 2003a.
- Akiyama, H. and Tsuruta, H.: Nitrous oxide, and nitrogen dioxide fluxes from soils after manure and urea application, *J. Environ. Qual.*, 32, 423–431, 2003b.
- Akiyama, H., Tsuruta, H., and Watanabe, T.: N<sub>2</sub>O and NO emissions from soils after the application of different chemical fertilizers, *Chemosphere*, 2, 313–320, 2000.
- Archer, S. L., Shultz, P. J., Warren, J. B., Hampl, V., and DeMaster, E. G.: Preparation of standards and measurement of nitric oxide, nitroxyl, and related oxidation products, *Methods*, 7, 21–34, 1995.
- Bakwin, P. S., Wofsy, S. C., and Fan, S.-M.: Measurement of NO<sub>x</sub> and NO<sub>y</sub> concentrations and fluxes over arctic tundra, *J. Geophys. Res.*, 97, 16 545–16 557, 1992.
- Bargsten, A., Falge, E., Pritsch, K., E., Huwe, B., and Meixner, F. X.: Laboratory measurements of nitric oxide release from forest soil with a thick organic layer under different understory types, *Biogeosciences*, 7, 1425–1441, doi:10.5194/bg-7-1425-2010, 2010.
- Batjes, N. H.: ISRIC-WISE derived soil properties on a 5 by 5 arcminutes global grid (ver. 1.1), Report 2006/02, ISRIC - World Soil Information [available through: <http://www.isric.org>], 2006.
- Beekmann, M. and Vautard, R.: A modelling study of photochemical regimes over Europe: robustness and variability, *Atmos. Chem. Phys. Discuss.*, 9, 1521–1560, doi:10.5194/acpd-9-1521-2009, 2009.
- Bertram, T. H., Heckel, A., Richter, A., Burrows, J. P., and Cohen, R. C.: Satellite measurements of daily variations in soil NO<sub>x</sub> emissions, *Geophys. Res. Lett.*, 32, L24 812, doi:10.1029/2005GL024640, 2005.
- Bouwman, A. F., Boumans, L. J. M., and Batjes, N. H.: Emissions of N<sub>2</sub>O and NO from fertilized fields: Summary of available measurement data, *Global Biogeochem. Cy.*, 16, 1058, doi:10.1029/2001GB001811, 2002a.
- Bouwman, A. F., Boumans, L. J. M., and Batjes, N. H.: Modeling global annual N<sub>2</sub>O and NO emissions from fertilized fields, *Global Biogeochem. Cy.*, 16, 1080, doi:10.1029/2001GB001812, 2002b.
- Brasseur, G. P., Orlando, J. J., and Tyndall, G. S., eds.: *Atmospheric chemistry and global change*, Oxford University Press, New York, 1999.



- Bridier, I., Caralp, F., Loirat, H., Lesclaux, R., Veyret, B., Becker, K. H., Reimer, A., and Zabel, F.: Kinetic and theoretical studies of the reactions  $CH_3C(O)O_2 + NO_2 + M \rightleftharpoons CH_3C(O)O_2NO_2 + M$  between 248 and 393 K and between 30 and 760 Torr, *J. Phys. Chem.*, 95, 3594–3600, 1991.
- Burrows, J. P., Weber, M., Buchwitz, M., Rozanov, V., Ladstätter-Weißmayer, A., Richter, A., DeBeek, R., Hoogen, R., Bramstedt, K., Eichmann, K.-U., Eisinger, M., and Perner, D.: The Global Ozone Monitoring Experiment (GOME): Mission concept and first scientific results, *J. Atmos. Sci.*, 56, 151–175, doi:10.1175/1520-0469(1999)056<0151: TGOMEG>2.0.CO;2, 1999.
- Chameides, W. L., Fehsenfeld, F., Rodgers, M. O., Cardelino, C., Martinez, J., Parrish, D., Lonneman, W., Lawson, D. R., Rasmussen, R. A., Zimmermann, P., Greenberg, J., Middleton, P., and Wang, T.: Ozone precursor relationships in the ambient atmosphere, *J. Geophys. Res.*, 97, 6037–6055, 1992.
- Chapin III, F. S., Matson, P. M., and Mooney, H. A.: Principles of terrestrial ecosystem ecology, Springer, New York, Berlin, 1 edn., 2002.
- Cleary, P. A., Wooldridge, P. J., Millet, D. B., McKay, M., Goldstein, A. H., and Cohen, R. C.: Observations of total peroxy nitrates and aldehydes: measurement interpretation and inference of OH radical concentrations, *Atmos. Chem. Phys.*, 7, 1947–1960, 2007.
- Conrad, R.: Soil microbial processes involved in production and consumption of atmospheric trace gases, *Adv. Microb. Ecol.*, 14, 207–250, 1995.
- Davidson, E. A.: Pulses of nitric oxide and nitrous oxide flux following wetting of dry soil: an assessment of probable sources and importance relative to annual fluxes, *Ecol. Bull.*, 42, 149–155, 1992.
- Davidson, E. A. and Kinglerlee, W.: A global inventory of nitric oxide emissions from soils, *Nutr. Cycl. Agroecosys.*, 48, 37–50, 1997.
- Davidson, E. A., Vitousek, P. M., Matson, P. A., Riley, R., García-Méndez, G., and Maass, J. M.: Soil emissions of nitric oxide in a seasonally dry tropical forest in México, *J. Geophys. Res.*, 96, 15 439–15 445, 1991.
- Davidson, E. A., Potter, C. S., Schlesinger, P., and Klooster, S. A.: Model estimates of regional nitric oxide emissions from soils of the southeastern United States, *Ecol. Appl.*, 8, 748–759, 1998.
- Delon, C., Serça, D., Boissard, C., Dupont, R., Dutot, A., Laville, P., de Rosnay, P., and Delmas, R.: Soil NO emissions modelling using artificial neural network, *Tellus*, 59, 502–513, doi:10.1111/j.1600-0889.2007.00254.x, 2007.
- Delon, C., Reeves, C. E., Stewart, D. J., Serça, D., Dupont, R., Mari, C., Chaboureaud, J.-P., and Tulet, P.: Biogenic nitrogen oxide emissions from

- soils - impact on  $\text{NO}_x$  and ozone over West Africa during AMMA (African Monsoon Multidisciplinary Experiment): modelling study, *Atmos. Chem. Phys.*, 8, 2351–2363, 2008.
- Deng, F., Chen, J. M., Plummer, S., Chen, M., and Pisek, J.: Algorithm for global Leaf Area Index retrieval using satellite imagery, *IEEE Trans. Geosci. Remote Sens.*, 44, 2219–2229, 2006.
- Denman, K. L., Brasseur, G., Chidthaisong, A., Ciais, P., Cox, P. M., Dickinson, R. E., Hauglustaine, D., Heinze, C., Holland, E., Jacob, D., Lohmann, U., Ramachandran, S., da Silva Dias, P. L., Wofsy, S. C., and Zhang, X.: Couplings Between Changes in the Climate System and Biogeochemistry, in: *Climate Change 2007: The Physical Science Basis. Contribution of Working Group I to the Fourth Assessment Report of the Intergovernmental Panel on Climate Change*, edited by Solomon, S., Qin, D., Manning, M., Chen, Z., Marquis, M., Averyt, K. B., Tignor, M., and Miller, H. L., pp. 499–587, Cambridge University Press, Cambridge, United Kingdom and New York, NY, USA, 2007.
- Drusch, M., Scipal, K., de Rosnay, P., Balsamo, G., Andersson, E., Bougeault, P., and Viterbo, P.: Towards a Kalman Filter based soil moisture analysis system for the operational ECMWF Integrated Forecast System, *Geophys. Res. Lett.*, 36, L10 401, doi:10.1029/2009GL037716, 2009.
- Eva, H. and Lambin, E. F.: Remote sensing of biomass burning in tropical regions: Sampling issues and multisensor approach, *Remote Sens. Environ.*, 64, 292–315, 1998.
- Fang, S. and Mu, Y.:  $\text{NO}_x$  fluxes from several typical agricultural fields during summer-autumn in the Yangtse Delta, China, *Atmos. Environ.*, 43, 2665–2671, doi:10.1016/j.atmosenv.2009.02.027, 2009.
- FAO and IFA: Global estimates of gaseous emissions of  $\text{NH}_3$ ,  $\text{NO}$  and  $\text{N}_2\text{O}$  from agricultural land, FAO and IFA, Rome, Italy, 2001.
- Feig, G. T.: Soil biogenic emissions of nitric oxide from arid and semi-arid ecosystems, Ph.D. thesis, Johannes Gutenberg-University, Mainz, Germany, 2009.
- Firestone, M. K. and Davidson, E. A.: Mikrobiological basis of  $\text{NO}$  and  $\text{N}_2\text{O}$  production and consumption in soil, in: *Exchange of trace gases between terrestrial ecosystems and the atmosphere*, edited by Andreae, M. O. and Schimel, D. S., pp. 7–21, 1989.
- Friedl, M. A., McIver, D. K., Hodges, J. C. F., Zhang, X. Y., Muchoney, D., Strahler, A. H., Woodcock, C. E., Gopal, S., Schneider, A., Cooper, A., Baccini, A., Gao, F., and Schaaf, C.: Global land cover mapping from MODIS: algorithms and early results, *Remote Sens. Environ.*, 83, 287–302, 2006.

- Fuglestedt, J. S., Berntsen, T. K., Isaksen, I. S. A., Mao, H., Liang, X.-Z., and Wang, W.-C.: Climatic forcing of nitrogen oxides through changes in tropospheric ozone and methane; global 3D model studies, *Atmos. Environ.*, **33**, 961–977, 1999.
- Galbally, I. E., Freney, J. R., Muirhead, W. A., Simpson, J. R., Trevitt, A. C. F., and Chalk, P. M.: Emission of nitrogen oxides ( $\text{NO}_x$ ) from a flooded soil fertilized with urea: relation to other nitrogen loss processes, *J. Atmos. Chem.*, **5**, 343–365, 1987.
- Galloway, J. N., Schlesinger, W. H., Levy II, H., Michaels, A., and Schnoor, J. L.: Nitrogen fixation: Anthropogenic enhancement-environmental response, *Global Biogeochem. Cy.*, **9**, 235–252, 1995.
- Galloway, J. N., Dentener, F. J., Capone, D. G., Boyer, E. W., Howarth, R. W., Seitzinger, S. P., Asner, G. P., Cleveland, C. C., Green, P. A., Holland, E. A., Karl, D. M., Michaels, A. F., Porter, J. H., Townsend, A. R., and Vörösmarty, C. J.: Nitrogen cycles: past, present, and future, *Biogeochemistry*, **70**, 153–226, 2004.
- Galloway, J. N., Cowling, E. B., Seitzinger, S. P., and Socolow, R. H.: Reactive nitrogen: Too much of a good thing?, *Ambio*, **31**, 60–63, doi:10.1579/0044-7447-31.2.6, 2002.
- Ganzeveld, L. N., Lelieveld, J., Dentener, F. J., Krol, M. C., Bouwman, A. F., and Roelofs, G.-J.: Global soil-biogenic  $\text{NO}_x$  emissions and the role of canopy processes, *J. Geophys. Res.*, **107**, 4321, doi:10.1029/2001JD001289, 2002a.
- Ganzeveld, L. N., Lelieveld, J., Dentener, F. J., Krol, M. C., and Roelofs, G.-J.: Atmosphere-biosphere trace gas exchanges simulated with a single-column model, *J. Geophys. Res.*, **107**, 4320, doi:10.1029/2001JD000684, 2002b.
- Ganzeveld, L. N., van Aardenne, J. A., Butler, T. M., Lawrence, M. G., Metzger, S. M., Stier, P., Zimmermann, P., and Lelieveld, J.: Technical Note: Anthropogenic and natural offline emissions and the online EMISSIONS and dry DEPOSITION submodel EMDEP of the Modular Earth Submodel system (MESSy), *Atmos. Chem. Phys. Discuss.*, **6**, 5457–5483, 2006.
- Garcia-Montiel, D. C., Steudler, P. A., Piccolo, M., Neill, C., Melillo, J., and Cerri, C. C.: Nitrogen oxide emissions following wetting of dry soils in forest and pastures in Rondônia, Brazil, *Biogeochemistry*, **64**, 319–336, 2003.
- Giglio, L., Kendall, J. D., and Mack, R.: A multi-year active fire dataset for the tropics derived from the TRMM VIRS, *Int. J. Remote Sens.*, **24**, 4505–4525, doi:10.1080/0143116031000070283, 2003.
- Gut, A., van Dijk, S. M., Scheibe, M., Rummel, U., Welling, M., Ammann,

- C., Meixner, F. X., Kirkman, G. A., Andreae, M. O., and Lehmann, B. E.: NO emission from Amazonian rain forest soil: continuous measurements of NO flux and soil concentration, *J. Geophys. Res.*, 107, 8057, doi:10.1029/2001JD000521, 2002.
- Hammer, M.-U., Vogel, B., and Vogel, H.: Findings on H<sub>2</sub>O<sub>2</sub>/HNO<sub>3</sub> as an indicator of ozone sensitivity in Baden-Württemberg, Berlin-Brandenburg, and the Po valley based on numerical simulations, *J. Geophys. Res.*, 107, 8190, doi:10.1029/2000JD000211, 2002.
- Hauglustaine, D. A., Hourdin, F., Jourdain, L., Filiberti, M.-A., Walters, S., Lamarque, J.-F., and Holland, E. A.: Interactive chemistry in the Laboratoire de Météorologie Dynamique general circulation model: Description and background tropospheric chemistry evaluation, *J. Geophys. Res.*, 109, D04341, doi:10.1029/2003JD003957, 2004.
- Holland, E. A., Dentener, F. J., Brasswell, B. H., and Sulzman, J. M.: Contemporary and pre-industrial global reactive nitrogen budgets, *Biogeochemistry*, 46, 7–43, 1999.
- Horowitz, L. W., Walters, S., Mauzerall, D. L., Emmons, L. K., Rasch, P. J., Granier, C., Tie, X., Lamarque, J.-F., Schultz, M. G., Tyndall, G. S., Orlando, J. J., and Brasseur, G. P.: A global simulation of tropospheric ozone and related tracers: Description and evaluation of MOZART, version 2, *J. Geophys. Res.*, 108, 4784, doi:10.1029/2002JD002853, 2003.
- Hudman, R. C., Russell, A. R., Valin, L. C., and Cohen, R. C.: Inter-annual variability in soil nitric oxide emissions over the United States as viewed from space, *Atmos. Chem. Phys.*, 10, 9943–9952, doi:10.5194/acp-10-9943-2010, 2010.
- Isaksen, I. S. A. and Hov, Ø.: Calculation of trends in the tropospheric concentration of O<sub>3</sub>, OH, CO, CH<sub>4</sub> and NO<sub>x</sub>, *Tellus*, 39B, 271–285, 1987.
- Jacob, D. J. and Bakwin, P. S.: Cycling of NO<sub>x</sub> in tropical forest canopies, in: *Microbial production and consumption of greenhouse gases: methane, nitrogen oxides, and halomethanes*, edited by Rogers, J. E. and Whitman, W. B., pp. 237–254, American Society for Microbiology, Washington, D. C., USA, 1991.
- Jaeglé, L., Steinberger, L., Martin, R. V., and Chance, K.: Global partitioning of NO<sub>x</sub> sources using satellite observations: relative roles of fossil fuel combustion, biomass burning and soil emissions, *Faraday Discuss.*, 130, 407–423, 2005.
- Jambert, C., Delmas, R. A., Labroue, L., and Chassin, P.: Nitrogen compound emissions from fertilized soils in a maize field pine tree forest agrosystem in the southwest of France, *J. Geophys. Res.*, 99, 16523–16530, 1994.

- Jöckel, P., Sander, R., Kerkweg, A., Tost, H., and Lelieveld, J.: Technical Note: The Modular Earth Submodel System (MESSy) - a new approach towards Earth System Modeling, *Atmos. Chem. Phys.*, 5, 433–444, 2005.
- Jöckel, P., Tost, H., Pozzer, A., Brühl, C., Buchholz, J., Ganzeveld, L., Hoor, P., Kerkweg, A., Lawrence, M. G., Sander, R., Steil, B., Stiller, G., Tanarhte, M., Taraborrelli, D., van Aardenne, J., and Lelieveld, J.: The atmospheric chemistry general circulation model ECHAM5/MESSy1: consistent simulation of ozone from the surface to the mesosphere, *Atmos. Chem. Phys.*, 6, 5067–5104, 2006.
- Johansson, C. and Galbally, I. E.: Production of nitric oxide in loam under aerobic and anaerobic conditions, *Appl. Environ. Microb.*, 47, 1284–1289, 1984.
- Ju, X., Liu, X., Zhang, F., and Roelcke, M.: Nitrogen fertilization, soil nitrate accumulation and policy recommendations in several agricultural regions of China, *Ambio*, 33, 300–305, 2004.
- Kampstra, P.: Beanplot: A boxplot alternative for visual comparison of distributions, *J. Stat. Softw.*, 28, 1–9, 2008.
- Kerkweg, A., Buchholz, J., , Ganzeveld, L., Pozzer, A., Tost, H., and Jöckel, P.: Technical Note: Technical Note: An implementation of the dry removal processes DRY DEPosition and SEDimentation in the Modular Earth Submodel System (MESSy), *Atmos. Chem. Phys.*, 6, 3603–3609, 2006a.
- Kerkweg, A., Sander, R., Tost, H., and Jöckel, P.: Technical Note: Implementation of prescribed (OFFLEM), calculated (ONLEM) and pseudo-emissions (TNUDGE) of chemical species in the modular earth submodel system (MESSy), *Atmos. Chem. Phys.*, 6, 3603–3609, 2006b.
- Kirkman, G. A.: The surface exchange of trace gases in the tropics and savannas, Ph.D. thesis, Johannes Gutenberg-University, Mainz, Germany, 2001.
- Kleinman, L. I., Daum, P. H., Lee, J. H., Lee, Y.-N., Nunnermacker, L. J., Springston, S. R., and Newman, L.: Dependence of ozone production on NO and hydrocarbons in the troposphere, *Geophys. Res. Lett.*, 24, 2299–2302, 1997.
- Kottek, M., Grieser, J., Beck, C., Rudolf, B., and Rubel, F.: World map of the Köppen-Geiger climate classification updated, *Meteorol. Z.*, 15, 259–263, 2006.
- Labrador, L., von Kuhlmann, R., and Lawrence, M. G.: The effects of lightning-produced  $\text{NO}_x$  and its vertical distribution on atmospheric chemistry: sensitivity simulations with MATCH-MPIC, *Atmos. Chem. Phys.*, 5, 1815–1834, 2005.

- Labrador, L. J., von Kuhlmann, R., and Lawrence, M. G.: Strong sensitivity of the global mean OH concentration and the tropospheric oxidizing efficiency to the source of NO<sub>x</sub> from lightning, *Geophys. Res. Lett.*, 31, L06 102, doi:10.1029/2003GL019229, 2004.
- Langaans, S.: Diurnal cycle in savanna fires, *Nature*, 363, 120, 1993.
- Lawrence, M. G., Crutzen, P. J., Rasch, P. J., Eaton, B. E., and Mahowald, N. M.: A model for studies of tropospheric photochemistry: Description, global distributions, and evaluation, *J. Geophys. Res.*, 104, 26 245–26 277, 1999.
- Lawrence, M. G., Jöckel, P., and von Kuhlmann, R.: What does the global mean OH concentration tell us?, *Atmos. Chem. Phys.*, 1, 37–49, 2001.
- Li, C., Aber, J., Stange, F., Butterbach-Bahl, K., and Papen, H.: A process-oriented model of N<sub>2</sub>O and NO emissions from forest soils: 1. Model development, *J. Geophys. Res.*, 105, 4369–4384, 2000.
- Logan, J. A.: Tropospheric chemistry: a global perspective, *J. Geophys. Res.*, 86, 7210–7254, 1981.
- Maggiotto, S. R., Webb, J. A., Wagner-Riddle, C., and Thurtell, G. W.: Nitrous and nitrogen oxide emissions from turfgrass receiving different forms of nitrogen fertilizer, *J. Environ. Qual.*, 29, 621–630, 2000.
- Maljanen, M., Martikkala, M., Koponen, H. T., Virkajärvi, P., and Martikainen, P. J.: Fluxes of nitrous oxide and nitric oxide from experimental excreta patches in boreal agricultural soil, *Soil Biol. Biochem.*, 39, 914–920, doi:10.1016/j.soilbio.2006.11.001, 2007.
- Martin, R. V., Jacob, D. J., Chance, K., Kurosu, T. P., Palmer, P. I., and Evans, M. J.: Global inventory of nitrogen oxide emissions constrained by space-based observations of NO<sub>2</sub> columns, *J. Geophys. Res.*, 108, 4537, doi:10.1029/2003JD003453, 2003.
- Martin, R. V., Sioris, C. E., Chance, K., Ryerson, T. B., Bertram, T. H., Wooldridge, P. J., Cohen, R. C., Neuman, J. A., Swanson, A., and Flocke, F. M.: Evaluation of space-based constraints on global nitrogen oxide emissions with regional aircraft measurements over and downwind of eastern North America, *J. Geophys. Res.*, 111, D15 308, doi: 10.1029/2005JD006680, 2006.
- Matson, P. A., Billow, C., and Hall, S.: Fertilization practices and soil variations control nitrogen oxide emissions from tropical sugar cane, *J. Geophys. Res.*, 101, 18 533–18 545, 1996.
- Matson, P. M., Lohse, K. A., and Hall, S. J.: The Globalization of Nitrogen Deposition: Consequences for Terrestrial Ecosystems, *Ambio*, 31, 113–119, doi:10.1579/0044-7447-31.2.113, 2002.
- Meixner, F. X. and Yang, W. X.: Biogenic emissions of nitric oxide and

- nitrous oxide from arid and semi-arid land, in: *Dryland Ecohydrology*, edited by D'Odorico, P. and Porporat, A., pp. 233–255, Springer, Dordrecht, The Netherlands, 2006.
- Meixner, F. X., Fickinger, T., Marufu, L., Serça, D., Nathaus, F. J., Makina, E., Mukurumbira, L., and Andreae, M. O.: Preliminary results on nitric oxide emission from a southern African savanna ecosystem, *Nutr. Cycl. Agroecosys.*, 48, 123–138, 1997.
- Milford, J. B., Gao, D., Sillman, S., Blossey, P., and Russel, A. G.: Total reactive nitrogen  $\text{NO}_y$  as an indicator of the sensitivity of ozone to reductions in hydrocarbon and  $\text{NO}_x$  emissions, *J. Geophys. Res.*, 99, 3533–3542, 1994.
- Moxim, W. J., Levy II, H., and Kasibhatla, P. S.: Simulated global tropospheric PAN: its transport and impact on  $\text{NO}_x$ , *J. Geophys. Res.*, 101, 12 621–12 638, 1996.
- Müller, J.-F. and Stavrou, T.: Inversion of CO and  $\text{NO}_x$  emissions using the adjoint of the IMAGES model, *Atmos. Chem. Phys.*, 5, 1157–1186, 2005.
- Navas, M. J., Jimenénez, A. M., and Galán, G.: Air analysis: determination of nitrogen compounds by chemiluminescence, *Atmos. Environ.*, 31, 3603–3608, 1997.
- Olivier, J. G. J., Bouwman, A. F., Vandermaas, C. W. M., and Berdowski, J. J. M.: Emission database for global atmospheric research (EDGAR), *Environ. Monit. Assess.*, 31, 93–106, 1994.
- Olivier, J. G. J., Bouwman, A. F., van der Hoek, K. W., and Berdowski, J. J. M.: Global air emission inventories for anthropogenic sources of  $\text{NO}_x$ ,  $\text{NH}_3$  and  $\text{N}_2\text{O}$  in 1990, *Environ. Pollut.*, 102, 135–148, 1998.
- Olson, J.: World ecosystems (WE1.4): Digital raster data on a 10 min geographic 1080x2160 grid square, in: *Global ecosystems database, Version 1.0: DISC A*, edited by Kineman, J. and Ochrensall, M., NOAA National Geophysical Data Center, Boulder, Colorado, USA, 1992.
- Pang, X., Mu, Y., Lee, X., Fang, S., Yuan, J., and Huang, D.: Nitric oxide and nitrous oxide fluxes from typical vegetables cropland in China: Effects of canopy, soil properties and field measurement, *Atmos. Environ.*, 43, 2571–2578, doi:10.1016/j.atmosenv.2009.02.016, 2009.
- Papke, H. and Papen, H.: Influence of acid rain and liming on fluxes of NO and  $\text{NO}_2$  from forest soil, *Plant Soil*, 199, 131–139, 1998.
- Perrson, J. and Näsholm, T.: Amino acid uptake: a widespread ability among boreal forest plants, *Ecol. Lett.*, 4, 434–438, 2001.
- Pongratz, J., Reick, C., Raddatz, T., and Claussen, M.: A reconstruction of global agricultural areas and land cover for the last millennium, *Global*

- Biogeochem. Cy., 22, GB3018, doi:10.1029/2007GB003153, 2008.
- Potter, C. S., Matson, P. A., and Vitousek, P. M.: Process modeling of controls on nitrogen trace gas emissions from soils worldwide, *J. Geophys. Res.*, 101, 1361–1377, 1996.
- Pryor, S. C. and Barthelmie, R. J.: Liquid and chemical fluxes in precipitation, throughfall and stemflow: observations from a deciduous forest and a red pine plantation in the midwestern U.S.A., *Water Air Soil Poll.*, 163, 203–227, 2005.
- Rabalais, N. N.: Nitrogen in Aquatic Ecosystems, *Ambio*, 31, 102–112, doi: 10.1579/0044-7447-31.2.102, 2002.
- Remde, A. and Conrad, R.: Role of nitrification and denitrification for NO metabolism in soil, *Biogeochemistry*, 12, 189–205, 1991.
- Richter, J. and Roelcke, M.: The N-cycle as determined by intensive agriculture – examples from central Europe and China, *Nutr. Cycl. Agroecosys.*, 57, 33–46, 2000.
- Roberts, J. M., Stroud, C. A., Jobson, B. T., Trainer, M., Hereid, D., Williams, E., Fehsenfeld, F., Brune, W., Martinez, M., and Harder, H.: Application of a sequential reaction model to PANs and aldehyde measurements in two urban areas, *Geophys. Res. Lett.*, 28, 4583–4586, 2001.
- Roeckner, E., Bäuml, G., Bonaventura, L., Brokopf, R., Esch, M., Giorgetta, M., Hagemann, S., Kirchner, I., Kornbluh, L., Manzini, E., Rhodin, A., Schlese, U., Schulzweida, U., and Tompkins, A.: The atmospheric general circulation model ECHAM5. PART I: Model description, Tech. Rep. MPI-Report 349, Max Planck Institute for Meteorology, <http://www.mpimet.mpg.de/en/wissenschaft/publikationen/mpi-report-1987-2004.html>, 2003.
- Roeckner, E., Brokopf, R., Esch, M., Giorgetta, M., Hagemann, S., Kornbluh, L., Manzini, E., Schlese, U., and Schulzweida, U.: Sensitivity of simulated climate to horizontal and vertical resolution in the ECHAM5 atmosphere model, *J. Climate*, 19, 3771–3791, 2006.
- Rondón, A., Johansson, C., and Sanhueza, E.: Emission of nitric oxide from soils and termite nests in a trachypogon savanna of the Orinoco Basin, *J. Atmos. Chem.*, 17, 293–306, 1993.
- Sander, R., Kerkweg, A., Jöckel, P., and Lelieveld, J.: Technical note: The new comprehensive atmospheric chemistry module MECCA, *Atmos. Chem. Phys.*, 5, 445–450, 2005.
- Sanhueza, E.: Impact of human activity on NO<sub>x</sub> soil fluxes, *Nutr. Cycl. Agroecosys.*, 48, 61–68, 1997.
- Scheffer, F. and Schachtschabel, P.: *Lehrbuch der Bodenkunde*, Spektrum Akademischer Verlag, Heidelberg, 15 edn., 2002.



- Schlesinger, W. H.: Biogeochemistry: An analysis of global change, Academic Press, Amsterdam, 2 edn., 1997.
- Schumann, U. and Huntrieser, H.: The global lightning-induced nitrogen oxides source, *Atmos. Chem. Phys. Discuss.*, 7, 2623–2818, 2007.
- Seinfeld, J. H. and Pandis, S. P.: Atmospheric Chemistry and Physics: from air pollution to climate change, Wiley & Sons, New York, 1998.
- Sillman, S.: The use of  $\text{NO}_y$ ,  $\text{H}_2\text{O}_2$ , and  $\text{HNO}_3$  as indicators for ozone- $\text{NO}_x$ -hydrocarbon sensitivity in urban locations, *J. Geophys. Res.*, 100, 14 175–14 188, 1995.
- Simpson, D.: Biogenic emissions in Europe: 2. Implications for ozone control strategies, *J. Geophys. Res.*, 100, 22 891–22 906, 1995.
- Sitch, S., Cox, P. M., Collins, W. J., and Huntingford, C.: Indirect radiative forcing of climate change through ozone effects on the land-carbon sink, *Nature*, 448, 791–794, doi:10.1038/nature06059, 2007.
- Slemr, F. and Seiler, W.: Field measurements of NO and  $\text{NO}_2$  emissions from fertilized and unfertilized soils, *J. Atmos. Chem.*, 2, 1–24, 1984.
- Slemr, F. and Seiler, W.: Field study of environmental variables controlling the NO emissions from soil and the NO compensation point, *J. Geophys. Res.*, 96, 13 017–13 031, 1991.
- Stavrakou, T., Müller, J.-F., Boersma, K. F., De Smedt, I., and van der A, R. J.: Assessing the distribution and growth rates of  $\text{NO}_x$  emission sources by inverting a 10-year record of  $\text{NO}_2$  satellite columns, *Geophys. Res. Lett.*, 35, L10 801, doi:10.1029/2008GL033521, 2008.
- Stehfest, E. and Bouwman, L.:  $\text{N}_2\text{O}$  and NO emission from agricultural fields and soils under natural vegetation: summarizing available measurement data and modeling of global annual emissions, *Nutr. Cycl. Agroecosys.*, 24, 207–228, 2006.
- Steinkamp, J.: Globale Stickstoffmonoxid-Emissionen aus dem Boden: Literatúrauswertung und Evaluierung des Modells ECHAM5/MESSy, Diploma thesis, Johannes-Gutenberg University, Mainz/Germany, 2007.
- Steinkamp, J. and Lawrence, M.: Improvement and evaluation of simulated global biogenic soil NO emissions in an AC-GCM, doi:10.5194/acpd-10-16007-2010, 2010.
- Steinkamp, J., Ganzeveld, L. N., Wilcke, W., and Lawrence, M. G.: Influence of modelled soil biogenic NO emissions on related trace gases and the atmospheric oxidizing efficiency, *Atmos. Chem. Phys.*, 9, 2663–2677, 2009.
- Sterling, S. and Ducharne, A.: Comprehensive data set of global land cover change for land surface model applications, *Global Biogeochem. Cy.*, 22,

- GB3017, doi:10.1029/2007GB002959, 2008.
- Stockwell, D. Z., Giannakopoulos, C., Plantevin, P.-H., Carver, G. D., Chipperfield, M. P., Law, K. S., Pyle, J. A., Shallcross, D. E., and Wang, K.-Y.: Modelling  $\text{NO}_x$  from lightning and its impact on global chemical fields, *Atmos. Environ.*, 33, 4477–4493, 1999.
- Taraborrelli, D., Lawrence, M. G., Butler, T. M., Sander, R., and Lelieveld, J.: Mainz Isoprene Mechanism 2 (MIM2): an isoprene oxidation mechanism for regional and global atmospheric modelling, *Atmos. Chem. Phys. Discuss.*, 8, 14 033–14 085, 2008.
- Taraborrelli, D., Lawrence, M. G., Butler, T. M., Sander, R., and Lelieveld, J.: Mainz Isoprene Mechanism 2 (MIM2): an isoprene oxidation mechanism for regional and global atmospheric modelling, *Atmos. Chem. Phys.*, 9, 2751–2777, doi:10.5194/acp-9-2751-2009, 2009.
- Taylor, K., Williamson, D., and Zwiers, F.: The sea surface temperature and sea ice concentration boundary conditions for AMIP II simulations; PCMDI Report, Tech. Rep. 60, Program for Climate Model Diagnosis and Intercomparison, 2000.
- Tilsner, J., Wrage, N., Lauf, J., and Gebauer, G.: Emission of gaseous nitrogen oxides from an extensively managed grassland in NE Bavaria, Germany. I. Annual budgets of  $\text{N}_2\text{O}$  and  $\text{NO}_x$  emissions, *Biogeochemistry*, 63, 229–247, 2003.
- Tost, H.: Global Modelling of Cloud, Convection and Precipitation Influences on Trace Gases and Aerosols, Ph.D. thesis, Rheinische Friedrich-Wilhelms-University, Bonn/Germany, 2006.
- Tost, H., Jöckel, P., Kerkweg, A., Sander, R., and Lelieveld, J.: Technical note: A new comprehensive SCAVenging submodel for global atmospheric chemistry modelling, *Atmos. Chem. Phys.*, 6, 565–574, 2006a.
- Tost, H., Jöckel, P., and Lelieveld, J.: Influence of different convection parameterisations in a GCM, *Atmos. Chem. Phys.*, 6, 5475–5493, 2006b.
- Tost, H., Jöckel, P., and Lelieveld, J.: Lightning and convection parameterization – uncertainties in global modelling, *Atmos. Chem. Phys.*, 7, 4553–4568, 2007.
- Uppala, S. M., Kallberg, P. W., Simmons, A. J., Andrae, U., Bechtold, V. D., Fiorino, M., Gibson, J. K., Haseler, J., Hernandez, A., Kelly, G. A., Li, X., Onogi, K., Saarinen, S., Sokka, N., Allan, R. P., Andersson, E., Arpe, K., Balmaseda, M. A., Beljaars, A. C. M., Van De Berg, L., Bidlot, J., Bormann, N., Caires, S., Chevallier, F., Dethof, A., Dragosavac, M., Fisher, M., Fuentes, M., Hagemann, S., Holm, E., Hoskins, B. J., Isaksen, I. J., Janssen, P. A. E. M., Jenne, R., McNally, A. P., Mahfouf, J. F., Morcrette, J. J., Rayner, N. A., Saunders, R. W., Simon, P., Sterl, A.,

- Trenberth, K. E., Untch, A., Vasiljevic, D., Viterbo, P., and Woollen, J.: The ERA-40 re-analysis, *Q. J. Roy. Meteor. Soc.*, 131, 2961–3012, doi:10.1256/qj.04.176, 2005.
- Valente, R. J., Thornton, F. C., and Williams, E. J.: Field comparison of static and flow through chamber techniques for measurement of soil NO emission, *J. Geophys. Res.*, 100, 21 147–21 152, 1995.
- van Cleemput, O. and Samater, A. H.: Nitrite in soils: accumulation and role in the formation of gaseous N compounds, *Fert. Res.*, 45, 81–89, 1996.
- van der A, R. J., Eskes, H. J., Boersma, K. F., van Noije, T. P. C., Van Roozendaal, M., De Smedt, I., Peters, D. H. M. U., and Meijer, E. W.: Trends, seasonal variability and dominant NO<sub>x</sub> sources derived from a ten year record of NO<sub>2</sub> measured from space, *J. Geophys. Res.*, 113, D04 302, doi:10.1029/2007JD009021, 2008.
- Vitousek, P. M. and Howarth, R. W.: Nitrogen limitation on land and in the sea: How can it occur, *Biogeochemistry*, 12, 87–115, 1991.
- Vitousek, P. M., Aber, J. D., Howarth, R. W., Likens, G. E., Matson, P. A., Schindler, D. W., Schlesinger, W. H., and Tilman, D. G.: Technical report: human alteration of the global nitrogen cycle: sources and consequences, *Ecol. Appl.*, 7, 737–750, 1997.
- Vogt, K. A., Grier, C. C., and Vogt, D. J.: Production, turnover, and nutrient dynamics of above- and belowground detritus of world forests, *Adv. Ecol. Res.*, 15, 303–377, 1986.
- von Kuhlmann, R., Lawrence, M. G., and Crutzen, P. J.: A model for studies of tropospheric ozone and nonmethane hydrocarbons: Medel description and ozone results, *J. Geophys. Res.*, 108, 4294, doi:10.1029/2002JD002893, 2003.
- Wang, Y., McElroy, M. B., Martin, R. V., Streets, D. G., Zhang, Q., and Fu, T.-M.: Seasonal variability of NO<sub>x</sub> emissions over east China constrained by satellite observations: Implications for combustion and microbial sources, *J. Geophys. Res.*, 112, D06 301, doi:10.1029/2006JD007538, 2007.
- Williams, E. J., Guenther, A., and Fehsenfeld, F. C.: An inventory of nitric oxide emissions from soils in the United States, *J. Geophys. Res.*, 97, 7511–7519, 1992a.
- Williams, E. J., Hutchinson, G. L., and Fehsenfeld, F. C.: NO<sub>x</sub> and N<sub>2</sub>O emissions from soil, *Global Biogeochem. Cy.*, 6, 351–388, 1992b.
- Yamulki, S., Harrison, R. M., Goulding, K. W. T., and Webster, C. P.: N<sub>2</sub>O, NO and NO<sub>2</sub> fluxes from grassland: effect of soil pH, *Soil Biol. Biochem.*, 29, 1199–1208, 1997.
- Yan, X., Ohara, T., and Akimoto, H.: Statistical modeling of global

- soil NO<sub>x</sub> emissions, *Global Biogeochem. Cy.*, 19, GB3019, doi:10.1029/2004GB002276, 2005.
- Yienger, J. J. and Levy, H.: Empirical model of global soil-biogenic NO<sub>x</sub> emissions, *J. Geophys. Res.*, 100, 11 447–11 464, 1995.
- Zaehle, S. and Friend, A. D.: Carbon and nitrogen cycle dynamics in the O-CN land surface model: 1. Model description, site-scale evaluation, and sensitivity to parameter estimates, *Global Biogeochem. Cy.*, 24, GB1005, doi:10.1029/2009GB003521, 2010.
- Zhao, C. and Wang, Y.: Assimilated inversion of NO<sub>x</sub> emissions over east Asia using OMI NO<sub>2</sub> column measurements, *Geophys. Res. Lett.*, 36, L06 805, doi:10.1029/2008GL037123, 2009.
- Zheng, X., Huang, Y., Wang, Y., and Wang, M.: Seasonal characteristics of nitric oxide emission from a typical Chinese rice-wheat rotation during the nonwaterlogged period, *Global Change Biol.*, 9, 219–227, 2003.

# Appendices



## **A Supplementary material for chapter 2**

A Supplementary material for chapter 2

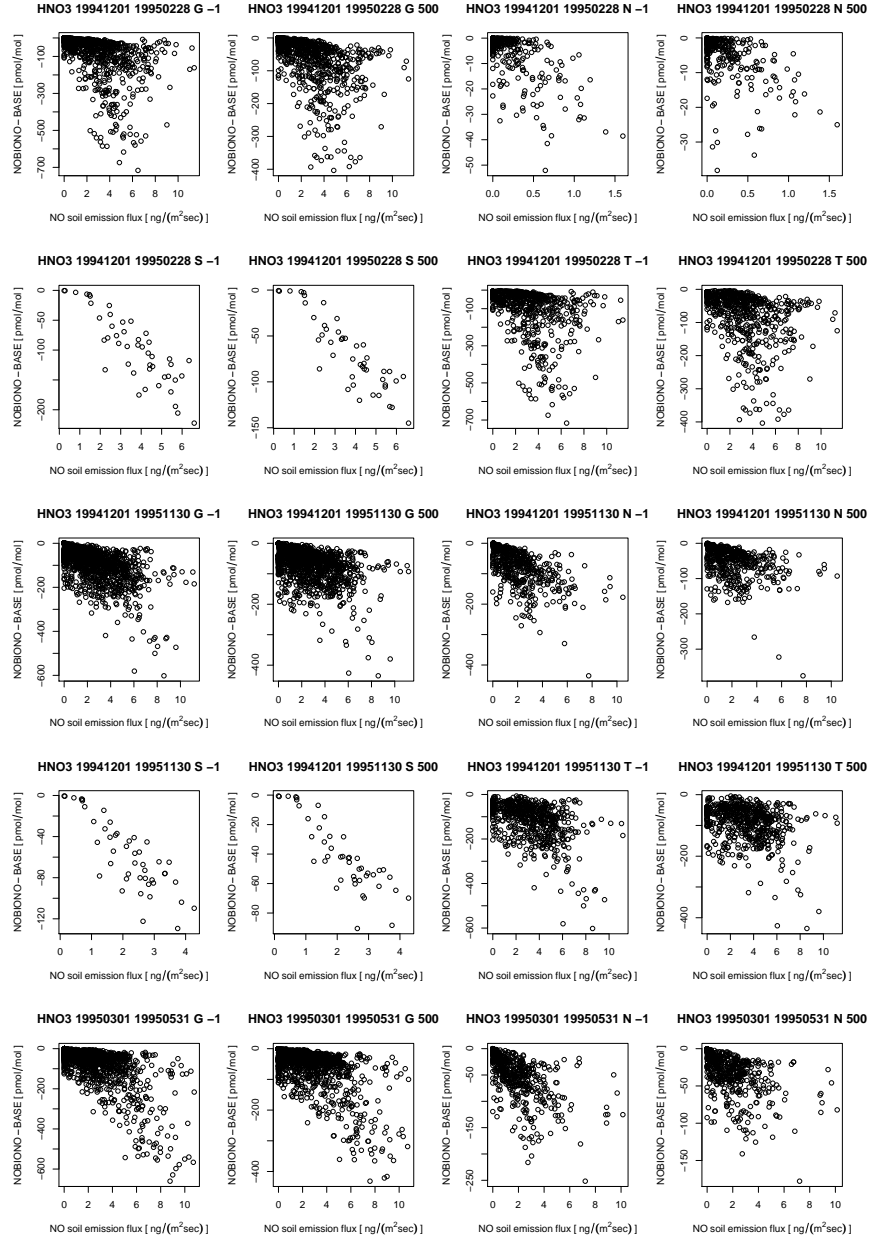


Figure A.1: Scatterplot of difference in the tracer mixing ratio/concentration (NOBIONO - BASE) versus soil NO emission. Naming of each plot: “tracer” “start date” “end date” “column height” (-1 for surface layer; 500 up to 500hPa) “domain” (G: global, N: 30–60degnorth, S: 30–60degsouth, T: 30degsouthth–30degnorth)



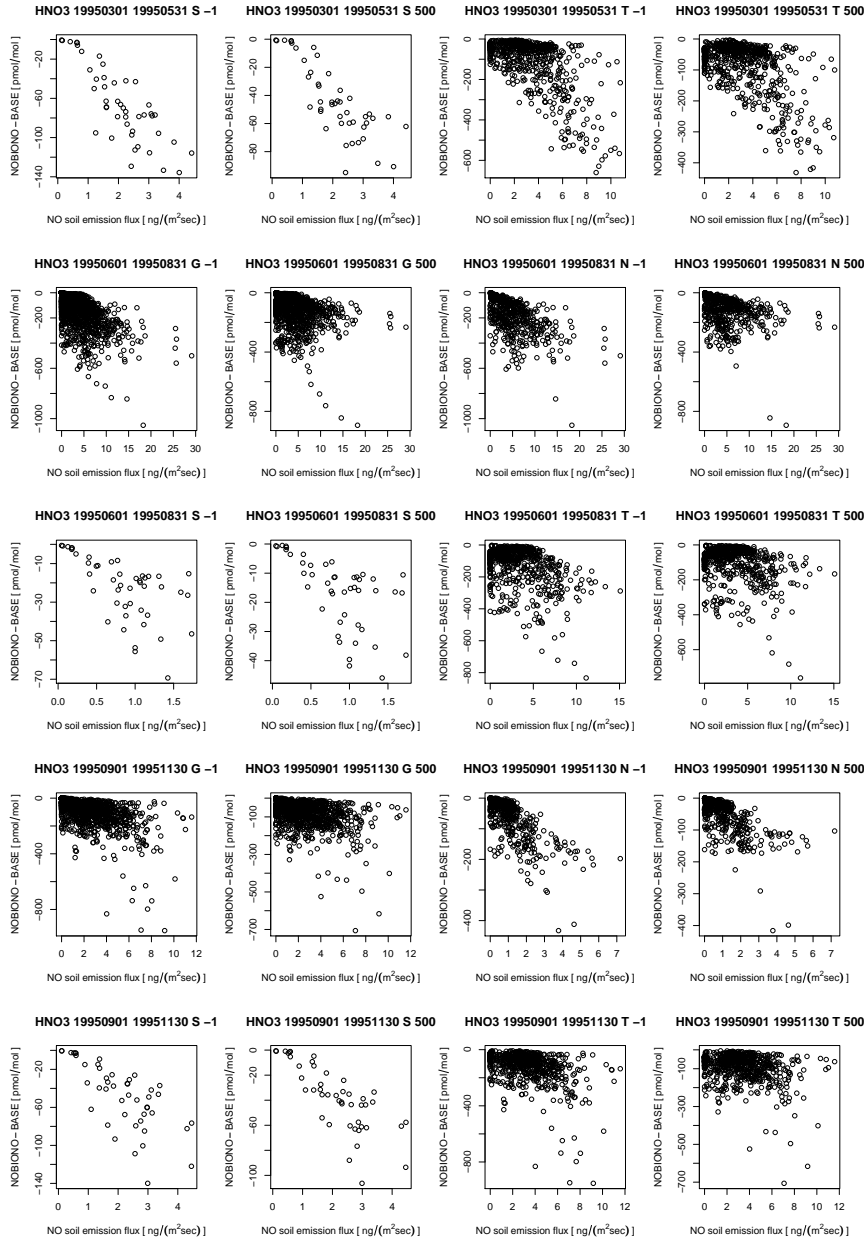


Figure A.1: Continued. Naming of each plot: “tracer” “start date” “end date” “column height” (-1 for surface layer; 500 up to 500hPa) “domain” (G: global, N: 30–60degnorth, S: 30–60degsouth, T: 30degsouthth–30degnorth)

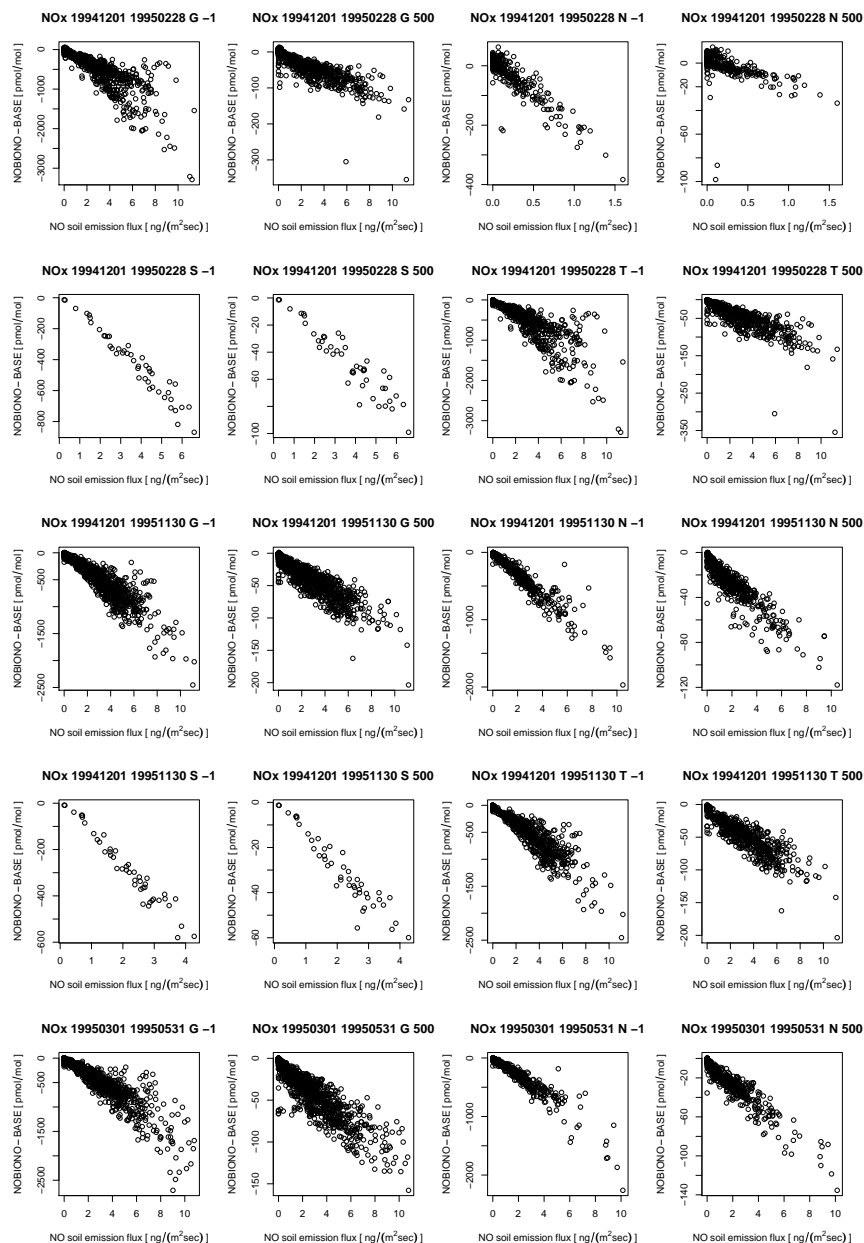


Figure A.1: Continued. Naming of each plot: “tracer” “start date” “end date” “column height” (-1 for surface layer; 500 up to 500hPa) “domain” (G: global, N: 30–60degnorth, S: 30–60degsouth, T: 30degsouthth–30degnorth)

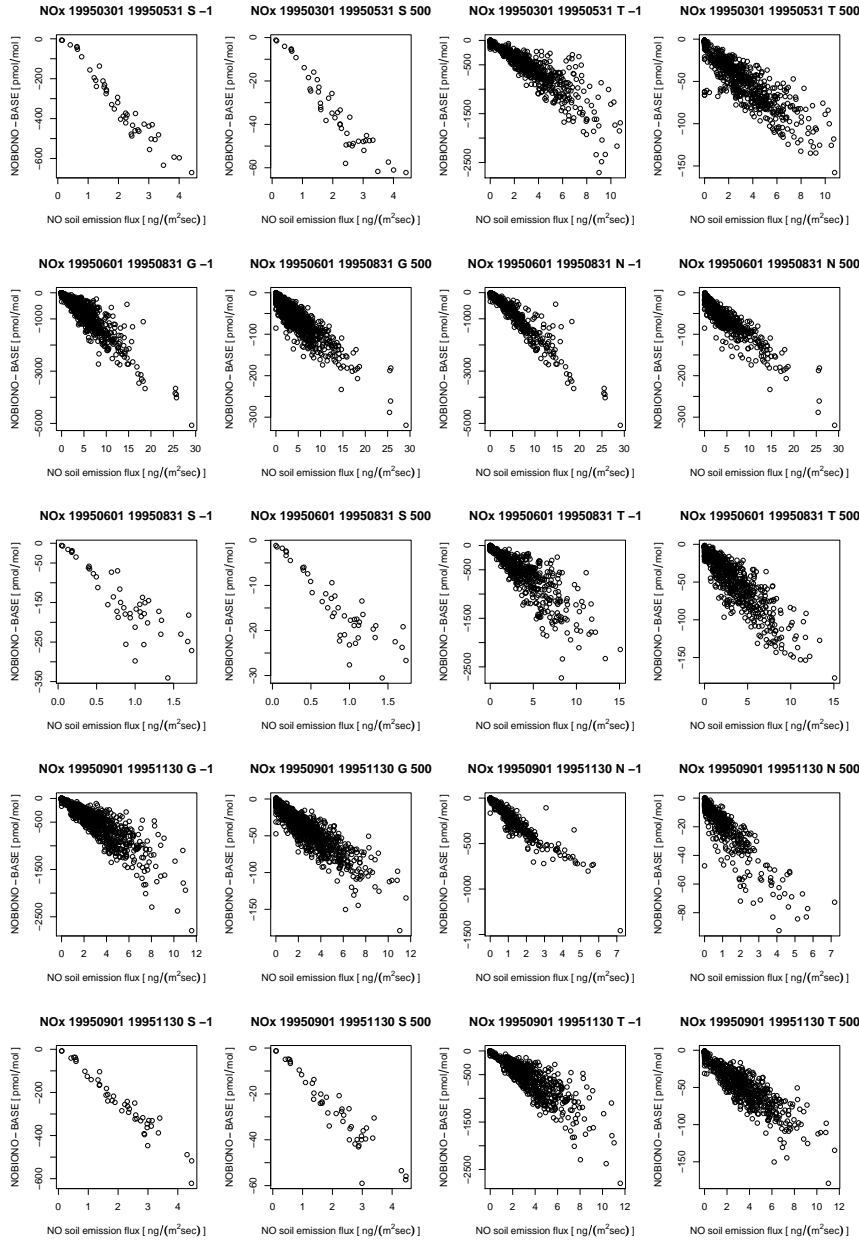


Figure A.1: Continued. Naming of each plot: “tracer” “start date” “end date” “column height” (-1 for surface layer; 500 up to 500hPa) “domain” (G: global, N: 30–60degnorth, S: 30–60degsouth, T: 30degsouthth–30degnorth)

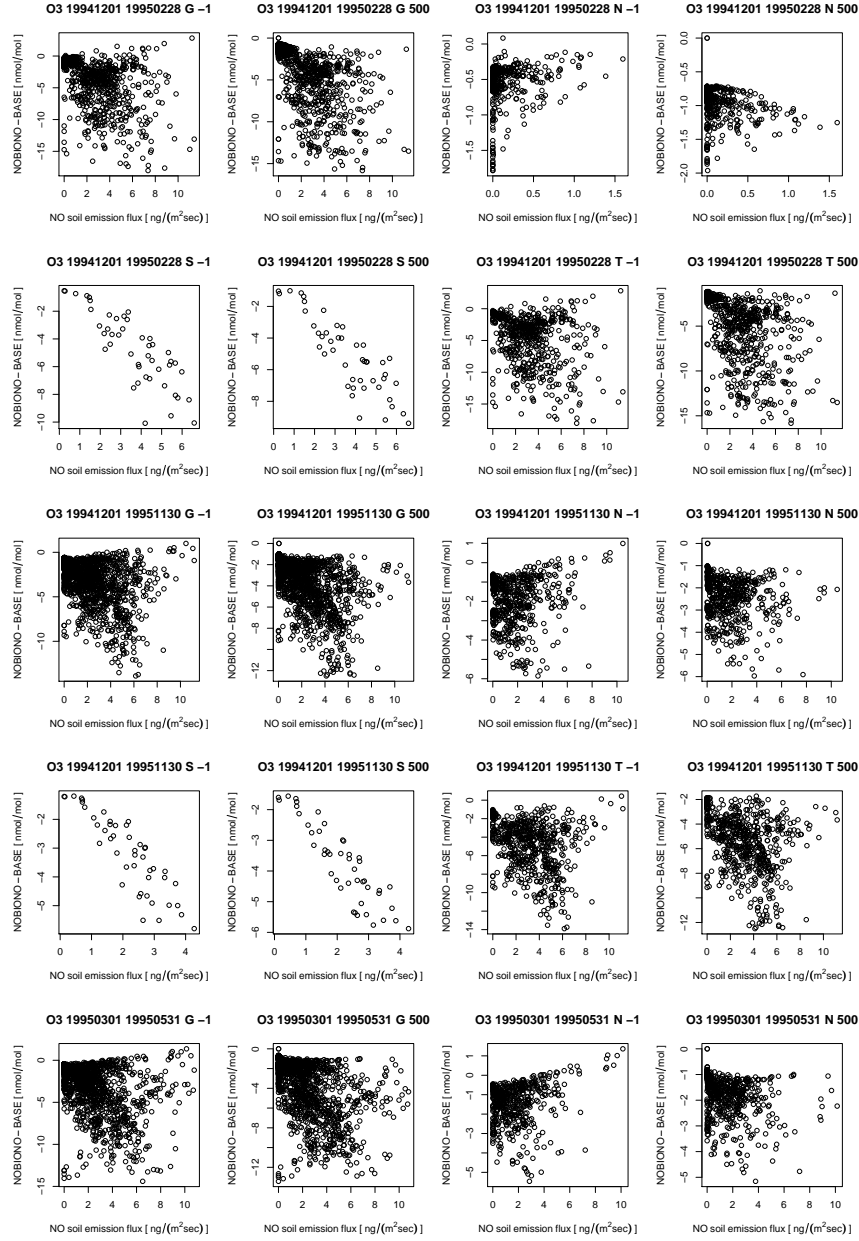


Figure A.1: Continued. Naming of each plot: “tracer” “start date” “end date” “column height” (-1 for surface layer; 500 up to 500hPa) “domain” (G: global, N: 30–60degnorth, S: 30–60degsouth, T: 30degsouthth–30degnorth)

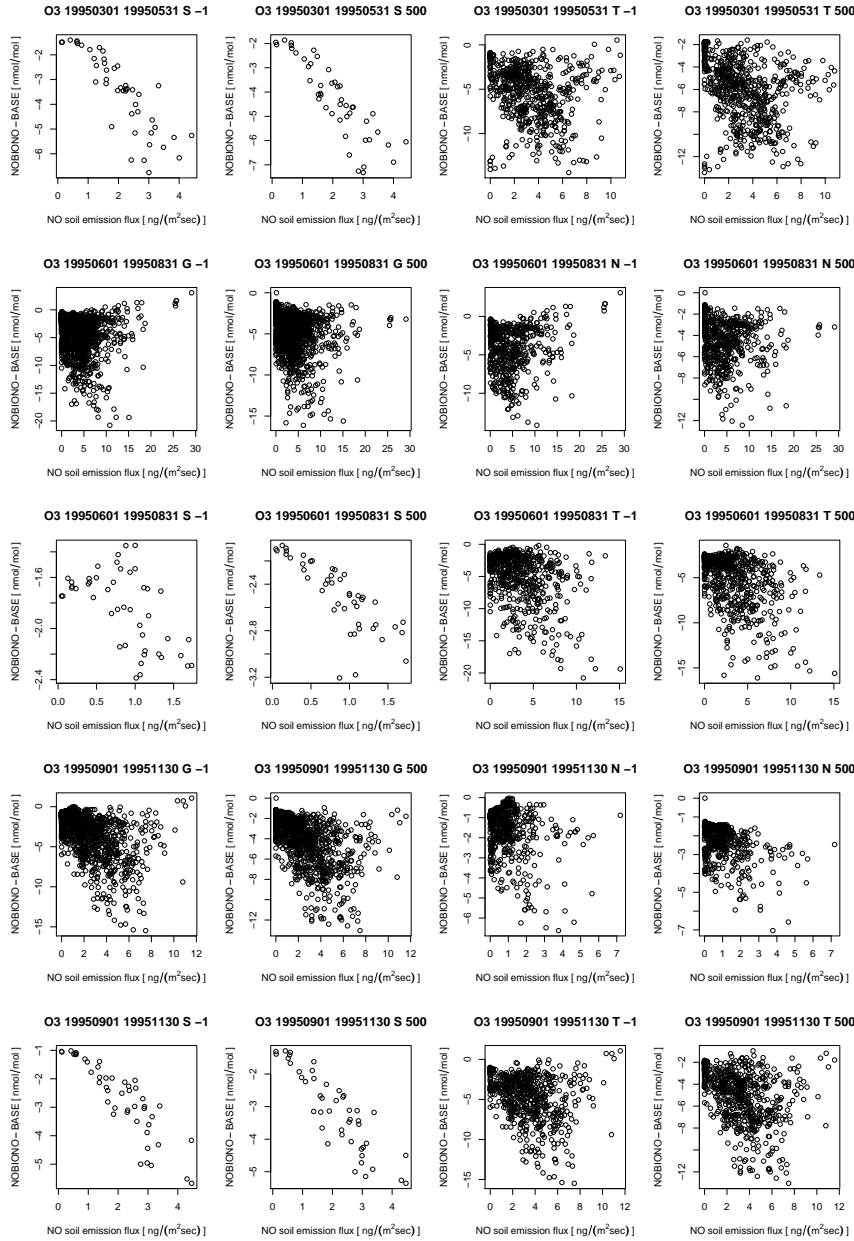


Figure A.1: Continued. Naming of each plot: “tracer” “start date” “end date” “column height” (-1 for surface layer; 500 up to 500hPa) “domain” (G: global, N: 30–60degnorth, S: 30–60degsouth, T: 30degsouthth–30degnorth)

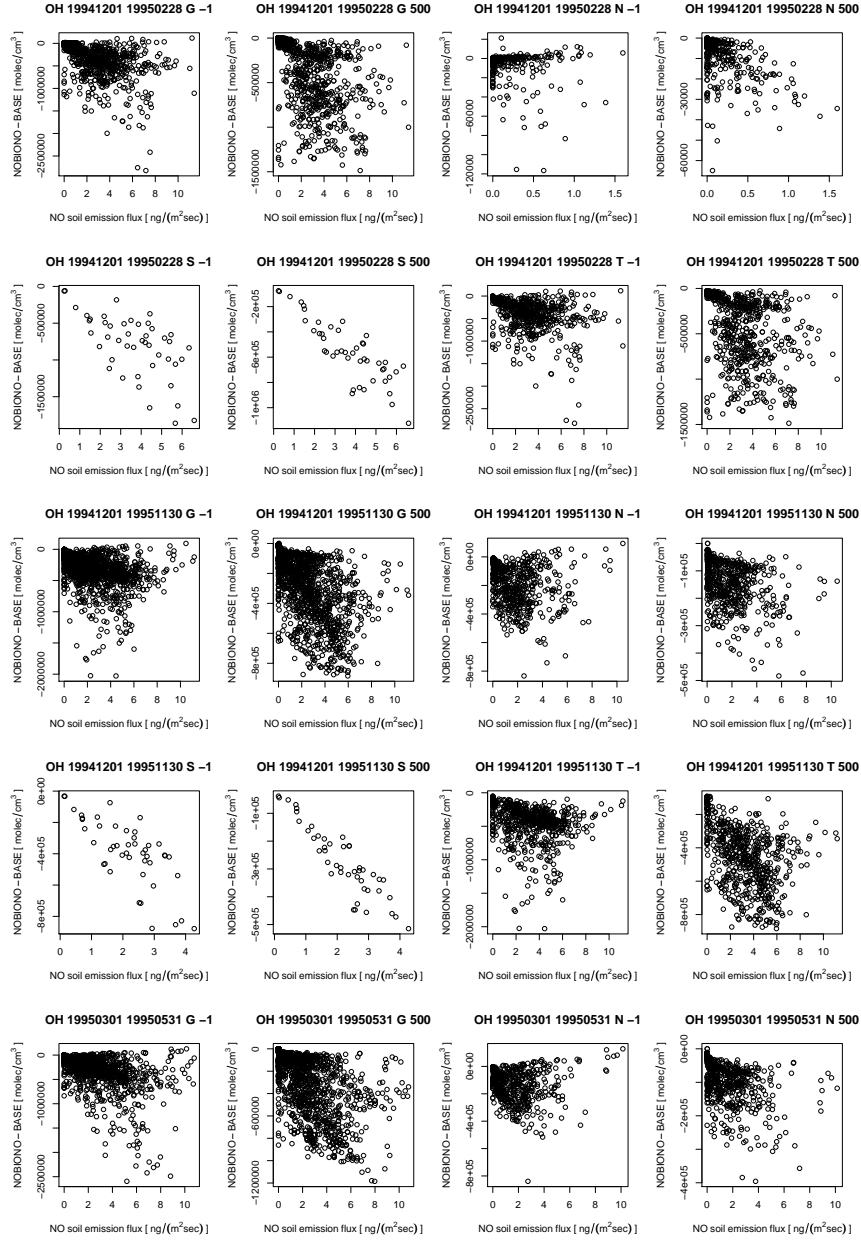


Figure A.1: Continued. Naming of each plot: “tracer” “start date” “end date” “column height” (-1 for surface layer; 500 up to 500hPa) “domain” (G: global, N: 30–60degnorth, S: 30–60degsouth, T: 30degsouthth–30degnorth)

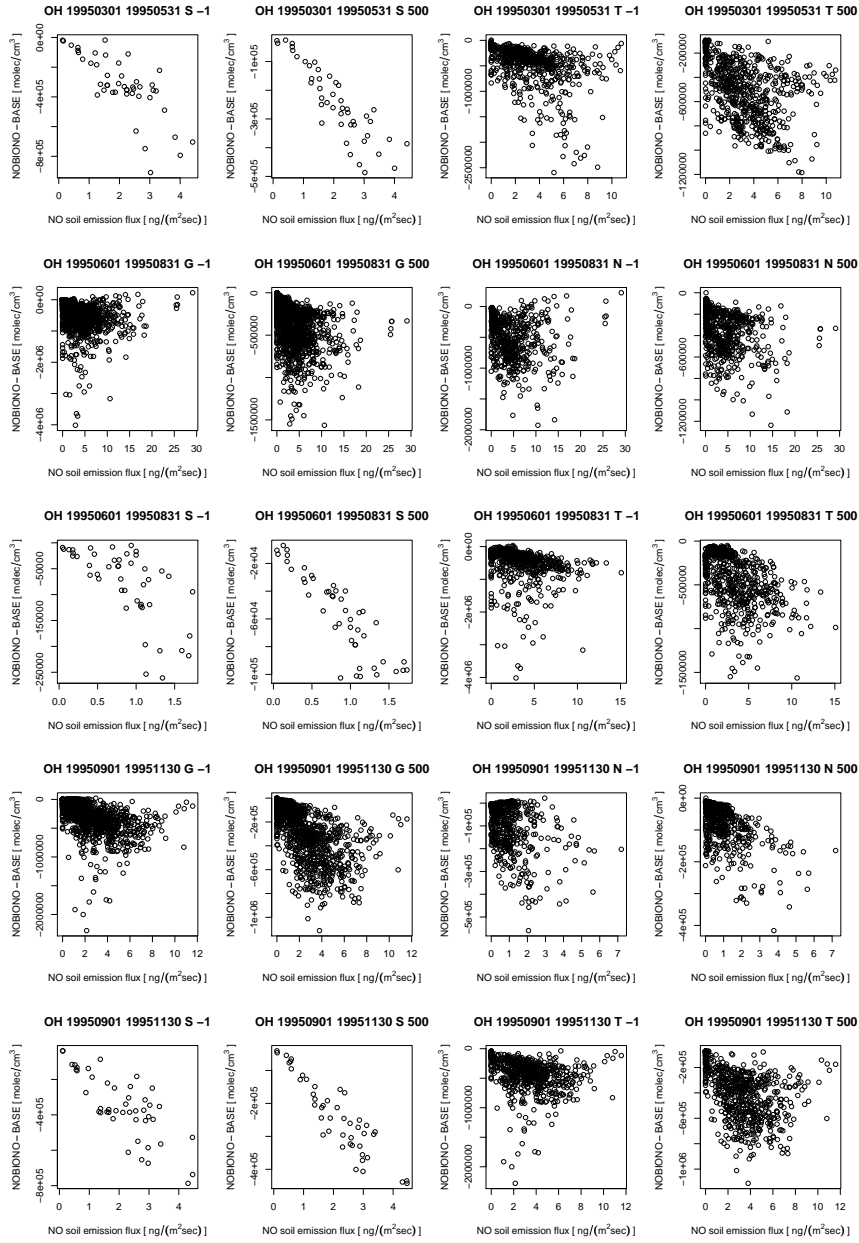


Figure A.1: Continued. Naming of each plot: “tracer” “start date” “end date” “column height” (-1 for surface layer; 500 up to 500hPa) “domain” (G: global, N: 30–60degnorth, S: 30–60degsouth, T: 30degsouthth–30degnorth)

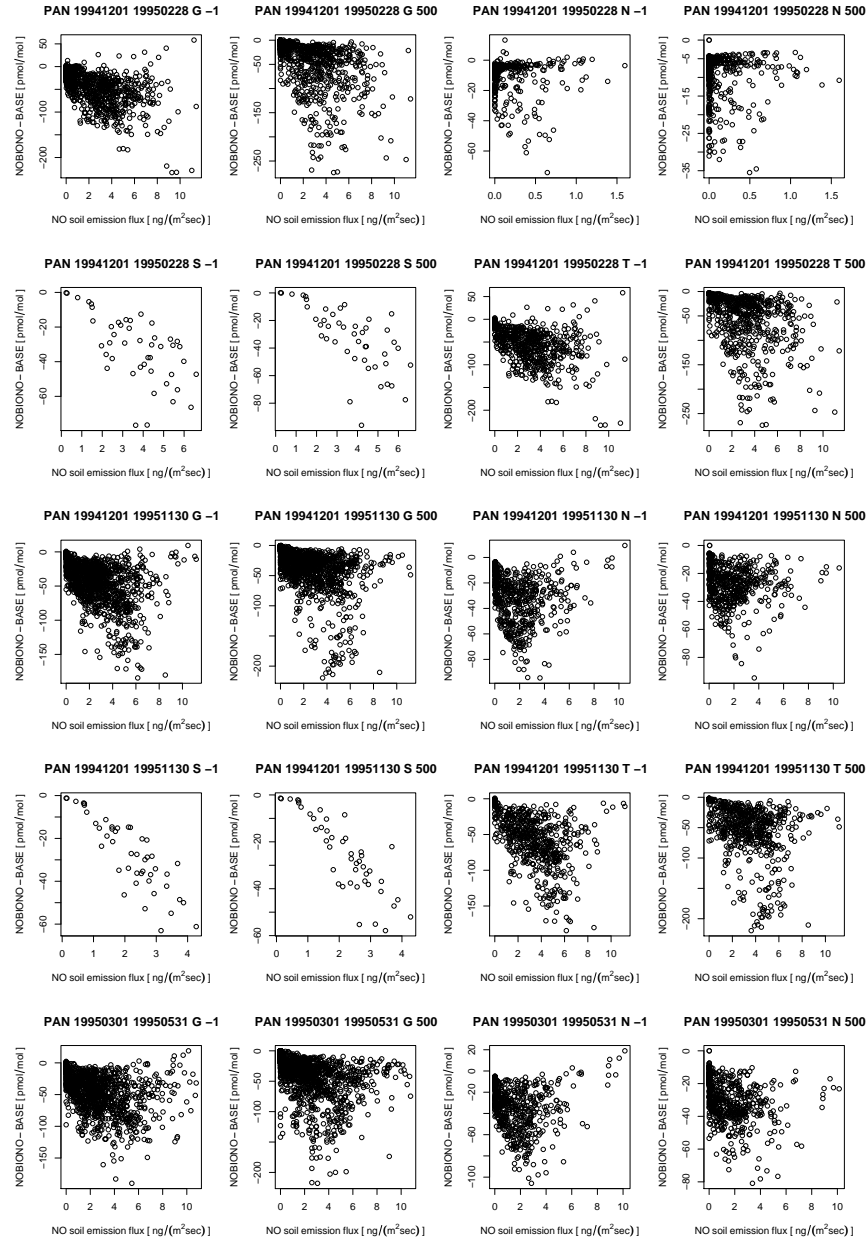


Figure A.1: Continued. Naming of each plot: “tracer” “start date” “end date” “column height” (-1 for surface layer; 500 up to 500hPa) “domain” (G: global, N: 30–60degnorth, S: 30–60degsouth, T: 30degsouthth–30degnorth)



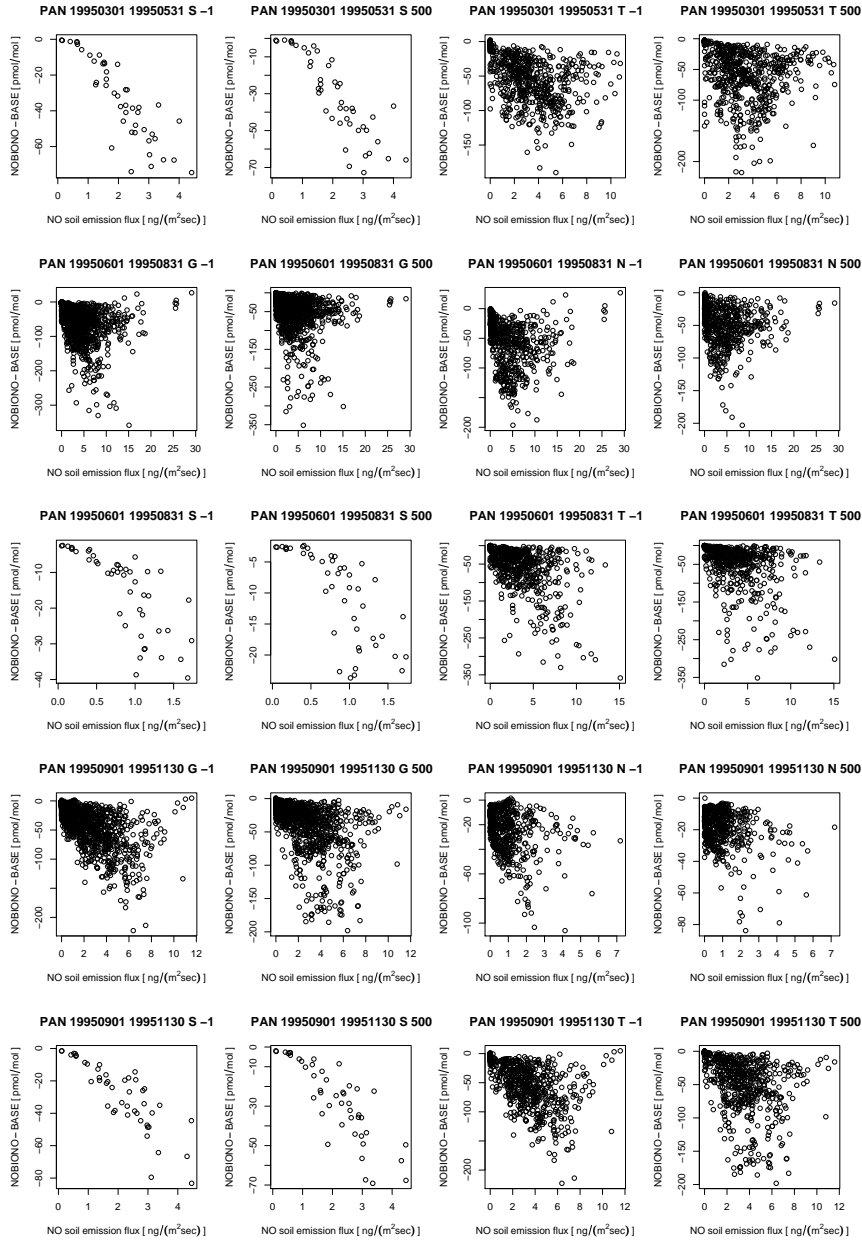


Figure A.1: Continued. Naming of each plot: “tracer” “start date” “end date” “column height” (-1 for surface layer; 500 up to 500hPa) “domain” (G: global, N: 30–60degnorth, S: 30–60degsouth, T: 30degsouthth–30degnorth)

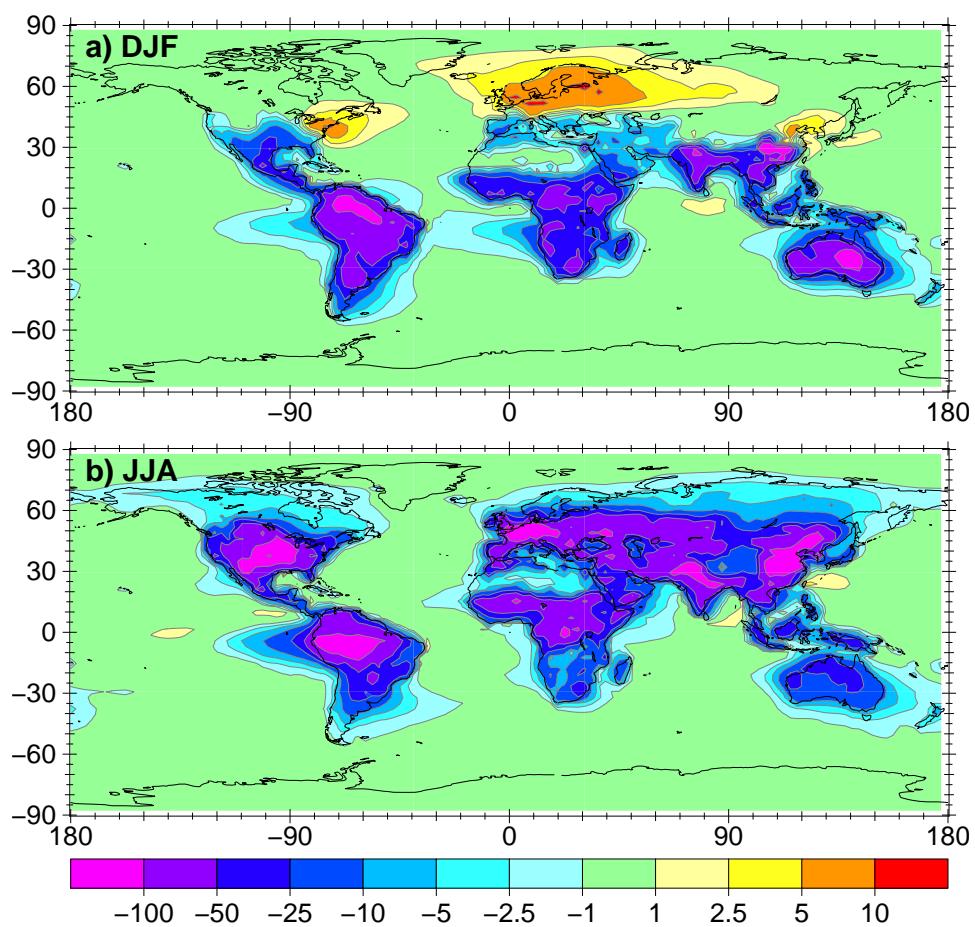


Figure A.2: Absolute difference (NOBIONO – BASE) of the lower tropospheric column mixing ratio of NO<sub>x</sub> in  $\frac{\text{pmol}}{\text{mol}}$  averaged for a) December, January, February and b) June, July and August

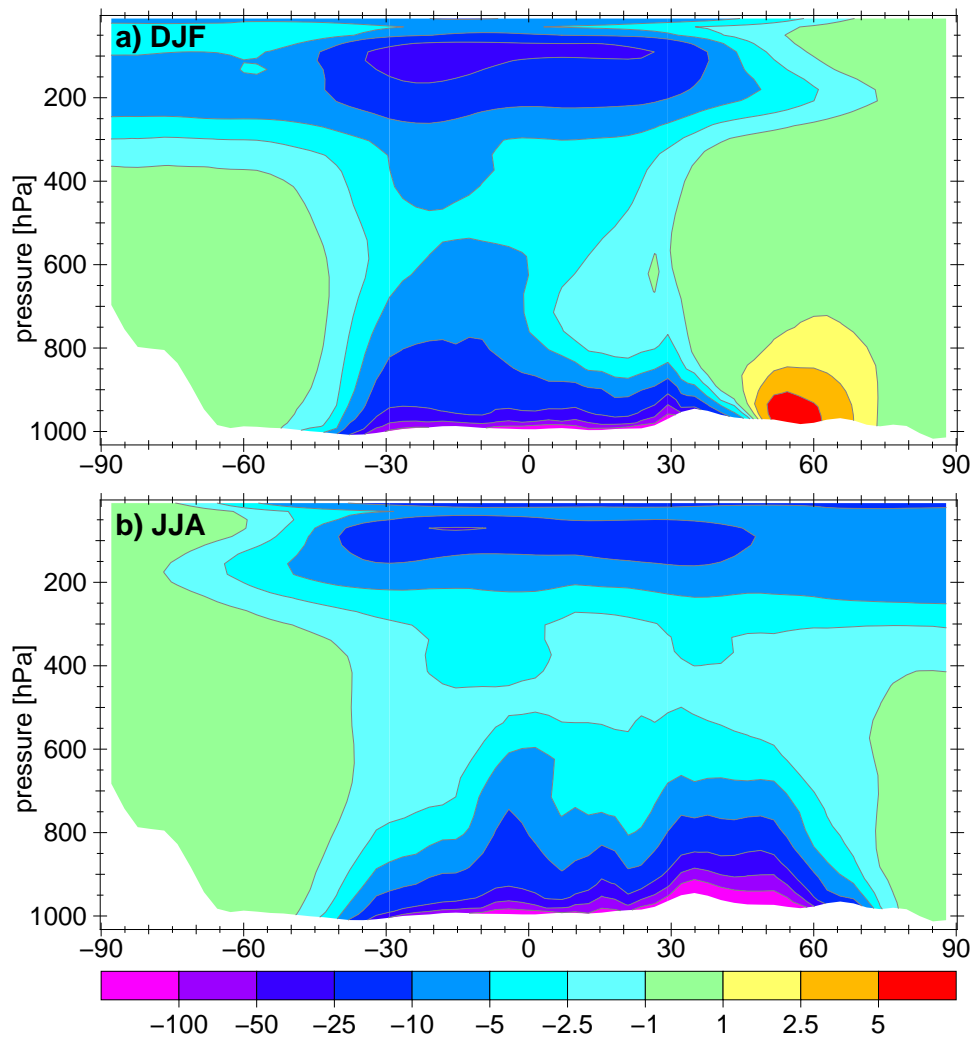


Figure A.3: Absolute difference (NOBIONO – BASE) of zonal mean mixing ratio of  $\text{NO}_x$  in  $\frac{\text{pmol}}{\text{mol}}$  averaged for a) December, January, February and b) June, July and August

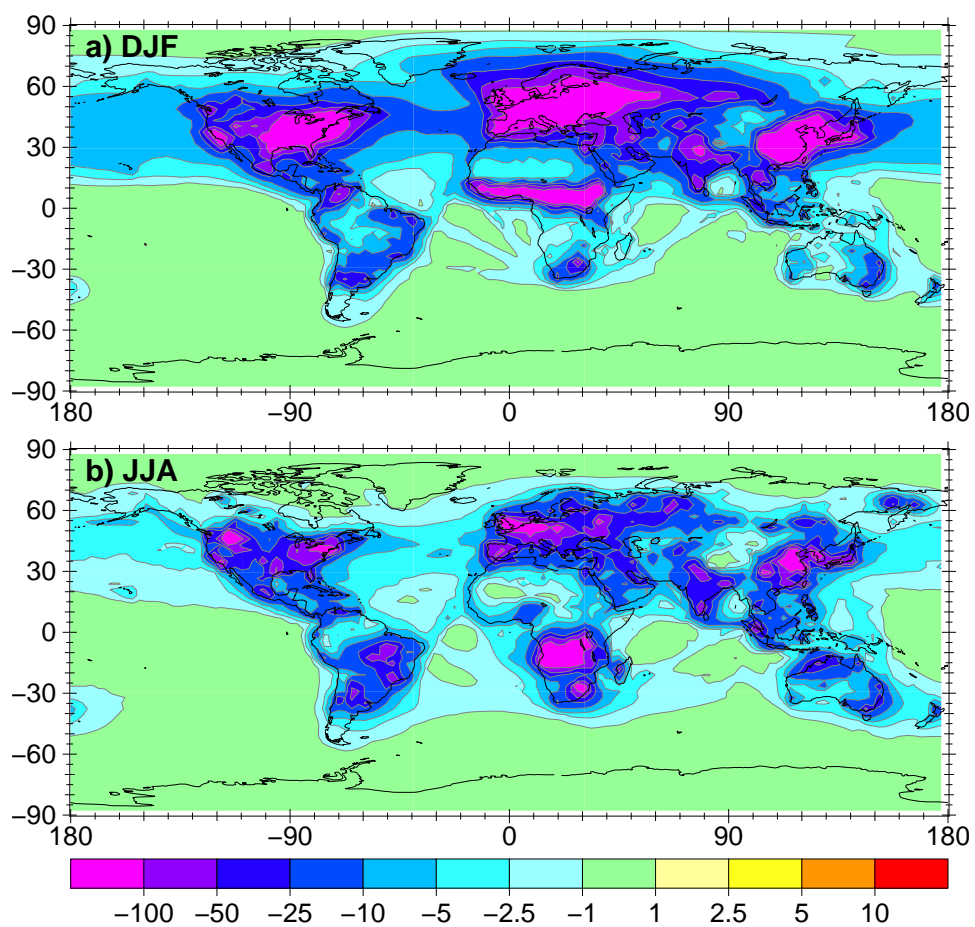


Figure A.4: Absolute difference (REDOTHER – BASE) of the lower tropospheric column mixing ratio of NO<sub>x</sub> in  $\frac{\text{pmol}}{\text{mol}}$  averaged for a) December, January, February and b) June, July and August

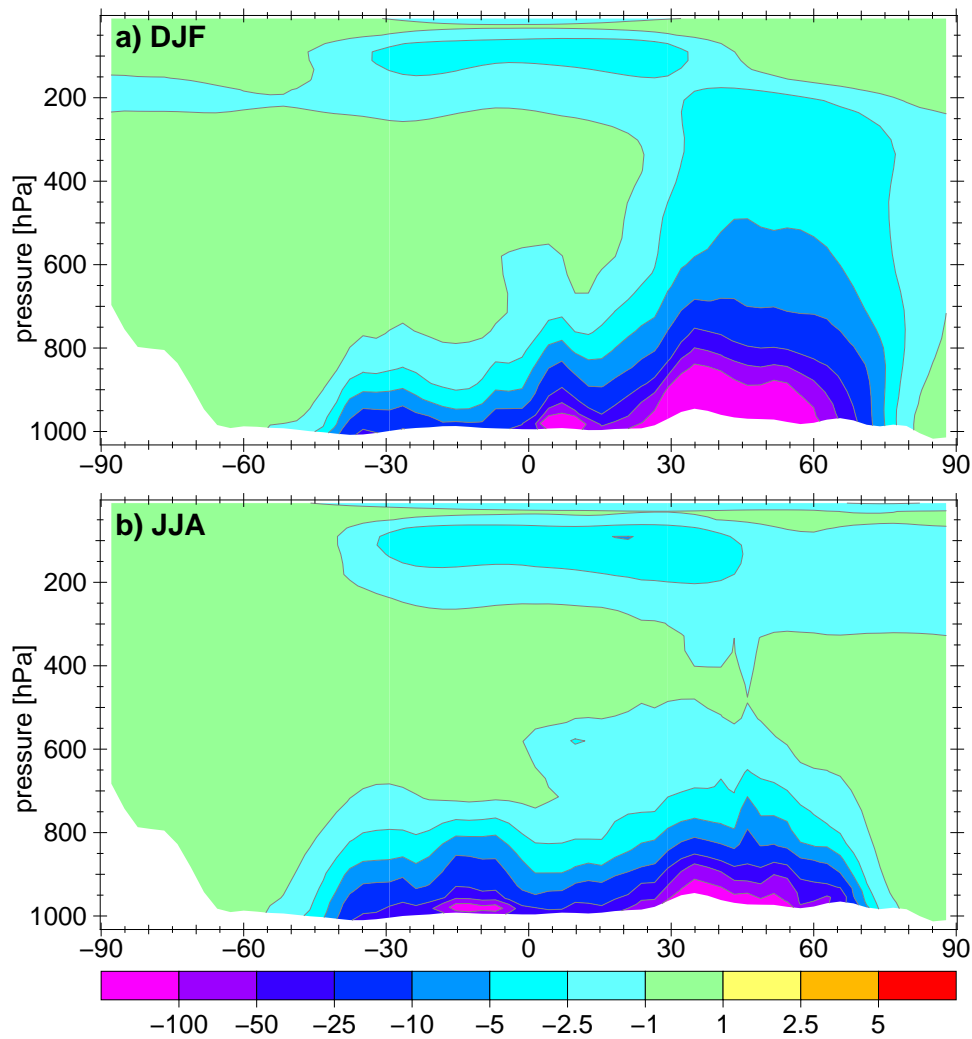


Figure A.5: Absolute difference (REDOTHER – BASE) of zonal mean mixing ratio of NO<sub>x</sub> in  $\frac{\text{pmol}}{\text{mol}}$  averaged for a) December, January, February and b) June, July and August

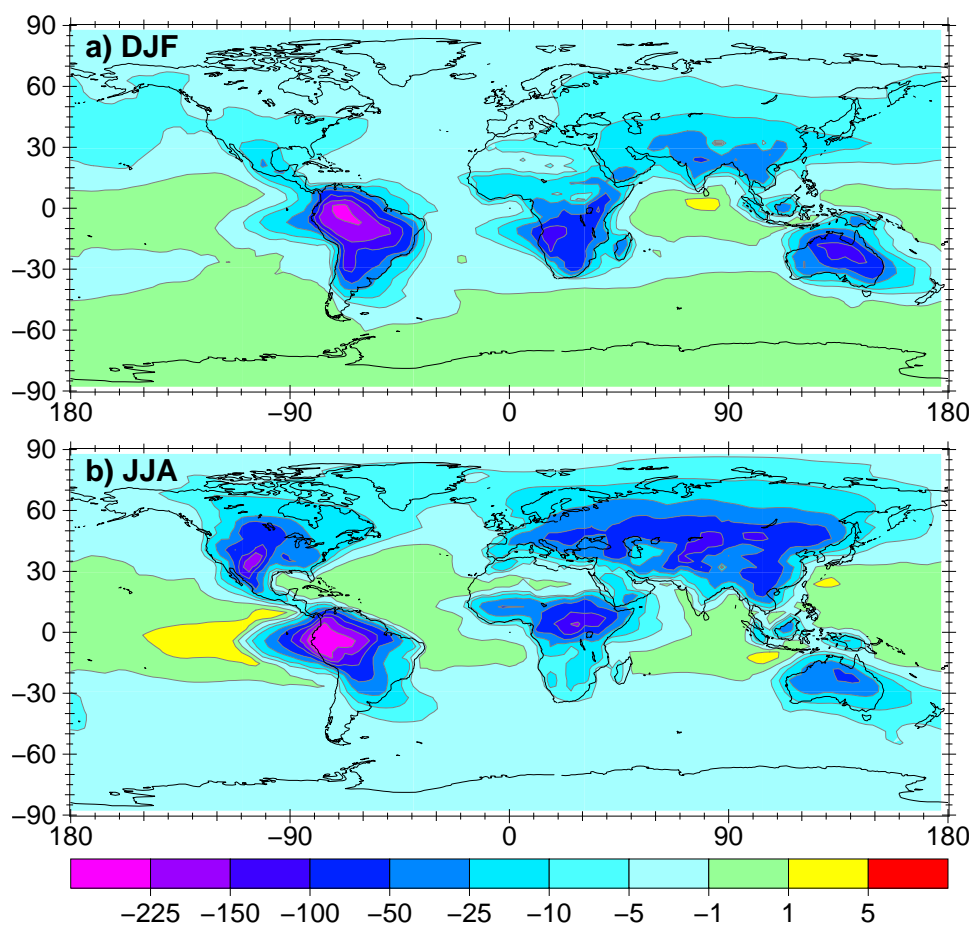


Figure A.6: Absolute difference (NOBIONO – BASE) of the lower tropospheric column mixing ratio of PAN in  $\frac{pmol}{mol}$  averaged for a) December, January, February and b) June, July and August

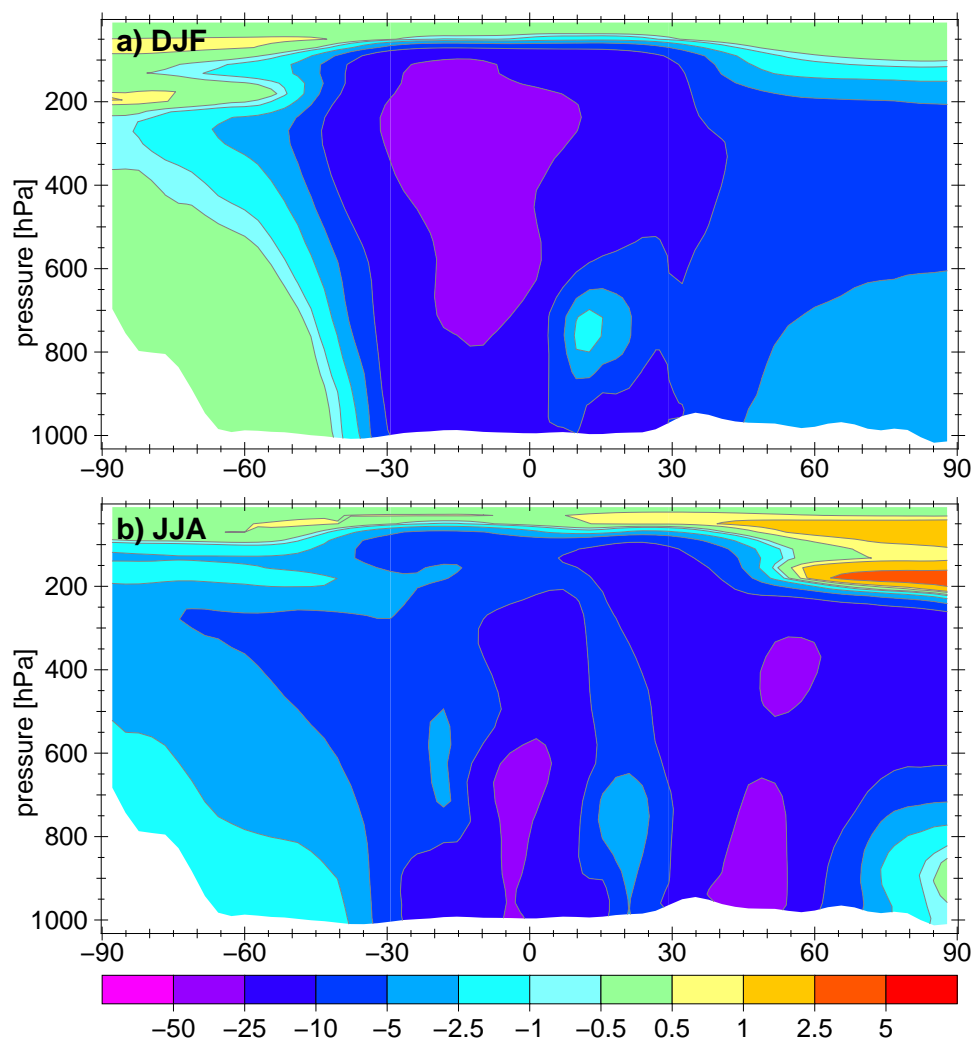


Figure A.7: Absolute difference (NOBIONO - BASE) of zonal mean mixing ratio of PAN in  $\frac{pmol}{mol}$  averaged for a) December, January, February and b) June, July and August

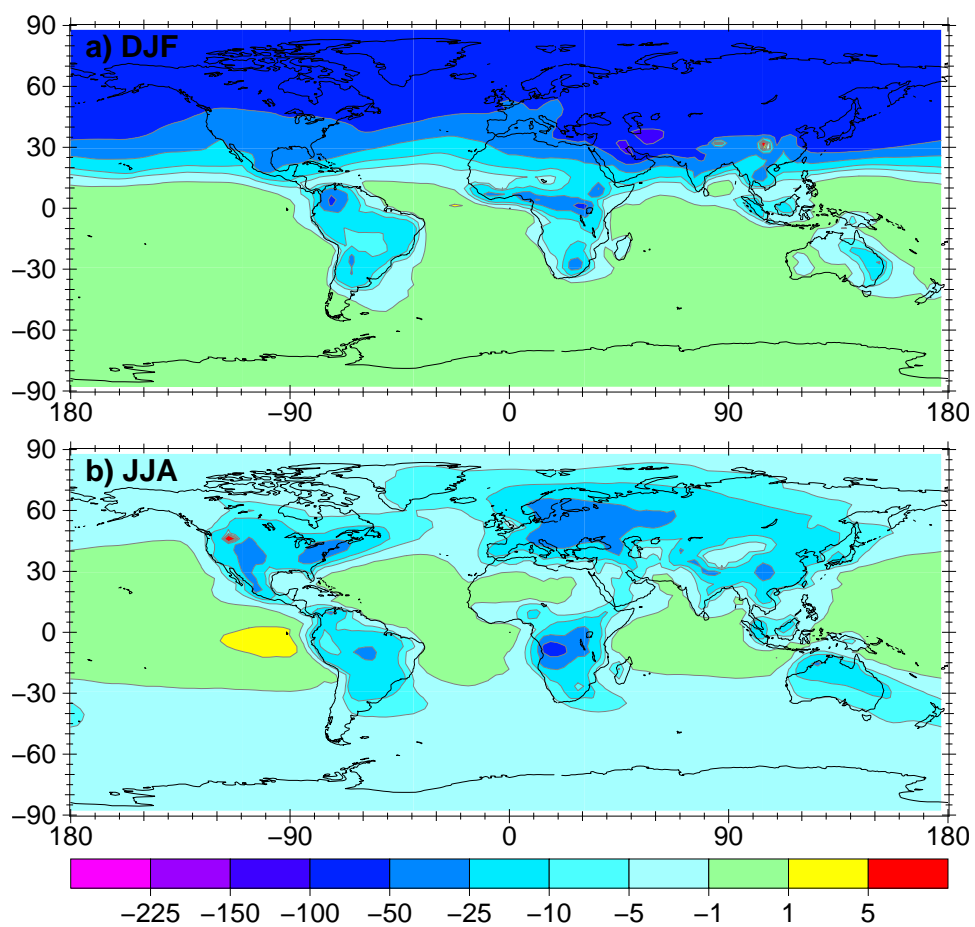


Figure A.8: Absolute difference (REDOTHER – BASE) of the lower tropospheric column mixing ratio of PAN in  $\frac{\text{pmol}}{\text{mol}}$  averaged for a) December, January, February and b) June, July and August



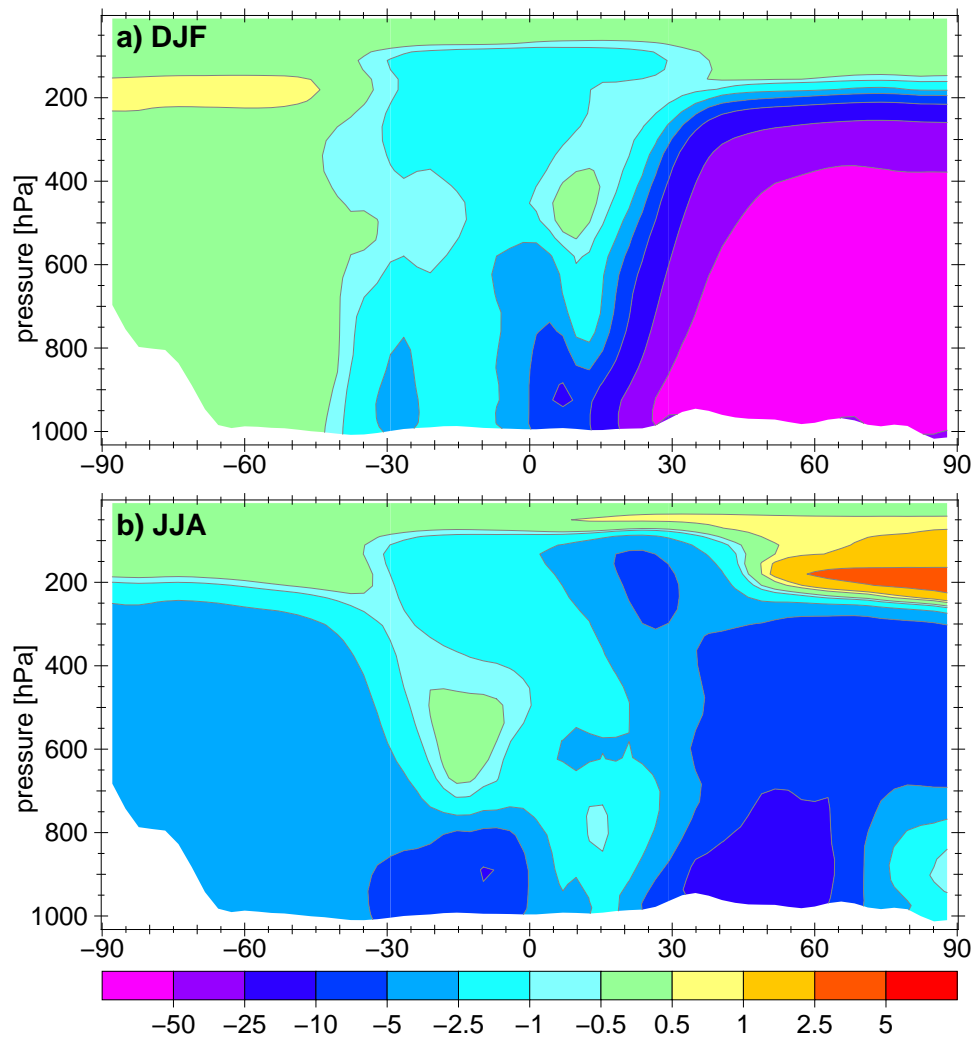


Figure A.9: Absolute difference (REDOTHER - BASE) of zonal mean mixing ratio of PAN in  $\frac{pmol}{mol}$  averaged for a) December, January, February and b) June, July and August

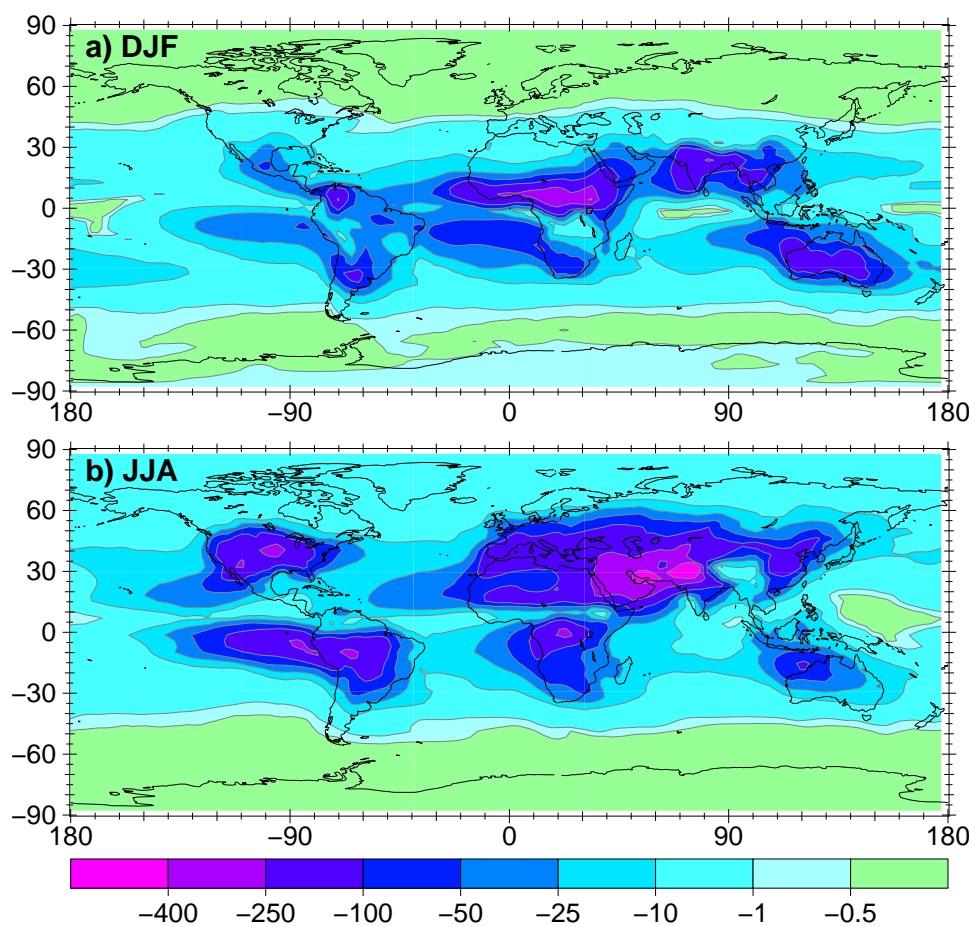


Figure A.10: Absolute difference (NOBIONO – BASE) of the lower tropospheric column mixing ratio of HNO<sub>3</sub> in  $\frac{\text{pmol}}{\text{mol}}$  averaged for a) December, January, February and b) June, July and August

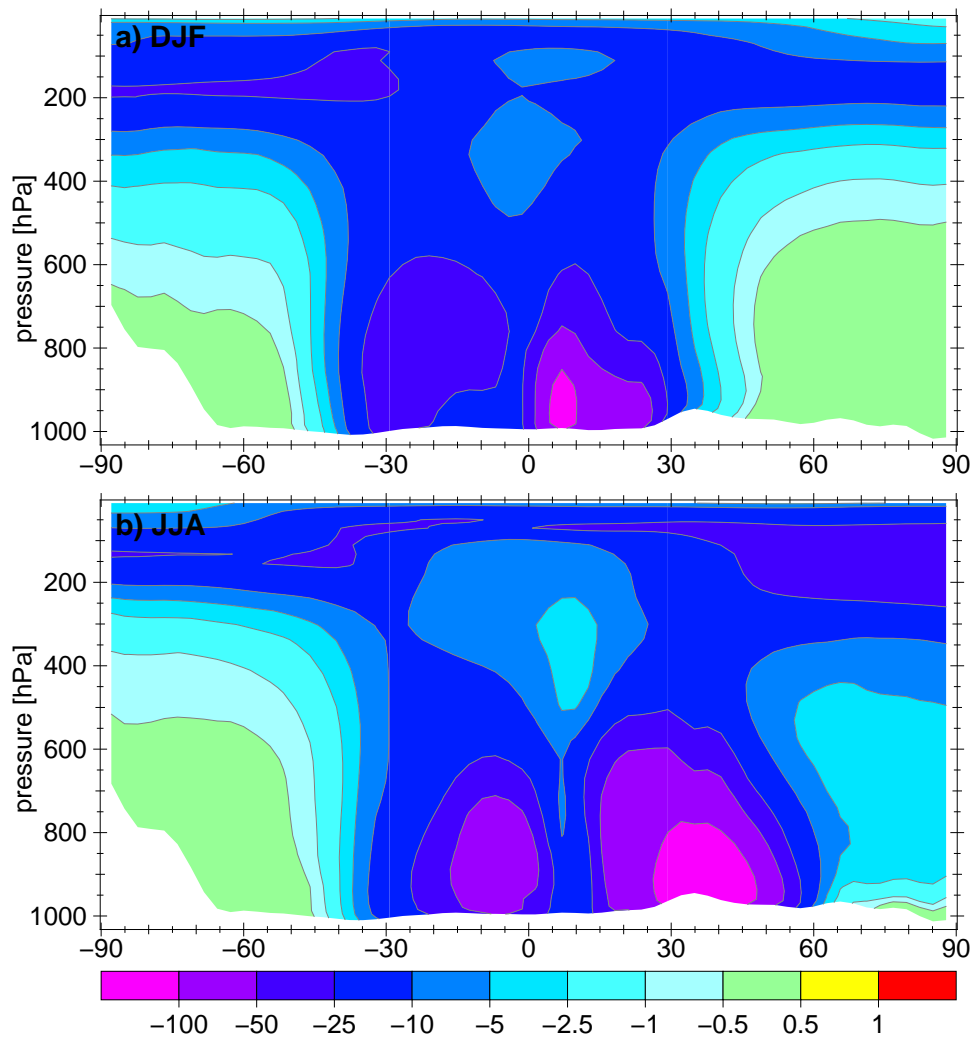


Figure A.11: Absolute difference (NOBIONO – BASE) of zonal mean mixing ratio of HNO<sub>3</sub> in  $\frac{pmol}{mol}$  averaged for a) December, January, February and b) June, July and August

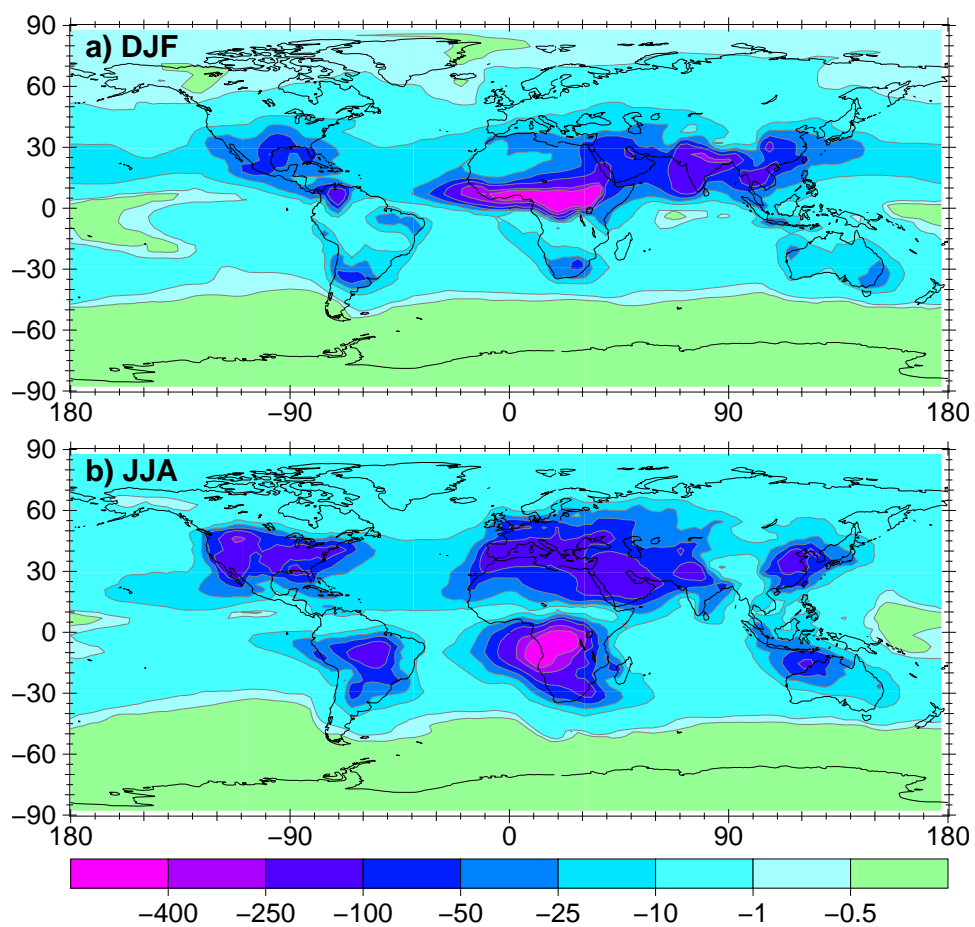


Figure A.12: Absolute difference (REDOTHER – BASE) of the lower tropospheric column mixing ratio of HNO<sub>3</sub> in  $\frac{\text{pmol}}{\text{mol}}$  averaged for a) December, January, February and b) June, July and August

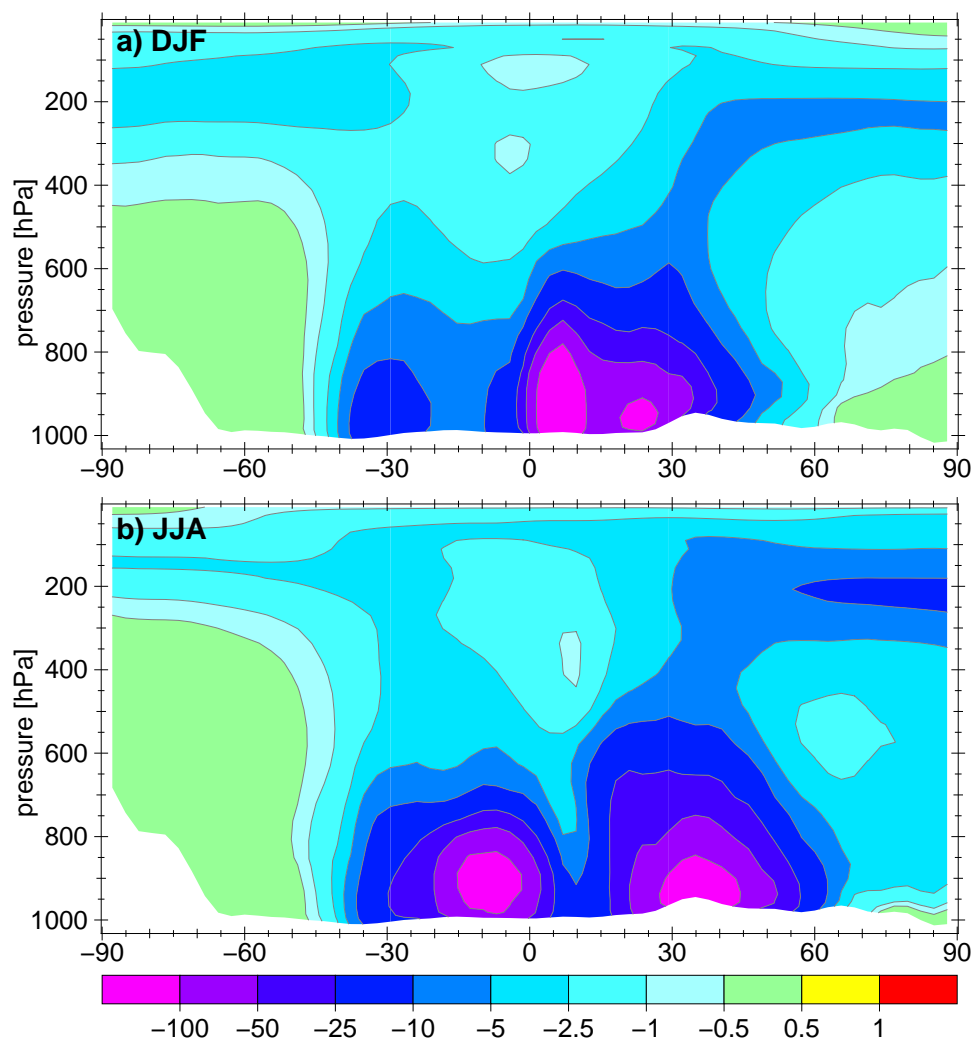


Figure A.13: Absolute difference (REDOTHER – BASE) of zonal mean mixing ratio of HNO<sub>3</sub> in  $\frac{\text{pmol}}{\text{mol}}$  averaged for a) December, January, February and b) June, July and August

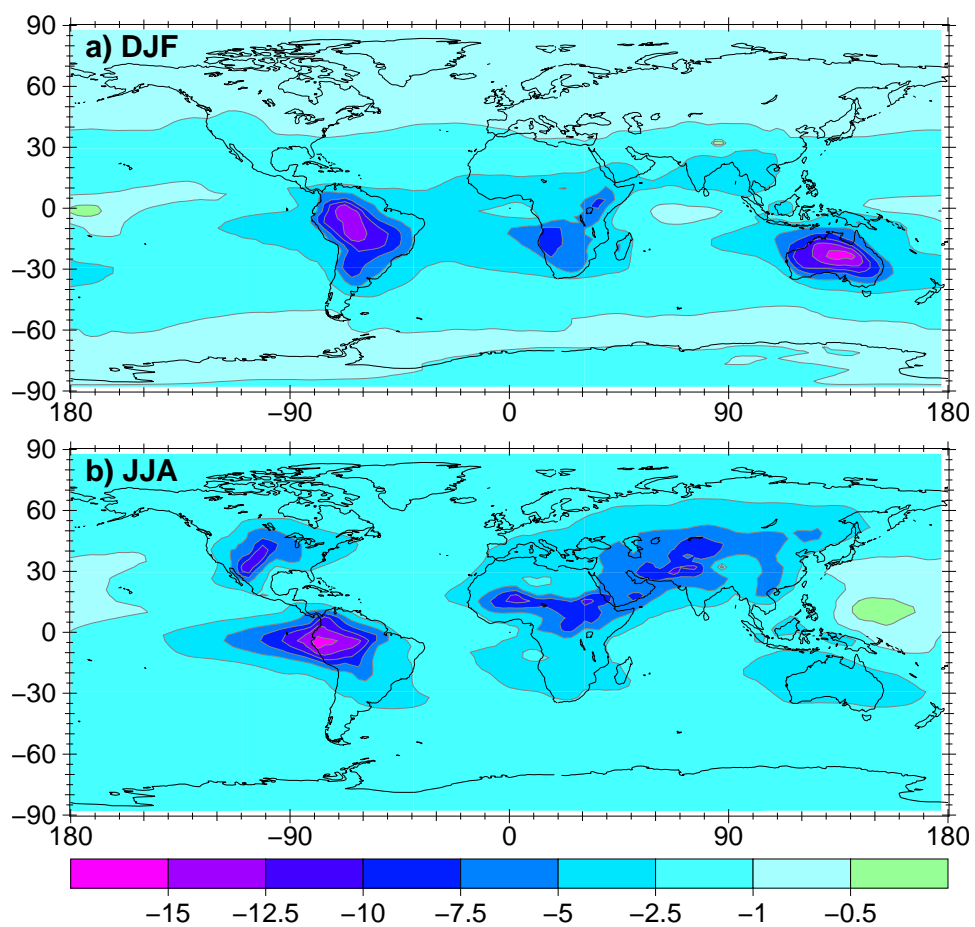


Figure A.14: Absolute difference (NOBIONO – BASE) of the lower tropospheric column mixing ratio of O<sub>3</sub> in  $\frac{\text{nmol}}{\text{mol}}$  averaged for a) December, January, February and b) June, July and August

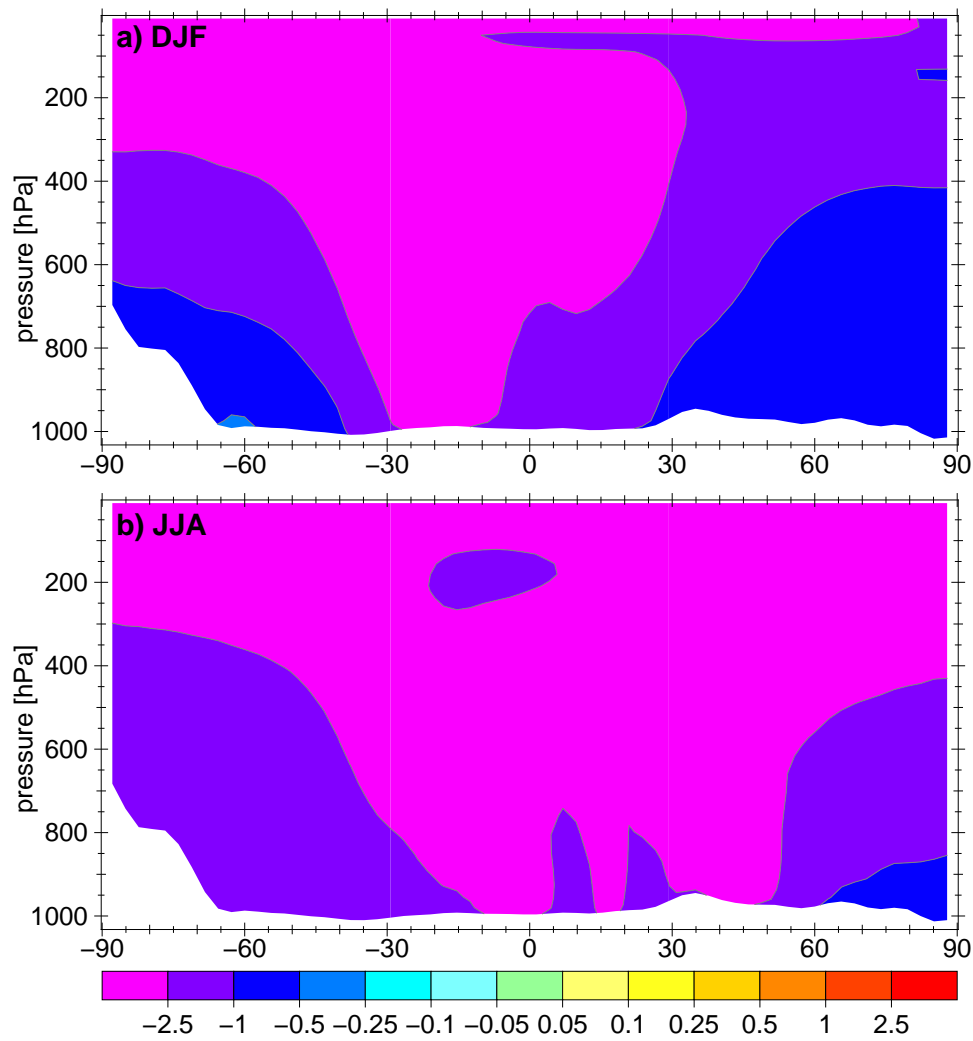


Figure A.15: Absolute difference (NOBIONO – BASE) of zonal mean mixing ratio of O<sub>3</sub> in  $\frac{\text{nmol}}{\text{mol}}$  averaged for a) December, January, February and b) June, July and August

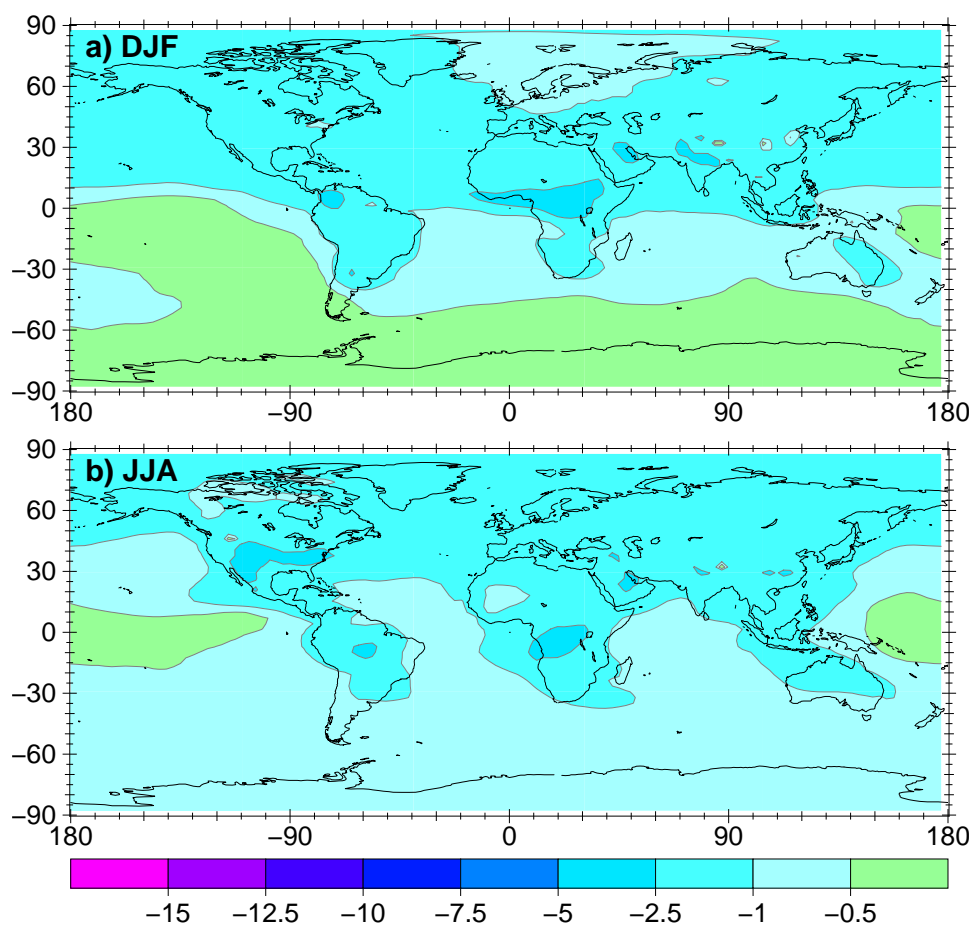


Figure A.16: Absolute difference (REDOTHER – BASE) of the lower tropospheric column mixing ratio of O<sub>3</sub> in  $\frac{\text{nmol}}{\text{mol}}$  averaged for a) December, January, February and b) June, July and August



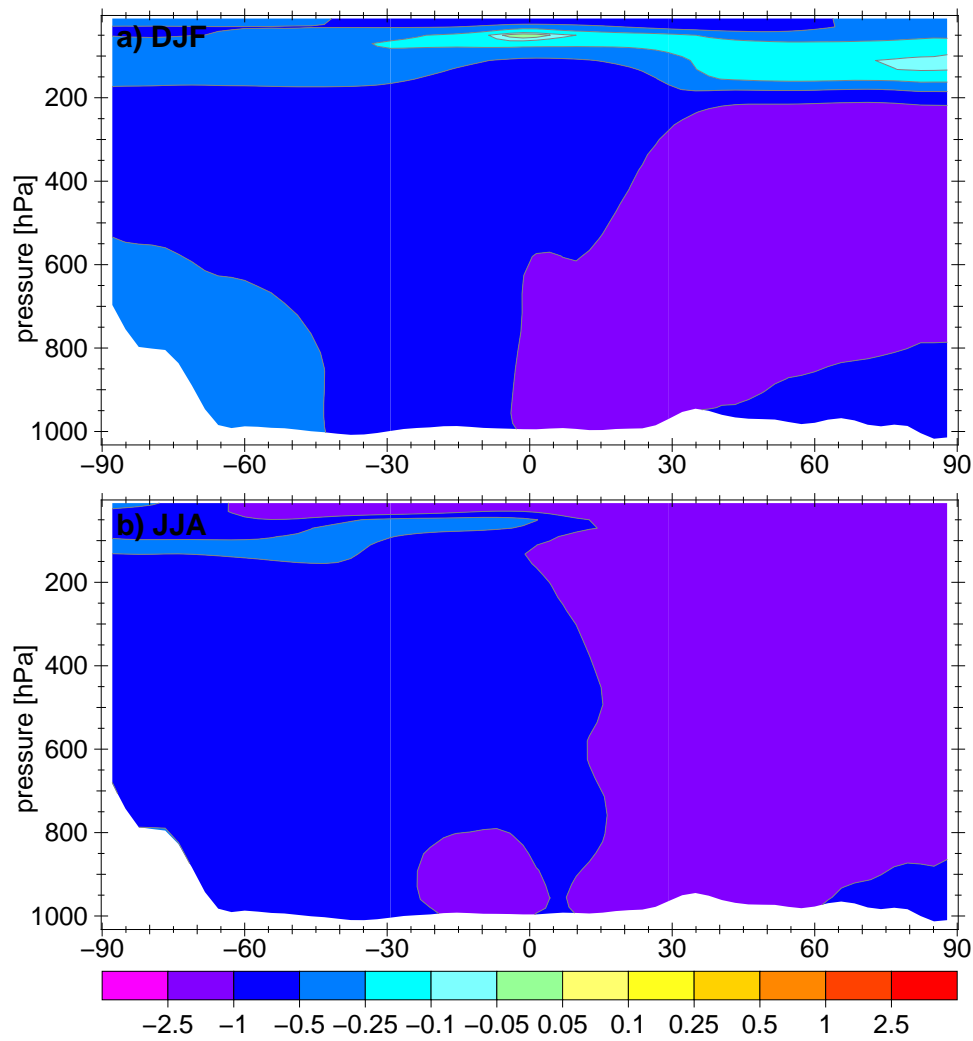


Figure A.17: Absolute difference (REDOTHER - BASE) of zonal mean mixing ratio of O<sub>3</sub> in  $\frac{\text{nmol}}{\text{mol}}$  averaged for a) December, January, February and b) June, July and August

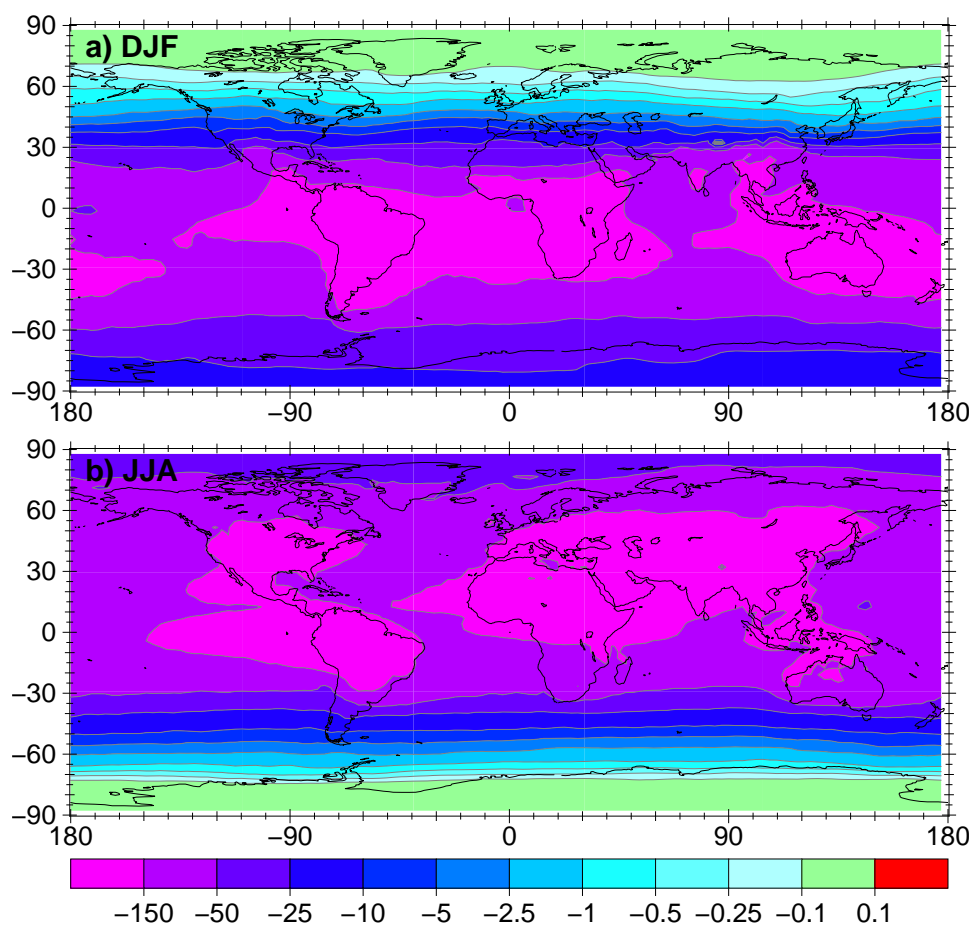


Figure A.18: Absolute difference (NOBIONO – BASE) of the lower tropospheric column mixing ratio of OH in  $10^3 \frac{\text{molec}}{\text{cm}^3}$  averaged for a) December, January, February and b) June, July and August

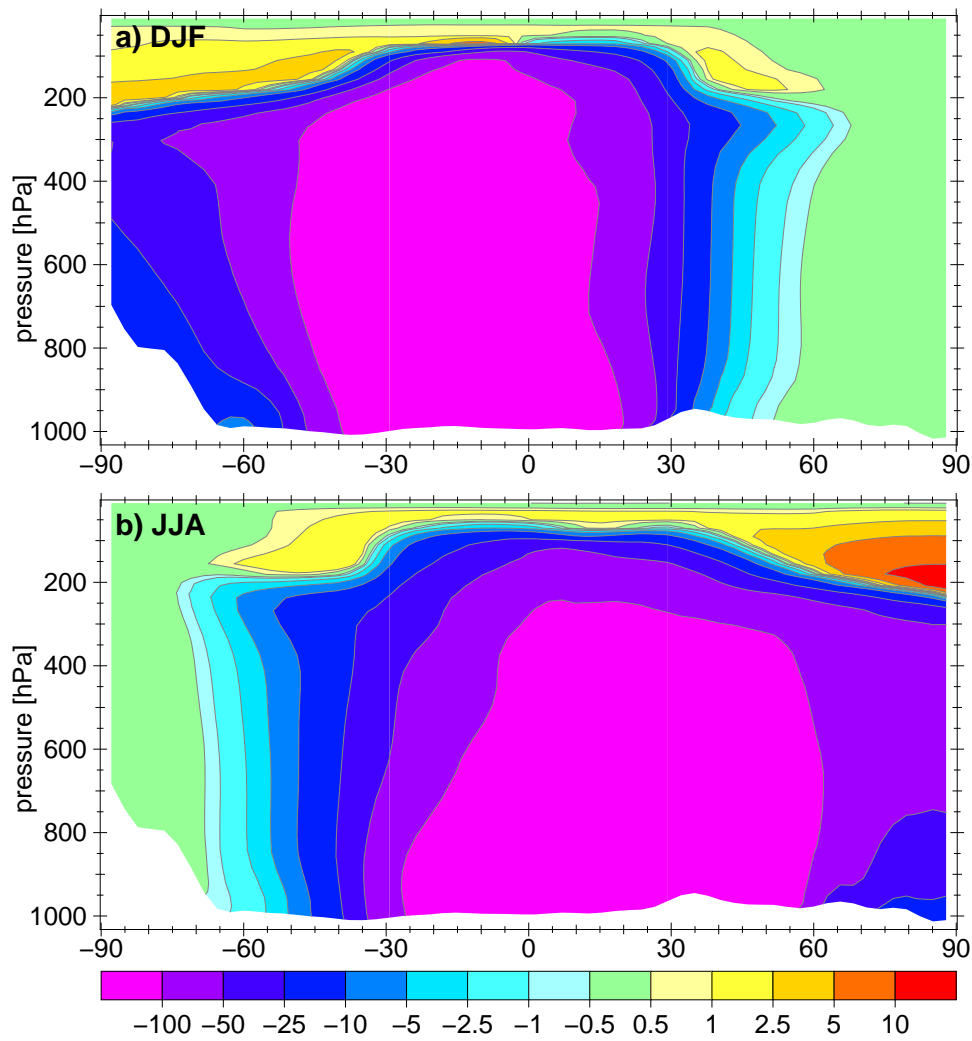


Figure A.19: Absolute difference (NOBIONO – BASE) of zonal mean mixing ratio of OH in  $10^3 \frac{\text{molec}}{\text{cm}^3}$  averaged for a) December, January, February and b) June, July and August

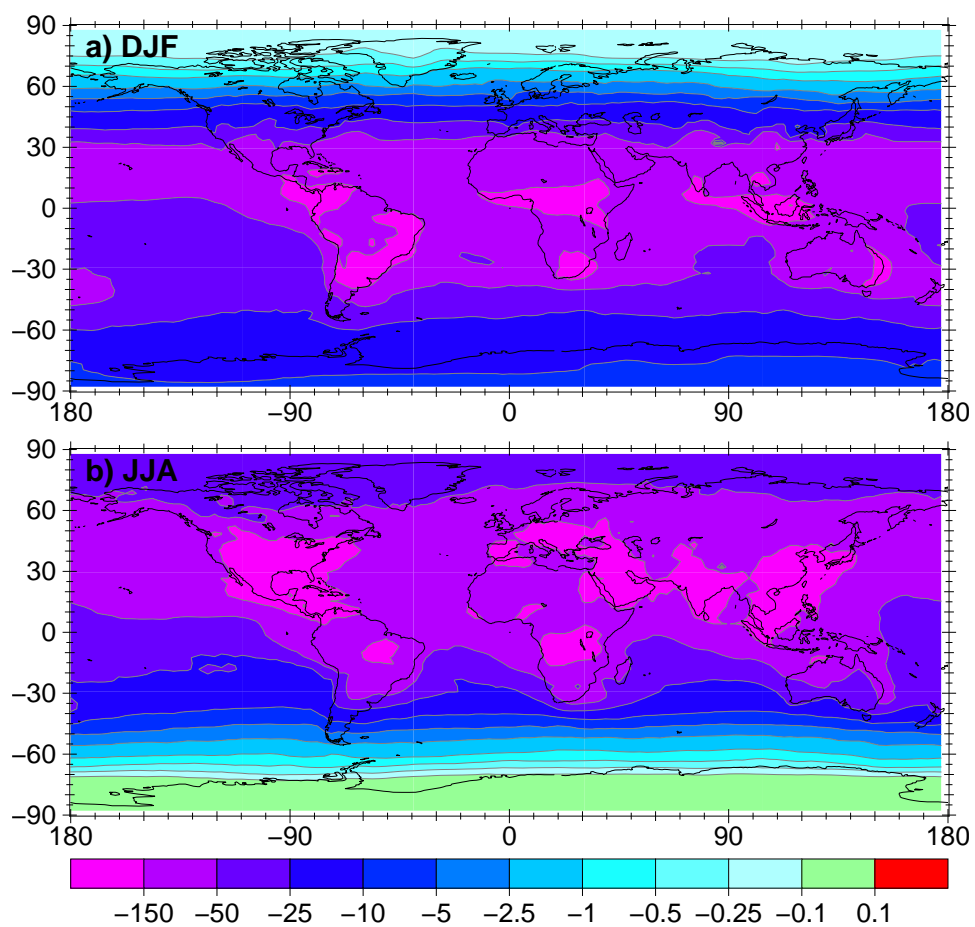


Figure A.20: Absolute difference (REDOTHER – BASE) of the lower tropospheric column mixing ratio of OH in  $10^3 \frac{\text{molec}}{\text{cm}^3}$  averaged for a) December, January, February and b) June, July and August

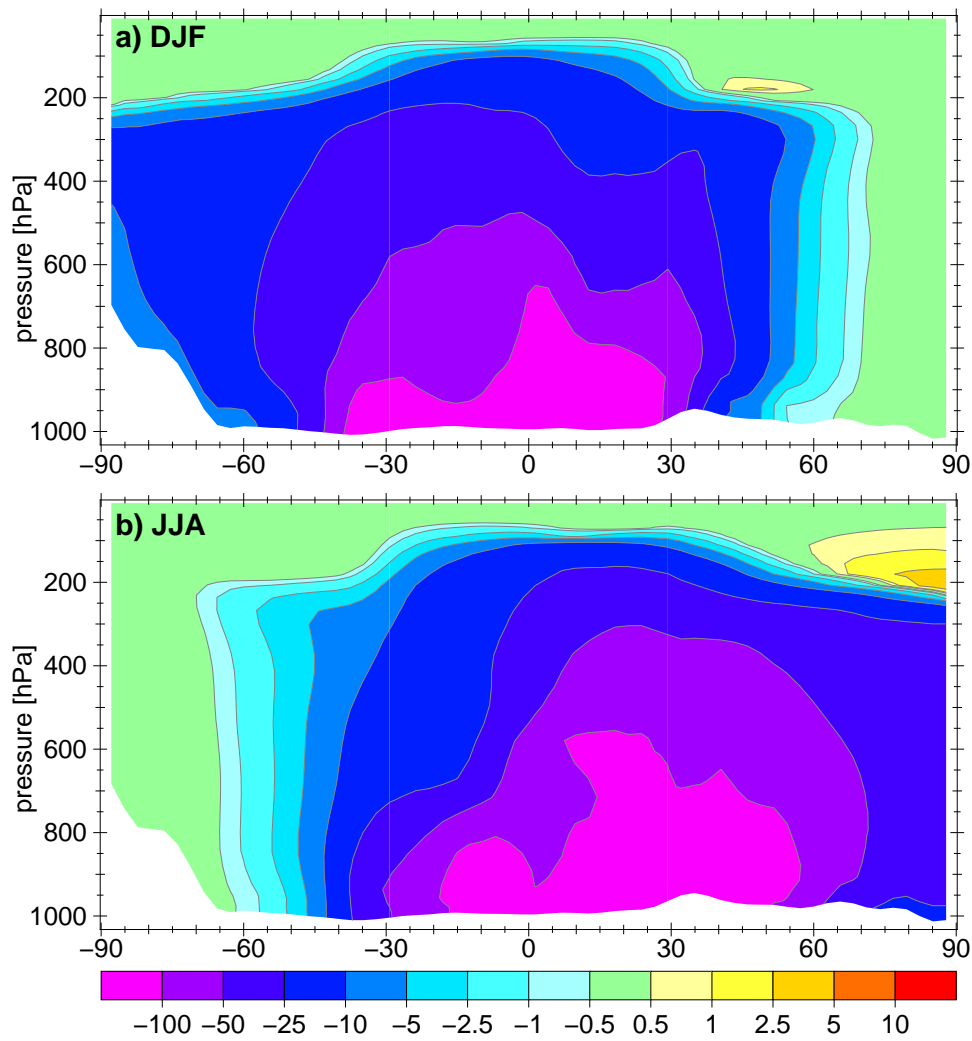


Figure A.21: Absolute difference (REDOTHER – BASE) of zonal mean mixing ratio of OH in  $10^3 \frac{\text{molec}}{\text{cm}^3}$  averaged for a) December, January, February and b) June, July and August

**B Supplementary material for chapter 3**

Table B.1: Adopted wet and dry emission factors of the soil biogenic NO emission algorithm based on the *Yienger and Levy (1995)* algorithm for different duration classes of the measurement (< 15, < 30, < 60, < 90, < 180, < 365 days). The number of simulated points and measured points (in brackets) is given below the emission factors. If no additional measurements were performed in the next class, we left the field empty.

LC	= 1	< 15	< 30	< 60	< 90	< 180	< 365
5			$0.07^{+0.03}_{-0.02}$ $0.54^{+0.20}_{-0.15}$ [11(1)]	$0.04^{+0.04}_{-0.02}$ $0.28^{+0.31}_{-0.15}$ [22(2)]			
6			$0.04^{+0.10}_{-0.03}$ $0.29^{+0.71}_{-0.20}$ [66(6)]	$0.04^{+0.12}_{-0.03}$ $0.32^{+0.87}_{-0.23}$ [198(18)]		$0.05^{+0.13}_{-0.04}$ $0.38^{+0.97}_{-0.28}$ [209(19)]	$0.09^{+0.31}_{-0.07}$ $0.65^{+2.24}_{-0.50}$ [220(20)]
8				$0.01^{+0.00}_{-0.00}$ $0.05^{+0.01}_{-0.01}$ [11(1)]			
10		$0.17^{+0.43}_{-0.12}$ $1.22^{+3.18}_{-0.88}$ [22(2)]		$0.83^{+2.33}_{-0.61}$ $6.09^{+17.26}_{-4.50}$ [55(5)]		$0.88^{+1.67}_{-0.58}$ $6.44^{+12.23}_{-4.22}$ [231(21)]	$0.84^{+1.43}_{-0.53}$ $6.17^{+10.42}_{-3.88}$ [242(22)]
11		$0.45^{+1.72}_{-0.36}$ $3.29^{+12.69}_{-2.61}$ [110(10)]	$0.16^{+2.17}_{-0.15}$ $1.21^{+15.98}_{-1.12}$ [220(20)]	$0.21^{+2.35}_{-0.19}$ $1.55^{+17.28}_{-1.42}$ [275(25)]	$0.24^{+1.71}_{-0.21}$ $1.76^{+12.56}_{-1.54}$ [308(28)]		
12		$0.27^{+1.19}_{-0.22}$ $1.97^{+8.75}_{-1.61}$ [187(17)]	$0.23^{+1.28}_{-0.19}$ $1.66^{+9.40}_{-1.41}$ [506(46)]	$0.15^{+0.93}_{-0.13}$ $1.11^{+6.78}_{-0.96}$ [682(62)]	$0.20^{+1.32}_{-0.17}$ $1.47^{+9.63}_{-1.28}$ [715(65)]	$0.55^{+5.67}_{-0.50}$ $4.00^{+41.41}_{-3.64}$ [803(73)]	$0.39^{+2.00}_{-0.33}$ $2.86^{+14.61}_{-2.39}$ [1019(94)]
13		$1.00^{+3.31}_{-0.77}$ $8.51^{+28.03}_{-6.53}$ [44(4)]	$0.63^{+1.05}_{-0.39}$ $5.34^{+8.87}_{-3.34}$ [55(5)]	$0.67^{+0.75}_{-0.35}$ $5.68^{+6.32}_{-2.99}$ [77(7)]	$0.35^{+0.58}_{-0.22}$ $2.97^{+4.88}_{-1.84}$ [88(8)]		$0.62^{+0.57}_{-0.30}$ $5.28^{+4.82}_{-2.52}$ [99(9)]
14		$0.03^{+0.23}_{-0.03}$ $0.25^{+1.68}_{-0.22}$ [44(4)]					
16			$0.53^{+1.32}_{-0.38}$ $3.53^{+8.78}_{-2.52}$ [55(5)]	$0.57^{+1.15}_{-0.38}$ $3.79^{+7.68}_{-2.54}$ [66(6)]	$0.56^{+0.88}_{-0.34}$ $3.71^{+5.88}_{-2.27}$ [77(7)]	$0.95^{+2.10}_{-0.65}$ $6.34^{+13.98}_{-4.36}$ [88(8)]	$0.34^{+0.85}_{-0.24}$ $2.23^{+5.65}_{-1.60}$ [198(19)]
18		$1.21^{+1.73}_{-0.71}$ $8.80^{+12.61}_{-5.18}$ [198(18)]	$1.17^{+1.66}_{-0.69}$ $8.56^{+12.17}_{-5.03}$ [319(29)]	$1.81^{+4.49}_{-1.29}$ $13.21^{+32.76}_{-9.42}$ [550(50)]	$2.12^{+6.05}_{-1.57}$ $15.46^{+44.14}_{-11.45}$ [583(53)]		$0.90^{+4.82}_{-0.76}$ $6.57^{+35.19}_{-5.53}$ [716(66)]
19		$0.17^{+0.16}_{-0.08}$ $1.21^{+1.18}_{-0.60}$ [66(6)]	$0.08^{+0.14}_{-0.05}$ $0.62^{+1.03}_{-0.39}$ [77(7)]				
20		$0.53^{+1.05}_{-0.35}$ $2.76^{+7.09}_{-1.99}$ [99(9)]	$0.73^{+0.65}_{-0.34}$ $2.66^{+2.59}_{-1.31}$ [132(12)]	$1.63^{+3.30}_{-1.09}$ $6.62^{+19.10}_{-4.91}$ [176(16)]	$2.44^{+4.49}_{-1.58}$ $12.31^{+35.81}_{-9.16}$ [198(18)]	$1.29^{+2.40}_{-0.84}$ $7.24^{+13.58}_{-4.72}$ [253(23)]	$0.64^{+1.41}_{-0.44}$ $3.50^{+6.68}_{-2.30}$ [561(52)]
21		$0.39^{+3.47}_{-0.35}$ $2.85^{+25.36}_{-2.56}$ [385(35)]	$0.26^{+3.37}_{-0.24}$ $1.87^{+24.60}_{-1.74}$ [616(56)]	$0.49^{+3.17}_{-0.42}$ $3.56^{+23.11}_{-3.09}$ [1133(103)]	$0.67^{+3.06}_{-0.55}$ $4.91^{+22.33}_{-4.03}$ [1397(127)]	$0.58^{+2.75}_{-0.48}$ $4.21^{+20.05}_{-3.48}$ [1814(165)]	$0.53^{+2.24}_{-0.43}$ $3.89^{+16.34}_{-3.14}$ [2158(199)]

Table B.2: Adopted wet and dry emission factors of the soil biogenic NO emission algorithm based on the *Yienger and Levy (1995)* algorithm for the regions of Fig. 1 with the number of simulated points and measured points (in brackets).

LC	EUR		NAM		SAM		ASA		AFR	
	wet	dry	wet	dry	wet	dry	wet	dry	wet	dry
5							0.06 <sup>+0.02</sup> <sub>-0.02</sub>	0.43 <sup>+0.15</sup> <sub>-0.11</sub>		
6			0.05 <sup>+0.13</sup> <sub>-0.04</sub>	0.38 <sup>+0.97</sup> <sub>-0.28</sub>			0.58 <sup>+0.11</sup> <sub>-0.10</sub>	4.27 <sup>+0.84</sup> <sub>-0.70</sub>		
8			0.01 <sup>+0.00</sup> <sub>-0.00</sub>	0.05 <sup>+0.01</sup> <sub>-0.01</sub>						
10	1.28 <sup>+1.43</sup> <sub>-0.68</sub>	9.47 <sup>+10.60</sup> <sub>-5.00</sub>	0.62 <sup>+1.14</sup> <sub>-0.40</sub>	4.58 <sup>+8.41</sup> <sub>-2.96</sub>						
11					0.15 <sup>+2.31</sup> <sub>-0.14</sub>	1.10 <sup>+16.99</sup> <sub>-1.04</sub>			0.28 <sup>+1.36</sup> <sub>-0.23</sub>	2.06 <sup>+10.04</sup> <sub>-1.71</sub>
12	2.52 <sup>+15.40</sup> <sub>-2.17</sub>	18.52 <sup>+113.35</sup> <sub>-15.92</sub>	0.37 <sup>+1.15</sup> <sub>-0.28</sub>	2.67 <sup>+8.41</sup> <sub>-2.03</sub>	0.32 <sup>+0.64</sup> <sub>-0.21</sub>	2.35 <sup>+4.70</sup> <sub>-1.57</sub>	3.69 <sup>+3.03</sup> <sub>-1.66</sub>	27.17 <sup>+22.29</sup> <sub>-12.24</sub>	0.46 <sup>+0.21</sup> <sub>-0.15</sub>	3.42 <sup>+1.56</sup> <sub>-1.07</sub>
13					0.79 <sup>+0.21</sup> <sub>-0.17</sub>	6.66 <sup>+1.78</sup> <sub>-1.40</sub>			0.30 <sup>+0.47</sup> <sub>-0.18</sub>	2.58 <sup>+3.97</sup> <sub>-1.56</sub>
14	0.20 <sup>+0.56</sup> <sub>-0.15</sub>	1.50 <sup>+4.08</sup> <sub>-1.09</sub>	0.00 <sup>+0.00</sup> <sub>-0.00</sub>	0.01 <sup>+0.00</sup> <sub>-0.00</sub>			0.07 <sup>+0.03</sup> <sub>-0.02</sub>	0.51 <sup>+0.24</sup> <sub>-0.16</sub>		
16	0.35 <sup>+1.11</sup> <sub>-0.27</sub>	2.36 <sup>+7.37</sup> <sub>-1.79</sub>	0.61 <sup>+1.42</sup> <sub>-0.42</sub>	4.04 <sup>+9.45</sup> <sub>-2.83</sub>						
18	1.70 <sup>+7.68</sup> <sub>-1.39</sub>	12.44 <sup>+56.15</sup> <sub>-10.18</sub>								
19					0.08 <sup>+0.12</sup> <sub>-0.05</sub>	0.58 <sup>+0.91</sup> <sub>-0.36</sub>			0.39 <sup>+0.53</sup> <sub>-0.22</sub>	2.85 <sup>+3.87</sup> <sub>-1.64</sub>
20					0.46 <sup>+2.82</sup> <sub>-0.40</sub>	2.66 <sup>+13.80</sup> <sub>-2.23</sub>	0.35 <sup>+0.30</sup> <sub>-0.16</sub>	1.15 <sup>+1.00</sup> <sub>-0.54</sub>	0.74 <sup>+0.33</sup> <sub>-0.23</sub>	2.46 <sup>+1.09</sup> <sub>-0.75</sub>
21	0.22 <sup>+1.86</sup> <sub>-0.20</sub>	1.64 <sup>+13.60</sup> <sub>-1.46</sub>	0.33 <sup>+0.45</sup> <sub>-0.19</sub>	2.41 <sup>+3.31</sup> <sub>-1.40</sub>	0.28 <sup>+1.09</sup> <sub>-0.22</sub>	2.03 <sup>+7.98</sup> <sub>-1.62</sub>	0.81 <sup>+2.80</sup> <sub>-0.63</sub>	5.89 <sup>+20.41</sup> <sub>-4.57</sub>	1.28 <sup>+1.04</sup> <sub>-0.58</sub>	9.35 <sup>+7.62</sup> <sub>-4.20</sub>



Table B.3: Measured SNOx for selected landcovers, classified by region (in  $\text{ng m}^{-2} \text{s}^{-1}$ ).

ID	EUR	NAM	SAM	ASA	AFR
10	$4.40^{+5.38}_{-2.42}$	$3.62^{+7.14}_{-2.40}$			
11			$7.29^{+123.90}_{-6.88}$		$2.28^{+11.43}_{-1.90}$
12	$5.22^{+31.72}_{-4.48}$	$0.73^{+3.71}_{-0.61}$	$3.51^{+8.51}_{-2.48}$	$6.69^{+14.06}_{-4.54}$	$4.53^{+3.48}_{-1.97}$
13			$14.90^{+32.74}_{-10.24}$		$2.37^{+5.53}_{-1.66}$
16	$1.11^{+3.43}_{-0.84}$	$2.51^{+6.92}_{-1.84}$			
20			$2.49^{+11.26}_{-2.04}$	$1.36^{+1.92}_{-0.80}$	$2.02^{+1.79}_{-0.95}$
21	$2.47^{+29.07}_{-2.28}$	$6.06^{+19.45}_{-4.62}$	$2.55^{+13.55}_{-2.15}$	$5.88^{+21.14}_{-4.60}$	$15.21^{+19.40}_{-8.52}$

Table B.4: Mean measured (number of measurements in brackets) and simulated (LC and YL95/SL10) SNOx for each landcover type with measurements for the exactly corresponding yearly period and for unperturbed as well as anthropogenically altered conditions.

ID	N	measured	LC	YL95/SL10
5	31(3)	$0.52^{+0.44}_{-0.24}$	0	$0.57^{+0.16}_{-0.12}$
6	220(20)	$0.74^{+2.25}_{-0.56}$	0	$0.77^{+0.32}_{-0.23}$
8	11(1)	0.03	$0.23^{+0}_{-0.04}$	$0.05^{+0.01}_{-0.01}$
10	242(22)	$3.28^{+5.04}_{-1.99}$	$0.27^{+0.41}_{-0.13}$	$3.63^{+2.78}_{-1.57}$
11	308(28)	$2.27^{+19.77}_{-2.04}$	$4.84^{+42.16}_{-2.08}$	$2.07^{+1.53}_{-0.88}$
12	1069(99)	$4.18^{+22.86}_{-3.53}$	$2.75^{+15.03}_{-1.3}$	$2.8^{+2}_{-1.17}$
13	99(9)	$7.85^{+23.84}_{-5.9}$	$3.1^{+9.41}_{-0.73}$	$9.93^{+3.63}_{-2.66}$
14	44(4)	$0.31^{+2.36}_{-0.27}$	$0.3^{+2.34}_{-0.18}$	$0.48^{+0.49}_{-0.24}$
16	227(22)	$1.11^{+3.29}_{-0.83}$	$0.1^{+0.28}_{-0.06}$	$1.06^{+1.58}_{-0.64}$
18	748(70)	$6.3^{+25.72}_{-5.06}$	$0.1^{+0.42}_{-0.08}$	$4.75^{+12.63}_{-3.45}$
19	77(7)	$0.97^{+1.54}_{-0.59}$	$0.77^{+1.22}_{-0.22}$	$0.8^{+0.35}_{-0.24}$
20	581(54)	$1.75^{+6.71}_{-1.39}$	$5.78^{+22.11}_{-1.88}$	$0.95^{+0.67}_{-0.39}$
21	2242(208)	$4.8^{+26.63}_{-4.06}$	$10.9^{+60.52}_{-7.71}$	$7.7^{+11.12}_{-4.55}$
All	5899(547)	$3.32^{+17.91}_{-2.8}$	$2.25^{+11.7}_{-1.96}$	$3.16^{+7.11}_{-2.19}$

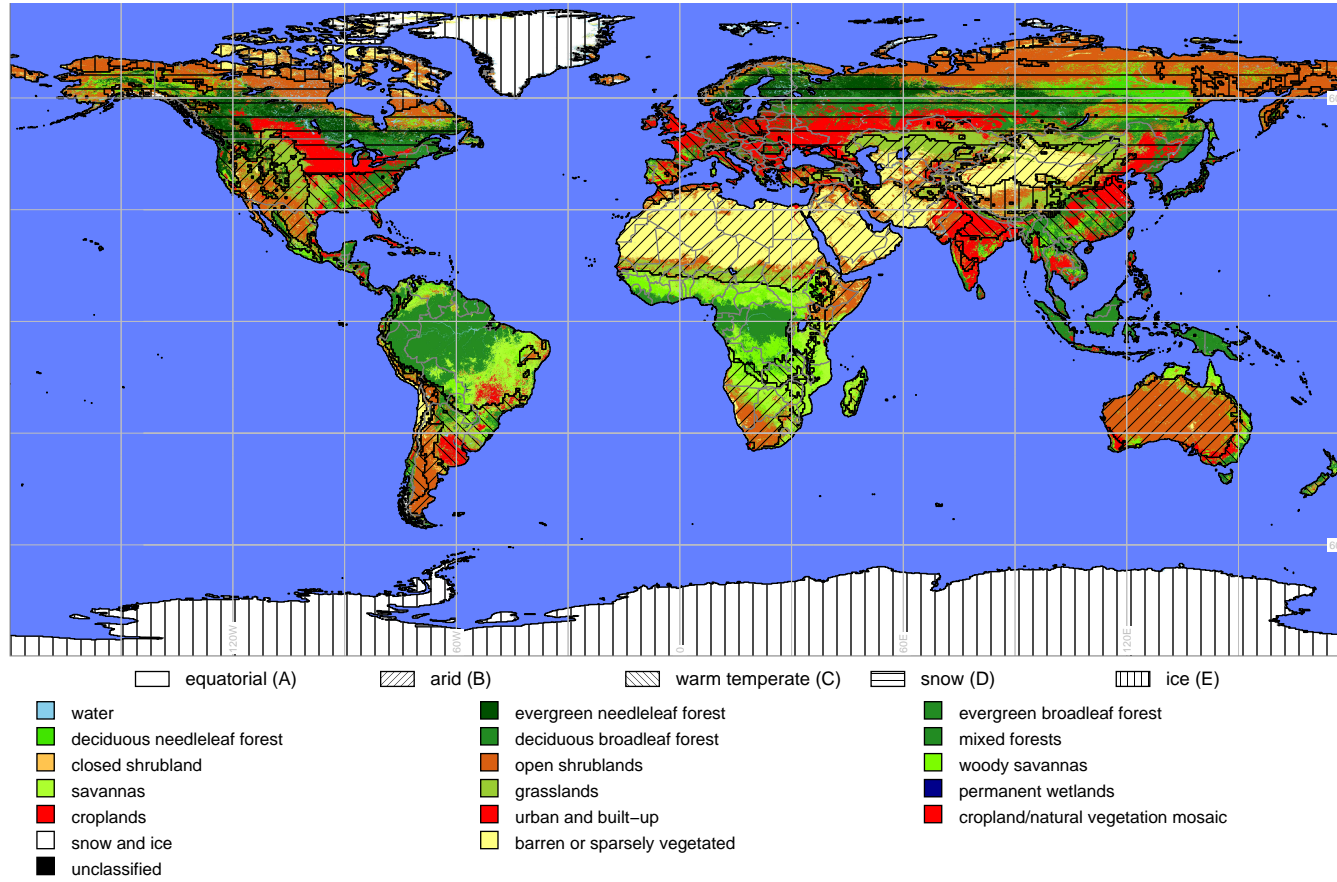


Figure B.1: MODIS landcover (colors) overlaid with the Koeppen main climate classes (hashes).

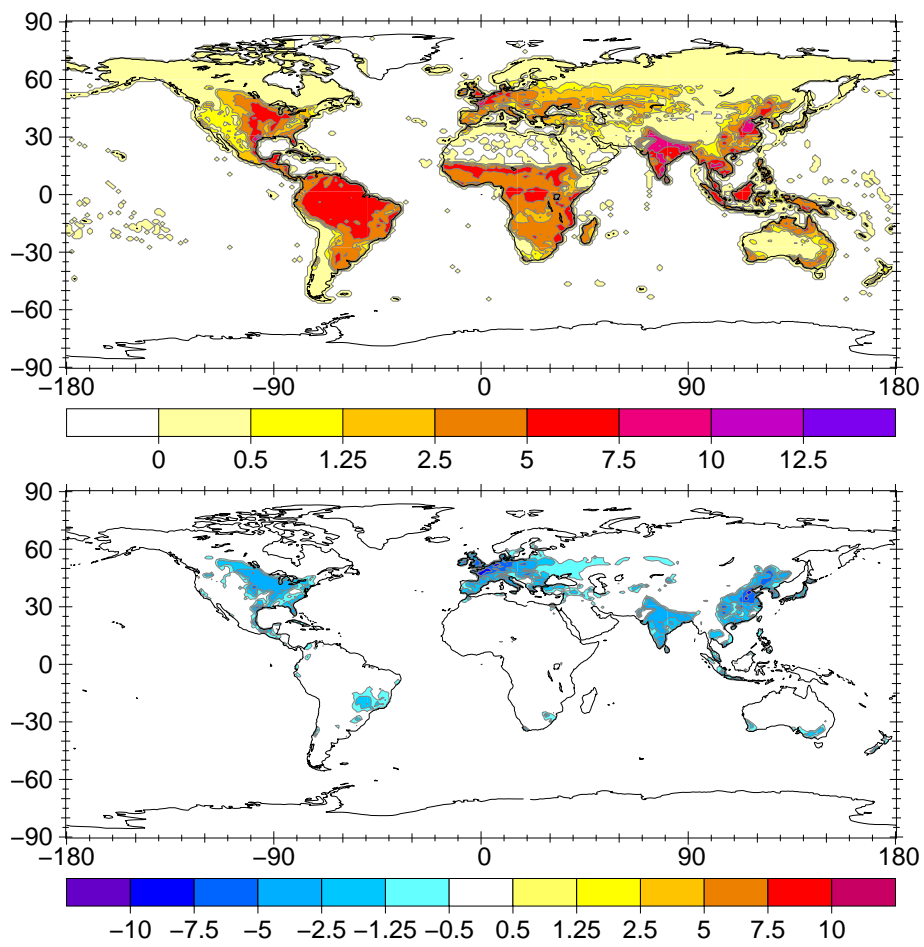


Figure B.2: Averaged SNO<sub>x</sub> flux in the whole simulation period (in  $\text{ng m}^{-2} \text{s}^{-1}$ ) for the LC+FIE simulation (upper panel) and the change compared to the LC simulation (lower panel).

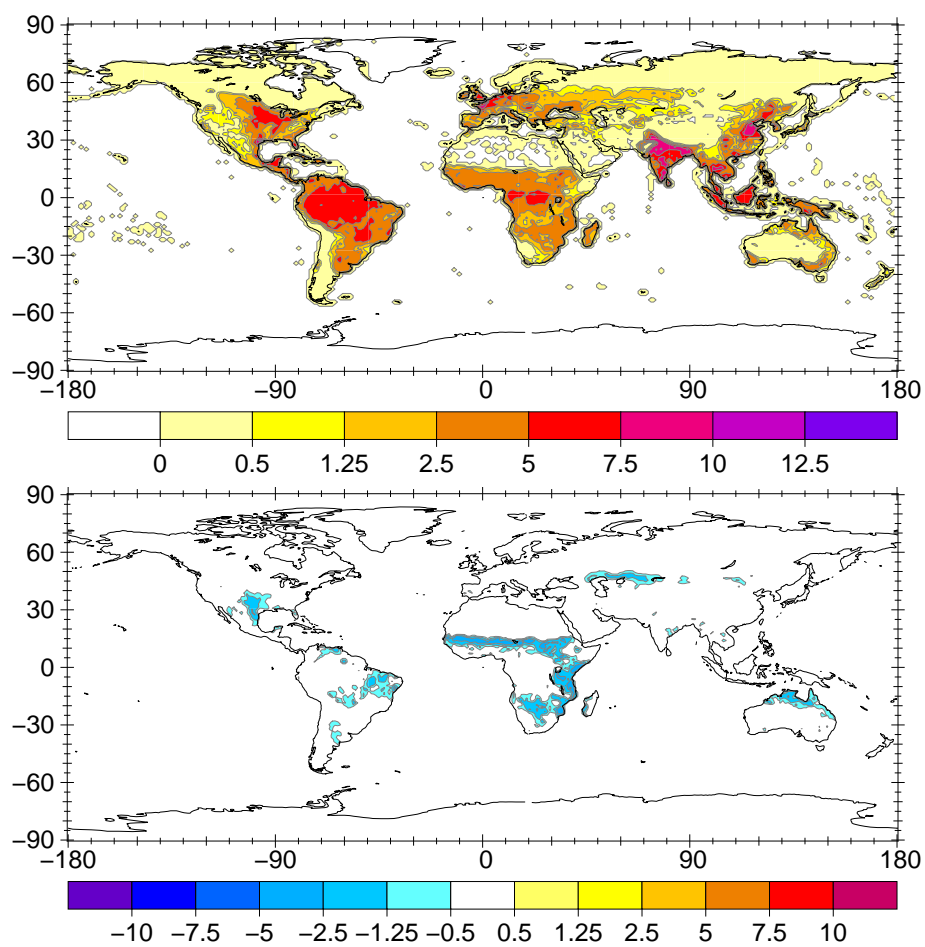


Figure B.3: Averaged SNOx flux in the whole simulation period (in  $\text{ng m}^{-2} \text{s}^{-1}$ ) for the LC+FIE+VSM simulation (upper panel) and the change compared to the LC+FIE simulation (lower panel).

## **C Supplementary material for chapter 4**

Table C.1: Allocation of PFTs from the ORCHIDEE model to the MODIS landcover classes

MODIS	ORCHIDEE
evergreen needleleaved forest	temperate needleleaved trees
evergreen broadleaved forest (A, B)	tropical broad-leaved evergreen trees
evergreen broadleaved forest (C, D, E)	temperate broad-leaved evergreen trees
deciduous needleleaved forest	boreal needleleaf summergreen trees
deciduous broadleaved forest (A, B)	tropical broad-leaved raingreen trees
deciduous broadleaved forest (C, D, E)	temperate broad-leaved summergreen trees
mixed forest	temperate broad-leaved summergreen trees
closed shrubland	temperate broad-leaved summergreen trees
open shrubland (A, B, C)	temperate broad-leaved evergreen trees
open shrubland (D, E)	boreal broad-leaved summergreen trees
savannah (A, B)	C4 grass natural
woody savannah	C4 grass natural
savannah (C, D, E)	C3 grass natural
grassland (A, B)	C4 grass natural
grassland (C, D, E)	C3 grass natural
cropland (A, B)	C4 grass agricultural
cropland (C, D, E)	C3 grass agricultural
barren	bare

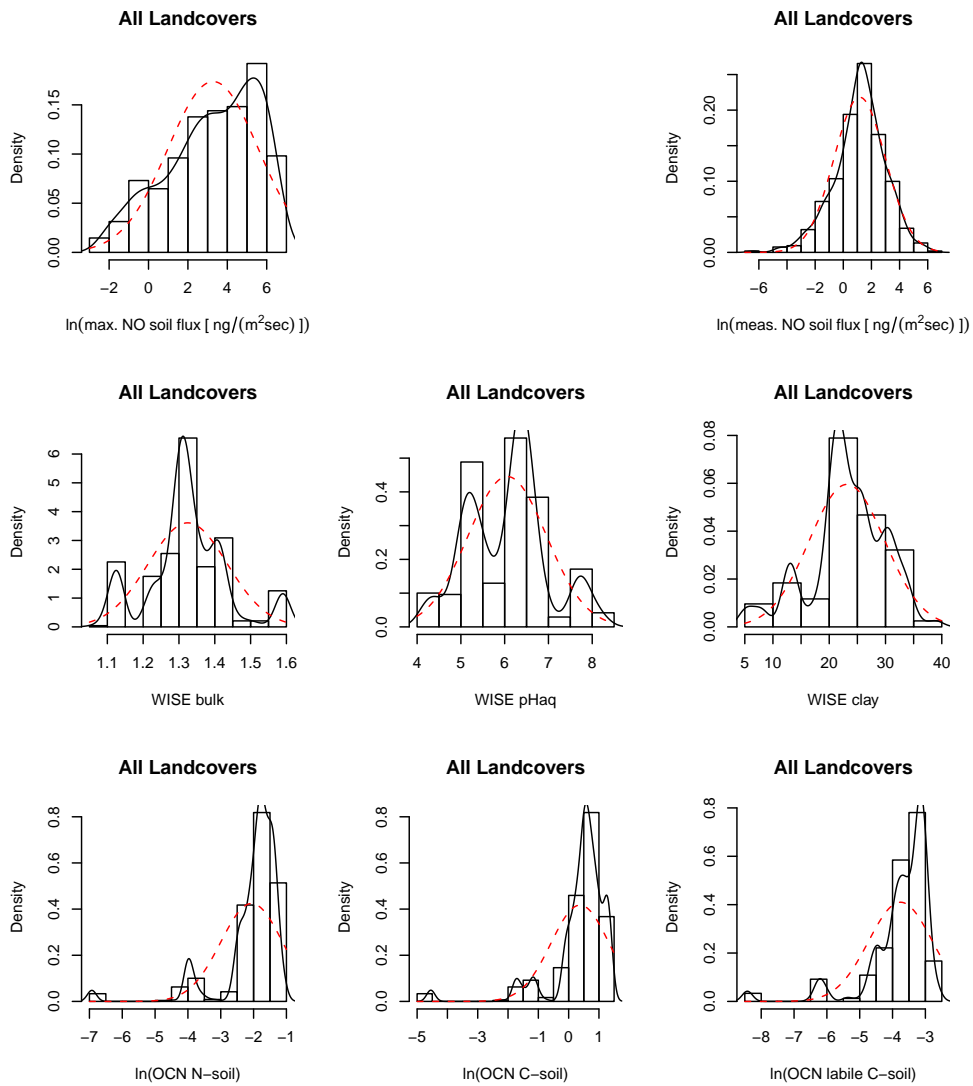


Figure C.1: Histograms of calculated NO emissions at optimum WFPS, measured NO emissions and the physical and chemical soil properties.

C Supplementary material for chapter 4

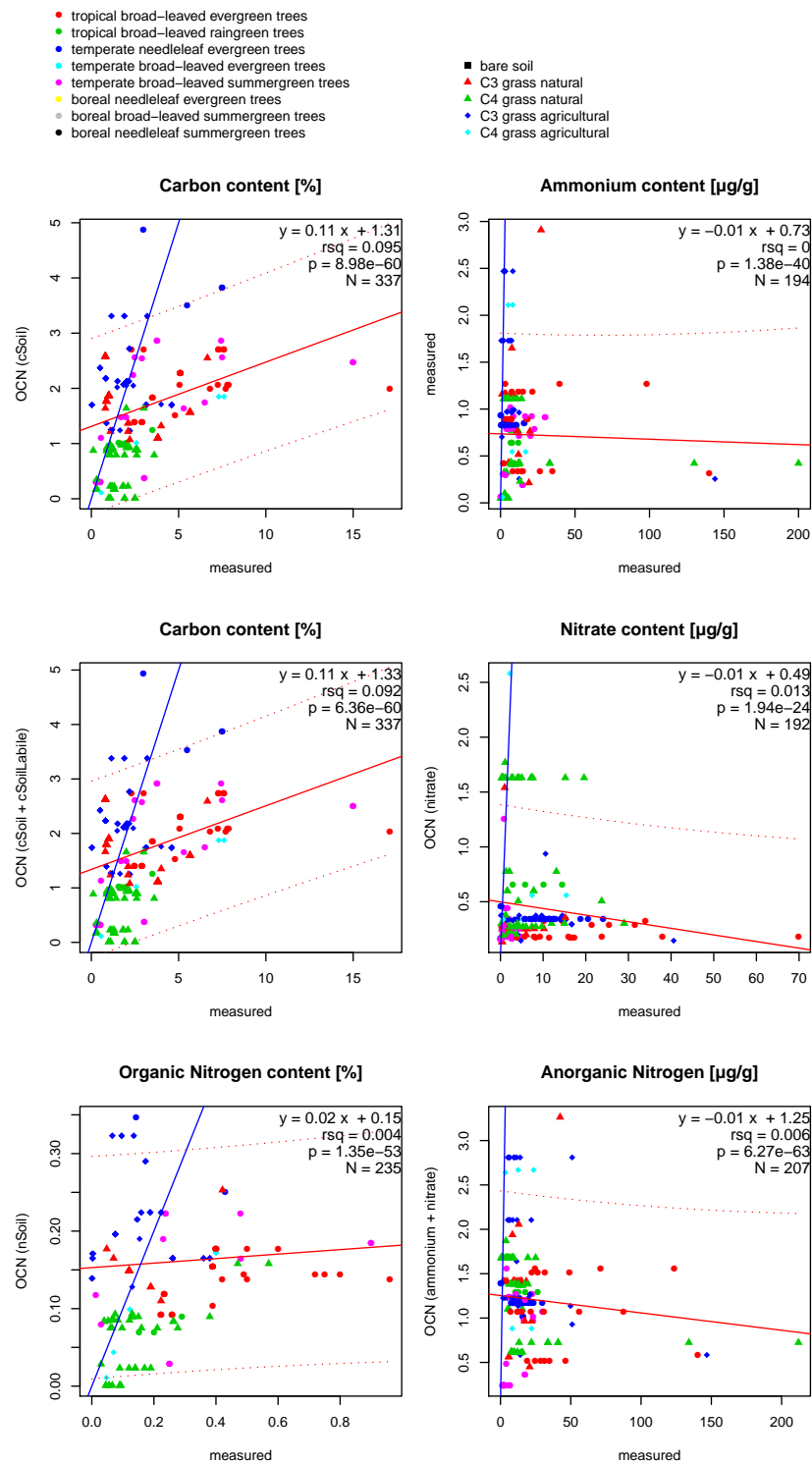


Figure C.2: Scatterplots/correlation of simulated (ORCHIDEE model) and measured chemical soil properties. All available data is included. Note the different scaling of x- and y-axis.  
 160



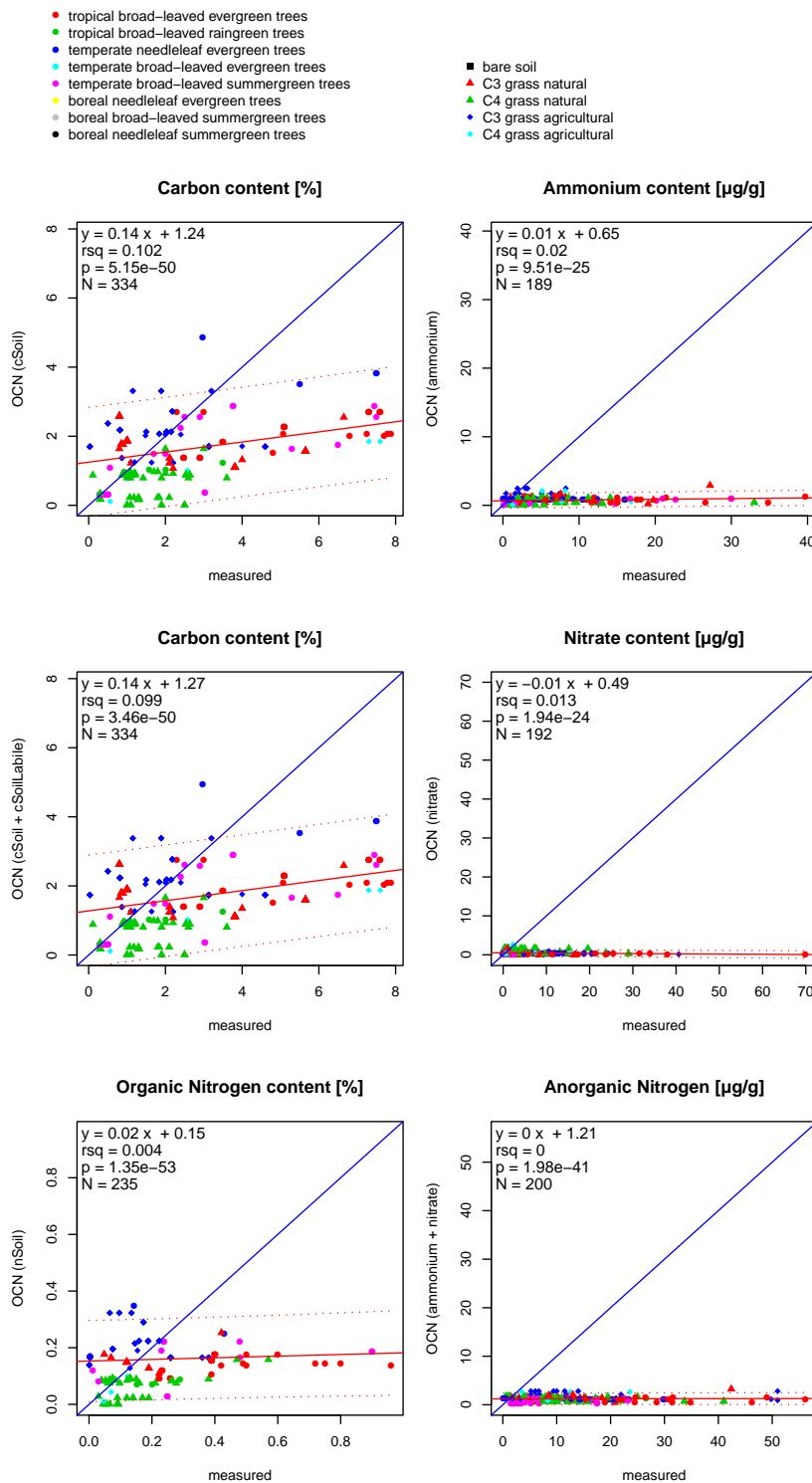


Figure C.3: Scatterplots/correlation of simulated (ORCHIDEE model) and measured chemical soil properties omitting extrem values from the measurement database.

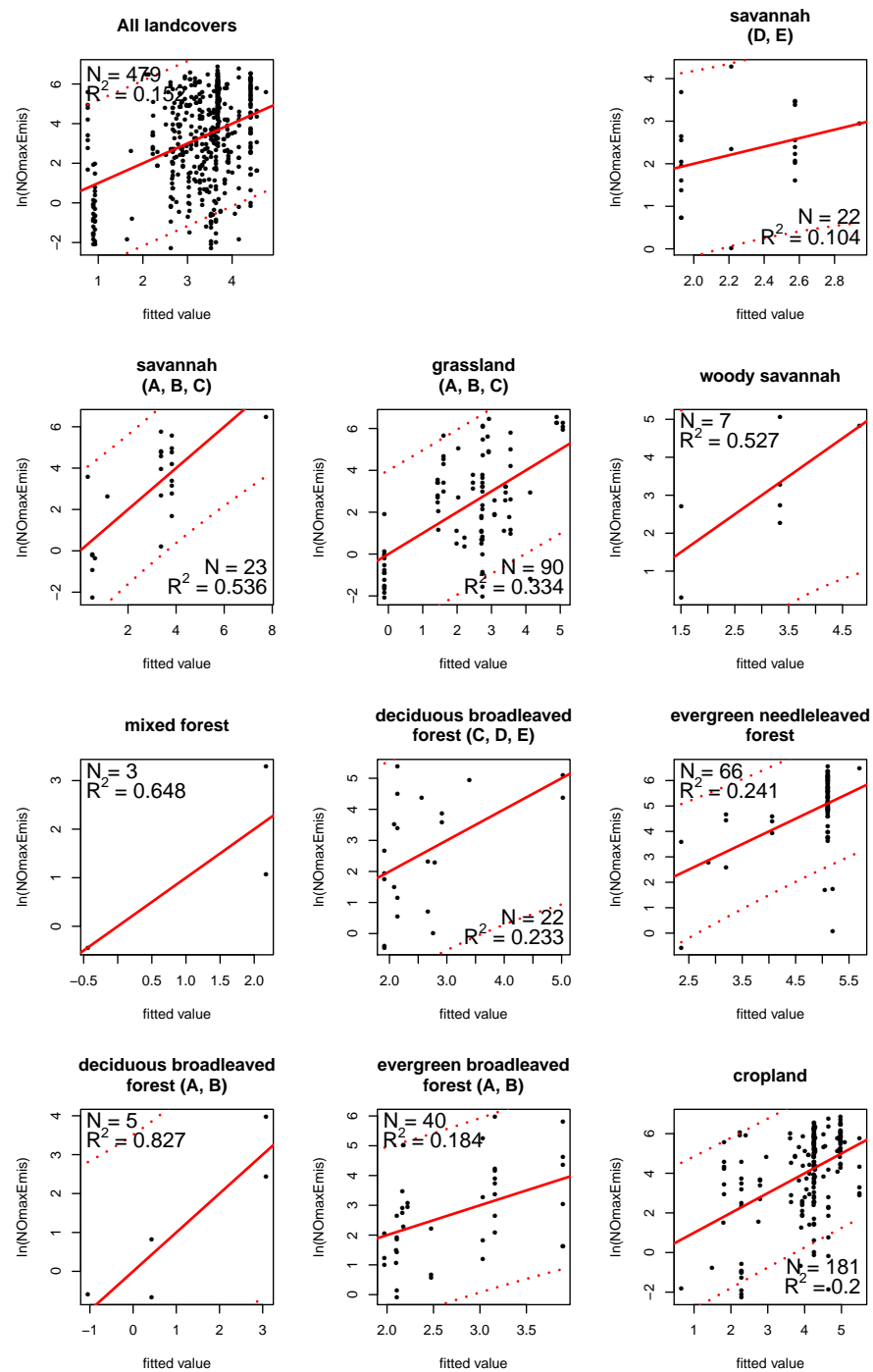


Figure C.4: Regressions of the logarithm of the calculated SNOx flux at the optimum WFPS versus the fitted values, calculated with the derived regression coefficients.

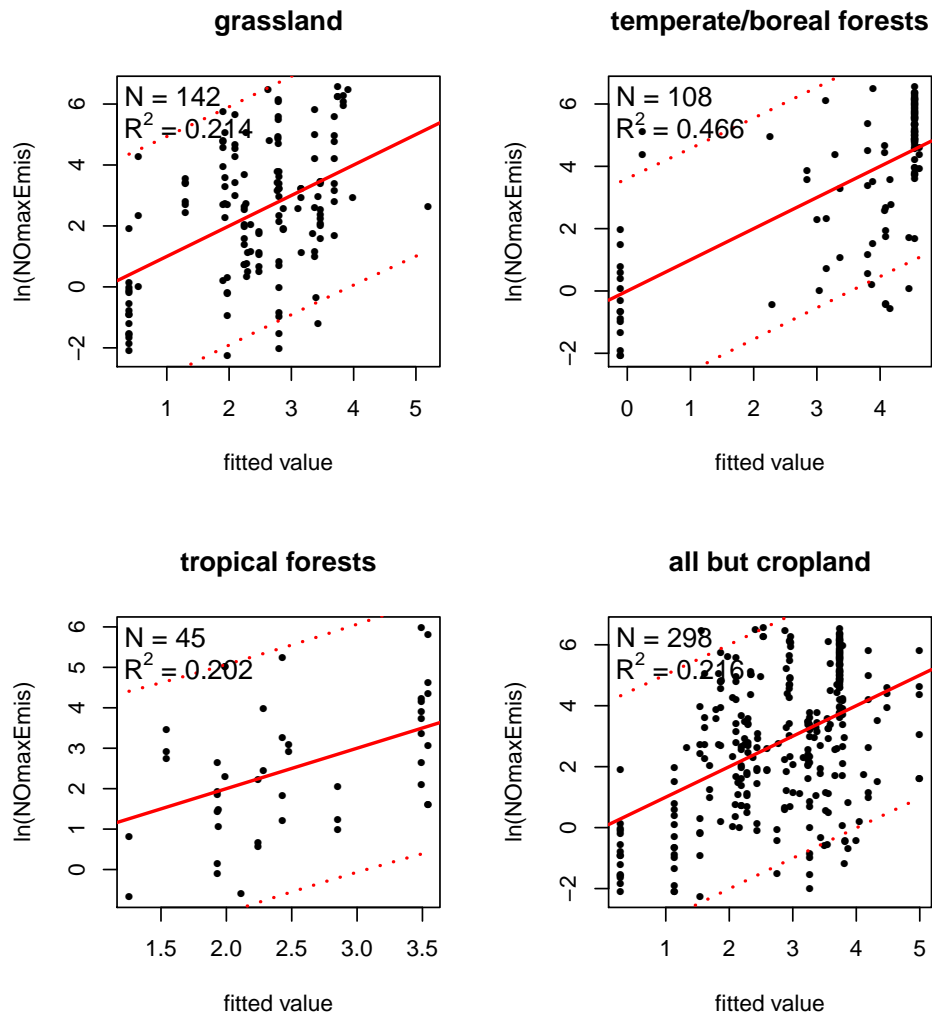


Figure C.5: Regressions of the logarithm of the calculated SNO<sub>x</sub> flux at the optimum WFPS versus the fitted values, calculated with the derived regression coefficients.